Design and advanced characterization of PMMA-coated Ti surfaces for biomedical applications

Melania Reggente

UNIVERSITÉ DE STRASBOURG

ÉCOLE DOCTORALE DE PHYSIQUE ET CHIMIE-PHYSIQUE

Institut de Physique et Chimie des Matériaux de Strasbourg

THÈSE

présentée par :

Melania REGGENTE

soutenue le: **31 Mal 2017**

pour obtenir le grade de : **Docteur de l'université de Strasbourg**

Discipline/ Spécialité : Physique- Chimie Physique

Synthèse et caractérisation multiéchelle de matériaux et de systèmes pour applications biomédicales

THÈSE dirigée par :

Mme CARRADÒ Adele	Professeur, Université de Strasbourg
M ROSSI Marco	Professeur, Sapienza Università di Rome

RAPPORTEURS :

Mme MIGONNEY Véronique	Professeur, Université Paris 13
Mme VERGANI Laura	Professeur, Politecnico di Milano

AUTRES MEMBRES DU JURY :

M PALKOWSKI Heinz	Professeur, Technische Universität Clausthal
Mme MOUGIN Karine	Maître de Conférences HDR, Université Haute-Alsace

Ecole Doctorale de Physique et Chimie-Physique,
Université de Strasbourg

Dottorato in Modelli matematici per l'ingegneria, elettromagnetismo e nanoscienze, XXIX ciclo,
Sapienza Università di Roma

Design and advanced characterization of PMMA-coated Ti surfaces for biomedical application

A Ph.D. Dissertation presented by
Melania Reggente
May 2017

Supervisors
Marco Rossi, Professor, Sapienza Università di Roma
Adele Carradó, Professor, Université de Strasbourg

Jury
Véronique Migonney, Professor, Université Paris 13
Laura Vergani, Professor, Politecnico di Milano
Karine Mougin, Maître de Conférences HDR, Université Haute-Alsace
Heinz Palkowski, Professor, Technische Universität Clausthal

Acknowledgments

First of all, I would like to thank my supervisors Prof. Marco Rossi and Prof. Adele Carradò for giving me the great opportunity to conduct this interesting work in the framework of a joint Ph.D. program between two prestigious Universities. I am sincerely grateful for their constant encouragement and advice to pursue all my objectives, helping me to become more self-confident and independent.

Moreover, I am really thankful to the thesis committee members, Prof. Véronique Migonney, Prof. Laura Vergani, Dr. Karine Mougin and Prof. Heinz Palkowski, for the time they spent to review my thesis.

I kindly acknowledge Prof. Stefan Haacke, the Director of the "Institut de Physique et Chimie des Matériaux de Strasbourg (IPCMS)", Dr. Fabrice Scheurer, leader of the surfaces and interfaces department as well as Prof. Laurent Douce, leader of the organic materials department, to have accepted me in their institute and laboratories.

This multidisciplinary work, at the interface between chemistry, materials science and engineering, gave me the opportunity to work closely with many collaborators from which I have daily "stolen" a bit of knowledge. I am particularly thankful to Dr. Patrick Masson, "mon père scientifique" who patiently introduced me in the chemistry world; his daily guidance has been an essential support for me and the added value for succeeding in this work. Further, I would like to warmly thank Dr. Geneviève Pourroy, for having followed each step of my research and pushing me in developing a more critical point of view. I will never forget their constant availability to discuss with me, helping answering each doubt.

Moreover I would like to thank Dr. Daniele Passeri and Dr. Emanuela Tamburri for inspiring and motivating me to continue doing research. I learned from them the creative part of this job which is become essential for me!

In addition, I am really grateful to Prof. Maria Letizia Terranova and all the students of the MinimaLab who have kindly opened the door of their lab allowing me to learn more about conducting polymers.

A special thanks to Dr. Francesco Mura and Dr. Jacques Faerber for all the hours we spent together in front of the scanning electron microscope; I thank Marco and Livia for all the moments we have shared during these three years and for the fruitful discussions; furthermore, I would like to thank Dr. Spiros Zafeiratos, Dr. Leandro jacomine, Dr. Nihal Engin Vrana for having performed XPS measurements, scratch tests as well as cytotoxicity tests of our samples, respectively. I am kindly thankful Dr. Mohamed Harhash for helping me in the sandwiches production.

I would like also to thank all the member of the "DMO" for the good time spent together. In particular my "Petite Rouge" Mathilde, Senthil and Yannick for their friendship as well as Nicolas Beyer, Emilie Voirin and Benoît Heinrich for the help in the sample preparation.

Furthermore, I would like to thank all my friends for their support. In particular, I would like to thank Giulia and Marzia for their constant presence and for adding colors to my life. Marco and Davide, the right persons met at the right moment, for remembering me how simple and wonderful is to be yourself without fear to be judged. Grazia for making me feel like home when I am far away.

Finally, I would like to greatly thank you my parents Graziella and Ennio for giving me the determination to pursue my goals. Further, I thank my sister Cristiana and my brother Matteo for their unconditional love. Then, I am greatly thankful to Rita, Adele, Nino and Rosy, new members of my family, for your encouragement.

Above all, thank you Totò: for being daily by my side, for giving me the strength when I lost it, for believing in me and for remembering me what love really means.

Contents

Nomenclature **ix**

Introduction **1**
Thesis outline . . . 3
Contribution . . . 4
Bibliography . . . 6

Introduction **8**
Plan de la thèse . . . 12
Bibliography . . . 12

1 Surface-confined polymers: background **15**
1.1 Synthesis of polymer brushes via atom transfer radical polymerization . . . 17
1.1.1 Surface-confined polymers as innovative adhesive layers . . . 19
1.2 Methods for characterizing polymer-coated flat substrates . . . 21
Bibliography . . . 21

2 Materials and methods for the fabrication of PMMA-coated Ti surfaces **31**
2.1 Materials . . . 33
2.1.1 Titanium . . . 33
2.1.2 Polymethyl methacrylate . . . 34
2.2 Synthesis procedure . . . 34
2.2.1 Titanium sample preparation . . . 34
Mechanical polishing . . . 34
Titanium electropolishing . . . 34
2.2.2 Step 1: alkaline activation of Ti substrates . . . 35
2.2.3 Step 2: preparation of ATRP initiator-modified Ti surfaces . . . 36
2.2.4 Step 3: Surface initiated atom transfer radical polymerization (SI-ATRP) of methyl methacrylate . . . 38
2.3 Characterization methodologies . . . 40
2.3.1 Physicochemical characterization . . . 40
2.3.2 Morphological characterization . . . 42
2.3.3 Wettability characterization . . . 42
2.3.4 Mechanical characterization . . . 43
2.3.5 In vitro cytotoxicity evaluation . . . 43
2.3.6 Stability of the tethered polymer layer in simulated body fluid . . . 44
Bibliography . . . 45

3 PMMA-coated Ti fabrication **49**
3.1 Titanium chemical activation: alkali treatment . . . 50
3.1.1 Process optimization: effect of the alkali time treatment . . . 50
3.1.2 Process optimization: effect of the alkali concentration . . . 53
3.1.3 Process optimization: effect of the surface polishing . . . 53
3.1.4 Structure, composition and wettability of the produced microporous interlayer . . . 54
3.2 Ti surface functionalization . . . 57
3.2.1 Structure, composition and wettability of initiator-modified titanium surfaces . . . 58
3.2.2 Removal of physisorbed initiator molecules: the effect of ultrasonic cleaning . . . 61
3.3 Polymerization . . . 64
3.3.1 Structure, composition and wettability of PMMA-coated Ti surfaces 64
3.3.2 PMMA-coated Ti: cross-section analysis . . . 65
3.3.3 Variation of the polymerization initiator size: effect on the PMMA thickness and structure . . . 67
3.3.4 Estimation of the PMMA layer thickness by TGA . . . 69
3.4 Stability and biological properties of PMMA-coated Ti surfaces . . . 70
3.4.1 Stability of PMMA-coated Ti surfaces soaked in saturated simulated body fluid . . . 70
3.4.2 Cytotoxicity evaluation of the PMMA-coated Ti surfaces . . . 72
3.5 Further considerations . . . 74
Bibliography . . . 76

4 Nanomechanical characterization through AFM-based techniques **79**
4.1 Atomic force microscopy: working principle . . . 80
4.1.1 Interaction forces and force-distance curves . . . 82
4.1.2 Operation modes . . . 84
Static modes . . . 85
Dynamic modes . . . 85
4.2 Mechanical characterization at the nanoscale . . . 87
4.2.1 AFM-based nanoindentation . . . 87
4.2.2 Contact Resonance Atomic Force Microscopy . . . 89
4.2.3 HarmoniX^{TM} mode . . . 93
4.2.4 Peak Force Quantitative Nanomechanical Mapping . . . 95
4.3 Case studies: validation of the AFM-based techniques . . . 95
4.3.1 Mechanical characterization of stiff samples: CR-AFM on a thermally treated diaspore . . . 95
4.3.2 Mechanical characterization of soft samples: CR-AFM and HarmoniX^{TM} on polianiline-based nanocomposites . . . 96
4.3.3 Mechanical characterization of soft samples at variable temperature: AFM nanoindentation and CR-AFM of low density polyethylene (LDPE) . . . 98
4.3.4 Viscoelastic characterization of soft samples: CR-AFM on PS-LDPE blends . . . 99

4.3.5 Mechanical characterization of biological samples: CR-AFM as subsurface nanomechanical imaging . . . 100
Bibliography . . . 101

5 Multiscale mechanical characterization of layered PMMA-coated Ti surfaces 107
5.1 Standard methods: depth sensing nanoindentation . . . 109
5.2 AFM-based methods . . . 111
5.2.1 AFM nanoindentation . . . 111
5.2.2 Contact Resonance Atomic Force Microscopy . . . 113
5.2.3 Torsional-harmonic AFM . . . 115
5.2.4 Peak-force quantitative nanomechanical mapping . . . 116
5.3 Comparison and further considerations . . . 117
5.3.1 Evaluation of the adhesion strength: preliminary results . . . 119
Bibliography . . . 122

6 Towards biocompatible Ti/PMMA/Ti sandwich materials 127
6.1 State of the art: sandwich materials as a means to reduce stress-shielding in implants . . . 128
6.2 Fabrication and characterization of Ti/PMMA/Ti sandwich . . . 130
6.2.1 Mechanical behavior of PMMA sheet . . . 131
6.2.2 Ti/PMMA half sandwich production . . . 132
6.2.3 Ti/PMMA bonding strength characterization: shear tests . . . 132
6.2.4 Ti/PMMA/Ti sandwich production . . . 133
6.2.5 Ti/PMMA/Ti bonding strength characterization: rupture tests . . . 133
6.2.6 Ti/PMMA/Ti formability behavior: bending tests . . . 134
6.3 Further considerations . . . 135
Bibliography . . . 135

Conclusion and perspectives 141

Conclusion et perspectives 145

Appendix A Contact resonance atomic force microscopy 145
A.1 Analytical model of the cantilever oscillating in air . . . 146
A.2 Analytical model of the cantilever oscillating in contact with the sample surface . . . 147
Bibliography . . . 148

Appendix B Differential Scanning Calorimetry measurement 151

Appendix C Publications 153

Nomenclature

Acronyms

Ti	Titanium
PMMA	Poly(methyl methacrylate)
ATRP	Atom transfer radical polymerization
Si-ATRP	Surface initiated atom transfer radical polymerization
CuBr	Copper bromide
PMDETA	N,N,N',N',N"- pentamethyldiethylenetriamine
PS	Polystyrene
SBF	Simulated body fluid
PBS	Phosphate-buffered saline solution
ATR-FTIR	Attenuated total reflection Fourier transform infrared spectroscopy
XPS	X-ray photoelectron spectroscopy
EDX	Energy dispersive x-ray diffraction
SEC	Size exclusion chromatography
TGA	Thermogravimetric analysis
ICP-AES	Inductively coupled plasma-atomic emission spectrometry
SEM	Scanning electron microscopy
FIB	Focus ion beam
AFM	Atomic force microscopy
DSI	Depth sensing indentation
R_{tip}	AFM tip radius
Δz	Displacement of the AFM piezoelectric scanner

k_c	AFM cantilever spring constant
f_{0n}	n-th flexural resonance frequency
F_{max}	Maximum applied load on the AFM tip
CR-AFM	Contact resonance atomic force microscopy
CRFs	Contact resonance frequencies
a_c	Tip-sample contact radius
k^*	AFM tip-sample contact stiffness
M_s	Sample's indentation modulus
E	Young's modulus
G	Shear modulus
PF-QNM	Peak force quantitative nanomechanical mapping
UTS	Ultimate tensile strength
USS	Ultimate shear strength

Notations

MP-Ti	Mechanically polished Ti
EP-Ti	Electropolished Ti
Alkali-activated Ti	Ti substrate activated with an alkali-treatment performed in a NaOH solution
C_x initiator-modified Ti	Ti substrate functionalized with an ATRP initiator consisting of x carbon atoms on the alkyl chains
PMMA-coated Ti	Tethered PMMA chains grown on initiator-modified Ti substrates
Ti/PMMA/Ti	Sandwich material
Ti/PMMA	Half sandwich material

Introduction

Skull injuries caused by trauma and pathologies, such as tumour or congenital deformities, require the reconstruction of complex craniofacial prostheses. The choice of suitable biomaterials is the main challenge. Currently, different classes of mono-materials, such as polymers, ceramics and light metals are employed to fabricate skull and mandible prostheses [1]. In particular, poly(methyl methacrylate) [2], polyether ether ketone [3, 4], hydroxyapatite [5–7] and titanium [4, 6, 8] are the most widely used materials in the cranoplasty reconstruction. The discrepancy existing between the mechanical properties and the density of the implant and the bone to be replaced results in stress shielding which represents the most limiting factor for a successful implant repair [9, 10].

Since the mono-materials alone cannot solve this discrepancy in an optimal way, our idea is to combine different monomaterials, such as polymers and metals, in order to design innovative hybrid structures [11]. Indeed, they take the advantage of exploiting both the low density and the lightweight, specific of polymers [12], and the high bending resistance and load capacity of the metals [11]. Therefore, by combining these two different materials, structures possessing new functionalities, such as high energy absorption, high corrosion and mechanical resistance coupled with a lightweight, can be fabricated [13].

In particular, layered structures, such as sandwich materials, composed of metallic skin sheets and a polymer core, can be an interesting alternative to design innovative biomedical prostheses [14]. They are employed in the aircraft and automotive industry because of their high stiffness and strength, good formability and lightweight [11, 15–17]. Previous works have shown that, following the rule of mixture, the mechanical properties of the whole sandwich can be tailored by tuning the thickness of the skin sheets and the core and desired properties can be achieved [14]. In this way, structures with the stiffness and the strength comparable with those of the bone can be fabricated decreasing the bio-mechanical impairment existing between the bone and the implant.

The problem related to these structures is the presence of the toxic epoxy resin, commonly used to stick the polymer core onto the metal skin sheets. The challenge of this work was to design innovative epoxy resin-free sandwich materials. Titanium (Ti) and Poly methymethacrilate (PMMA), the most extensively materials used for biomedical applications, have been used. Our idea is to employ surface-confined PMMA layers as adhesives to stick the polymer core on the metallic skins to design resin-free sandwiches.

To this purpose, a three steps strategy based on a suitable functionalization of Ti surface has been developed (Fig. 1). First of all, a chemical activation of the Ti surface has been performed. Then, a "grafting from" method has been used to immobilize a polymerization initiator on the activated Ti surface. Finally, the polymer chains have been grown from the initiator layer using a surface initiation atom transfer radical polymerization (SI-ATRP). Sandwiches have been then prepared inserting between the two polymer-coated Ti surfaces a thick polymer foil and pressing the three components together above the glass transition temperature of the polymer.

In particular, we have individuated three main objectives to demonstrate the possibility to fabricate resin-free sandwich materials:

- Firstly, the development of a strategy to grow a thick PMMA layer covalently bound on the Ti substrate and to characterize their structural and morphological properties together with the evaluation of their adhesion strength and biocompatibility.

- Secondly, to study the mechanical properties of the grown PMMA layer using ad-

vanced and emerging atomic force (AFM)-based techniques developed for this purpose.

- Thirdly, as proof of concept, the possibility to use tethered polymers as an adhesive layer to fabricate biocompatible two layered Ti/PMMA and three layered Ti/PMMA/Ti sandwiches.

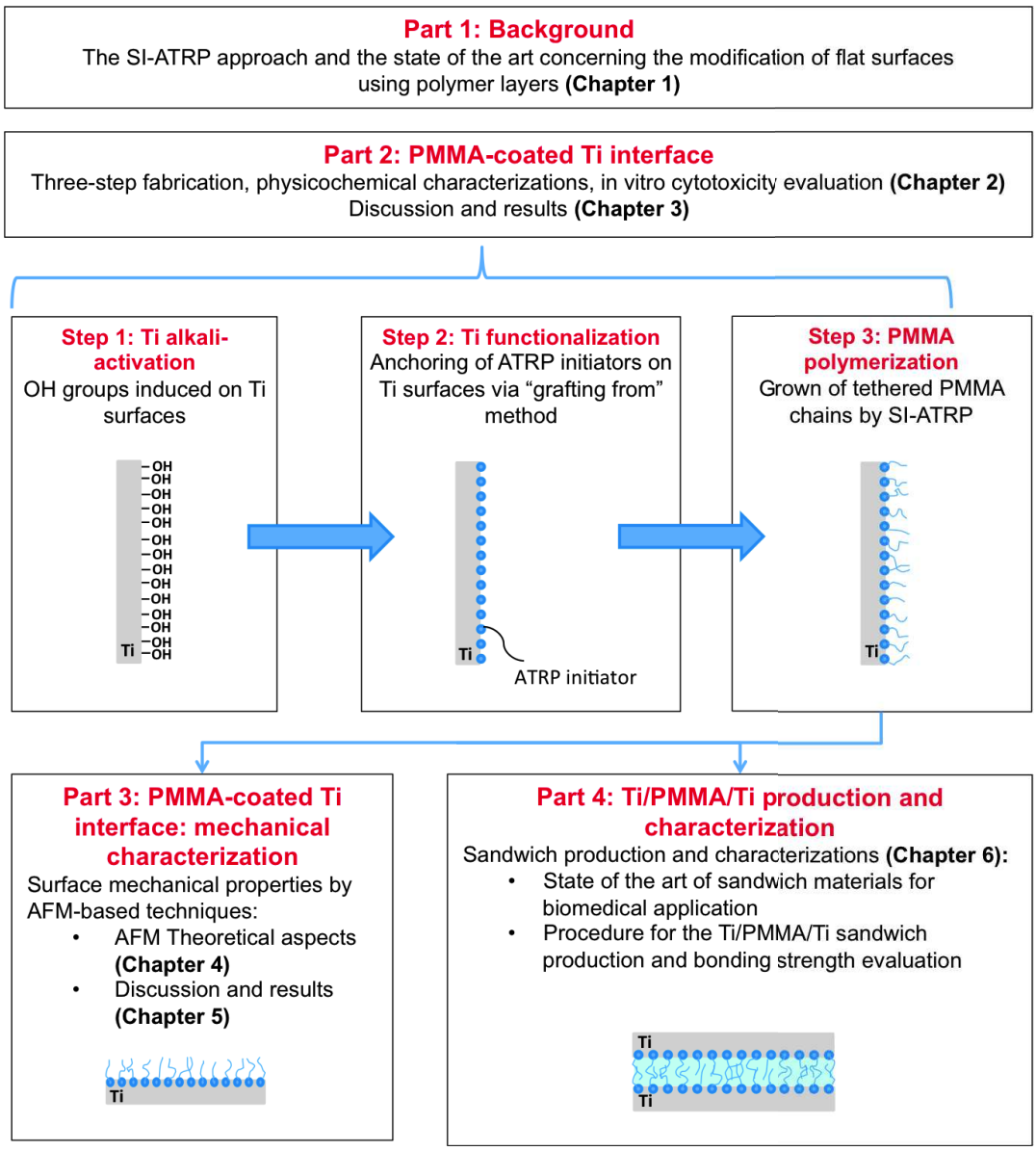

Figure 1: Schematization of the thesis structure.

Thesis outline

The thesis is composed of four main parts. The first one contains the state of the art concerning the fabrication of tethered polymer layers by means of SI-ATRP, focusing on

their application as adhesives. The second reports the three-step methodology employed for covalently binding PMMA chains on the activated Ti surfaces. The structural, chemical and physical characterizations performed after each step of the procedure are presented and discussed. The third part comprises a detailed description of the developed AFM techniques and the procedure employed to analyze the surface mechanical behavior of the PMMA-coated Ti surface. The fourth shows the feasibility of our approach for the fabrication of biocompatible sandwich structures.

More in detail, the six chapters of the thesis are organized as follows.

Chapter 1 contains a general overview about the growth mechanism of tethered polymeric layers on flat metallic substrate, performed by SI-ATRP, and their potential applications as adhesive layers.

Chapter 2 describes the experimental methods employed for the fabrication and characterization of PMMA-coated Ti substrate.

Chapter 3 shows the fabrication of the PMMA-coated Ti samples obtained using the three-steps strategy detailed in Chapter 2. The structure, morphology and chemical composition of the samples after each step of the procedure are detailed. Preliminary investigations of the PMMA-coated Ti biocompatibility and the stability in simulated body fluid (SBF) are also reported.

Chapter 4 illustrates the atomic force microscopy (AFM) based techniques for the mechanical characterization of the PMMA-coated Ti surfaces. It includes: (*i*) a description of AFM working principle; (*ii*) a description of advanced AFM-based techniques for the surface mechanical characterization; (*iii*) an investigation of the surface properties performed on hard and soft specimens, prior to the PMMA-coated Ti. These studies allowed us to validate our approach.

Chapter 5 reports the mechanical characterization of the PMMA-coated Ti interfaces. The results achieved by AFM-based techniques are compared with those extrapolated by standard depth sensing indentation (DSI). The need of a multi-scale characterization in the case of layered material is discussed. Furthermore the semi-quantitative evaluation of the PMMA adhesion strength, determined performing scratch tests, is included.

Chapter 6 briefly illustrates the possibility to tune the sandwich mechanical properties to reach values close to those of the bone. Furthermore, as proof of concept, the preliminary results achieved by using the grown PMMA layer as adhesive agents for the fabrication of in principle biocompatible Ti/PMMA/Ti sandwich materials are illustrated. The parameters of the fabrication and the evaluation of the bonding strength are also presented.

Conclusion completes the thesis summarizing the achieved results and traces the lines for future work.

Contribution

The work was performed by alternating research periods at the Electron Microscopies and Nanoscopies (EMiNa) Laboratory (Sapienza University of Rome) and at the Institut de

Physique et Chimie des Matériaux de Strasbourg (IPCMS, Strasbourg University) in the framework of a joint Ph.D. program, under the supervision of Prof. Marco Rossi, Prof. Adele Carradó, Dr. Geneviève Pourroy and Dr. Patrick Masson. The complementary scientific skills and technological platforms of the two laboratories allowed the synthesis of PMMA-coated Ti layered materials and the development of atomic force microscopy based techniques for the characterization of their surface mechanical properties.

Part of the work of this thesis has been presented at international conferences and in specialized journals. In particular, the work related to the development of AFM-based techniques for the characterization of the surface mechanical properties have been included in the following publications:

- M. Reggente, D, Passeri, L. Angeloni, M. Barteri, F. De Angelis, M. Rossi, "Detection of stiff nanoparticles with cellular structures by contact resonance atomic force microscopy as subsurface nanomechanical imaging", *Accepted to Nanoscale.*

- M. Natali, M. Reggente, D. Passeri, M. Rossi, "Elastic modulus measurements at variable temperature: Validation of atomic force microscopy techniques", *AIP Conference Proceedings* 1749 (1), 020007.

- M. Natali, D. Passeri, M. Reggente, E. Tamburri, M.L. Terranova, M. Rossi, "Contact resonance atomic force microscopy for viscoelastic characterization of polymer-based nanocomposites at variable temperature", *AIP Conference Proceedings* 1749 (1), 020008.

- D. Passeri, M. Reggente, M. Rossi, S.N. Cesaro, V. Guglielmotti, J.J. Vlassak, A.M. De Francesco, R. Scarpelli, M. Hatipoğlu, David Ajó "Contact resonance atomic force microscopy (CR-AFM) in applied mineralogy: the case of natural and thermally treated diaspore", *European Journal of Mineralogy* 28 (2), 273-283.

- M. Reggente, M. Rossi, L. Angeloni, E. Tamburri, M. Lucci, I. Davoli, M.L. Terranova, D. Passeri, "Atomic force microscopy techniques for nanomechanical characterization: A polymeric case study", *JOM*, (4), 849-857.

The multiscale mechanical characterization of PMMA-coated Ti interfaces (shown in Chapter 5) have been presented at the *30th Conference of the European Colloid and Interface Society (ECIS), Rome, 9th September 2016* and included in:

- M. Reggente, M. Natali, D. Passeri, M. Lucci, G. Pourroy, P. Masson, H. Palkowski, M. Rossi, A. Carradó, "Multiscale characterization of hybrid Ti/PMMA materials", *Submitted to Colloids and Surfaces A: Physicochemical and Engineering Aspects.*

The strategy developed to synthesize tethered PMMA chains on alkali-activated Ti surfaces, the evaluation of their adhesion strength and biocompatibility have been comprised in:

- M. Reggente, P. Masson, H. Palkowski, S. Zafeiratos, M. Rossi, G. Pourroy, A. Carradó, "Thick PMMA layer covalently grafted on alkali-activated Titanium surfaces using surface initiated atom transfer radical polymerization", *In preparation.*

Bibliography

[1] S. Aydin, B. Kucukyuruk, B. Abuzayed, S. Aydin, G. Z. Sanus, *et al.*, "Cranioplasty: review of materials and techniques," *Journal of Neurosciences in Rural Practice*, vol. 2, no. 2, p. 162, 2011.

[2] T. Origitano, R. Izquierdo, and L. B. Scannicchio, "Reconstructing complex cranial defects with a preformed cranial prosthesis," *Skull Base Surgery*, vol. 5, no. 02, pp. 109–116, 1995.

[3] B. Lethaus, Y. Safi, M. ter Laak-Poort, A. Kloss-Brandstätter, F. Banki, C. Robbenmenke, U. Steinseifer, and P. Kessler, "Cranioplasty with customized titanium and PEEK implants in a mechanical stress model," *Journal of Neurotrauma*, vol. 29, no. 6, pp. 1077–1083, 2012.

[4] A. Thien, N. K. King, B. T. Ang, E. Wang, and I. Ng, "Comparison of polyetheretherketone and titanium cranioplasty after decompressive craniectomy," *World neurosurgery*, vol. 83, no. 2, pp. 176–180, 2015.

[5] B. L. Eppley, L. Hollier, and S. Stal, "Hydroxyapatite cranioplasty: 2. clinical experience with a new quick-setting material," *Journal of Craniofacial Surgery*, vol. 14, no. 2, pp. 209–214, 2003.

[6] Y. Ducic, "Titanium mesh and hydroxyapatite cement cranioplasty: a report of 20 cases," *Journal of Oral and Maxillofacial Surgery*, vol. 60, no. 3, pp. 272–276, 2002.

[7] P. D. Costantino, C. D. Friedman, K. Jones, L. C. Chow, and G. A. Sisson, "Experimental hydroxyapatite cement cranioplasty.," *Plastic and Reconstructive Surgery*, vol. 90, no. 2, pp. 174–hyhen, 1992.

[8] M. Cabraja, M. Klein, and T.-N. Lehmann, "Long-term results following titanium cranioplasty of large skull defects," *Neurosurgical Focus*, vol. 26, no. 6, p. E10, 2009.

[9] M. Ridzwan, S. Shuib, A. Hassan, A. Shokri, and M. M. Ibrahim, "Problem of stress shielding and improvement to the hip implant designs: a review," *Journal of Medical Science*, vol. 7, no. 3, pp. 460–467, 2007.

[10] A. J. Ruys, *Biomimetic biomaterials: structure and applications*. Elsevier, 2013.

[11] B. Harris, "A perspective view of composite materials development," *Materials & Design*, vol. 12, no. 5, pp. 259–272, 1991.

[12] R. F. Landel and L. E. Nielsen, *Mechanical properties of polymers and composites*. CRC Press, 1993.

[13] O. T. Thomsen, E. Bozhevolnaya, and A. Lyckegaard, *Sandwich Structures 7: Advancing with Sandwich Structures and Materials: Proceedings of the 7th International Conference on Sandwich Structures, Aalborg University, Aalborg, Denmark, 29-31 August 2005*. Springer Science & Business Media, 2006.

[14] M. Harhash, A. Carradò, and H. Palkowski, "Lightweight titanium/polymer/titanium sandwich sheet for technical and biomedical application," *Materialwissenschaft und Werkstofftechnik*, vol. 45, no. 12, pp. 1084–1091, 2014.

[15] G. D. Parfitt, *Adsorption from solution at the solid/liquid interface*. Academic Pr, 1983.

[16] L. Librescu and T. Hause, "Recent developments in the modeling and behavior of advanced sandwich constructions: a survey," *Composite structures*, vol. 48, no. 1, pp. 1–17, 2000.

[17] O. A. Sokolova, A. Carradò, and H. Palkowski, "Metal–polymer–metal sandwiches with local metal reinforcements: A study on formability by deep drawing and bending," *Composite Structures*, vol. 94, no. 1, pp. 1–7, 2011.

Introduction

Les dispositifs prothétiques constituent actuellement un domaine de recherché très actif aussi bien en recherche fondamentale, pour améliorer les propriétés mécaniques ou la biocompatibilité, qu'en ingénierie pour concevoir les formes les mieux adaptées pour remplacer la partie défectueuse du squelette. Pour certaines parties de ce dernier, et plus particulièrement en chirurgie cranio-faciale, il faut construire des dispositifs capables par exemple de résister à des sollicitations mécaniques complexes (mâchoire), de protéger le cerveau (boite crânienne) et cela tout en respectant les conditions de biocompatibilité. Les matériaux habituellement utilisés pour fabriquer des prothèses crâniennes ou mandibulaires sont des polymères, des céramiques ou des métaux légers [1]. Les plus utilisés sont le polyméthacrylate de méthyle (PMMA) [2], le polyétheréthercétone [3, 4], l'hydroxyapatite [5–7]ou le titane [4, 6, 8]. Cependant, l'écart entre la densité et les propriétés mécaniques de l'implant et celles de l'os conduit à une mauvaise répartition des contraintes mécaniques, ou "stress shielding", entre l'os environnant et l'implant. Ceci est le facteur qui limite le plus le succès de la prothèse [9, 10].

Un matériau seul ne peut pas supprimer cet écart et les contrainte induites, donc nous avons décidé de combiner des matériaux métalliques et polymères afin d'allier leurs propriétés dans un matériau innovant [11]. En effet, de tels systèmes peuvent tirer avantage de la faible densité et du faible poids des polymères d'une part [12], et de la résistance à la flexion et à la charge des métaux d'autre part [11]. La combinaison de ces deux types de matériaux entre eux permettra d'obtenir des dispositifs possédant de nouvelles propriétés comme une absorption d'énergie élevée, une bonne résistance mécanique et à la corrosion couplé avec un faible poids [13].

Les structures en couches, comme les matériaux sandwichs, formées de deux feuilles métalliques séparées par une feuille de polymère sont de bons candidats pour des prothèses innovantes [14]. Les matériaux sandwichs sont très utilisés dans l'industrie automobile et aéronautique à cause de leur rigidité et résistance élevées, leur bonne formabilité et leur faible poids [11, 15–17]. D'autre part des études antérieurs ont montré que les propriétés mécaniques du sandwich suivent une loi de mélange et que les caractéristiques voulues peuvent être obtenues en contrôlant l'épaisseur des feuilles de métal et de polymère [14]. Ainsi, des matériaux structurés avec une rigidité et une résistance proche de celle de l'os peuvent être obtenues, rendant possible une bonne adaptation de l'implant à l'os.

L'adhésion entre le polymère et le métal des sandwichs produit actuellementest obtenue par utilisation de colle époxy qui n'est pas biocompatible. Le but de notre travail a donc été de concevoir des matériaux sandwichs sans cette colle époxy. Le titane et le PMMA sont les matériaux les plus utilisés dans les applications biomédicales, aussi nous les avons choisis comme composants de base. Pour cela, nous avons élaboré des interfaces Ti/polymère dans lesquelles le métal et le polymère sont liés par une liaison covalente; cette couche polymère permettra ultérieurement l'adhésion entre le métal et une feuille de polymère qui constituera le cœur du sandwich. Dans ce but, nous avons développé une stratégie en trois étapes permettant d'obtenir une fonctionnalisation de la surface du titane. Tout d'abord, cette surface a été activée chimiquement; ensuite un initiateur de polymérisation y a été greffé defaçon covalente. Enfin, la croissance des chaines polymères a été obtenue en utilisant une polymérisation par transfert d'atomes à partir de l'initiateur (SI-ATRP). Les sandwichs ont été préparés en insérant une feuille de polymère entre les deux feuilles de Ti recouvertes de polymère greffé et en pressant les trois composants à une température supérieure à celle de la transition vitreuse du polymère. La réussite de notre projet, à savoir la fabrication d'un sandwich Ti/polymère/Ti biocompatible sans colle époxy a nécessité

trois avancées scientifiques et technologiques :

- Le développement d'une stratégie pour faire croître une couche de PMMA épaisse liée de manière covalente sur le substrat de Ti, puis la caractérisation morphologique et structurale et également l'évaluation de l'adhésion et de la biocompatibilité.
- Le développement des technique AFM, mise au point et testée sur d'autres matériaux, qui a permis d'étudier les propriétés mécaniques de la couche de polymère greffé.
- La possibilité d'utiliser cette couche de polymère lié à la surface du titane comme couche adhésive pour fabriquer des matériaux biocompatibles soit bi-couches Ti/PMMA soit des matériaux sandwichs tri-couches Ti/PMMA/Ti.

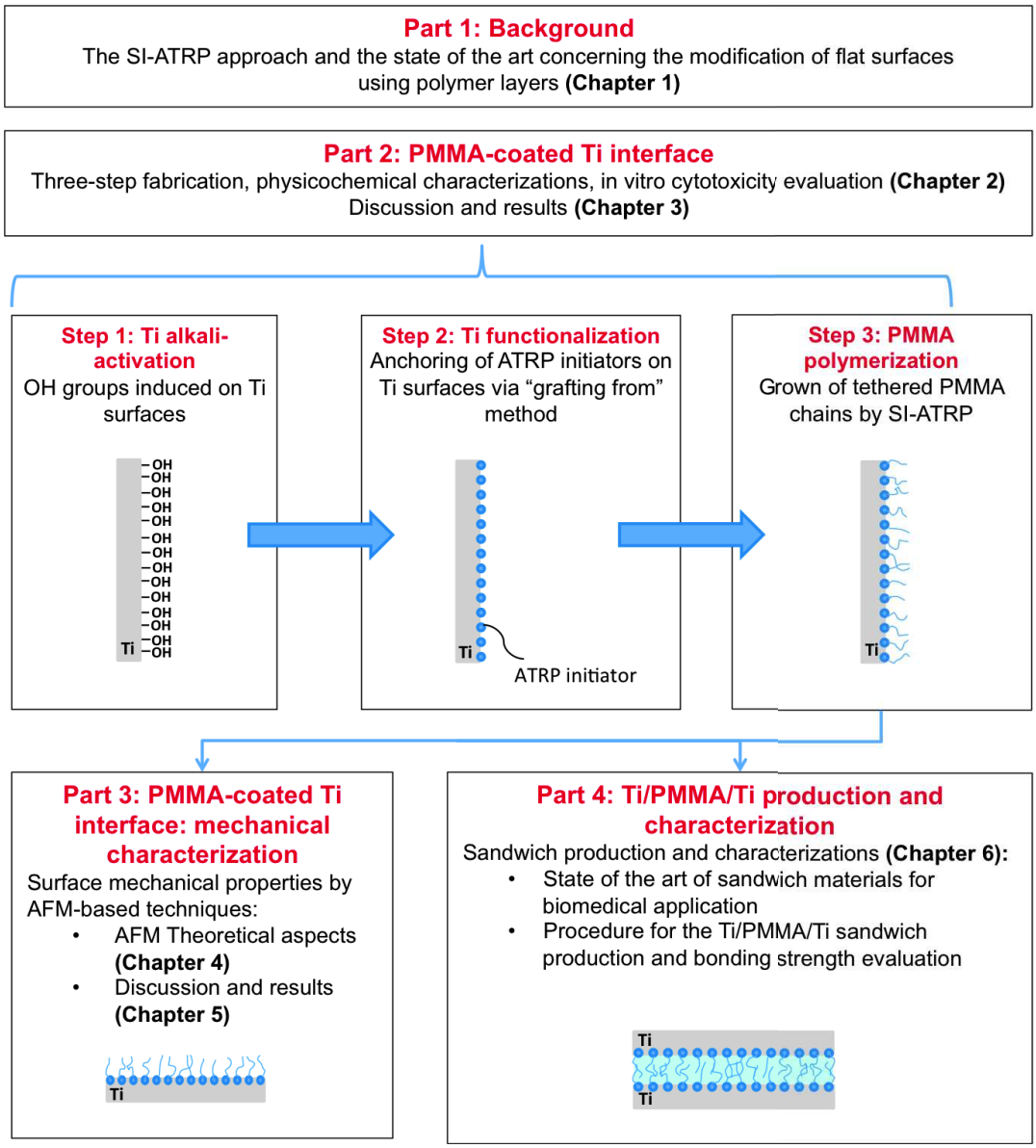

Figure 2: Schematization of the thesis structure.

Plan de la thèse

La thèse comporte quatre parties principales (Fig. 2). La première présente l'état de l'art sur la fabrication de couches de polymères attachées à une surface par Si-ATRP, en mettant l'accent sur leur utilisation comme adhésifs. La deuxième expose les trois étapes de l'élaboration d'une couche de PMMA fixée par une liaison covalente à la surface du titane. Les caractérisations physico-chimiques réalisées après chaque étape sont présentées. Une description détaillée de la technique AFM et de la procédure utilisée pour analyser les propriétés mécaniques du système Ti/PMMA sont exposées dans la troisième partie. Enfin, la dernière partie traite de la possibilité d'obtenir des biomatériaux sandwichs.

La thèse est organisée en six chapitres:

Le **chapitre 1** présente une vue générale sur les mécanismes de croissance de couches de polymères attachées sur des surfaces métalliques planes, obtenues par SI-ATRP et la possibilité de les utiliser comme couche adhésive.

Dans le **chapitre 2**, les méthodes expérimentales utilisées pour la fabrication et la caractérisation du système Ti/PMMA sont décrites.

Les résultats des caractérisations physico-chimiques après chaque étape de l'élaboration du système bi-couche Ti/PMMA sont détaillés dans le **chapitre 3**. Les premiers résultats de l'étude de la biocompatibilité de l'interface Ti/PMMA et de sa stabilité dans un fluide corporel simulé sont exposés.

La technique de microscopie par force atomique (AFM) utilisée pour caractériser les propriétés mécaniques de l'interface Ti/PMMA fait l'objet du **chapitre 4**. Il comprend (*i*) une description du principe de fonctionnement de l'AFM ; (*ii*) une description de la technique AFM mise au point dans cette thèse pour la caractérisation des propriétés mécaniques de la surface ; (*iii*) une étude des propriétés de surface d'échantillons durs et mous avant l'étude de l'interface Ti/PMMA. Ces études nous permettent de valider notre méthode.

Le **chapitre 5** est consacré à la caractérisation des propriétés mécaniques du système Ti/PMMA. Les résultats obtenus par la technique AFM sont comparés à ceux obtenus par nanoindentation. La nécessité d'une caractérisation multi échelle dans le cas de matériaux en couches est discutée. De plus, l'évaluation semi-quantitative de la force d'adhésion par des scratch tests est incluse.

Le **chapitre 6** montre la possibilité de contrôler les propriétés mécaniques des sandwichs pour obtenir un matériau proche de l'os dans ses caractéristiques mécaniques et d'utiliser la couche de PMMA greffée sur le titane comme adhésif. Les paramètres de fabrication et l'évaluation de la liaison titane/polymère sont présentés.

La **conclusion** résume les résultats obtenus et présente les perspectives de ce travail.

Bibliography

[1] S. Aydin, B. Kucukyuruk, B. Abuzayed, S. Aydin, G. Z. Sanus, *et al.*, "Cranioplasty: review of materials and techniques," *Journal of Neurosciences in Rural Practice*, vol. 2, no. 2, p. 162, 2011.

[2] T. Origitano, R. Izquierdo, and L. B. Scannicchio, "Reconstructing complex cranial defects with a preformed cranial prosthesis," *Skull Base Surgery*, vol. 5, no. 02, pp. 109–116, 1995.

[3] B. Lethaus, Y. Safi, M. ter Laak-Poort, A. Kloss-Brandstätter, F. Banki, C. Robbenmenke, U. Steinseifer, and P. Kessler, "Cranioplasty with customized titanium and PEEK implants in a mechanical stress model," *Journal of Neurotrauma*, vol. 29, no. 6, pp. 1077–1083, 2012.

[4] A. Thien, N. K. King, B. T. Ang, E. Wang, and I. Ng, "Comparison of polyetheretherketone and titanium cranioplasty after decompressive craniectomy," *World neurosurgery*, vol. 83, no. 2, pp. 176–180, 2015.

[5] B. L. Eppley, L. Hollier, and S. Stal, "Hydroxyapatite cranioplasty: 2. clinical experience with a new quick-setting material," *Journal of Craniofacial Surgery*, vol. 14, no. 2, pp. 209–214, 2003.

[6] Y. Ducic, "Titanium mesh and hydroxyapatite cement cranioplasty: a report of 20 cases," *Journal of Oral and Maxillofacial Surgery*, vol. 60, no. 3, pp. 272–276, 2002.

[7] P. D. Costantino, C. D. Friedman, K. Jones, L. C. Chow, and G. A. Sisson, "Experimental hydroxyapatite cement cranioplasty.," *Plastic and Reconstructive Surgery*, vol. 90, no. 2, pp. 174–hyhen, 1992.

[8] M. Cabraja, M. Klein, and T.-N. Lehmann, "Long-term results following titanium cranioplasty of large skull defects," *Neurosurgical Focus*, vol. 26, no. 6, p. E10, 2009.

[9] M. Ridzwan, S. Shuib, A. Hassan, A. Shokri, and M. M. Ibrahim, "Problem of stress shielding and improvement to the hip implant designs: a review," *Journal of Medical Science*, vol. 7, no. 3, pp. 460–467, 2007.

[10] A. J. Ruys, *Biomimetic biomaterials: structure and applications*. Elsevier, 2013.

[11] B. Harris, "A perspective view of composite materials development," *Materials & Design*, vol. 12, no. 5, pp. 259–272, 1991.

[12] R. F. Landel and L. E. Nielsen, *Mechanical properties of polymers and composites*. CRC Press, 1993.

[13] O. T. Thomsen, E. Bozhevolnaya, and A. Lyckegaard, *Sandwich Structures 7: Advancing with Sandwich Structures and Materials: Proceedings of the 7th International Conference on Sandwich Structures, Aalborg University, Aalborg, Denmark, 29-31 August 2005*. Springer Science & Business Media, 2006.

[14] M. Harhash, A. Carradò, and H. Palkowski, "Lightweight titanium/polymer/titanium sandwich sheet for technical and biomedical application," *Materialwissenschaft und Werkstofftechnik*, vol. 45, no. 12, pp. 1084–1091, 2014.

[15] G. D. Parfitt, *Adsorption from solution at the solid/liquid interface*. Academic Pr, 1983.

[16] L. Librescu and T. Hause, "Recent developments in the modeling and behavior of advanced sandwich constructions: a survey," *Composite structures*, vol. 48, no. 1, pp. 1–17, 2000.

[17] O. A. Sokolova, A. Carradò, and H. Palkowski, "Metal–polymer–metal sandwiches with local metal reinforcements: A study on formability by deep drawing and bending," *Composite Structures*, vol. 94, no. 1, pp. 1–7, 2011.

Chapter 1

Surface-confined polymers: background

Modification of the metal surface properties by coating them with organic layers is a field of extreme interest in many industrial sectors, such as electronics, automotive and biomedical applications. In fact, it allows tailoring several interfacial properties, such as adhesion, wetting, elasticity and biocompatibility [1]. In particular, in the field of biomaterials, polymeric coatings can be used to achieve specific properties. Among the others, they can improve the osseointegration between the implant and the surrounding bone [2, 3] and/or producing antibacterial or protein-repellent surfaces [4–6].

In general, the metal-polymer adhesion involves many types of interactions, ranging from weak interactions to covalent bonds. The first ones include the electrostatic and the hydrophobic interactions, as well as the hydrogen bondings. They are mainly due to physical adsorptions of the polymer chains onto metal substrates produced by: chemical/physical deposition techniques (i.e., spin-coating, dip-coating or spray-coating), layer-by-layer deposition (driven by electrostatic interactions), absorption from solution (i.e. self assembly monolayers) or Langmuir-Blodgett technique (generated by hydrophobic interactions) [7, 8]. Even though these techniques allow a simple fabrication of polymer-coated surfaces, their durability is strictly related to the nature of the polymer-metal interface which strongly depends on the adhesion strength between the two components. Indeed, since chemical bonding between the metal and the polymer layer does not occur spontaneously, layered hybrid organic-inorganic materials may undergo premature and undesirable delamination phenomena, caused by the weak adhesion existing between the organic layer and the metal [9], affecting the life-time of the entire system [10].

In order to improve their long-term stability and in-service durability, grafted polymers (namely, polymer chains covalently bound to the surfaces) have been recently proposed as adhesive layers to be inserted between the metal substrate and the polymer coating to strengthen their adhesion [10, 12–14]. Thus, many efforts have been devoted to synthesize grafted polymers controlling both the polymer thickness and the adhesion strength. As depicted in Fig. 1.1, two different approaches can be used to link polymers chains on metal surfaces: "grafting to" or "grafting from" methods [15–17]. The former requires the synthesis of end-functionalized polymers, i.e. polymer chains (blue lines in Fig. 1.1) terminated with functional groups (pink spheres) and their adsorption, through either physical or covalent bonds, to surface functional groups (pink semi-spheres) [18]. Although it allows fully characterizing the polymer before the grafting reaction, its efficiency decreases with the increase of the polymer weight. Indeed, steric repulsions generated by the already anchored chains, may obstruct the diffusion of the macromolecules toward the surface, preventing the formation of thick and dense polymer layers [18, 19].

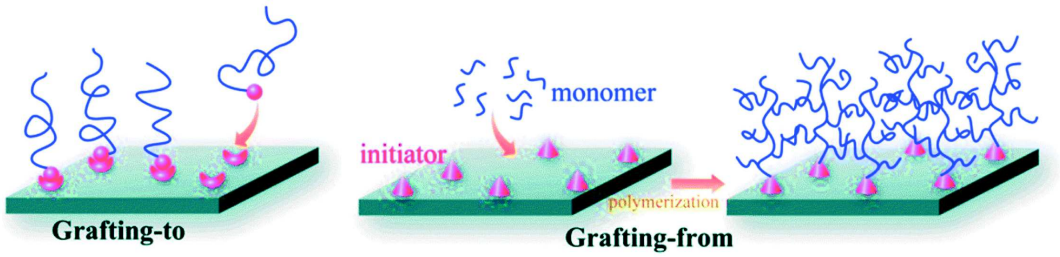

Figure 1.1: Schematic illustration of the polymer chains anchorage on solid surfaces: 'grating to' and 'grafting from' methods [11].

Whereas, the "grafting from" method involves the growth of the polymer chains from initiator-modified surfaces (in Fig. 1.1 the initiators are depicted as pink cones) through surface-initiated polymerizations [20]. It allows an easier diffusion of monomer molecules toward the surface-attached propagating radicals. This implies a higher graft densities enabling the fabrication of denser, thicker and more stable organic layers with a better control of the polymer thickness [19, 21].

Surfaces of almost any kind of nature (oxide, metals and/or polymers) and geometries (nanoparticles, porous and flat surfaces) have been covalently modified with the 'grafting from' method using several anchoring groups, such as, thiols ($-$SH) [22, 23], silanes ($-SiH_4$) [24] and phosphonic acids ($-PO(OH)_2$) [25, 26]. Besides, from these initiator-modified surfaces, polymer chains can be grown adopting controlled radical polymerization techniques [27]: atom transfer radical polymerization (ATRP) [28–30], ring opening metathesis polymerization (ROMP) [31], nitroxide-mediated polymerization (NMP) [32], or reversible addition fragmentation chain transfer (RAFT) polymerization [33]. carboxylic acids ($-$COOH) [34], Among them, ATRP is one of the most interesting and versatile methods to grow polymer controlling chains length and composition. Since ATRP has been the technique used in this thesis, in the following sections we will present its general mechanism giving an overview of the works related to the surface modification performed by ATRP, focusing on the growth of PMMA brushes on metallic flat surfaces.

1.1 Synthesis of polymer brushes via atom transfer radical polymerization

SI-ATRP is the most widespread method used to synthesize polymer brushes (i.e. polymer chains with an end tethered on a surface) through the "grafting from" approach [20, 27, 35, 36] allowing an accurate control on their molecular weight and polydispersity. It is based on the ATRP, introduced in the 1995 by Matyjaszewski et al. [37], who proposed a controlled radical polymerization of acrylates, based on the radical addition reaction of the monomer catalyzed by a reversible redox reaction of a transition metal complex. The task of the transition metal complex is to produce active species - radicals and/or macro radicals - where the monomer can be added [20, 29, 30, 38].

The general mechanism of the reaction is depicted in Fig. 1.2. At the beginning of the reaction, the system is composed of a monomer (M), a polymerization initiator (R$-$X, called dormant species) and a catalyst consisting in a transition metal ($M_t{}^nX$) complexed with a suitable ligand (L). L has to enhance the solubility of the transition metal salt in organic media and adjust the redox potentials of the transition metal. In most cases, copper salts (e.g. copper bromide) are used as transition metal complex and nitrogen-based ligands are used as catalysts [35].

The reaction starts when the homolytic dissociation of the carbon-halogen bond (C$-$X), in the initiator chains, takes place. The transfer of the halogen element (X) from the dormant species to the transition metal complex (i.e. ATRP catalyst), results in a reversible oxidation of the metal complex. It causes the simultaneous formation of (*i*) the complex in its higher degree of oxidation ($X-M_t{}^{n+1}$), and (*ii*) the active species ($R\cdot$). At this point, the monomer (M) can either be added at the active species or react with ($X-M_t{}^{n+1}$/L, called *deactivator*) to form the dormant species R$-$X regenerating the *activator* ($M_t{}^n$/L).

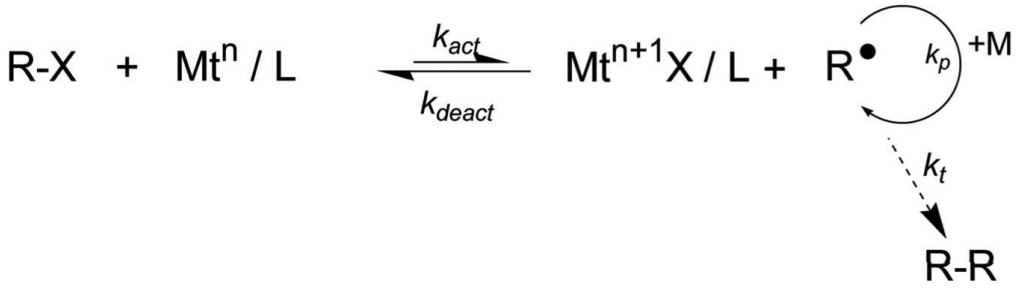

Figure 1.2: Schematization of the general ATRP mechanism, where: Mt^n is the transition metal; L is the complexing ligand; R the initiate or polymer chain and X the halogen element.

Then, the R−X species can be further activated, by transferred the halogen to the regenerated metal complex, and can react again with the monomer letting the polymerization proceed.

In this polymerization technique, the control over molecular weight, composition, and polydispersity is maintained establishing a rapid equilibrium between the dormant and the propagating species that is predominately shifted to the side of the dormant species ($k_{act} \ll k_{deact}$). In this way, the radical-radical termination reactions are prevented and each growing chain has the same probability to propagate resulting in polymer layers characterized by narrow molecular weight distributions and low polydispersity.

The use of SI-ATRP to grow poly(acrylamide) brushes from benzylchloride-functionalized silica particles has been firstly reported in 1997 by Huang et al. [39]. Successively, Ejaz et al. grown PMMA brushes from 2-(4-chlorosulfonylphenyl)ethyl silane self-assembled monolayers. They have reported that, because of the low concentration and accessibility of the dormant species attached on the surface, with respect to conventional solution ATRP, the introduction (in the reactive media) of sacrificial initiators, allows a better control over the polymerization reaction [40, 41]. Furthermore, assuming that the surface polymerization occurs with the same rate as solution polymerization, the polymer grown by the sacrificial initiator addition can be used to measure its molecular weight (M_w) [27, 42]. It can be useful especially to analyze polymers grown on flat macroscopic substrates that prevent their measurement with a conventional technique, such as, the size-exclusion chromatography (SEC). Nonetheless, it was recently reported that while M_w of tethered chains grown on convex geometry (e.g. spherical nanoparticles) is close to the M_w of polymer grown in solution [43,44]; it is usually lower than that of free polymers [45]. Indeed, surface-confined chains grown on flat or porous (concave) substrates have less degree of freedom and the diffusion of catalysts and monomers towards the growing chains are limited by confinement effects [46–48]. In particular, it has been reported that, as the confinement effect increases, the M_w of the PMMA brushes diminishes [45].

Another way to deal with the low dormant species concentration was proposed by Matyjaszewski et al. studying the synthesis of polystyrene (PS) brushes from bromoisobutyrate-functionalized silicon wafers. They underlined that by adding deactivators (e.g. copper(II)bromide) a linear growth of the polymer thickness as function of the time can be

achieved, suggesting the living character of the reaction [29]. Moreover, the effect of different high CuII/CuI ratios on the synthesis of PMMA brushes was studied. It was shown that high CuII/CuI ratio gives rise to a denser polymer layers highlighting that chain termination reactions are mainly provoked by a crowded environment [48, 49].

Furthermore, it has been shown that the rate of the polymerization can be further enhanced by adding an accelerator of polymerization, such as malononitrile, in the reactive media [50]. According to the proposed mechanism, the malononitrile reacts with the ligand to weaken the transition metal coordination favoring its oxidation [50].

SI-ATRP allows polymer brushes of different compositions to be grown from substrates of various geometry and nature (silica nanoparticles, silicon wafers, titanium, stainless steel, gold, carbon, and polymers) [20] through the immobilization of several anchoring groups. Among them, a large number of works relate with the modification of nanoparticles. Gold nanoparticles, generally functionalized through thiols groups, have been coated with PMMA layers [22,51]; whereas, silica (modified by silylated initiators) [46,52] and iron oxide (functionalized via phosponic acid and sulfonyl chloride goups) [53, 54] nanoparticles have been modified with both PS and PMMA brushes.

Moreover, even though most of the works concerns the modification of spherical nanoparticles, in the last years a growing interest on the SI-ATRP from flat surfaces has been observed. PMMA has been grown on silicon surfaces, modified with dimethylchlorosilane [55] and on trichlorosilane-functionalied porous alumina [45, 56]; whereas Borozenko et al. have reported the controlled ATRP of polyelectrolytes using organophosphonic acids as initiators covalently linked to silica and mica substrates [57].

Regarding metal surfaces, the majority of works, pertains to their growth of thin polymeric layers for the fabrication of joints with an increased polymer-metal adhesion [12, 13, 25, 58] or to confer biocompatibility and/or antimicrobial properties [59, 60]. In particular, stainless steel has been covered with few dozens of nanometers of PMMA anchored on the surface through a phosphonate or a benzyl group. [12, 58]. Besides, the work of Minet et al. [58] showes, for the first time, the possibility to graft PS, PMMA and a diblock copolymer (PS-b-PMMA) from flat metallic surfaces (stainless steel) modified with 11-(2-bromoisobutyrate)-undecyl-1-phosphonic acid initiatiors. The same initiator has been successfully grafted on Ti substrates and used as initiator for the ATRP of PS [25]. Compared to solution ATRP and SI-ATRP from nanoparticles, in which the same molar quantities of initiator and catalysts have been used, SI-ATRP from flat surfaces have been generally performed with an excess of catalysts [19, 25, 58, 61, 62].

1.1.1 Surface-confined polymers as innovative adhesive layers

In this context, in the last decades, grafted polymers have been proposed as adhesives layers to be introduced between two components requiring to be connected (e.g. a metal substrates and a polymer coating) [10, 12, 14, 63]. In particular, it has been shown that by exploiting the miscibility between the surface-confined polymer chains and those of a bulk [64–66], melt [12] or solution polymer [14], the metal/polymer adhesion strength can be enhanced and their durability ameliorated [10, 12, 14]. Indeed, when two compatible polymers (i.e. polymer of the same nature) enter in intimate contact, a partial interpenetration between the chains of two materials is established, according to the diffusion theory described by the reptation model [67–69]. As a result, entanglements points are created and a mixing zone achieved [65,66] (see Fig. 1.3 in the particular case of tethered polymer

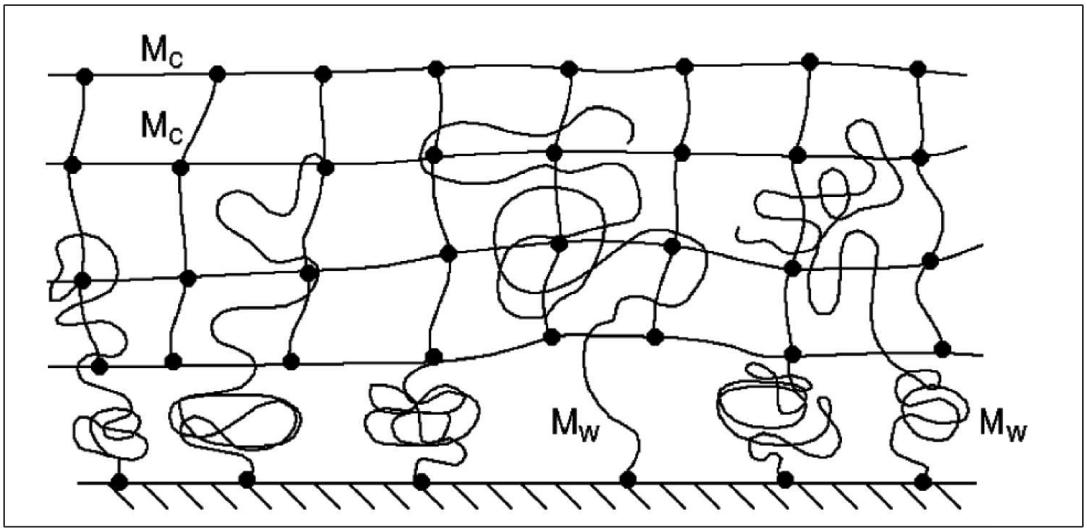

Figure 1.3: Schematic representation of surface-confined polymer chains (with a defined molecular weight equal to M_w) interpenetrating in a cross-linked polymer matrix characterized by a molecular weight of M_c [65].

adhering on cross-linked polymer matrix).

Theoretical studies and simulations have highlighted that the degree of interpenetration depends on three main factors: (*i*) the brushes surface density (i.e. the number of grafted chain per nm^2, σ); (*ii*) the brushes chains lenght; and (*iii*) the molecular weight dispersity (MWD) [65, 66, 70, 71]. In general, long chains in the low-density regime (also called as *mushroom regime*) are required to obtain a good penetration. Indeed, in the mushroom regime the overlap between adjacent chains are avoided or reduced and, since they are separated enough from one another, they can move and interpenetrate in the adhering material. If the surface density increases exceeding a threshold value, the chains start to loss their mobility and flexibility, because of their reduced free volume, and the adhesion decreases. A further increase of σ leads to an overlapping of the grafted-chains. These last one phase separate from the adhering material, preventing the chains interpenetration [65, 66].

Moreover, it has been demonstrated that higher chain lengths results in an improvement of the adhesiveness between the polymer bulk and the brushes [65]. Thus, the possibility to use tethered polymers as innovative adhesive has been experimentally proven. According to the theoretical results [65], an increase of the tensile strength of a junction formed by PMMA tethered chains interpenetrating in a melted PMMA matrix has been reported when longer brushes chain have been considered, thanks to a deeper penetration of the PMMA brushes into the bulk PMMA [12]. Furthermore, since it has been demonstrated that brushes with a degree of polymerization (i.e. the ratio between the molecular weight of the grafted chains and the molecular mass of the monomer) greater than or equal to 200 is necessary to establish physical entanglements with the adjacent polymer bulk [65], the optimization of coating methods enabling the production of film with large thickness (tens of micrometers) are desired [72].

In addition, recently it has also been experimentally proven that the interfacial mixing between the brushes and the polymer matrix augments as the molecular weight dispersity increases [73], according to the theoretical study performed by Laub et al. [71].

This is of particular interest because, even if the brushes at low grafting density are able to interpenetrate in a polymer matrix and form entanglements, the polymer-brush interfacial strength is generally weaker than that produced by a denser polydisperse brush layer [73].

1.2 Methods for characterizing polymer-coated flat substrates

The characterization of layered materials, composed of metallic surfaces covered by a polymeric coating, requires a particular attention. Indeed, depending on the brush synthesis process as well as on the substrate surface finishing, smooth or porous and rough layers with different molecular weights can be fabricated [74]. Thus, to have a better control over the synthesis process, and to optimize it, the surface morphology and the chemical composition of the interface have to be characterized. Moreover, the majority of well established techniques haves been developed to investigate the properties of the solution polymerization. Thus, the characterization of tethered polymer layers, tens of nanometers thick on flat or porous macroscopic substrates, is a challenging task which requires further modification of the techniques already existing. Generally, the chemical composition of the surface is assessed by Fourier transform infrared spectroscopy (FTIR), x-ray photoelectron spectroscopy (XPS) and energy dispersive x-ray diffraction (EDX). FTIR allows detecting the presence of functional groups on the surface [34,57,58,61,75]; XPS is used to quantitatively evaluate the composition and the bond-type [3,12,19,25,58,76,77]; EDX is employed to estimate and map the elemental composition of the surface [72, 78]. Moreover, another conventional way to map the surface elemental composition is time-of-flight secondary ion mass spectroscopy (TOF-SIMS) [79–83], which uses a beam of primary ions to produce an ejection of secondary ions.

An accurate measurement of the chains molecular weight (M_w) can be assessed operating a degrafting procedure. In this way, the polymer layer is detached from the substrates, using an appropriate chemical reagent to break the bonds established between the polymer and the substrates. M_w is evaluated using conventional gel permeation chromatography (GPC) [45, 49, 84–86] or size exclusion chromatography (SEC) [62, 87]. Otherwise, the amount of the polymer grafted on the substrates is determined by toluidine blue colorimetric assays [59, 60, 88, 89].
However, the grafting density can be also roughly calculated using the estimated M_w, the bulk density (ρ) and the thickness t of the polymer brush, according to according to $\sigma = \frac{\rho t N_A}{M_w}$ [19], where N_A is the Avogadro's number. Whereas, the brush thickness is generally measured by ellipsometry [19, 85, 90, 91].

The polymer brush morphology is investigated with scanning electron microscopy (SEM) [25, 61, 75, 92, 93] as well as atomic force microscopy (AFM) [3, 19, 34, 57, 75]. This latter was also used to estimate the mechanical properties of the polymers performing either nanoindentation tests [94] or scratching tests [95, 96].

Bibliography

[1] L. Wu and J. Baghdachi, *Functional Polymer Coatings: Principles, Methods, and Applications*, vol. 12. John Wiley & Sons, 2015.

[2] J. E. Raynor, J. R. Capadona, D. M. Collard, T. A. Petrie, and A. J. García, "Polymer brushes and self-assembled monolayers: versatile platforms to control cell adhesion to biomaterials (review)," *Biointerphases*, vol. 4, no. 2, pp. FA3–FA16, 2009.

[3] A. Michiardi, G. Hélary, P.-C. Nguyen, L. J. Gamble, F. Anagnostou, D. G. Castner, and V. Migonney, "Bioactive polymer grafting onto titanium alloy surfaces," *Acta Biomaterialia*, vol. 6, no. 2, pp. 667–675, 2010.

[4] J. Huang, H. Murata, R. R. Koepsel, A. J. Russell, and K. Matyjaszewski, "Antibacterial polypropylene via surface-initiated atom transfer radical polymerization," *Biomacromolecules*, vol. 8, no. 5, pp. 1396–1399, 2007.

[5] R. Tejero, E. Anitua, and G. Orive, "Toward the biomimetic implant surface: Biopolymers on titanium-based implants for bone regeneration," *Progress in Polymer Science*, vol. 39, no. 7, pp. 1406–1447, 2014.

[6] P. Cools, N. De Geyter, E. Vanderleyden, F. Barberis, P. Dubruel, and R. Morent, "Adhesion improvement at the PMMA bone cement-titanium implant interface using methyl methacrylate atmospheric pressure plasma polymerization," *Surface and Coatings Technology*, vol. 294, pp. 201–209, 2016.

[7] G. D. Parfitt, *Adsorption from solution at the solid/liquid interface*. Academic Pr, 1983.

[8] R. A. Jones and R. W. Richards, *Polymers at surfaces and interfaces*. Cambridge University Press, 1999.

[9] M. Godoy-Gallardo, C. Mas-Moruno, K. Yu, J. M. Manero, F. J. Gil, J. N. Kizhakkedathu, and D. Rodriguez, "Antibacterial properties of hlf1–11 peptide onto titanium surfaces: A comparison study between silanization and surface initiated polymerization," *Biomacromolecules*, vol. 16, no. 2, pp. 483–496, 2015.

[10] C. Sun, F. Zhou, L. Shi, B. Yu, P. Gao, J. Zhang, and W. Liu, "Tribological properties of chemically bonded polyimide films on silicon with polyglycidyl methacrylate brush as adhesive layer," *Applied Surface Science*, vol. 253, no. 4, pp. 1729–1735, 2006.

[11] D. Li, Q. Zheng, Y. Wang, and H. Chen, "Combining surface topography with polymer chemistry: exploring new interfacial biological phenomena," *Polymer Chemistry*, vol. 5, no. 1, pp. 14–24, 2014.

[12] K. Shimizu, K. Malmos, A. H. Holm, S. U. Pedersen, K. Daasbjerg, and M. Hinge, "Improved adhesion between PMMA and stainless steel modified with PMMA brushes," *ACS Applied Materials & Interfaces*, vol. 6, no. 23, pp. 21308–21315, 2014.

[13] K. Shimizu, K. Malmos, S.-A. Spiegelhauer, J. Hinke, A. H. Holm, S. U. Pedersen, K. Daasbjerg, and M. Hinge, "Durability of peek adhesive to stainless steel modified with aryldiazonium salts," *International Journal of Adhesion and Adhesives*, vol. 51, pp. 1–12, 2014.

[14] O. Alageel, M.-N. Abdallah, Z. Y. Luo, J. Del-Rio-Highsmith, M. Cerruti, and F. Tamimi, "Bonding metals to poly (methyl methacrylate) using aryldiazonium salts," *Dental Materials*, vol. 31, no. 2, pp. 105–114, 2015.

[15] A. C. Balazs, C. Singh, E. Zhulina, S.-S. Chern, Y. Lyatskaya, and G. Pickett, "Theory of polymer chains tethered at interfaces," *Progress in Surface Science*, vol. 55, no. 3, pp. 181–269, 1997.

[16] B. Zhao and W. J. Brittain, "Polymer brushes: surface-immobilized macromolecules," *Progress in Polymer Science*, vol. 25, no. 5, pp. 677–710, 2000.

[17] A. Bhattacharya and B. Misra, "Grafting: a versatile means to modify polymers: techniques, factors and applications," *Progress in Polymer Science*, vol. 29, no. 8, pp. 767–814, 2004.

[18] B. Zdyrko and I. Luzinov, "Polymer brushes by the "grafting to" method," *Macromolecular Rapid Communications*, vol. 32, no. 12, pp. 859–869, 2011.

[19] D. P. Sweat, M. Kim, X. Yu, and P. Gopalan, "A single-component inimer containing cross-linkable ultrathin polymer coating for dense polymer brush growth," *Langmuir*, vol. 29, no. 11, pp. 3805–3812, 2013.

[20] R. Barbey, L. Lavanant, D. Paripovic, N. Schüwer, C. Sugnaux, S. Tugulu, and H. A. Klok, "Polymer brushes via surface-initiated controlled radical polymerization: synthesis, characterization, properties, and applications," *Chemical Reviews*, vol. 109, no. 11, pp. 5437–5527, 2009.

[21] S. Minko, "Grafting on solid surfaces: "grafting to" and "grafting from" methods," in *Polymer Surfaces and Interfaces*, pp. 215–234, Springer, 2008.

[22] M. Tintoré, S. Mazzini, L. Polito, M. Marelli, A. Latorre, Á. Somoza, A. Aviñó, C. Fàbrega, and R. Eritja, "Gold-coated superparamagnetic nanoparticles for single methyl discrimination in DNA aptamers," *International Journal of Molecular Sciences*, vol. 16, no. 11, pp. 27625–27639, 2015.

[23] J. Rundqvist, J. H. Hoh, and D. B. Haviland, "Poly (ethylene glycol) self-assembled monolayer island growth," *Langmuir*, vol. 21, no. 7, pp. 2981–2987, 2005.

[24] M. Godoy-Gallardo, C. Mas-Moruno, K. Yu, J. M. Manero, F. J. Gil, J. N. Kizhakkedathu, and D. Rodriguez, "Antibacterial properties of hLf1–11 peptide onto titanium surfaces: A comparison study between silanization and surface initiated polymerization," *Biomacromolecules*, vol. 16, no. 2, pp. 483–496, 2015.

[25] B. Barthélémy, S. Devillers, I. Minet, J. Delhalle, and Z. Mekhalif, "Induction heating for surface triggering styrene polymerization on titanium modified with ATRP initiator," *Journal of Colloid and Interface Science*, vol. 354, no. 2, pp. 873–879, 2011.

[26] R. Boissezon, J. Muller, V. Beaugeard, S. Monge, and J. J. Robin, "Organophosphonates as anchoring agents onto metal oxide-based materials: synthesis and applications," *RSC Advances*, vol. 4, no. 67, pp. 35690–35707, 2014.

[27] S. Edmondson, V. L. Osborne, and W. T. Huck, "Polymer brushes via surface-initiated polymerizations," *Chemical Society Reviews*, vol. 33, no. 1, pp. 14–22, 2004.

[28] J. Wang, D. Greszta, and K. Matyjaszewski, "Atom-transfer radical polymerization (ATRP)-a new approach towards well-defined (co) polymers," in *ABSTRACTS OF*

PAPERS OF THE AMERICAN CHEMICAL SOCIETY, vol. 210, pp. 227–PMSE, AMER CHEMICAL SOC PO BOX 57136, WASHINGTON, DC 20037-0136, 1995.

[29] K. Matyjaszewski, P. J. Miller, N. Shukla, B. Immaraporn, A. Gelman, B. B. Luokala, T. M. Siclovan, G. Kickelbick, T. Vallant, H. Hoffmann, *et al.*, "Polymers at interfaces: using atom transfer radical polymerization in the controlled growth of homopolymers and block copolymers from silicon surfaces in the absence of untethered sacrificial initiator," *Macromolecules*, vol. 32, no. 26, pp. 8716–8724, 1999.

[30] K. Matyjaszewski and J. Xia, "Atom transfer radical polymerization," *Chemical reviews*, vol. 101, no. 9, pp. 2921–2990, 2001.

[31] N. Y. Kim, N. L. Jeon, I. S. Choi, S. Takami, Y. Harada, K. R. Finnie, G. S. Girolami, R. G. Nuzzo, G. M. Whitesides, P. E. Laibinis, *et al.*, "Surface-initiated ring-opening metathesis polymerization on Si/SiO_2," *Macromolecules*, vol. 33, no. 8, pp. 2793–2795, 2000.

[32] L. Ghannam, J. Parvole, G. Laruelle, J. Francois, and L. Billon, "Surface-initiated nitroxide-mediated polymerization: a tool for hybrid inorganic/organic nanocomposites "in situ" synthesis," *Polymer International*, vol. 55, no. 10, pp. 1199–1207, 2006.

[33] M. Baum and W. J. Brittain, "Synthesis of polymer brushes on silicate substrates via reversible addition fragmentation chain transfer technique," *Macromolecules*, vol. 35, no. 3, pp. 610–615, 2002.

[34] H. Marie, A. Barrere, F. Schoentstein, M.-H. Chavanne, B. Grosgogeat, and L. Mora, "Pem anchorage on titanium using catechol grafting," *PloS one*, vol. 7, no. 11, p. e50326, 2012.

[35] C. Boyer, N. A. Corrigan, K. Jung, D. Nguyen, T. K. Nguyen, N. N. M. Adnan, S. Oliver, S. Shanmugam, and J. Yeow, "Copper-mediated living radical polymerization (atom transfer radical polymerization and copper (0) mediated polymerization): From fundamentals to bioapplications," *Chemical Reviews*, vol. 116, no. 4, pp. 1803–1949, 2015.

[36] C. J. Fristrup, K. Jankova, and S. Hvilsted, "Surface-initiated atom transfer radical polymerization: A technique to develop biofunctional coatings," *Soft Matter*, vol. 5, no. 23, pp. 4623–4634, 2009.

[37] J. S. Wang and K. Matyjaszewski, "Controlled/"living" radical polymerization. atom transfer radical polymerization in the presence of transition-metal complexes," *Journal of the American Chemical Society*, vol. 117, no. 20, pp. 5614–5615, 1995.

[38] P. V. Mendonça, A. C. Serra, J. F. Coelho, A. V. Popov, and T. Guliashvili, "Ambient temperature rapid ATRP of methyl acrylate, methyl methacrylate and styrene in polar solvents with mixed transition metal catalyst system," *European Polymer Journal*, vol. 47, no. 7, pp. 1460–1466, 2011.

[39] X. Huang and M. J. Wirth, "Surface-initiated radical polymerization on porous silica," *Analytical chemistry*, vol. 69, no. 22, pp. 4577–4580, 1997.

[40] M. Ejaz, S. Yamamoto, K. Ohno, Y. Tsujii, and T. Fukuda, "Controlled graft polymerization of methyl methacrylate on silicon substrate by the combined use of the langmuir- blodgett and atom transfer radical polymerization techniques," *Macromolecules*, vol. 31, no. 17, pp. 5934–5936, 1998.

[41] H. Fischer, "The persistent radical effect: a principle for selective radical reactions and living radical polymerizations," *Chemical Reviews*, vol. 101, no. 12, pp. 3581–3610, 2001.

[42] Y. Tsujii, K. Ohno, S. Yamamoto, A. Goto, and T. Fukuda, "Structure and properties of high-density polymer brushes prepared by surface-initiated living radical polymerization," in *Surface-initiated polymerization I*, pp. 1–45, Springer, 2006.

[43] T. von Werne and T. E. Patten, "Atom transfer radical polymerization from nanoparticles: a tool for the preparation of well-defined hybrid nanostructures and for understanding the chemistry of controlled/"living" radical polymerizations from surfaces," *Journal of the American Chemical Society*, vol. 123, no. 31, pp. 7497–7505, 2001.

[44] C. Perruchot, M. Khan, A. Kamitsi, S. v. Armes, T. Von Werne, and T. Patten, "Synthesis of well-defined, polymer-grafted silica particles by aqueous ATRP," *Langmuir*, vol. 17, no. 15, pp. 4479–4481, 2001.

[45] C. B. Gorman, R. J. Petrie, and J. Genzer, "Effect of substrate geometry on polymer molecular weight and polydispersity during surface-initiated polymerization," *Macromolecules*, vol. 41, no. 13, pp. 4856–4865, 2008.

[46] P. Pasetto, H. Blas, F. Audouin, C. Boissiere, C. Sanchez, M. Save, and B. Charleux, "Mechanistic insight into surface-initiated polymerization of methyl methacrylate and styrene via ATRP from ordered mesoporous silica particles," *Macromolecules*, vol. 42, no. 16, pp. 5983–5995, 2009.

[47] C. Huang, T. Tassone, K. Woodberry, D. Sunday, and D. L. Green, "Impact of ATRP initiator spacer length on grafting poly (methyl methacrylate) from silica nanoparticles," *Langmuir*, vol. 25, no. 23, pp. 13351–13360, 2009.

[48] C. Kang, R. Crockett, and N. D. Spencer, "The influence of surface grafting on the growth rate of polymer chains," *Polymer Chemistry*, vol. 7, no. 2, pp. 302–309, 2016.

[49] R. R. Patil, S. Turgman-Cohen, J. ęrogl, D. Kiserow, and J. Genzer, "On-demand degrafting and the study of molecular weight and grafting density of poly (methyl methacrylate) brushes on flat silica substrates," *Langmuir*, vol. 31, no. 8, pp. 2372–2381, 2015.

[50] Z. Jiaming, H. Jianying, C. Jiayan, L. Xurong, L. Yutai, Z. Yousi, *et al.*, "A novel rate-accelerating additive for atom transfer radical polymerization of styrene," *Journal of Polymer Science Part A: Polymer Chemistry*, vol. 45, no. 17, pp. 4082–4090, 2007.

[51] K. Ohno, K.-m. Koh, Y. Tsujii, and T. Fukuda, "Synthesis of gold nanoparticles coated with well-defined, high-density polymer brushes by surface-initiated living radical polymerization," *Macromolecules*, vol. 35, no. 24, pp. 8989–8993, 2002.

[52] H. Zou, S. Wu, and J. Shen, "Polymer/silica nanocomposites: preparation, characterization, properties, and applications," *Chem. Rev*, vol. 108, no. 9, pp. 3893–3957, 2008.

[53] I. Garcia, N. Zafeiropoulos, A. Janke, A. Tercjak, A. Eceiza, M. Stamm, and I. Mondragon, "Functionalization of iron oxide magnetic nanoparticles with poly (methyl methacrylate) brushes via grafting-from atom transfer radical polymerization," *Journal of Polymer Science Part A: Polymer Chemistry*, vol. 45, no. 5, pp. 925–932, 2007.

[54] V. Vergnat, G. Pourroy, and P. Masson, "Enhancement of styrene conversion in organic/inorganic hybrid materials by using malononitrile in controlled radical polymerization," *Polymer International*, vol. 62, no. 6, pp. 878–883, 2013.

[55] A. Ramakrishnan, R. Dhamodharan, and J. Rühe, "Growth of poly (methyl methacrylate) brushes on silicon surfaces by atom transfer radical polymerization," *Journal of Polymer Science Part A: Polymer Chemistry*, vol. 44, no. 5, pp. 1758–1769, 2006.

[56] L. Sun, J. Dai, G. L. Baker, and M. L. Bruening, "High-capacity, protein-binding membranes based on polymer brushes grown in porous substrates," *Chemistry of materials*, vol. 18, no. 17, pp. 4033–4039, 2006.

[57] O. Borozenko, V. Machado, W. Skene, and S. Giasson, "Organophosphonic acids as viable linkers for the covalent attachment of polyelectrolyte brushes on silica and mica surfaces," *Polymer Chemistry*, vol. 5, no. 19, pp. 5740–5750, 2014.

[58] I. Minet, J. Delhalle, L. Hevesi, and Z. Mekhalif, "Surface-initiated ATRP of PMMA, PS and diblock PS-b-PMMA copolymers from stainless steel modified by 11-(2-bromoisobutyrate)-undecyl-1-phosphonic acid," *Journal of Colloid and Interface Science*, vol. 332, no. 2, pp. 317–326, 2009.

[59] G. Hélary, F. Noirclère, J. Mayingi, and V. Migonney, "A new approach to graft bioactive polymer on titanium implants: improvement of MG 63 cell differentiation onto this coating," *Acta Biomaterialia*, vol. 5, no. 1, pp. 124–133, 2009.

[60] H. Chouirfa, V. Migonney, and C. Falentin-Daudré, "Grafting bioactive polymers onto titanium implants by uv irradiation," *RSC Advances*, vol. 6, no. 17, pp. 13766–13771, 2016.

[61] B. Barthélémy, S. Devillers, I. Minet, J. Delhalle, and Z. Mekhalif, "Surface-initiated ATRP of 2-(methacryloyloxy) ethyl 2-(trimethylammonio) ethyl phosphate on phynox," *Applied Surface Science*, vol. 258, no. 1, pp. 466–473, 2011.

[62] C. Kang, R. M. Crockett, and N. D. Spencer, "Molecular-weight determination of polymer brushes generated by SI-ATRP on flat surfaces," *Macromolecules*, vol. 47, no. 1, pp. 269–275, 2013.

[63] Y. Shaulov, R. Okner, Y. Levi, N. Tal, V. Gutkin, D. Mandler, and A. J. Domb, "Poly (methyl methacrylate) grafting onto stainless steel surfaces: application to drug-eluting stents," *ACS Applied Materials & Interfaces*, vol. 1, no. 11, pp. 2519–2528, 2009.

[64] M. Aubouy, G. Fredrickson, P. Pincus, and E. Raphaeel, "End-tethered chains in polymeric matrixes," *Macromolecules*, vol. 28, no. 8, pp. 2979–2981, 1995.

[65] W. S. Gutowski, S. Li, C. Filippou, P. Hoobin, and S. Petinakis, "Interface/interphase engineering of polymers for adhesion enhancement: Part ii. theoretical and technological aspects of surface-engineered interphase-interface systems for adhesion enhancement," *The Journal of Adhesion*, vol. 79, no. 5, pp. 483–519, 2003.

[66] S. W. Sides, G. S. Grest, M. J. Stevens, and S. J. Plimpton, "Effect of end-tethered polymers on surface adhesion of glassy polymers," *Journal of Polymer Science Part B: Polymer Physics*, vol. 42, no. 2, pp. 199–208, 2004.

[67] E. Raphael and P. De Gennes, "Rubber-rubber adhesion with connector molecules," *The Journal of Physical Chemistry*, vol. 96, no. 10, pp. 4002–4007, 1992.

[68] K. Kunz and M. Stamm, "Initial stages of interdiffusion of PMMA across an interface," *Macromolecules*, vol. 29, no. 7, pp. 2548–2554, 1996.

[69] R. Schnell, M. Stamm, and C. Creton, "Direct correlation between interfacial width and adhesion in glassy polymers," *Macromolecules*, vol. 31, no. 7, pp. 2284–2292, 1998.

[70] C. Gay, "Wetting of a polymer brush by a chemically identical polymer melt," *Macromolecules*, vol. 30, no. 19, pp. 5939–5943, 1997.

[71] C. F. Laub and J. T. Koberstein, "Effect of brush polydispersity on the interphase between end-grafted brushes and polymeric matrixes," *Macromolecules*, vol. 27, no. 18, pp. 5016–5023, 1994.

[72] J. E. Friis, K. Brøns, Z. Salmi, K. Shimizu, G. Subbiahdoss, A. H. Holm, O. Santos, S. U. Pedersen, R. L. Meyer, K. Daasbjerg, *et al.*, "Hydrophilic polymer brush layers on stainless steel using multilayered ATRP initiator layer," *ACS Applied Materials & Interfaces*, vol. 8, no. 44, pp. 30616–30627, 2016.

[73] H. Arita, K. Mitamura, M. Kobayashi, N. L. Yamada, H. Jinnai, and A. Takahara, "Chain-mixing behavior at interface between polystyrene brushes and polystyrene matrices," *Polymer Journal*, vol. 45, no. 1, pp. 117–123, 2013.

[74] D. Julthongpiput, M. LeMieux, and V. Tsukruk, "Micromechanical properties of glassy and rubbery polymer brush layers as probed by atomic force microscopy," *Polymer*, vol. 44, no. 16, pp. 4557–4562, 2003.

[75] G. Zorn, J. E. Baio, T. Weidner, V. Migonney, and D. G. Castner, "Characterization of poly (sodium styrene sulfonate) thin films grafted from functionalized titanium surfaces," *Langmuir*, vol. 27, no. 21, pp. 13104–13112, 2011.

[76] C. Haensch, S. Hoeppener, and U. S. Schubert, "Chemical modification of self-assembled silane based monolayers by surface reactions," *Chemical Society Reviews*, vol. 39, no. 6, pp. 2323–2334, 2010.

[77] C. Viornery, Y. Chevolot, D. Léonard, B.-O. Aronsson, P. Péchy, H. J. Mathieu, P. Descouts, and M. Grätzel, "Surface modification of titanium with phosphonic acid to improve bone bonding: characterization by XPS and ToF-SIMS," *Langmuir*, vol. 18, no. 7, pp. 2582–2589, 2002.

[78] M. S. Park, B. Ramaraj, and K. R. Yoon, "A new strategy to grow polymer brush on graphene oxide surface through microwave assisted polymer synthesis," *Applied Surface Science*, vol. 258, no. 22, pp. 8656–8661, 2012.

[79] X. Fan, L. Lin, J. L. Dalsin, and P. B. Messersmith, "Biomimetic anchor for surface-initiated polymerization from metal substrates," *Journal of the American Chemical Society*, vol. 127, no. 45, pp. 15843–15847, 2005.

[80] Y.-P. Kim, B. S. Lee, E. Kim, I. S. Choi, D. W. Moon, T. G. Lee, and H.-S. Kim, "Activity-based assay of matrix metalloproteinase on nonbiofouling surfaces using time-of-flight secondary ion mass spectrometry," *Analytical Chemistry*, vol. 80, no. 13, pp. 5094–5102, 2008.

[81] C. Rodriguez-Emmenegger, C. M. Preuss, B. Yameen, O. Pop-Georgievski, M. Bachmann, J. O. Mueller, M. Bruns, A. S. Goldmann, M. Bastmeyer, and C. Barner-Kowollik, "Controlled cell adhesion on poly (dopamine) interfaces photopatterned with non-fouling brushes," *Advanced Materials*, vol. 25, no. 42, pp. 6123–6127, 2013.

[82] A. Kuzmyn, A. de los Santos Pereira, O. Pop-Georgievski, M. Bruns, E. Brynda, and C. Rodriguez-Emmenegger, "Exploiting end group functionalization for the design of antifouling bioactive brushes," *Polymer Chemistry*, vol. 5, no. 13, pp. 4124–4131, 2014.

[83] O. Roling, K. De Bruycker, B. Vonhören, L. Stricker, M. Körsgen, H. F. Arlinghaus, B. J. Ravoo, and F. E. Du Prez, "Rewritable polymer brush micropatterns grafted by triazolinedione click chemistry," *Angewandte Chemie International Edition*, vol. 54, no. 44, pp. 13126–13129, 2015.

[84] A. P. Martinez, J. M. Y. Carrillo, A. V. Dobrynin, and D. H. Adamson, "Distribution of chains in polymer brushes produced by a "grafting from" mechanism," *Macromolecules*, vol. 49, no. 2, pp. 547–553, 2016.

[85] R. Patil, D. Kiserow, and J. Genzer, "Creating surface patterns of polymer brushes by degrafting via tetrabutyl ammonium fluoride," *RSC Advances*, vol. 5, no. 105, pp. 86120–86125, 2015.

[86] J. B. Kim, W. Huang, M. L. Bruening, and G. L. Baker, "Synthesis of triblock copolymer brushes by surface-initiated atom transfer radical polymerization," *Macromolecules*, vol. 35, no. 14, pp. 5410–5416, 2002.

[87] M. Gaborieau and P. Castignolles, "Size-exclusion chromatography (SEC) of branched polymers and polysaccharides," *Analytical and Bioanalytical Chemistry*, vol. 399, no. 4, pp. 1413–1423, 2011.

[88] M. Ciobanu, A. Siove, V. Gueguen, L. Gamble, D. Castner, and V. Migonney, "Radical graft polymerization of styrene sulfonate on poly (ethylene terephthalate) films for ACL applications: "grafting from" and chemical characterization," *Biomacromolecules*, vol. 7, no. 3, pp. 755–760, 2006.

[89] B. Gupta, C. Plummer, I. Bisson, P. Frey, and J. Hilborn, "Plasma-induced graft polymerization of acrylic acid onto poly (ethylene terephthalate) films: characterization and human smooth muscle cell growth on grafted films," *Biomaterials*, vol. 23, no. 3, pp. 863–871, 2002.

[90] J.-B. Kim, W. Huang, M. D. Miller, G. L. Baker, and M. L. Bruening, "Kinetics of surface-initiated atom transfer radical polymerization," *Journal of Polymer Science Part A: Polymer Chemistry*, vol. 41, no. 3, pp. 386–394, 2003.

[91] N. A. Alcantar, E. S. Aydil, and J. N. Israelachvili, "Polyethylene glycol-coated biocompatible surfaces," *Journal of Biomedical Materials Research*, vol. 51, no. 3, pp. 343–351, 2000.

[92] C. J. Pan, Y. H. Hou, B. B. Zhang, Y. X. Dong, and H. Y. Ding, "Blood compatibility and interaction with endothelial cells of titanium modified by sequential immobilization of poly (ethylene glycol) and heparin," *Journal of Materials Chemistry B*, vol. 2, no. 7, pp. 892–902, 2014.

[93] E. Cao, E. Prouzet, and V. Héroguez, "Organic–inorganic hybrid materials designed by controlled radical polymerization and mediated using commercial dual functional organophosphorous coupling agents," *New Journal of Chemistry*, vol. 38, no. 12, pp. 6081–6087, 2014.

[94] D. Tranchida, E. Sperotto, A. Chateauminois, and H. Schönherr, "Entropic effects on the mechanical behavior of dry polymer brushes during nanoindentation by atomic force microscopy," *Macromolecules*, vol. 44, no. 2, pp. 368–374, 2010.

[95] M. E. Dokukin, H. Kuroki, S. Minko, and I. Sokolov, "Afm study of polymer brush grafted to deformable surfaces: Quantitative properties of the brush and substrate mechanics," *Macromolecules*, 2016.

[96] M. Stamm, "Polymer surfaces and interfaces," *Polymer Surfaces and Interfaces: Characterization, Modification and Applications, ISBN 978-3-540-73864-0. Springer Berlin Heidelberg*, vol. 1, 2008.

Chapter 2

Materials and methods for the fabrication of PMMA-coated Ti surfaces

Titanium is a widely used metal in biomedical applications due to its biocompatibility; however the significant difference between the Ti and the surrounding tissues results in a stress shielding which is detrimental particularly for load bearing tissues. In order to overcome this problem, a technique to incorporate a polymer component to Ti implants has been developed to attenuate stress shielding.

An new strategy to obtain thick PMMA layer strongly linked on Ti surfaces by a covalent bond has been established. Indeed, PMMA and Ti are usually mechanical interlocked by linking the PMMA into the irregularities of the Ti [1]; thus, further improvement in the bonding strength between Ti and PMMA is still needed to prevent debonding which can provoke catastrophic and premature mechanical failures of the implants [2–4]. For this purpose, following the previous work of Vergnat et al. [5, 6], "grafting from" method has been employed to grow PMMA chains on Ti surfaces using phosphonic acids as coupling agents [7, 8]. The three steps strategy, schematized in Fig. 2.1, has been followed. First, a chemical activation of the Ti surfaces in a basic media has been performed to increase the hydroxyl groups content on surface (Ti activation in Fig. 2.1). In the second step, the initiator has been immobilized on the activated Ti surfaces using a "grafting from" method (Ti functionalization, Fig. 2.1). Finally, the third step has been devoted to the polymer chains growth starting from the initiator-modified Ti surfaces using ATRP technique (Polymerization, Fig. 2.1).

Then, a procedure to stick a 0.25 mm thick PMMA sheet (also called bulk PMMA in the text) on the the synthesized PMMA-coated Ti substrate has been developed demonstrating that, in the sandwich production, epoxy-resin can be replaced by tethered polymer chains.

In this chapter the materials and the methods employed to design and characterize the hybrid PMMA-coated Ti surfaces are explained.

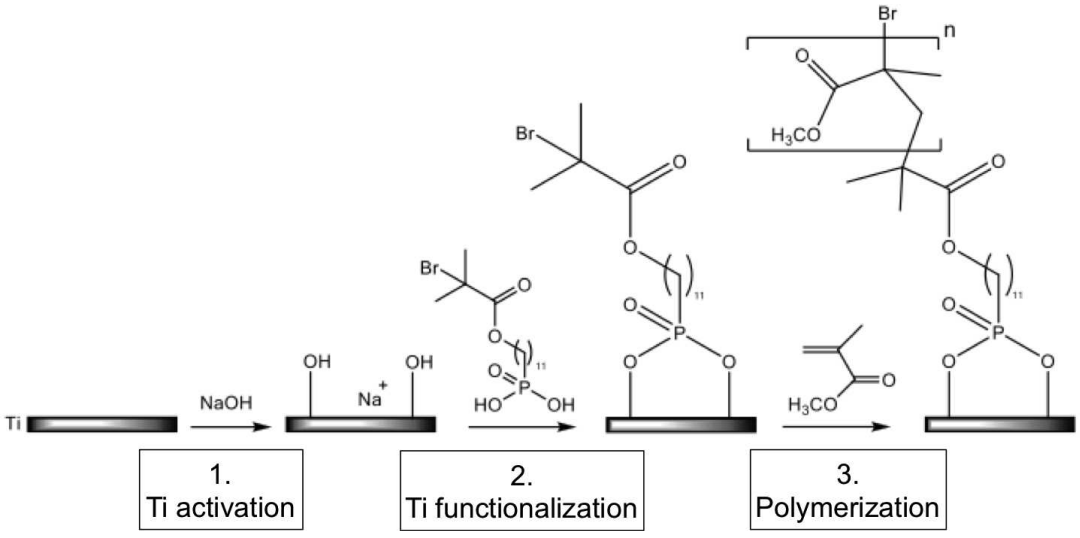

Figure 2.1: Chemical strategy followed to design the PMMA-coated Ti surfaces.

2.1 Materials

2.1.1 Titanium

Ti and its alloys have been successfully used to fabricate implants especially for orthopedic and dental implants [9] because of their inertness, low density, high biocompatibility, good resistance to corrosion, ductility and a Young's modulus closer to that of the human bone compared to other materials of interest in the biomedical fields (e.g. steel) [10–14].

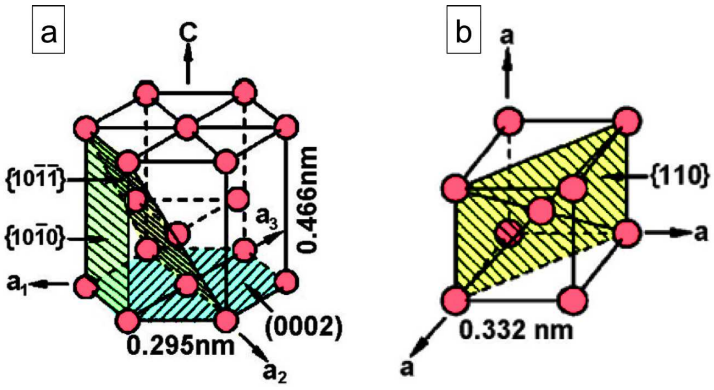

Figure 2.2: α (a) and β (b) crystal structures of Ti.

Ti has an hexagonal closed packed (hcp) crystal structure, referred to as α phase, that undergoes an allotropic modification at a temperature of 882 °C (T_β) to a body centered cubic (bcc) crystal structure, known as β phase (Fig. 2.2). At this temperature, which can slightly change in the presence of different grades of impurities (reported in Tab. 2.1), the denser (0001) α planes become the basic (110) planes of the β phase [15]. In particular, a T_β of 890 °C has been reported for a commercially pure (cp) Ti grade 1 (Ti Gr. 1), and $T_\beta = 950$ °C has been found for a cp Ti Gr. 4.

Moreover, it can be further modified by adding alloying element which can sensibly tune the physical properties of Ti. Based on the phase that their introduction can produce, Ti alloying elements are divided in: (*i*) α phase stabilizers (i.e. aluminum (Al), tin (Sn) or most interstitial elements) which produce an increase of T_β; (*ii*) β phase stabilizers which include vanadium (V), molybdenum (Mo), niobium (Nb), chromium (Cr), iron (Fe) and manganese (Mn); (*iii*) $\alpha + \beta$ stabilizers which simultaneously contain both α and β elements [15].

Cp Ti is considered a good biocompatible metallic material because its surface is spon-

Table 2.1: The chemical composition of the different grades of commercially pure Ti and Ti-6Al-4V alloy, generally, used for implants [16].

Material	N %	C %	H %	Fe %	O %	Al %	V %	Ti %
Ti Gr. 1	0.03	0.1	0.015	0.02	0.18	-	-	balance
Ti Gr. 2	0.03	0.1	0.015	0.03	0.25	-	-	balance
Ti Gr. 3	0.03	0.1	0.015	0.03	0.35	-	-	balance
Ti Gr. 4	0.03	0.1	0.015	0.05	0.40	-	-	balance
Ti-6Al-4V	0.05	0.08	0.015	0.3	0.28	5.5-6.75	3.5-4.5	balance

taneously passivated by a stable and inert oxide layer which confers a good corrosion resistance. Cp Ti Gr. 2 is the most used for industrial dental implant applications [16, 17] and employed in this study.

2.1.2 Polymethyl methacrylate

Commercial PMMA is an amorphous material with good resistance against dilute alkalis and other inorganic solutions. It is a transparent material (92% light transmission) with a high refractive index (1.49), good weathering resistance and biocompatibility [18].

Currently, among the biocompatible polymers, is one of the most widely used as implantable materials, in the fabrication of bone cements, contact lens and restorative dental composites [18–20].

2.2 Synthesis procedure

2.2.1 Titanium sample preparation

In this thesis, two types of Ti sample geometries have been employed for the fabrication of PMMA-coated Ti surfaces: (*i*) commercially pure Ti Gr. 2 disks (20 mm in diameter and 3 mm thick) cut from a Ti bar and (*ii*) 0.5 mm thick Ti Gr. 2 sheets (square-shaped 20×20 mm^2 or rectangular-shaped 20×60 mm^2).

To decrease their surface roughness, as summarized in Tab. 2.2, two different Ti treatments have been performed: (*i*) Ti disks have been mechanically polished and used to develop the PMMA-coated Ti surfaces; (*ii*) Ti sheets have been electrochemical polished due to great surface required for the Ti/PMMA/Ti production.

Table 2.2: List of the sample geometries and the polishing methods used to reduce their surface roughness with respect of their applicative purpose.

Sample	Ti treatment	Purpose
Ti Gr. 2 disk	Mechanical polishing	PMMA-coated Ti fabrication
Ti Gr. 2 sheet	Electropolishing	Ti/PMMA/Ti sandwich production

Mechanical polishing

Ti disks, used to prepare the PMMA-coated Ti surfaces (Tab. 2.2), have been mechanically polished (MP) with 320, 600, 1000, 2400 and 4000 grit silicon carbide (SiC) papers. Successively, they have been treated with colloidal silica suspension (particle size: 0.05 μm) to achieve a bright reflective, mirror like, surfaces. Then, all the samples have been cleaned by ultrasonication in acetone, ethanol and deionized water, 10 min each solvent, to remove the residues of the treatment. Hereafter, such substrates will be defined as *MP-Ti disks*.

Titanium electropolishing

Ti sheets have been employed for the TI/PMMA/Ti sandwich production (Tab. 2.2). Because of their greater surface area and smaller thickness, an electropolished method has

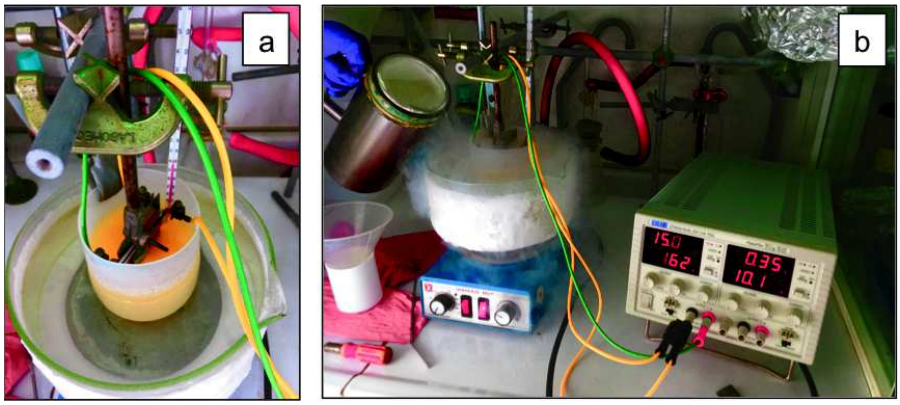

Figure 2.3: Experimental set-up for the electropolishing of Ti sheets. a) A two electrodes cell has been used. Both the cathode and the anode consist in a Ti sheet with the same geometry. The anode is the working electrode where a potential of 15 V for 10 min has been applied. b) During the reaction the operating temperature has been maintained below -35 °C by adding liquid nitrogen in the cooling bath.

been used to reduce their roughness. The electropolishing of Ti substrates has been performed in a two electrodes electrochemical cell, shown in Fig. 2.3a. In order to prevent contamination of the electrolyte solution, both the cathode and the anode consisted of a Ti sheet with identical geometry. They have been mounted in a polyethylene (PE) beaker containing the electrolyte solution, composed of 54 mL methanol, 25 mL 1-butanol, and 6 mL perchloric acid [21, 22]. During the process the solution has been stirred. The electrolyte temperature has been set to -40 °C by putting the electrochemical cell in a cooling bath containing a mixture of liquid nitrogen and ethanol. When the chosen temperature has been established an anodic potential of 15 V for 10 min has been applied. The temperature of the solution has been constantly monitored during the reaction and maintained lesser then -35 °C by adding liquid nitrogen in the cooling bath (Fig. 2.3b). Immediately after the electropolishing, Ti substrates have been sonicated in acetone, ethanol, and deionized water, 10 min each solvent, in order to remove residues of the treatment. Hereafter, such substrates will be defined as *EP-Ti sheets*.

2.2.2 Step 1: alkaline activation of Ti substrates

In the first step, a Ti activation has been carried out in order to obtain active sites where the phosphonate groups can anchor. In particular, an alkali treatment using sodium hydroxide (NaOH) solution has been performed to increase the number of hydroxyl groups (OH) present on the surface.

Previous works have shown that an alkali treatment leads to the formation of a microporous layer of $Na_2Ti_5O_{11}$ [23]. Indeed, during the alkali treatment, the TiO_2 native oxide layer, which covers and passivates the Ti surfaces (see Sec. 2.1.1), partially dissolves in the alkali solution because of the attack by hydroxyl groups (see reaction (2.1) below and Fig. 2.4). This mechanism involves local cathodic and anodic reactions. The former leads to a hydration of Ti with generation of H_2 partially adsorbed in the near-surface region of the Ti substrates (see Eq. (2.4) below). The latter produces a further hydroxyl attack of TiO_2 which leads to negatively charged and hydrates substrates (Eq. (2.5)). These negatively charged species combine with the alkali ions in the aqueous solution to produce a

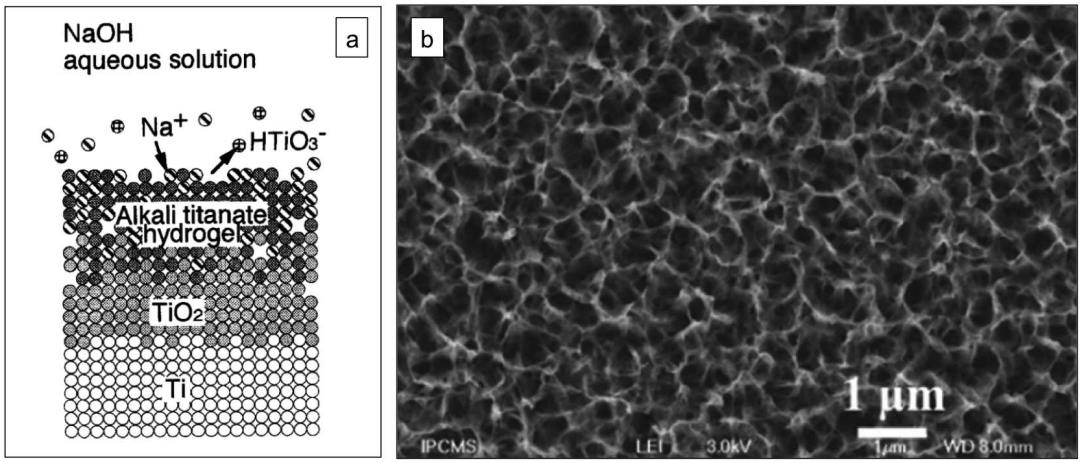

Figure 2.4: a) Schematization of the alkali titanate hydrogel formation by alkali treatment [24]; b) surface morphology of a Ti surface after an alkali treatment.

porous sodium titanate hydrogel layer [25].

The reactions between NaOH and Ti are described by the following chemical reactions [24–27]:

$$TiO_2 + NaOH \longrightarrow HTiO_3^- + Na^+ \tag{2.1}$$

$$Ti + 3\,OH^- \longrightarrow Ti(OH)_3^+ + 4\,e^- \tag{2.2}$$

$$Ti(OH)_3^+ + OH^- \longleftrightarrow Ti(OH)_4 \tag{2.3}$$

$$Ti(OH)_3^+ + e^- \longrightarrow TiO_2 \cdot H_2O + 0.5\,H_2\uparrow \tag{2.4}$$

$$TiO_2 \cdot nH_2O + OH^- \longleftrightarrow HTiO_3^- \cdot nH_2O \tag{2.5}$$

Both the Ti disks and sheets have been immersed into a Teflon becker containing an aqueous NaOH solution at a temperature of 80 °C. Samples have been kept suspended in the reactive media with a Teflon wire avoiding any contact between them and with the magnetic stirrer. This prevents undesired surface chemical reactions. These samples have been labeled *alkali-activated Ti*. At the end of the process, they have been copiously rinsed with deionized water.

2.2.3 Step 2: preparation of ATRP initiator-modified Ti surfaces

In the second step, the ATRP initiator has been grafted of the alkali-activated Ti surfaces. Indeed, as described in Chap. 1 (Sec. 1.1), SI-ATRP requires the anchoring of organic molecules, acting as polymerization initiators, on the metallic surfaces. Firstly, an organic polymerization initiator is grafted on the metallic surfaces. Secondly, polymeric chains are grown starting from the functionalized surfaces leading to the fabrication of metal-polymer interfaces, following the process schematized in Fig. 2.1.

In this thesis, among the various anchoring groups, phosphonate groups ($-PO(OH)_2$) have been selected. Indeed, they appear to be very promising with the possibility to develop covalent monodentate, bidentate and tridentate bondings (see Fig. 2.5) [7, 28]. These anchoring groups have the advantage to be biocompatible and have been successfully used to functionalize magnetic iron oxide contrast agent [29].

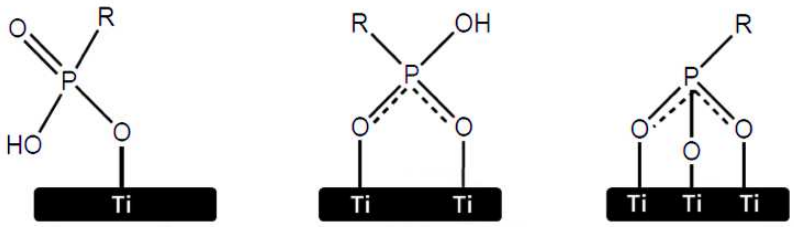

Figure 2.5: Monodentate, bidentate and tridentate phosphonates bonding modes at metal surfaces.

Hereafter, the methodology employed to functionalize the alkali-activated Ti surfaces with phosphate anchoring groups will be shown.

Initiator molecule

In order to achieve a high grafting density, polymer chains have been grafted at the pre-activated Ti surfaces by using a "grafting from" approach to covalently bound the ATRP initiators.

The effect of two organic initiators: (*i*) a commercial bromoisobutyrate-propyl-1-phosphonic acid ($C_7H_{14}O_5PBr$) and (*ii*) a homemade bromoisobutyrate-undecenyl-1-phosphonic acid ($C_{15}H_{30}O_5PBr$), has been investigated. Both contain different extremities: a phosphonic acid, used as anchoring group that covalently links onto the surface and an α-bromo ester group used as ATRP initiator, which are separated by a different alkyl chain length (see Fig. 2.6) [6].

In the first initiator, the two extremities are separated by an alkyl chain of three carbons ($n = 3$ in Fig. 2.6), whereas the second one involves an eleven carbons chain ($n = 11$). They have been labeled *C_3 initiator* and *C_{11} initiator*, respectively.

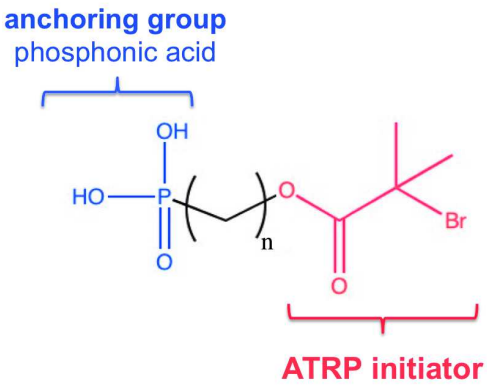

Figure 2.6: Polymerization initiator consisting of a phosponic acid, as anchoring group, and an α-bromo ester group, as SI-ATRP initiator.

The alkyl chains lengths have been chosen on the basis of the work done by Cao et al. [28] which pointed out that to ensure the stability of the molecules, the phosphonate group must be separated from the reactive group by more than one hydrocarbon spacer.

A successful grafting of these molecules is obtained by increasing the content of the hydroxyl groups present on the surface [7]. The polymerization initiator selected contains a phosphonic acid as surface-anchoring group (Fig. 2.6). Thus, its anchorage is expected to involve the interaction between the P−OH, of the phosphoryl groups, with the surface hydroxyl groups Ti−OH, according to the following relation:

$$\mathrm{Ti{-}OH} + \mathrm{P{-}O{-}X} \longrightarrow \mathrm{Ti{-}O{-}P} + \mathrm{X{-}OH} \tag{2.6}$$

Therefore, the covalent link between the metal substrate and the organic molecule is ensured by the creation of Titanium-Oxygen-Phosphorus (Ti−O−P) bonds [7].

Protocols

The functionalization of the alkali-activated Ti substrates has been achieved following the protocol proposed by Mutin et al. regarding the grafting of a phosphate group at the surface of titanium dioxide nanoparticles [6, 7]. In particular, the grafting reaction has been performed in a heated aqueous media.

After washing with deionized water, the alkali-activated Ti disks have been suspended in a glass flask containing a 2 mM initiator concentrated aqueous solution. For the preparation of C_3-modified Ti surfaces, the solution has been stirred and immediately warmed up to 100 °C. The reaction lasted for 24 h in the dark. Instead, to favor the dissolution of the longer C_{11} initiator, the stirring has been previously maintained at 55 °C for 10 min; then, the solution has been heated up to 100 °C and maintained for 24 h in the dark.

A large excess of initiator, with respect to that required for a complete surface covering, has been used in order to ensure a complete covering of the Ti surfaces [1]. This excess can be evaluated by considering the area occupied by each initiator molecule and the surface of the Ti substrates. In particular, hypothesizing that only tripod bonding modes (see Fig. 2.5) are established between the surface OH-groups and the phosponic acids, the area occupied by each molecule (calculated following the procedure proposed by Vergnat et al. [6]) is equal to 0.35 nm^2. Without considering the increase of specific surface caused by the alkali-treatment, the surface of the Ti disk is equal to 314 mm^2. Thus, the quantity of the initiator utilized is approximately 3000 times greater than that requires to cover a smooth Ti substrates.

Even though this excess can diminish, considering the nanostructuration of the surface (caused by the alkali treatment), is still high enough to result in physisorbed initiator multilayers. Therefore, to remove the ungrafted molecules, at the end of the reaction, samples have been cleaned by ultrasonication in dichloromethane and deionized water.

2.2.4 Step 3: Surface initiated atom transfer radical polymerization (SI-ATRP) of methyl methacrylate

In the third step, the hybrid PMMA-coated Ti surfaces have been obtained by growing the polymer chains from the initiator-modified Ti surfaces by a SI-ATRP process. The initiator-modified surfaces have been transferred in a reactor where all the other reagents have been successively incorporated and stirred. In the following paragraphs, considerations concerning the reagents and the protocol chosen will be given. The characterization of the polymer layer will be shown in Sec. 3.3.1.

[1] Comparable amounts of initiator have been already used in literature for the SI-ATRP from flat surfaces [4, 30, 31].

As presented in Chap. 1 (Sec. 1.1), during the ATRP reaction, the active species (or radicals) are generated by a reversible oxidation-reduction reaction catalyzed by a transition metal complex (i.e., the ATRP catalyst), whose function is to produce the active species on which the monomer can be added. The transition metal complex selected results from the in-situ addition of copper(I) bromide (CuBr) and the ligand N,N,N',N',N"- pentamethyldiethylenetriamine (PMDETA), whose chemical structure is reported in Fig. 2.7a. They have been added in a [CuBr/PMDETA] molar ratio equal to 1. Generally, in bulk (or solution) polymerization these molar quantities are calculated in relation to the ATRP initiator quantity, using a [initiator/catalyst] molar ratio equal to 1 [32]. Instead, in flat surface-confined polymerization, the exact amount of grafted initiator (i.e. the grafting density) is not easily measured, because of the macroscopic dimension of the substrates. In our case this rule could not be followed, thus the following approximation has been used.

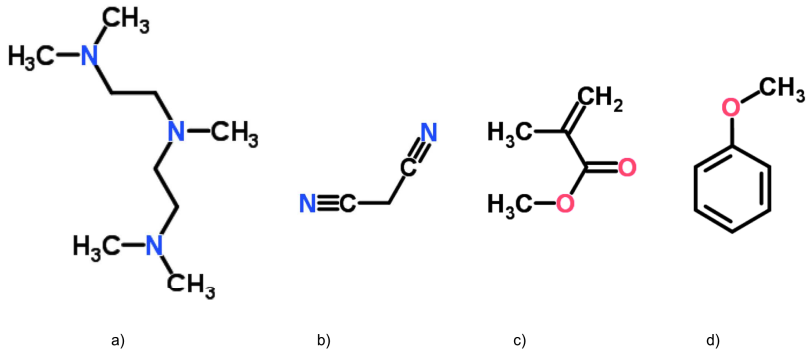

Figure 2.7: Chemical structures of: a) N,N,N',N',N"- pentamethyldiethylenetriamine; b) malononitrile ; c) Methyl methacrylate and d) anisole.

The reagent quantities have been calculated with regard to all the amount of initiator used in the grafting reaction (explained in Sec. 2.2.3), much more higher than that actually grafted. Hereafter, this quantity has been defined "apparent initiator". Essentially, it has been supposed that all the initiator added in the reactive media during the grafting reaction has been immobilized on the surface and the amount of the catalysts have been successively derived from this value. Moreover, it has been noticed that the accessibility of the initiator immobilized on the rough surfaces decreased with respect to flat and smooth substrates. Thus, a large excess of CuBr and PMDETA, with respect to the "apparent initiator quantity", has been required[2]. In particular, a [catalyst/"apparent initiator"] molar ratio equal to 5 has been used. In addiction, to increase the thickness of the polymer layer, malononitrile (which is known to enhance the polymerization rate [33,34]), has been added in the same concentration as copper bromide (Fig. 2.7b). Finally the quantity of the chosen monomer (MMA, Fig. 2.7c), has been optimized in order to get a 5.3 M concentrated solution maintaining a [MMA/"apparent initiator"] ratio equal to 2000.

All these products have been dissolved in anisole (Fig. 2.7d) and the ATRP reaction proceeded according to the following procedure.

[2]Comparable excess of catalysts and monomer have been already reported in literature [4, 30, 31].

Protocols

First of all, the reactor, equipped with the initiator-modified substrates and a magnetic stirrer, has been degassed three times, alternating vacuum and argon, and finally filled up with argon.

Successively, 14 mM of CuBr and PMDETA have been incorporated and dissolved in 9 mL of anisole and then stirred to yield an homogeneous solution. Then, 14 mM of malononitrile has been added in the reactive media.

Finally, 5.3 M of MMA - purified from its stabilizer by column chromatography on basic aluminum oxide - has been joined in the flask and the reaction has been allowed to proceed at 35 °C for 24 h under argon. Once the selected time has been reached, the substrates have been removed from the polymerization medium, rinsed and washed by ultrasounds in methanol in order to remove the residues of CuBr and PMDETA.

These samples have been defined *PMMA-coated Ti*.

2.3 Characterization methodologies

Suitable characterization methods are required to control and optimize the functionalization of the investigated surfaces. Thus, after each step of the procedure, both sampless morphology and their chemical characteristics, have been extensively characterized using standard imaging techniques (i.e. SEM and AFM) as well as surface spectroscopies (such as, FTIR, XPS and EDX). The results are given in Chap. 3.

Moreover, advanced AFM-based techniques for the surface mechanical characterization have been developed and used for the analysis of specific issues related to the development and fabrication of new hybrid materials.

In the following sections, the standard methodologies and the experimental set-up employed for the physicochemical characterization of the samples are presented. Particularly attention will be given to the AFM-based techniques, whose development has been part of this research work, in the dedicated Chapter 4.

2.3.1 Physicochemical characterization

Fourier transform infrared spectroscopy

Fourier transform infrared spectroscopy (FTIR) spectroscopy is based on the interaction between an infrared radiation and the investigated sample. Indeed, when an infrared light interact with a material, molecular vibrations are generated. By detecting the frequencies of these molecular vibrations specific bonds and functional groups characteristics of the surface are determined.

In this study attenuated total reflection infrared spectroscopy (ATR-FTIR) analysis has been performed in order to examine the bonds exposed on Ti surfaces after the three steps of the synthesis procedure (namely, the alkali treatment, the grafting of the initiator and the polymerization). Specifically, after the NaOH treatment the presence of OH groups has been examined; the successful grafting has been evaluated by the presence of the Ti−O−P bonds vibrations in the FTIR spectra. Whereas the presence of the PMMA layer has been assessed by signals related to the carbonyl group (C=O) and α-methyl (αCH_3) vibrations.

All the spectra reported in this thesis have been obtained with a Perkin Elmer FTIR spectrometer with a resolution of 4 cm^{-1}.

X-ray photoelectron spectroscopy

X-ray photoelectron spectroscopy (XPS) allows to obtain quantitative information of surface chemical composition. It is based on the photoelectric effect: when light photons hit the surface of a material, electrons with a specific kinetic energy are emitted. Since, the kinetic energy of photoemitted electrons is associated with their binding energy (i.e. the energy with whom they are bound to the nucleus of the atoms), by recording it, a quantitative evaluation of the elements of the surface and their concentration is obtained.

The XPS spectra here reported have been recorded with a MULTILAB 2000 (THERMO VG) spectrometer equipped with an Al Kα anode (hν 1486.6 eV). The C 1s peak at 284.6 eV has been used to correct charging effects.

Energy dispersive X-ray microanalysis

The elemental composition of the surfaces has been investigated by collecting the X-rays emitted by the sample surface stricken by the electron beam, performing the so-called energy dispersive X-ray microanalysis (EDX). In this technique, the energies associated with these emitted X-rays, is related to the characteristic energy of the surface elements. Thus, detecting them it is possible to determine the composition of the surface.

The spectra reported in this thesis, have been recorded at 4 keV on the top-view of the surface and throughout the sample cross-section (cut by FIB). In particular, referring to Fig. 3.21, the variation of the relative element concentration, from the bulk Ti substrate towards the polymer surface, has been determined by collecting 29 numbers of EDX spectra, each for 30 s, along a line of 880 nm (black arrow in Fig. 3.21a). Whereas, the spatial concentration of the bromine surface concentration after the grafting procedure (Fig. 3.18) has been determined performing high resolution EDX maps. In all the cases, quantitative values have been calculated using Bruker Esprit software.

Thermogravimetric Analysis

In thermogravimetric analysis (TGA) physicochemical changes (such as mass loss or decomposition) of the investigated material are measured as temperature increases. In this study TGA, has been employed to determine the glass transition temperature of the a commercial PMMA sheet and to estimate the average thickness of the PMMA layer grown on a modified Ti substrate. Both analyses have been performed with a Q50 apparatus of TA Instruments under air using a heating rate of 5 °C/min.

Inductively coupled plasma-atomic emission spectrometry

Inductively coupled plasma-atomic emission spectrometry (ICP-AES) is an analytical method to measure the elemental composition of samples. Sample solution, made in the aerosol form by a nebulizer, is introduced in a plasma (composed of ionized argon) whose high temperature ($\approx$ 7000 °C) excites the outer-shell electrons of the elements. This results in the emission of electromagnetic radiation at wavelengths characteristic of a particular element. In this thesis, the ICP-AES analysis has been used to evaluate the release of sodium (Na) ions during the grafting reaction and to determine the composition of simulated body fluid solutions, in which the PMMA-coated Ti samples have been soaked.

2.3.2 Morphological characterization

Scanning Electron Microscopy

The sample surface morphology has been investigated by SEM analysis through a CrossBeam®Workstation (FIB-SEM) AURIGA-Zeiss 405 Microscopy equipped with a Quantax energy dispersive X-ray (EDX) system.

Basically, the electron beam generated by a field emission gun is accelerated toward the sample's surface by a high voltage (10-30 keV). The electron beam passes through a system of electromagnetic lenses producing a thinner and focused beam of electrons. When the beam hits the sample, the scanning of the surface starts. Secondary electrons are, thus, emitted from the surface, because of the interaction between the scanning beam and the sample, and collected by a suitable detector to form an image reproducing the features of the sample morphology.

However, the beam-sample interaction generates a variety of additional signals (such as, Auger electrons emission, X-ray emission and cathodoluminescence) which, once detected, allow to obtain further information on the sample's elemental composition.

Focus ion beam

Focused ion beam (FIB, Cobra, Physics d'Orsay) has been used to obtain sample cross-sections. The surface of the sample is tilted of an angle equal to 54° with respect to the horizontal line. It is hit by a focused beam of gallium ions (Ga^+) which sputters a small amount of material, producing a cut on the sample.

Simultaneously, secondary electrons are also collected to form an image of the cross-section. In this way, the cut can be followed in real time, allowing the optimization of the beam currents. This prevents the damage of the interface and minimizes the redeposition of Ga. The cross-sections display in this thesis have been cut with an ion's current of 120 pA for 30 s.

Atomic Force Microscopy

Atomic Force Microscopy (AFM) exploits the interactions between the atoms of a sharp probe and those of the sample's surface to reconstruct its topography with nanometer spatial resolution. In this work, to investigate the sample surface roughness and morphology a Dimension Icon microscope (Bruker) equipped with stiff silicon cantilever (RTESP, Bruker) has been employed.

2.3.3 Wettability characterization

Contact angle measurements, performed with an home-made apparatus, have been employed to determine the wettability of the surface after each step of the process. If the contact angle value is in the range 0-90° the surface has a good wettability and it is defined hydrophilic. Otherwise, for contact angle values greater than 90°, the surface is called hydrophobic. Samples have been arranged on a horizontal table and a drop (1 mL) of distilled water has been deposited on the surface using a micropipette. The contact angle has been then measured by a high resolution camera. Each sample has been measured at least three times.

2.3.4 Mechanical characterization

Depth sensing indentation

The indentation modulus of PMMA-coated Ti and of the bulk PMMA sheet have been determined using standard depth sensing indentation (DSI, Nano Test Micro Mateirals Ltd.) using a diamond cone tip with an angle of 90° and a radius of 25 μm. Force-indentation curves have been obtained with maximum load values of 0.2 mN, 0.4 mN, 0.6 mN, 1 mN, 3 mN, and 5 mN. For each value of maximum load, 25 force-indentation curves have been acquired. The time of maximum applied load and the penetration time, using load control, were 10 s 30 s, respectively. Indentation modulii, calculated using data taken from the slope of the tangent to the unloading curve, are given in Chap. 5.

AFM-based techniques

Four different, static and dynamic, AFM-based techniques have been developed and employed to study the mechanical properties of the samples' surface using two different AFM apparatus (namely, Dimension Icon (Bruker) and a Solver Pro equipped with a Smena head (NT-MDT). More details of the AFM working principle and of the mechanical characterization methods are give in Chap. 4. The mechanical characterization of the PMMA-coated Ti interfaces is illustrated in Chap. 5.

2.3.5 In vitro cytotoxicity evaluation

Cell culture

Preliminary investigation of the samples biocompatibility has been performed BJ2 human fibroblasts (obtained from ATCC). They have been cultured in Eagle's Minimum Essential Medium (EMEM, ATCC) supplemented with 10% fetal bovine serum, 1% antibiotics (penicillin-streptomycin), 0.2% fungizone at 37 °C in a 5% CO_2 atmosphere. Prior to seeding, cells have been harvested using 0.05% trypsin/0.02% EDTA, centrifuged, resuspended in media and used for essays.

Metabolic activity: Alamar Blue assay

After 1 day and 6 days, cells viability has been evaluated performing colorimetric metabolic Alamar Blue assay. Essentially, samples were incubated with 10% resazurin (Fluorimetric cell viability kit I, PromoKine) in cell culture medium for 2 h. The reduction of resazurin as an indirect measure of cellular metabolic activity has been assessed per manufacturer's instructions. The amount of fluorescence has been monitored with a SAFAS Xenius XML fluorescence reader (SAFAS, Monaco) at excitation wavelength of 560 nm and emission wavelength of 590 nm.

Cells morphology

Cells have been fixed with 4% glutaraldehyde washed with Phosphate-buffered saline solution (PBS) and dehydrated using an alcohol series of increasing concentration (50%, 70%, 95% and 3Œ100%, 5 min each). Subsequently, samples have been incubated in 100% ethanol/hexamethyl disilazane (HMDS) (1:1) for 5 min, then only in HMDS for 10 min and dried overnight. Then, they have been mounted onto SEM stubs using a conductive

carbon tape and coated with gold/palladium in a sputter coater under angon atmosphere (using a current of 7.5 mA for 3 min). Images, with various magnifications, have been acquired using a scanning electron microscope (Hitachi TM1000). The morphology of cells cultivated directly onto the samples surface has evaluated by SEM analysis.

Fluorescence microscopy

The effect of the gelatin functionalization on the cells behavior has been assessed by Immunofluorescence staining. Visualization of f-actin filaments has been done using fluorophore conjugated phalloidin (Alexa-Fluor 568, Invitrogen). For this purpose, cells have been fixed with 4% paraformaldehyde in PBS for 10 min at room temperature (RT). Then, they have been washed twice with PBS and permeabilized with 0.2% Triton X-100 for 5 min at RT, and washed with PBS two times. Successively, cells have been incubated in PBS, containing 1% bovine serum albumin (BSA), for 20 min prior to the addition of phalloidin. Phalloidin has been added and cells were incubated for 30 min at room temperature in the dark. Subsequently, DAPI solution (Promocell) has been added to label the nuclei, for 5 min in the dark at RT. Then, the cells have been washed in PBS to remove the unbound phalloidin and DAPI and samples kept in PBS for imaging. Fluorescence images, have been captured using Nikon Elipse Ti-S with 10X and 40X objectives equipped with Nikon Digital Camera (equipped with NIS-Elements software).

2.3.6 Stability of the tethered polymer layer in simulated body fluid

The stability and durability of the PMMA layer has been assed by soaking the samples in a simulated body fluid (SBF) and investigating their morphology and chemical composition. SBF is a solution that has an inorganic ion concentrations similar to those of the human extracellular fluid. It is generally employed to reproduce *in vitro* the formation of apatite on bioactive materials [35]. Whereas, a SBF contains a higher ions concentration, with respect to the standard SBF, is called saturated SBF [36]. In this thesis, it has been used a solution containing an ion concentration 1.5 times higher than standard SFB, called 1.5×SBF solution. In Tab. 2.3 the ion concentrations of both the standard and the saturated 1.5×SBF solutions as well as those of the human blood plasma are reported.

Table 2.3: Ion concentrations of: SBF, 1.5×SBF and human blood plasma.

Ion	SBF [mM]	1.5×SBF [mM]	Human blood plasma [mM]
Na^+	142.0	213.0	142.0
K^+	5	7.5	5
Mg_2^+	1.5	2.3	1.5
Ca_2^+	2.5	3.8	2.5
Cl^-	147.8	221.7	103.0
HCO_3^-	4.2	6.3	27.0
HPO_4^{2-}	1.0	1.5	1.0
SO_4^{2-}	0.5	0.8	0.5

PMMA-coated Ti discs have been soaked in a 1.5×SBF solution maintained at 37 °C whose pH has been set to 7.3 ± 0.1 using a titrate solution consisting of tris-(hydroxymethyl)aminomethane

($(CH_2OH)_3CNH_2$) and hydrochloric acid (HCl). Three different immersion periods (2, 14 and 21 days) have been chosen; their surface morphology and composition evolution have been checked performing SEM observation and FTIR analysis, respectively. The 1.5×SBF solution has been refreshed each 7 days.

Bibliography

[1] Y. Matsuda, H. Yanagida, T. Ide, H. Matsumura, and N. Tanoue, "Bond strength of poly (methyl methacrylate) denture base material to cast titanium and cobalt-chromium alloy.," *Journal of Adhesive Dentistry*, vol. 12, no. 3, 2010.

[2] L. G. Rothfuss, S. D. Hokett, S. O. Hondrum, and C. W. Elrod, "Resin to metal bond strengths using two commercial systems," *The Journal of Prosthetic Dentistry*, vol. 79, no. 3, pp. 270–272, 1998.

[3] O. Alageel, M.-N. Abdallah, Z. Y. Luo, J. Del-Rio-Highsmith, M. Cerruti, and F. Tamimi, "Bonding metals to poly (methyl methacrylate) using aryldiazonium salts," *Dental Materials*, vol. 31, no. 2, pp. 105–114, 2015.

[4] B. Barthélémy, S. Devillers, I. Minet, J. Delhalle, and Z. Mekhalif, "Induction heating for surface triggering styrene polymerization on titanium modified with ATRP initiator," *Journal of Colloid and Interface Science*, vol. 354, no. 2, pp. 873–879, 2011.

[5] V. Vergnat, *Matériaux hybrides organiques-inorganiques par greffage covalent de polymères sur des oxydes métalliques*. PhD thesis, Strasbourg, 2011.

[6] V. Vergnat, T. Roland, G. Pourroy, and P. Masson, "Effect of covalent grafting on mechanical properties of TiO_2/polystyrene composites," *Materials Chemistry and Physics*, vol. 147, no. 1, pp. 261–267, 2014.

[7] G. Guerrero, P. Mutin, and A. Vioux, "Anchoring of phosphonate and phosphinate coupling molecules on titania particles," *Chemistry of Materials*, vol. 13, no. 11, pp. 4367–4373, 2001.

[8] R. Boissezon, J. Muller, V. Beaugeard, S. Monge, and J.-J. Robin, "Organophosphonates as anchoring agents onto metal oxide-based materials: synthesis and applications," *RSC Advances*, vol. 4, no. 67, pp. 35690–35707, 2014.

[9] E. P. Lautenschlager and P. Monaghan, "Titanium and titanium alloys as dental materials.," *International Dental Journal*, vol. 43, no. 3, pp. 245–253, 1993.

[10] M. Long and H. Rack, "Titanium alloys in total joint replacement: a materials science perspective," *Biomaterials*, vol. 19, no. 18, pp. 1621–1639, 1998.

[11] M. Niinomi, "Mechanical properties of biomedical titanium alloys," *Materials Science and Engineering: A*, vol. 243, no. 1, pp. 231–236, 1998.

[12] C. Oldani, A. Dominguez, and T. Eli, *Titanium as a Biomaterial for Implants*. Citeseer, 2012.

[13] F. Rodriguez-Gonzalez, "Introduction to biomaterials in orthopaedic surgery," *Biomater Orthop Surg*, pp. 1–10, 2009.

[14] Q. Chen and G. A. Thouas, "Metallic implant biomaterials," *Materials Science and Engineering: R: Reports*, vol. 87, pp. 1–57, 2015.

[15] C. Leyens and M. Peters, *Titanium and titanium alloys: fundamentals and applications*. John Wiley & Sons, 2003.

[16] M. McCracken, "Dental implant materials: commercially pure titanium and titanium alloys," *Journal of Prosthodontics*, vol. 8, no. 1, pp. 40–43, 1999.

[17] C. Elias, J. H. Lima, R. Valiev, and M. Meyers, "Biomedical applications of titanium and its alloys," *JOM Journal of the Minerals, Metals and Materials Society*, vol. 60, no. 3, pp. 46–49, 2008.

[18] R. Q. Frazer, R. T. Byron, P. B. Osborne, and K. P. West, "Pmma: an essential material in medicine and dentistry," *Journal of Long-Term Effects of Medical Implants*, vol. 15, no. 6, 2005.

[19] S. Kenny and M. Buggy, "Bone cements and fillers: a review," *Journal of Materials Science: Materials in Medicine*, vol. 14, no. 11, pp. 923–938, 2003.

[20] T. Goda and K. Ishihara, "Soft contact lens biomaterials from bioinspired phospholipid polymers," *Expert Review of Medical Devices*, vol. 3, no. 2, pp. 167–174, 2006.

[21] E. Ajami and K.-F. Aguey-Zinsou, "Functionalization of electropolished titanium surfaces with silane-based self-assembled monolayers and their application in drug delivery," *Journal of Colloid and Interface Science*, vol. 385, no. 1, pp. 258–267, 2012.

[22] B. Chou, R. Jain, D. McGervey, U. Landau, and G. Welsch, "Electropolishing of titanium," *Proceedings of the Electrochemical Society*, vol. 2002, p. 1, 2002.

[23] S.-i. Tanaka, H. Tobimatsu, Y. Maruyama, T. Tanaki, and G. Jerkiewicz, "Preparation and characterization of microporous layers on titanium," *ACS Applied Materials & Interfaces*, vol. 1, no. 10, pp. 2312–2319, 2009.

[24] H.-M. Kim, F. Miyaji, T. Kokubo, and T. Nakamura, "Preparation of bioactive Ti and its alloys via simple chemical surface treatment," *Journal of Biomedical Materials Research*, vol. 32, no. 3, pp. 409–417, 1996.

[25] M. Ramalingam, S. Ramakrishna, and S. Best, *Biomaterials and stem cells in regenerative medicine*. CRC Press, 2012.

[26] F. Gil, A. Padrós, J. Manero, C. Aparicio, M. Nilsson, and J. Planell, "Growth of bioactive surfaces on titanium and its alloys for orthopaedic and dental implants," *Materials Science and Engineering: C*, vol. 22, no. 1, pp. 53–60, 2002.

[27] Y. Chen, X. Zheng, H. Ji, and C. Ding, "Effect of Ti−OH formation on bioactivity of vacuum plasma sprayed titanium coating after chemical treatment," *Surface and Coatings Technology*, vol. 202, no. 3, pp. 494–498, 2007.

[28] E. Cao, E. Prouzet, and V. Héroguez, "Organic–inorganic hybrid materials designed by controlled radical polymerization and mediated using commercial dual functional organophosphorous coupling agents," *New Journal of Chemistry*, vol. 38, no. 12, pp. 6081–6087, 2014.

[29] A. Walter, A. Garofalo, A. Parat, J. Jouhannaud, G. Pourroy, E. Voirin, S. Laurent, P. Bonazza, J. Taleb, C. Billotey, *et al.*, "Validation of a dendron concept to tune colloidal stability, MRI relaxivity and bioelimination of functional nanoparticles," *Journal of Materials Chemistry B*, vol. 3, no. 8, pp. 1484–1494, 2015.

[30] I. Minet, J. Delhalle, L. Hevesi, and Z. Mekhalif, "Surface-initiated ATRP of PMMA, PS and diblock PS-b-PMMA copolymers from stainless steel modified by 11-(2-bromoisobutyrate)-undecyl-1-phosphonic acid," *Journal of Colloid and Interface Science*, vol. 332, no. 2, pp. 317–326, 2009.

[31] B. Barthélémy, S. Devillers, I. Minet, J. Delhalle, and Z. Mekhalif, "Surface-initiated ATRP of 2-(methacryloyloxy) ethyl 2-(trimethylammonio) ethyl phosphate on phynox," *Applied Surface Science*, vol. 258, no. 1, pp. 466–473, 2011.

[32] K. Matyjaszewski and J. Xia, "Atom transfer radical polymerization," *Chemical Reviews*, vol. 101, no. 9, pp. 2921–2990, 2001.

[33] Z. Jiaming, H. Jianying, C. Jiayan, L. Xurong, L. Yutai, Z. Yousi, *et al.*, "A novel rate-accelerating additive for atom transfer radical polymerization of styrene," *Journal of Polymer Science Part A: Polymer Chemistry*, vol. 45, no. 17, pp. 4082–4090, 2007.

[34] V. Vergnat, G. Pourroy, and P. Masson, "Enhancement of styrene conversion in organic/inorganic hybrid materials by using malononitrile in controlled radical polymerization," *Polymer International*, vol. 62, no. 6, pp. 878–883, 2013.

[35] T. Kokubo, H. Kushitani, S. Sakka, T. Kitsugi, and T. Yamamuro, "Solutions able to reproduce in vivo surface-structure changes in bioactive glass-ceramic A-W3," *Journal of biomedical materials research*, vol. 24, no. 6, pp. 721–734, 1990.

[36] M. Tanahashi, T. Yao, T. Kokubo, M. Minoda, T. Miyamoto, T. Nakamura, and T. Yamamuro, "Apatite coating on organic polymers by a biomimetic process," *Journal of the American Ceramic Society*, vol. 77, no. 11, pp. 2805–2808, 1994.

Chapter 3

PMMA-coated Ti fabrication

This Chapter will report the results of the PMMA-coated Ti fabrication obtained following the three-step strategy explained in Chap. 2.

3.1 Titanium chemical activation: alkali treatment

First of all, Ti Gr. 2 disks have been mechanically polished, according to the procedure described in Sec. 2.2.1, in order to reduce its surface roughness and obtained a mirror-like surface, whose microstructure is reported in Fig. 3.1.

Then, the samples have been activated using an alkali treatment performed in a NaOH solution (see Sec. 2.2.2). The aim of this study was to find the best conditions ensuring a high content of hydroxyl together with the desired surface roughness.
Indeed, as already reported in literature [1], this alkali treatment etches the Ti samples producing superhydrophylic amorphous sodium titanate with a high open nanometric porosity, as described in Sec. 2.2.2).

The effect of different treatment times and NaOH concentrations have been investigated and the results are discussed in Sec. 3.1.1 and Sec. 3.1.2.

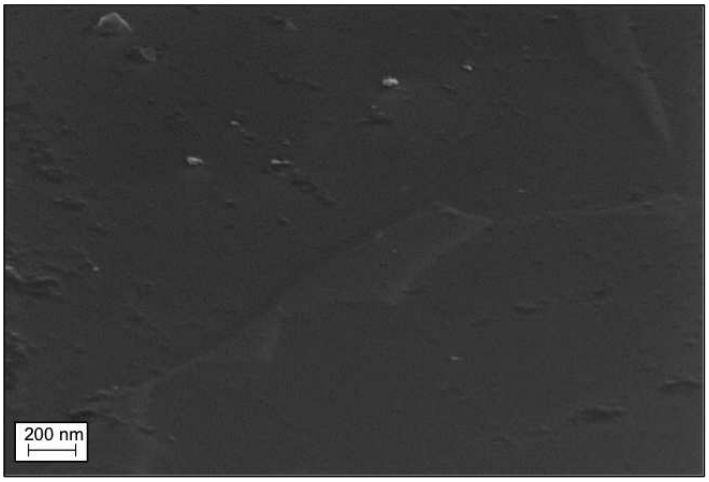

Figure 3.1: SEM micrograph of a mirror-like mechanically polished Ti Gr. 2 surfaces.

3.1.1 Process optimization: effect of the alkali time treatment

The goal has been to find the time required to induce, on the Ti surfaces, an amount of OH groups ensuring a good grafting of the initiator molecules. A 2 M concentrated NaOH solution (already used to favor the adsorption of collagen on Ti substrates [2]) and a temperature of 80 °C has been chosen. The effect of five different treatment times (1 h, 3 h, 6 h, 12 h, and 24 h) have been studied. Shorter times treatment resulted in a non homogeneous microporous layer. The surface morphology of the substrates subjected to the alkali treatment mentioned above, have been investigated by SEM.

The alkali treatment leads to the formation of a hierarchical porous interlayer, with a pore size ranging between 50 nm to 200 nm, consisting of regular pillared and cone-shaped structure which covers the entire surface (Fig. 3.2 to Fig.3.4). The surface morphology of the sample treated for 1 h is made up of a nanostructured network with interconnected

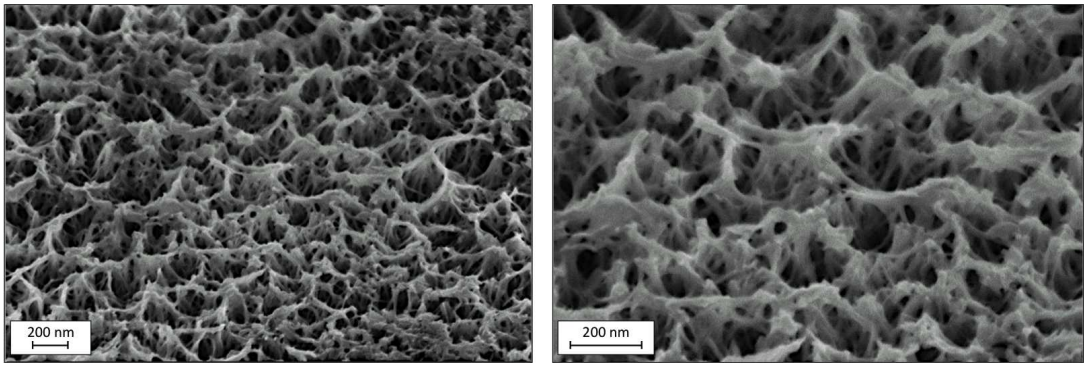

Figure 3.2: SEM micrographs of the sodium titanate interlayer produced on Ti substrates after an alkaline treatment of 1 h in a 2 M concentrated NaOH aqueous solution.

pillars tens of nanometers width. This results in a highly open porosity (Fig. 3.2). An increase of the treatment time produces a reduction of the specific surface: the pillars become thicker and the porous less interconnected (Fig. 3.3). In particular, Fig. 3.3a (100 000 X) and Fig. 3.3b (200 000 X) refer to surfaces treated for 3 h, whereas the surface features obtained after a NaOH treatment lasted for 6 h are depicted in Fig. 3.3c and Fig. 3.3d. A further increase of the treatment (12 h) produces a less branched network composed of facets rather than pillars, as highlighted in Fig. 3.4a-b.

For longer time treatment (24 h, reported in Fig. 3.4c-d), the typical surface features of the layer do not uniformly cover the Ti surfaces. This could be due to a too long reaction

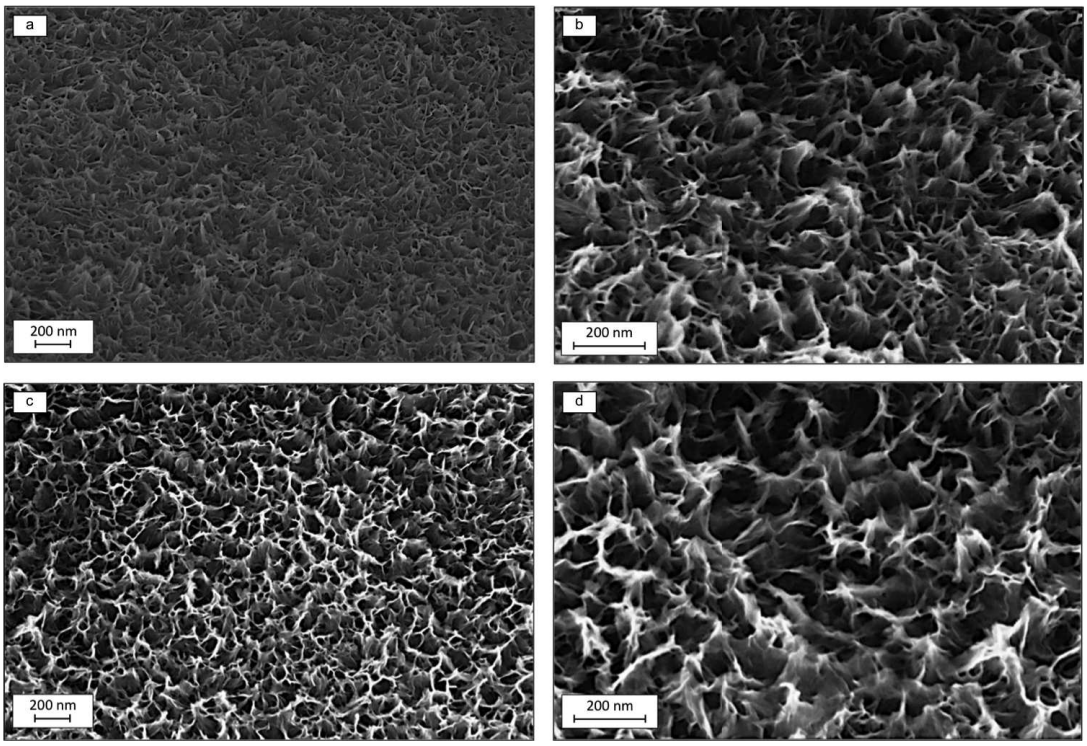

Figure 3.3: SEM micrographs of the Ti surfaces activated in a 2 M concentrated NaOH aqueous solution for: a-b) 3 h; c-d) 6 h.

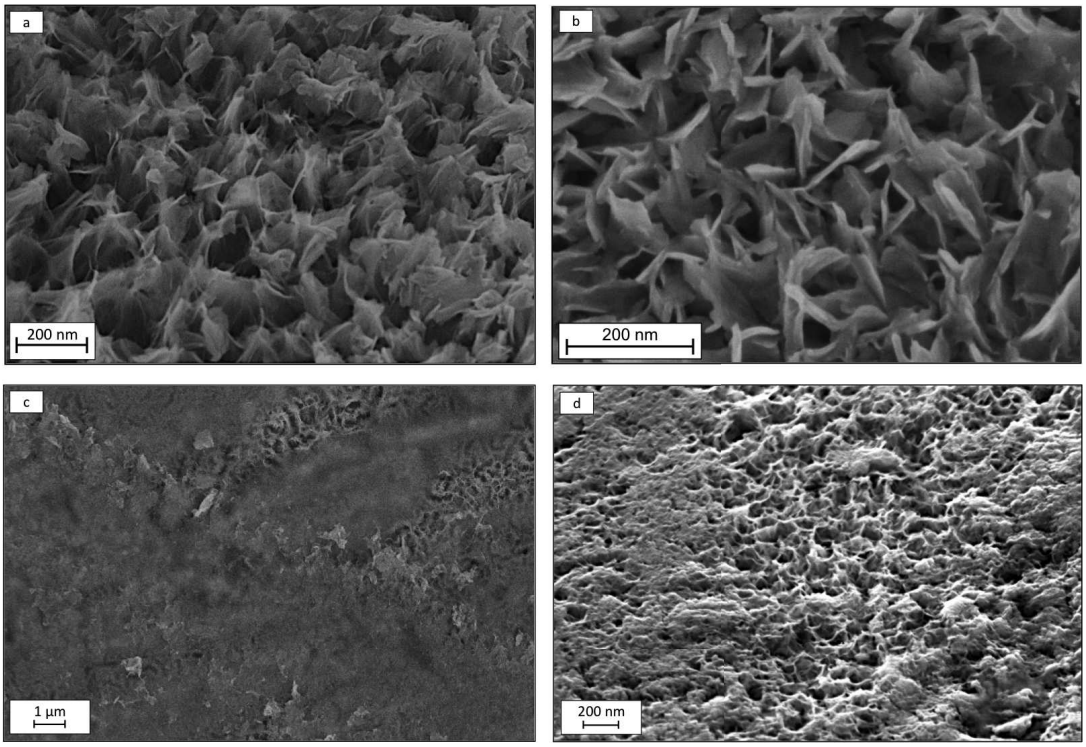

Figure 3.4: Morphologies of the Ti surfaces after an alkali treatment in a 2 M concentrated NaOH aqueous solution for: a-b) of 12 h; c-d) 24 h.

time provoking an agglomeration of the already "etched/reacted" material which causes a more compact structure. It has been pointed out that, maintaining a constant 2 M NaOH concentration, for treatment time longer than 6 h, the surface porosity decreases by increasing the time. Compared to the results reported in literature, in which more concentrated solutions (5 M and/or 10 M) are generally employed [1,3,4], these observations are in agreement with the hypothesis that, for the chosen concentration, there is a threshold time; above it the NaOH species are not enough to continue reacting with the Ti surfaces and the produced interlayer collapses. Instead, for more concentrated solutions (5 M and 10 M), even after a treatment of 24 h, there are more NaOH species available to react creating a porous layer uniformly distributed on the surface [4–6].

In Fig. 3.5, the FTIR spectra of the Ti and alkali-activated Ti substrates are reported. The broad band at 3600 cm^{-1} and 3100 cm^{-1} is assigned to the fundamental stretching vibrations of different OH hydroxyl groups [7–9]. The shoulder around 958 cm^{-1}, whose intensity increases for longer treatment time, indicates the presence of Ti-OH species [7]. Finally, the peak between 650 cm^{-1} and 400 cm^{-1}, whose width decreases by diminishing the treatment time, is assigned to the Ti-O-Ti stretching vibrations [9].

It can be concluded that the shorter the alkali treatment time, the lesser the quantity of oxide. Furthermore, no diffraction lines, except those of Ti substrates, have been detected in the X-ray diffraction pattern showing that the microporous layer is amorphous.

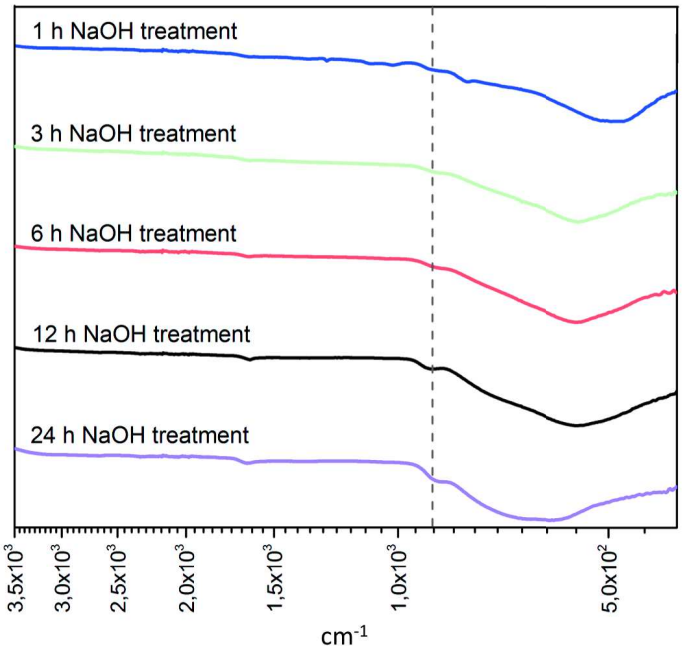

Figure 3.5: ATR-FTIR spectra of the Ti surfaces activated in a 2 M concentrated NaOH solution for 1 h (blue), 3 h (green), 6 h (red), 12 h (black) and 24 h (pink).

3.1.2 Process optimization: effect of the alkali concentration

By fixing a treatment time of 1 h, which ensures a high open porosity of the surface, the effect of different NaOH concentration has been studied. Fig. 3.6a and Fig. 3.6b report the surface morphologies achieved employing 0.1 M and 0.5 M NaOH concentrations, respectively. They give rise to a sodium titanate hydrogel appearing less structured and thinner compared to that obtained with a 1 M concentrated solution (Fig. 3.6c).

Whereas a solution of 5 M (Fig. 3.6e) produces a thicker interconnected layer with pillars wider even compared to those obtained after a treatment with a 2 M concentrated NaOH solution (Fig. 3.6d). This is also confirmed by the elemental analysis performed by EDX measurements which highlighted an increase in the oxygen (O) and sodium (Na) content as the concentration increases (Fig. 3.6f).

3.1.3 Process optimization: effect of the surface polishing

Finally, the surface morphology after an alkaline treatment performed on a mechanically polished Ti and an unpolished Ti substrates has been investigated. The surface morphologies, reported in Fig. 3.7, clearly show that the polishing pre-treatment leads to smoother and more uniform morphology (Fig. 3.7a and Fig. 3.7b) compared to the one obtained starting from an unpolished Ti substrates. Indeed, in this last case, the surfaces is characterized by some fissures and rose-shaped structures (highlighted with yellow lines in Fig. 3.7c and Fig. 3.7d). Thus, since a smoother surface finishing seems to result in a more uniform titanate layer, a surface polishing treatment, before the activation step, has been performed.

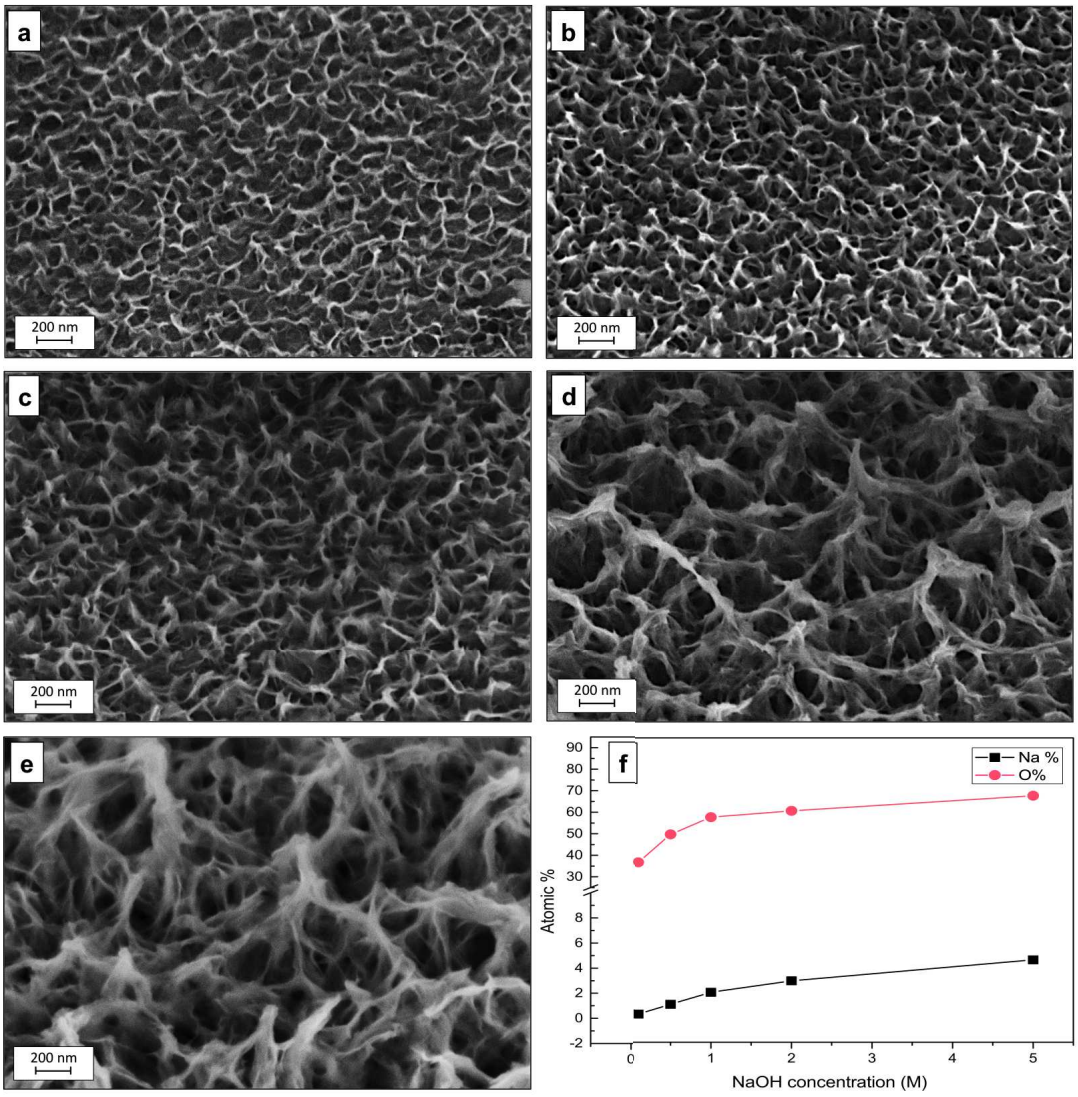

Figure 3.6: SEM micrographs of Ti surfaces after an alkali treatment of 1 h in: a) 0.1 M NaOH concentrated solution; b) 0.5 M NaOH concentrated solution; c) 1 M NaOH concentrated solution; d) 2 M NaOH concentrated solution; e) 5 M NaOH concentrated solution; f) Variation of the Na and O atomic percentage, determined by EDX measurements, as function of the NaOH solution concentration.

3.1.4 Structure, composition and wettability of the produced microporous interlayer

The hierarchical structure of the microporous layer, produced by the alkali treatment, has been used as a scaffold able to drive the following polymerization in order to achieve thick and porous polymer coating. Thus, it has been necessary to have a highly open structure of few hundreds of nanometers thick. A thicker structure could limit the further growth of the polymer brushes, diminishing their adhesiveness power. For this reason, an alkali treatment of 1 h in a 2 M concentrated NaOH solution has been chosen. Hereafter, these substrates are labeled *2 M 1 h alkali-activated Ti*.

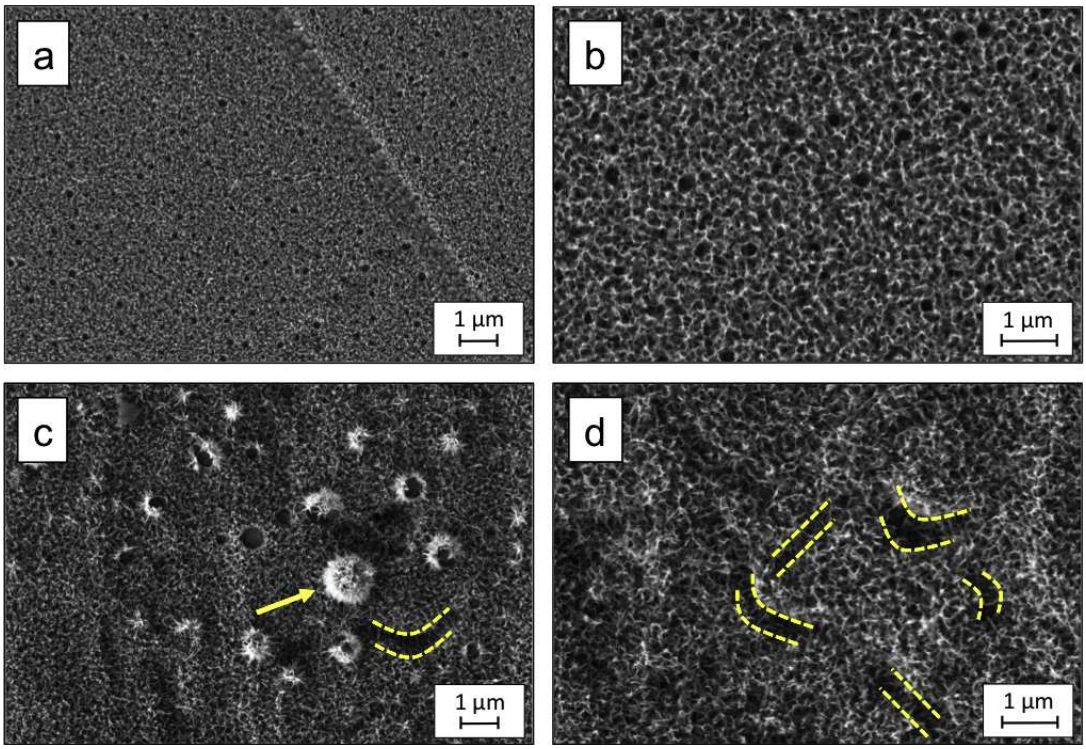

Figure 3.7: Effect of the Ti surface polishing on the formation of the titanate layer. Surface morphology of (a-b) mechanical polished Ti and (c-d) unpolished Ti surfaces, subjected to an alkali-treament of 1 h in a 2 M NaOH concentrated solution.

As already specified in Sec. 3.1.1, these conditions lead to a microporous layer which uniformly covers the entire surface, as highlighted by the low-magnified SEM micrograph reported in Fig. 3.8a. The Na ions into the sodium titanate layer have been checked by XPS analysis, whose spectra are reported in Fig. 3.8b. As expected, the survey spectrum

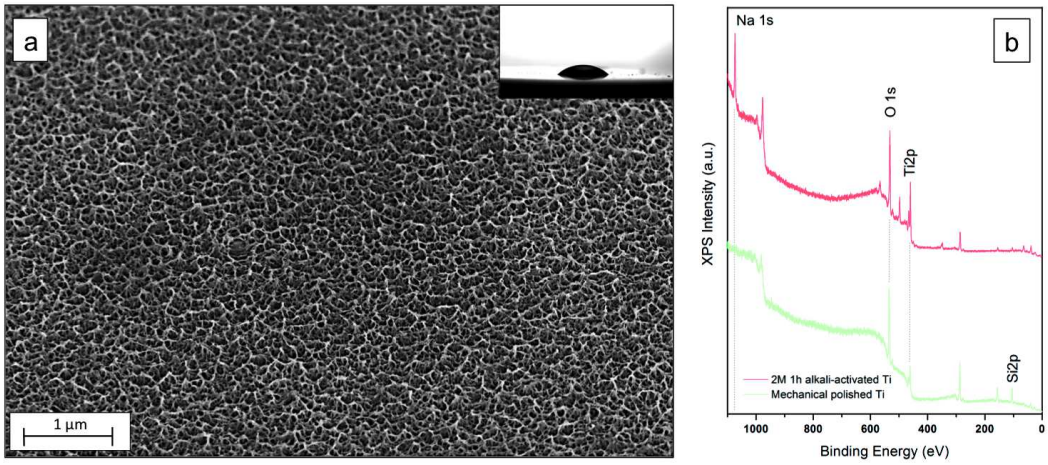

Figure 3.8: a) SEM image of a 2 M 1 h alkali-activated Ti surfaces (inset of a contact angle measurement); b) XPS survey spectra of: mechanical polished (green curve) and a 2 M 1h alkali-activated Ti surfaces (red curve).

of a 2 M 1h alkali activated surface (red curve) clearly exhibits the Na 1s peak at 1071 eV which is not detected in the spectrum of a mechanical polished Ti (green curve).

Moreover, the XPS spectrum in the O 1s region (Fig. 3.9) reveals two peaks at 530 eV and 531.9 eV which are attributed to the titanium oxide (TiO_2) and to surface acidic (OH^-) hydroxyl groups, respectively [10–12].

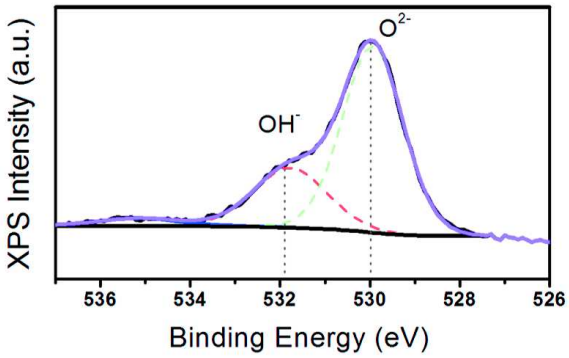

Figure 3.9: XPS narrow-scan spectra of O 1s peak of 2M 1h alkali activated Ti surfaces.

The titanate layer thickness has been evaluated using FIB coupled with SEM which allowed to cut the sample and analyze its cross-section, as reported in Fig. 3.10. As schematized in Fig. 3.10a, the sample has been tilted of an angle α of 54°, with respect to the horizontal line, and a focused beam of gallium ions (Ga^+) hit the sample surface sputtering a small amount of material and producing a cut on the sample. Meanwhile, secondary electrons have been collected to form an image so that the cut of the sample has been followed in real time, allowing the optimization of the beam currents in order to prevent the damage of the interface and to minimize the redeposit of Ga. Considering the scheme reported in Fig. 3.10a, for geometrical consideration also the angle formed between the electron beam and ion beam is equal to α. The thickness measured on the SEM image ((350 ± 50 nm), in Fig. 3.10b), is an "apparent" value since, it is the projection of the

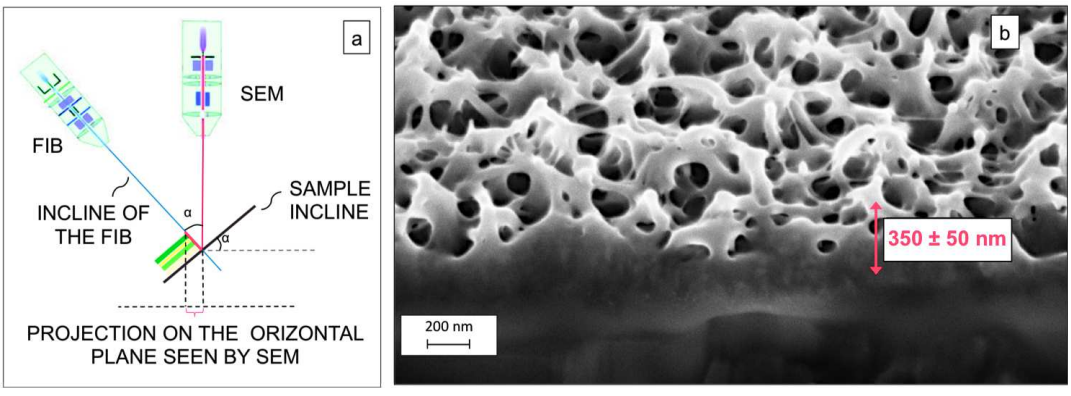

Figure 3.10: a) Schematization of the working principle of a FIB-SEM coupled system; b) cross-section of a 2 M 1 h alkali-activated Ti surface. The "apparent" value of the titanate layer thickness seen by the SEM is depicted in red. Considering the incline of the sample-holder with respect to the horizontal plane (α), the real value of the thickness is derived dividing the "apparent" value by $sin\alpha$.

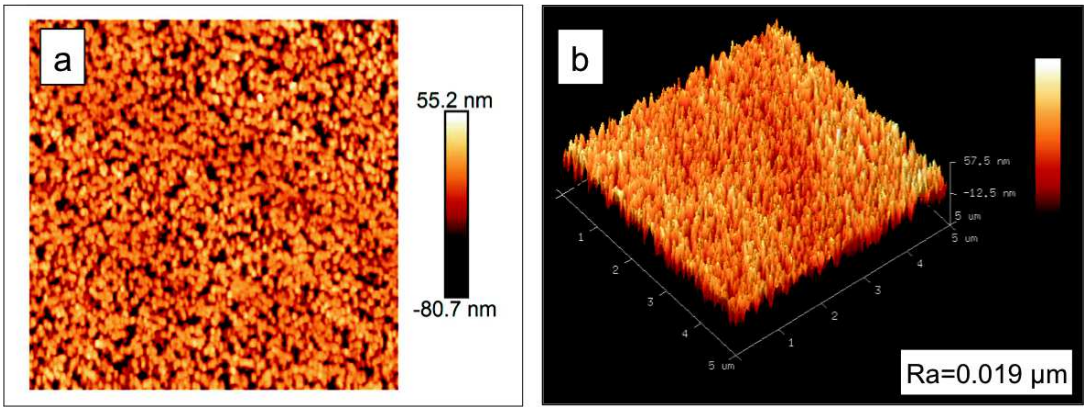

Figure 3.11: 5 μm^2 2D AFM topography of alkali activated Ti surface (s) and its 3D reconstruction.

inclined cross-section on the horizontal plane seen by the SEM. Thus, in order to derive the real value of the thickness, the "apparent" thickness has to be divided by $\sin(\alpha)$. This brings to a sodium titanate thickness of about 400 nm.

Furthermore, the mean value of the surface roughness has been measured by AFM images which provided an average roughness of (0.019 $\pm$ 0.004) μm. In Fig. 3.11a, a representative AFM topography of the activated Ti surface, with its 3D reconstruction (Fig. 3.11b), are reported. Furthermore, the wettability of the surface has been investigated by the contact angle analysis revealing that after the activation step the surface becomes hydrophilic with a contact angle equal to (25 $\pm$ 9)°(inset in Fig. 3.8a). This can be attributed to two main reasons: (*i*) an increase of the surface porosity and roughness (from (2.9 $\pm$ 1.3) nm of a polished Ti to (19 $\pm$ 4) nm of an alkali-activated Ti) and (*ii*) an increase the OH groups content, as proved by infrared-spectroscopy whose spectra revealed the bands of the Ti$-$OH bonds vibrations (Fig. 3.5).

3.2 Ti surface functionalization

This section the preparation of ATRP initiator modified surfaces obtained by a "grafting from" method, as described in Sec. 2.2.3, will be shown. The samples have been suspended in a 2 mM initiator concentrated aqueous solution heated at 100 °C and the reaction lasted 24 h in the dark. As explained in Sec. 2.2.3, the effect of two initiators (the bromoisobutyrate-propyl-1-phosphonic acid ($C_7H_{14}O_5PBr$) and the home-made bromoisobutyrate-undecenyl-1-phosphonic acid ($C_{15}H_{30}O_5PBr$), differing only for the number of carbon atoms in the alkyl chain, has been investigated. In the former, the anchoring phosphonic acid group is separated from α-bromo ester group by 11 carbons; the latter comprises an alkyl chain of 3 carbons. It should be noted that few grafting experiments performed of a not activated Ti surfaces, resulted in a poor anchoring of the initiator. Fig. 3.12 shows morphologies of the initiator-modified surfaces, in which stacking of physisorbed initiator layers have been observed. As illustrated in Sec. 2.2.3, this phenomenon is probably due to the large excess of initiator used with respect to that required for a complete surface covering. Thus, to remove the ungrafted molecules, at the end of the reaction, samples were cleaned by ultrasonication in dichloromethane and deionized water. The effect of four different time treatment (1 min, 3 min, 5 min and 10 min each solvent) on

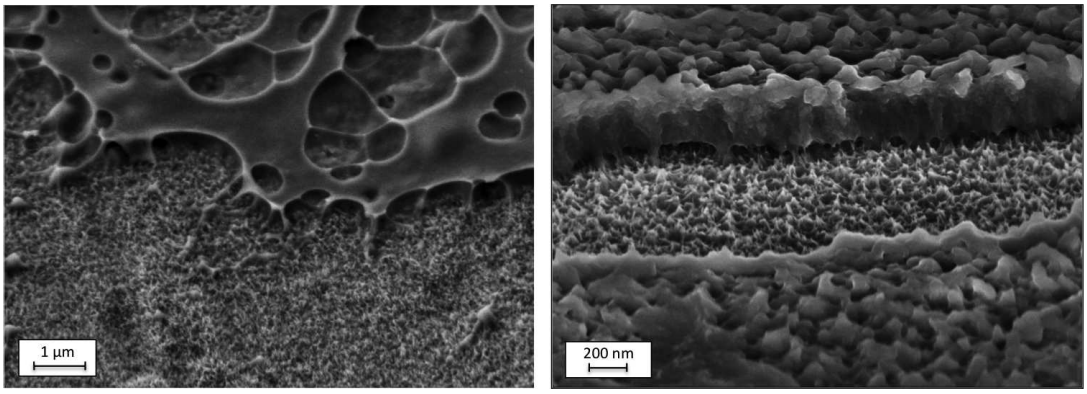

Figure 3.12: SEM micrograph of stacking physisorbed initiator layer on the long-initiator modified surfaces.

both the surface composition and morphology have been investigated by XPS, ATR-FTIR, EDX and SEM analysis (see Sec. 3.2.2).

3.2.1 Structure, composition and wettability of initiator-modified titanium surfaces

The anchorage of the two initiators on the 2 M 1h alkali-activated Ti-surfaces was checked by ATR-FTIR spectroscopy whose spectra are reported in Fig. 3.13.

The infrared absorption spectra of the polymerization initiators (black lines), in the 3100-2750 cm^{-1} range, exhibit: the asymmetric (νas CH_2) and symmetric (νs CH_2) stretching vibrations of the methylene groups, respectively at 2924 cm^{-1} and 2852 cm^{-1}, as well as the asymmetric methyl vibrations νas (CH_3) at 2960 cm^{-1}. Moreover, the peak at 1730 cm^{-1}, ascribed to the carbonyl C=O stretching vibrations is also present. Instead, the large number of peaks in the range 1300-900 cm^{-1} corresponds to the vibrations of P=O

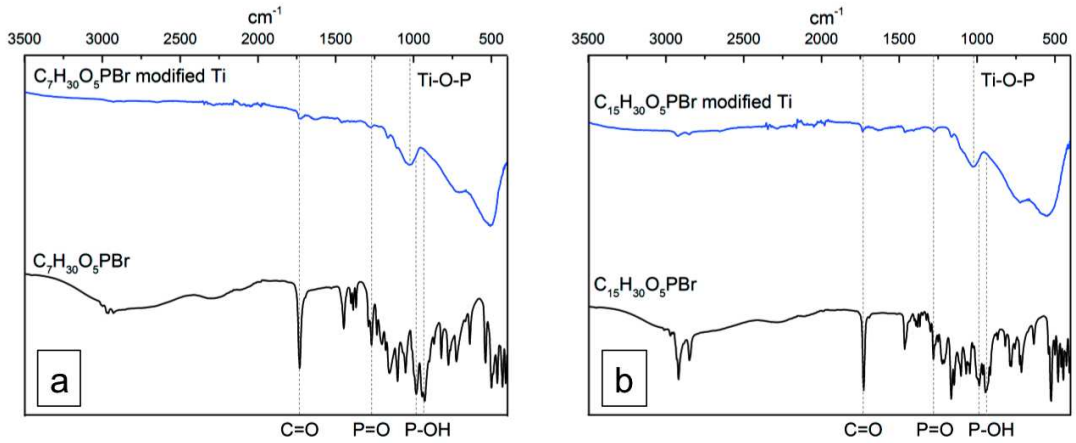

Figure 3.13: a) Infrared absorption spectra of the C_3 short polymerization initiator ($C_7H_{14}O_5PBr$) (black curve) and of the Ti surface after the grafting of the C_3 initiator (blue); b) Infrared absorption spectra of the C_{11} long polymerization initiator ($C_{15}H_{30}O_5PBr$) (black curve) and of the C_{11}-modified Ti surface initiator (blue).

and P−O groups. In particular, the band at 1270 cm^{-1} is attributed to the stretching vibration of the P=O bonds and the three peaks centered in 1052 cm^{-1}, 983 cm^{-1} and 944 cm^{-1} are assigned to the P−OH vibrations. The comparison between the spectra of initiators and those of the initiator-modified Ti surfaces (blue lines) confirms that the initiator has been successfully grafted on the activated Ti substrate. In particular, in accordance with previous studies [9,13], the disappearance of the P−O−H stretching at 1052 cm^{-1} and the simultaneous presence of the band at 1028 cm^{-1}, assigned to the formation of Ti−O−P bonds, confirm that the organic initiator has been preferentially grafted via the formation of tridentate bonding modes. However, the presence of some low intensity peaks and shoulders in correspondence of the acid function (P−OH) and phosphonyl group (P=O) vibrations, shows the simultaneous coexistence of some monodentate and bidentate modes (see Fig. 2.5). It is also important to note that the intensities of the P=O stretching and P−OH vibrations increase if the samples were not cleaned with ultrasound implying a higher content of physisorbed molecules (see Fig. 3.17 below). Lastly, the infrared spectrum of the initiator-modified Ti surfaces shows also the absorption bands characteristic of the Ti−O between 850 cm^{-1} and 400 cm^{-1}. Additionally, a comparison between the surface morphologies before and after the grafting of the initiator molecules is presented in Fig. 3.14 together with the corresponding EDX spectra. Figure 3.14a displays the morphology of the Ti surfaces after the alkali treatment lasted for 1 h in a 2 M concentrated NaOH solution. Whereas, the surface morphology achieved after the modification of the 2 M 1 h alkali-activate surfaces with the short C_3 initiator (Fig. 3.14b) and that functionalized with the longer C_{11} (Fig. 3.14c) are also shown. These SEM micrographs highlight that the surface features change after the grafting reaction. In particular, in the case of the shorter initiator (Fig. 3.14b), the surface is characterized by the organic molecules covalently attached around the pillars leaving a morphology similar to that of the microporous layer but less branched. Instead, the grafting of the longer initiator leads to a more compact structure composed of sharper pillars. Thus, as expected, the longer initiator filled up better the pores left by the alkali treatment.

This reorganization of the surfaces has been also confirmed by EDX analysis, whose spectra have been used to determine their elemental composition. After the grafting reactions (Fig. 3.14e and Fig. 3.14f), the organic content (carbon peak at 0.277 keV) increases and the signals related to the bromine (Br), typical of the α-bromo ester group, and that attributed to the phosphorous (P) of the phosphonates appear. Instead, the absence of the peak pertained to the sodium suggests that the grafting reaction leads to a re-organization of both the surface morphology and composition. In order to better clarify if, during the grafting reaction, the Na incorporated in the microporous layer has been released in solution, the residual solution after the grafting of the initiator has been analyzed by ICP-AES measurements. A Na concentration of (4.4 ± 0.04) mg/kg^{-1}, which corresponds to $4.6 \cdot 10^{18}$ atoms of Na, was determined. Assuming a Na atomic radius of 180 pm and a flat Ti surface, it has been calculated that at least $2.9 \cdot 10^{16}$ Na atoms are required to cover the Ti disk surfaces (diameter of 20 mm). Since the alkaline treatment produces nanostructured surfaces with higher specific area, a greater number of Na atoms are therefore probably involved in the reaction.

This hypothesis and approximated calculation suggest that, during the grafting reaction, the Na atoms have been released in solution leading to a change of the porous layer chemical composition. This can be also proven analyzing the survey XPS spectrum of the initiator-modified Ti (Fig. 3.15a), where: (*i*) the Na 1s peak (at 1071 eV), visible after the

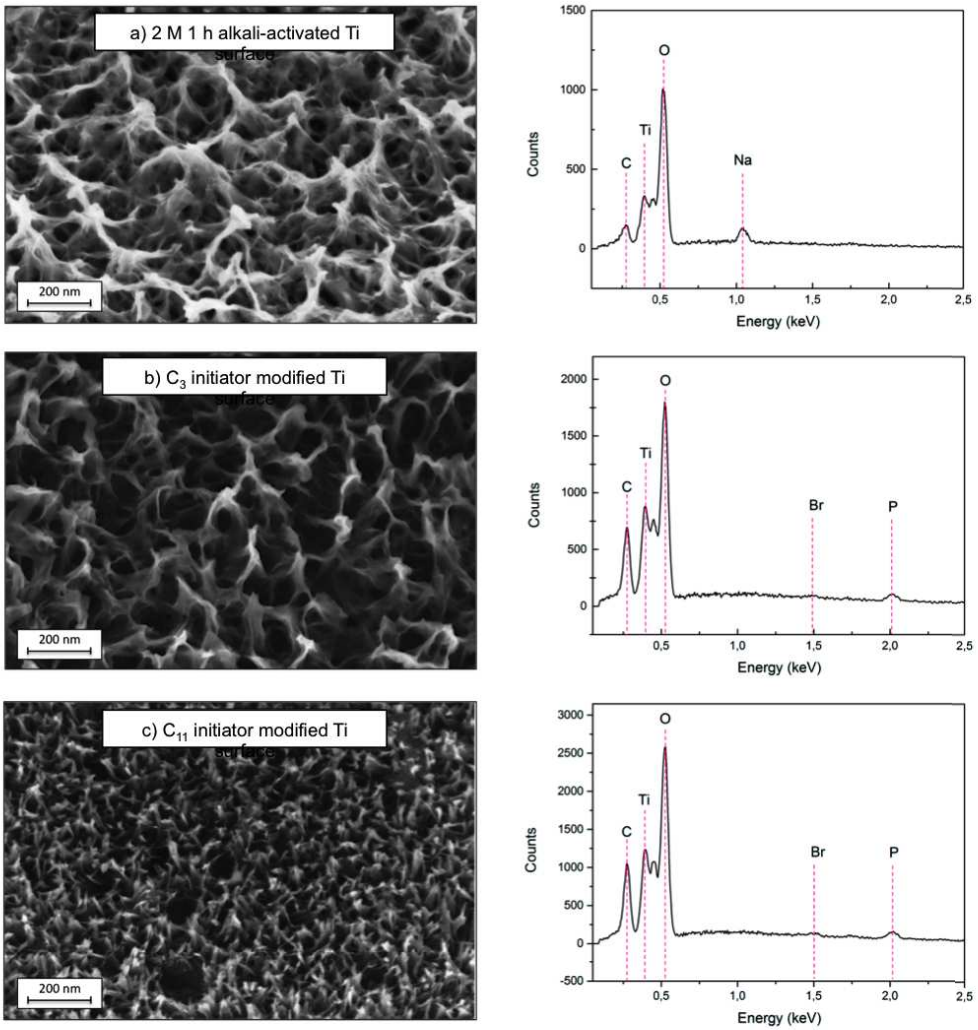

Figure 3.14: SEM micrographies and EDX spectra of a: a) 2 M 1h alkali-activated surface; b) C_3 initiator modified surface and c) C_{11} initiator modified surface.

activation step, has been not detected; and (*ii*) the presence of O 1s (531.8 eV), C 1s (284.5 eV), P 2s (192 eV), Br 3p (185 eV), P 2p (134 eV), and Br 3d (72 eV) peaks confirme the success of the grafting.

Moreover, the investigation of the unsymmetrical O 1s peak (Fig. 3.15b), which can be deconvoluted into two peaks centered at 531.2 eV and 533.1 eV, mainly assigned respectively to Ti−O−P and P−O−H bonds [14], confirms the covalent adsorption of the initiator molecules at the Ti surfaces. Instead, the deconvolution of the C 1s peak highlights the presence of four peaks. The one centered at 284.5 eV is attributed to the aliphatic carbons C−C and C−H of the chain; whereas, the component at 285.2 eV is assigned to the carbon-phosphorus bonding and those centered in 286.4 eV and 289 eV corresponds to the carbons attached to oxygen, C−O and C=O respectively [13].

Besides, as better explained in Sec. 3.3.3, the short initiator-modified surfaces lead to less thick and uniform polymer layers, in this work longer molecules have been used to fabricate PMMA-coated Ti surfaces. Hereafter, these samples will be labeled *C11 initiator-*

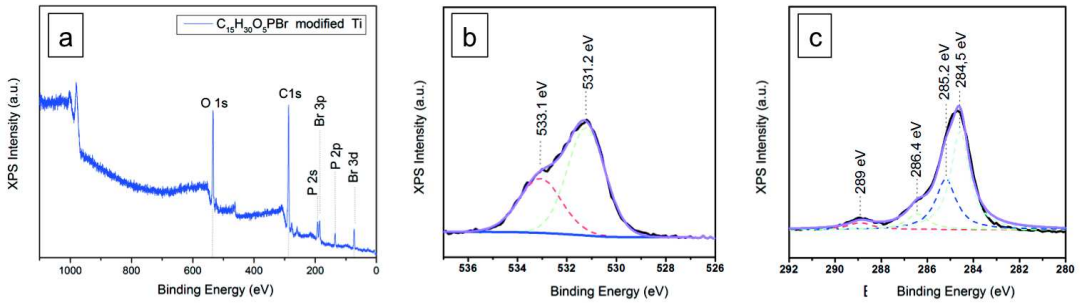

Figure 3.15: a) XPS survey spectrum of a long-initiator modified Ti surface; b-c) XPS spectra of O 1s and C 1s peaks of the initiator-modified Ti surface, respectively.

modified Ti surfaces. Their surface topography and 3D reconstruction are reported in Fig. 3.16. In particular, the grafting reaction leads to a more compact and pointed organic pillared structure resulting in an increase of the surface wettability (contact angle equal to $(97 \pm 3)°$, inset Fig. 3.16a) and in a slight decrease of the surface roughness (Ra = (14 ± 1) nm) due to the organic initiator covalently attached inside the pores left by the activation step.

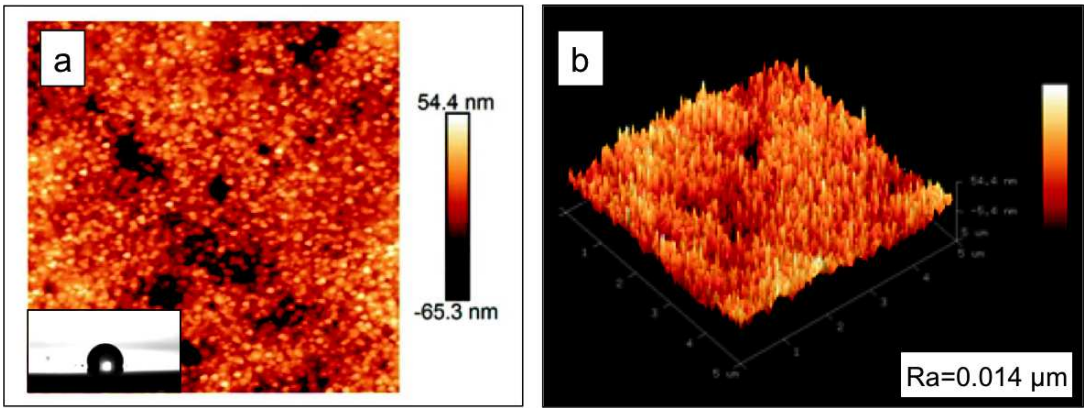

Figure 3.16: AFM topography of the initiator-modified Ti surfaces.

3.2.2 Removal of physisorbed initiator molecules: the effect of ultrasonic cleaning

As previously explained (Sec. 2.2.3), after the grafting reaction organic multilayers caused by the physical absorption of initiator molecules were observed (see Fig. 3.12) and a cleaning procedure in ultrasonic bath was required in order to remove or, at least, to reduce the excess of initiator. The cleaning treatment has been performed using dichloromethane (CH_2Cl_2) and deionized water (H_2O) and the effects of four different treatment times (1 min, 3 min, 5 min, 10 min each solvent) on the surface composition and morphology have been investigated by ATR-FTIR, EDX and SEM analyses.

As evidenced in Fig. 3.17a and Fig. 3.17b, the sonication in (CH_2Cl_2) and deionized-(H_2O), 1 min each solvent, allows removing the more external physisorbed multilayers.

Indeed, even if big organic agglomerates still remained attached (Fig. 3.17a) some holes have been produced in these multilayers making visible the pillared structure left by the alkaline treatment (Fig. 3.17b). Therefore, the sonication time has been increased up to 3 min each solvent and the surface appears smoother Fig. 3.17d and Fig. 3.17e. The external organic agglomerates have been removed and only few nanometer thick organic layers have been found (Fig. 3.17d). The sodium titanate microporous layer has been filled up with organic molecules (Fig. 3.17e). A further increase of the treatment time (5 min each solvent) leads to the removal of the external thin organic layers (Fig. 3.17g) but molecules, still trapped between the pillars of the surface network (Fig. 3.17h), have

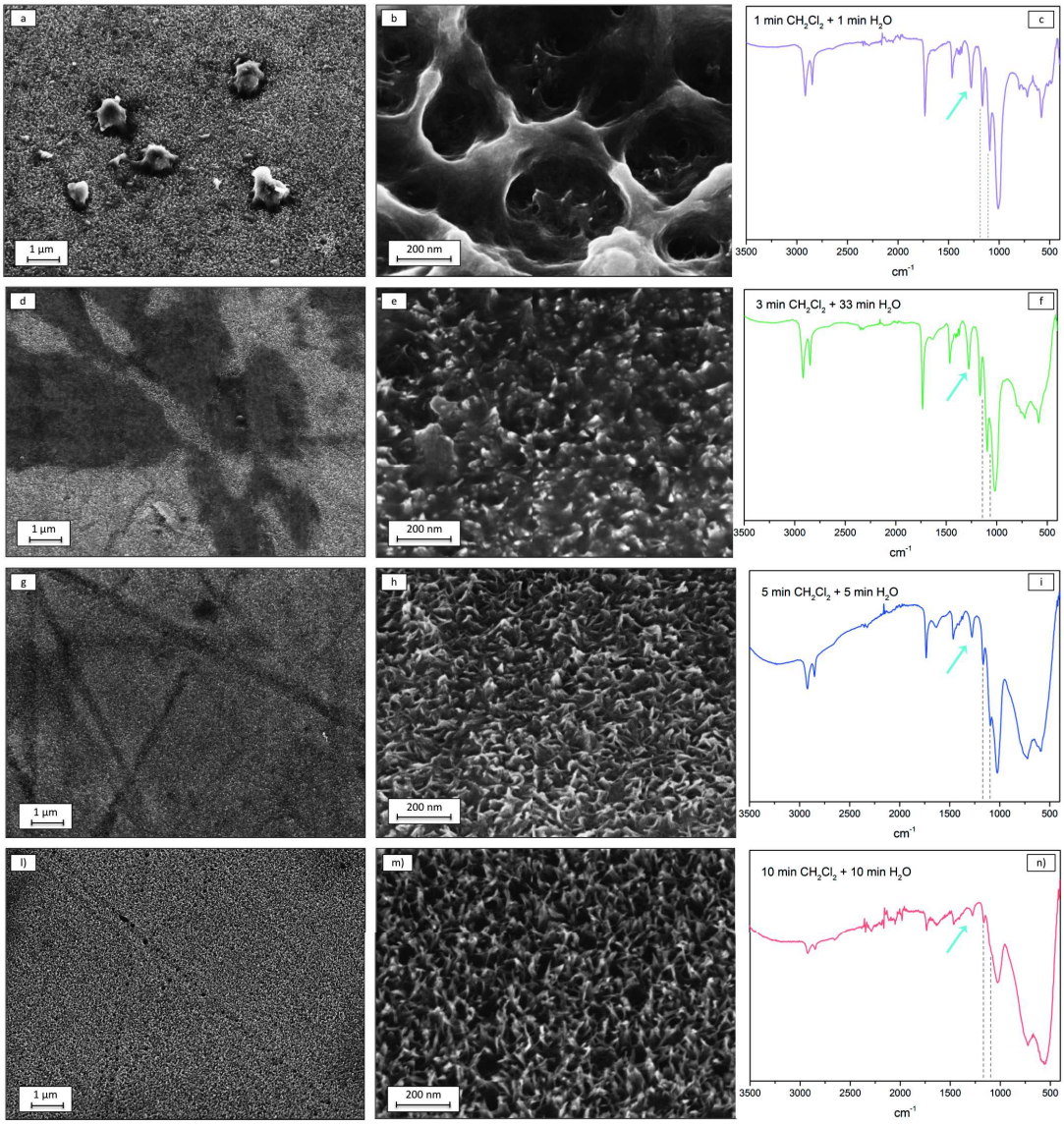

Figure 3.17: Effect of the ultrasonic cleaning on the removal of physisorbed initiator molecules. SEM micrographs and FTIR spectra of C11 initiator modified surfaces after a cleaning treatment of: a-c) 1 min in CH_2Cl_2 + 1 min in deionized-H_2O; d-f) 3 min in CH_2Cl_2 + 3 min in deionized-H_2O; g-i) 5 min in CH_2Cl_2 + 5 min in deionized-H_2O and l-n) 10 min in CH_2Cl_2 + 10 min in deionized-H_2O.

been observed. Finally, a treatment time of 10 min for each solvent has been considered sufficient to pull out the majority of the molecules not covalently bound at the surface. Indeed, agglomerates were not visible (Fig. 3.17l) and the surface has been characterized by pointed and ordered pillars (Fig. 3.17m). This trend has been also evidenced by analyzing the IR spectra. Indeed, in both the spectra recorded after a treatment time of 1 min (Fig. 3.17c) and 3 min (Fig. 3.17d), high intensity peaks in the 3000-2700 cm^{-1} and 1200-1000 cm^{-1} ranges suggest the presence of a high content of organic moieties. Moreover, by increasing the treatment time a progressive reduction of the carbonyl group P=O peak intensity was observed (Fig. 3.17i). In particular, after a treatment of 10 min for each solvent (Fig. 3.17n) even the signals in the 1200-1000 cm^{-1} range were no more well distinguishable suggesting that the majority of the organic physisorbed molecules have been removed. Thus, a ultrasonic treatment of 20 min (10 min in CH_2Cl_2 + 10 min in H_2O) has been chosen. The following surface elemental concentration has been evaluated by XPS: C 70%, O 21%, P 1.3%, Br 2.2%, Na 0%. The P to Br (P/Br) ratio has been calculated, using literature sensitive factors [15], equal to 1.3 ± 0.1.The difference of these values compared to the one expected for the stoichiometry of the molecule could be attributed to a slightly lost of bromine of the ester group, notably a labile group, caused by the sonication.

Finally, in order to evaluate the spatial distribution of the molecule on the surface, high resolution EDX maps have been reconstructed. As an example, a map of the bromine concentration on the surface is reported in Fig. 3.18.

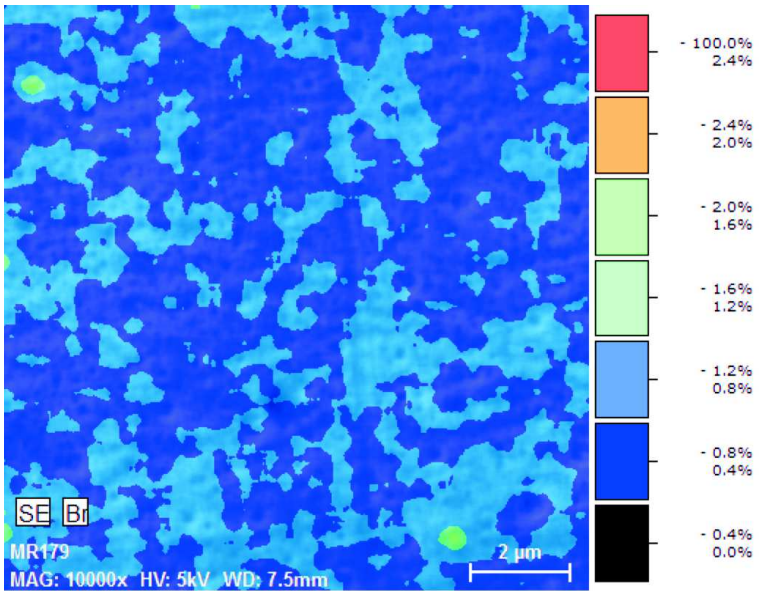

Figure 3.18: EDX high resolution map of the bromine atomic percentage surface distribution.

It has been pointed out that the bromine was almost uniformly spread all over the surface with an atomic percentage comprise between 0.4% and 1.2%. The quantitative atomic percentage of the element has been achieved performing a standardless analysis with the EDX software integrated in the microscope.

3.3 Polymerization

The grown of the PMMA chains have been performed using a SI-ATRP method, according to the procedure reported in Sec. 2.2.4. First, 14 mM of CuBr and PMDETA and 9 mL of anisole have been added in the reactor previously degassed, filled with argon and incorporated with the initiator-modified Ti substrates. Then, 14 mM of malononitrile following by 5.3 M of MMA have been joint in the reactive media. The reaction lasted for 24 h at 35 °C. In the following sections the results achieved will be shown.

3.3.1 Structure, composition and wettability of PMMA-coated Ti surfaces

The polymerization reaction led to a rounded polymer layer which covers the entire surface, as shown in Fig. 3.19. Low magnification SEM image (Fig. 3.19a) highlights that the polymer uniformly spreads all over the surface resulting in a smoothness of the surface structure. Indeed, as better clarify by higher magnified micrographs reported in Fig. 3.19b and Fig. 3.19c, the titanate pillars are hidden inside the polymer layer and anymore visible. This produces also an increase of the average roughness (Ra=(310 ± 12) nm) as demonstrated by the AFM topographies (Fig. 3.19 bottom) as well as a slight increment of the surface wettability (contact angle (104 ± 8)°, inset Fig. 3.19a).

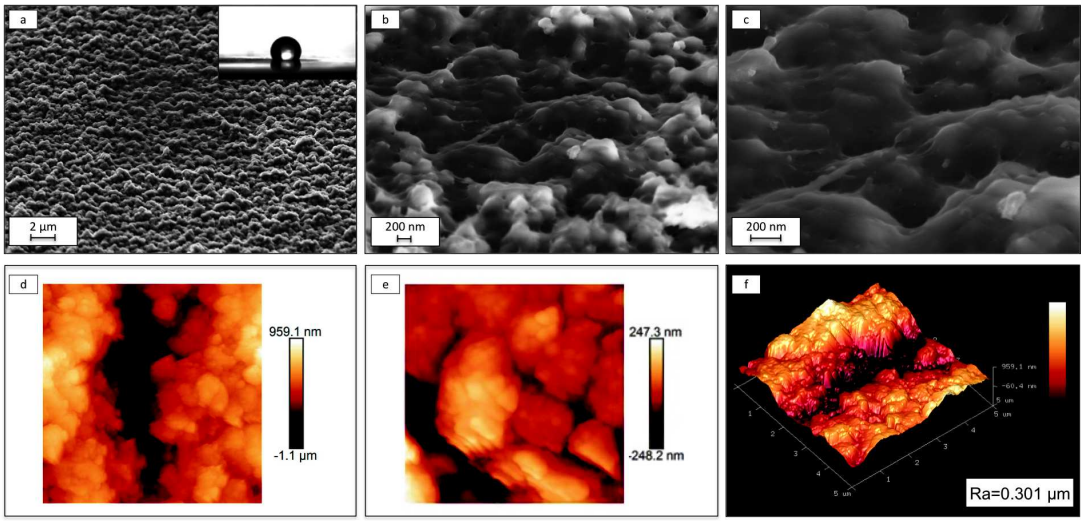

Figure 3.19: Top: different magnification SEM images of the PMMA-coated Ti surface morphology registered by tilting the sample holder of an angle equal to 54 deg with respect to the horizontal plane. Bottom: AFM topography of the PMMA surface: d) (5x5) μm^2 2D topography; e) (1.5x1.5) μm^2 2D topography and f) 3D reconstruction of the (5x5) μm^2 sized image.

Instead the FTIR spectra of the surface-confined PMMA brushes (red curve) and that of a synthesized PMMA powder (black curve) are shown in Fig. 3.20a. They both contain the peaks related to the carbonyl groups (C=O) and the α-methyl group vibrations (α-CH_3), confirming that the PMMA layer has been successfully grown. More in detail, the spectrum of the PMMA brushes reveals the presence of three peaks in the 2800-3000 cm^{-1} region: the characteristic peaks at 2924 cm^{-1} and 2852 cm^{-1} proper of asymmetric and symmetric stretching vibrations of the methylene groups (CH_2) and the broad band corresponding to the methyl asymmetric stretch νas(CH_3) at 2960 cm^{-1}. The sharp peak at 1730 cm^{-1} is

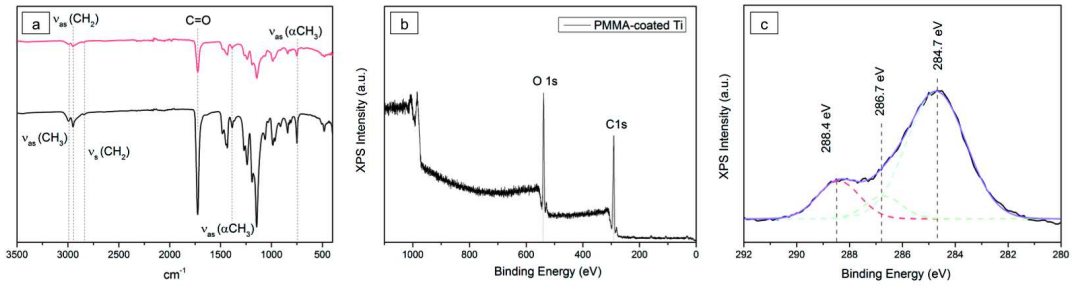

Figure 3.20: Chemical and structural composition of the the PMMA-coated Ti: a) comparison between the FTIR spectra of PMMA powder (in black) and the tethered PMMA layer produced (in red); b) XPS survey spectrum of PMMA-coated Ti; c) C 1s XPS spectrum of the PMMA layer.

assigned to the carbonyl group stretching [16]. Whereas, the two bands at 1382 cm^{-1} and 747 cm^{-1} are attributed to the α-methyl group vibrations [16]. Moreover, in the survey XPS spectra of the polymer film (Fig. 3.20b), only the intense peaks of C 1s at 284.7 eV and O 1s at 531.8 eV are visible, indicating that the polymer layer is dense without cracks and covers the entire surface. The absence of peaks related to the Ti substrate is due to the thickness of the organic layer which is higher than the photoelectron escape depth ($\approx$ 5 nm in the experimental condition used).

The analysis of the C 1s peak, in Fig. 3.20c, highlights the presence of three peaks which correspond to the different bondings involving the carbon atoms of the PMMA chain. In particular, peak centered at 284.7 eV is attributed to the C−C and C−H bonds; whereas, the last two are assigned to the C−O bonds (at 286.7 eV) and to the presence of the carbonyl groups C=O (at 288.4 eV).

The polymer grown in solution during the SI-ATRP reaction, due to the presence of physisorbed initiator in excess, allows the estimation of its molecular weight by SEC. It has been found that: (*i*) the weight average molecular weight (M_w) is $2.2 \cdot 10^5$ and (*iii*) the polydispersity (M_w/Mn) is 1.5.

3.3.2 PMMA-coated Ti: cross-section analysis

Cross-sections of the PMMA-coated Ti have been obtained using FIB-SEM techniques (Fig. 3.21). Three areas are visible: at the bottom the Ti and its columnar structure, in the middle the microporous interlayer above Ti and at the top the polymer. Referring to the geometrical considerations explained in Sec. 3.1.4 (Fig. 3.10), a PMMA-thickness of $\approx$400 nm has been estimated. Moreover, local and global EDX analyses have been performed to highlight the variation and spatial distribution of the cross-section elemental composition. In particular, the variation of the relative element concentration from the Ti substrate toward the polymer surface according to the black arrow depicted in Fig. 3.21a, is shown in Fig. 3.21b. In the interlayer, the C content increases and simultaneously the Ti one decreases. The O signal reaches a maximum in the middle of the interlayer then decreases up to a constant value in the polymer layer. Whereas, EDX maps enabling the visualization of Ti (violet), O (green) and C (red) elements are reported in Fig. 3.21c. The Ti and the polymer zones are easily distinguishable in Ti and C maps, whereas the O signal is detected in the interlayer and in the polymer, as already highlighted by the cross-line (Fig. 3.21b). These variations are in agreement with a strong interpenetration of

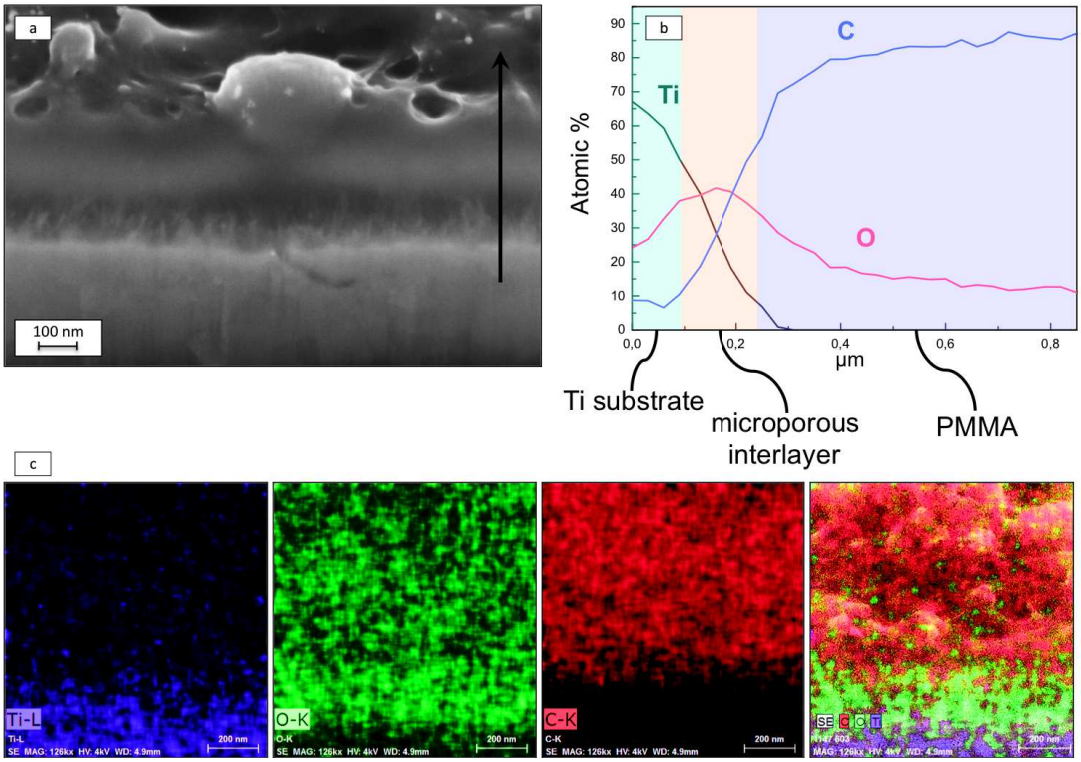

Figure 3.21: a) SEM image on a PMMA-coated sample cross-section cut by FIB; b) Elemental atomic concentration along the cross line (black arrow) obtained by EDX analysis; c) EDX maps showing from left to right the Ti (violet), oxygen (green) and carbon (red) elemental distribution and the three elements together.

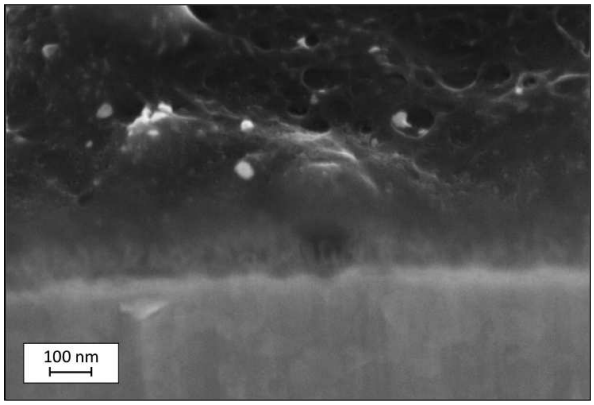

Figure 3.22: Cross-section of the PMMA-coated Ti interface grown without adding malononitrile in the ATRP reactive media.

the polymer inside the microporous layer created by the alkali treatment of Ti substrate. The covalent link between the organic part and the metallic one is proven by the Ti−O−P band visible in the ATR-FTIR spectra of the initiator-modified Ti and PMMA-coated Ti. In addition, in order to study the effect of adding malononitrile in the ATRP reactive media, the cross-section of a PMMA-coated Ti interface grown without malononitrile has been checked. As evidenced by the micrograph reported in Fig. 3.22, the polymer layer

results less compact and thinner confirming that malononitrile enhances the reaction rate producing a higher polymer thickness (Fig. 3.21a).

This confirms that the alkali treatment and the addition of the malononitrile, represents the key element of our approach. Indeed, it leads to the formation of a hierarchical porous interlayer consisting of regular pillared and cone-shaped structure which has a double functionality. Firstly, it promotes the grafting reaction due to the high hydroxyl groups' content. Secondly, it drives the growth of the polymer chains along the pillared structure avoiding their collapse and enhancing the development of the polymer thickness. The synergic growth of polymer within the porosity of the substrate and their covalent link allows elaborating a compact and thicker hybrid material.

3.3.3 Variation of the polymerization initiator size: effect on the PMMA thickness and structure

The effect of using a shorter ATRP initiator on the polymer thickness and structure has been investigated. The polymer layer has been prepared following the procedure described in Sec. 2.2.4. Ti surfaces have been activated in a 2 M concentrated NaOH solution for 1 h and successively functionalized with a C_3 initiator ($C_7H_{30}O_{15}$PBR, reported in Fig. 2.6). Then, taking into account the difference in the number of mols produced by using shorter molecules, the reagents quantity has been recalculateted in function of the initiator's number of mols and added in the flask. In particular, 19 mM of CuBr, PMDETA and malononitrile have been stirred in 12 mL of anisole. Thereafter, 5.3 M of MMA has been added and the polymerization reaction carried out by stirring the solution for 24 h at 35 °C. As expected, the intensity of the EDX spectra, reported in Fig. 3.23, confirmed that also in this case the C content is slower for the polymer grown without adding the malononitrile (Fig. 3.23a) than that detected in the case of polymer synthesized by adding the polymerization activator in the reactive media (Fig. 3.23b). Moreover, for comparison, the morphology of the polymer grown in the presence and in the absence of malononitrile have been investigated. SEM micrographs taken at different magnification are shown in Fig. 3.24. The first column refers to the polymer grown without adding malononitrile which appears highly porous. This is probably due to a preferential polymer growth around the pillars of the titanate layer. Indeed, as previously underlined (see Sec. 3.2.1 and Fig. 3.14),

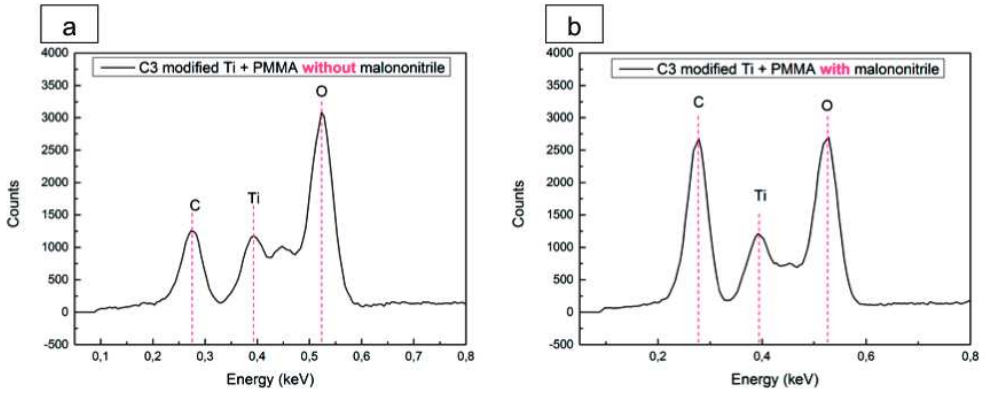

Figure 3.23: EDX spectra of the PMMA grown (a) without and (b) with the addition of malononitrile.

the grafting reaction with the shorter initiator leads to a more open surfaces structure which probably results in the growth of less densely packed polymer chains. On the other hand, the polymer achieved by adding the malononitrile, (right column, Fig. 3.24), is characterized by globules of organic materials that fill up the polymeric porous structure bringing to a more packed polymer layer.

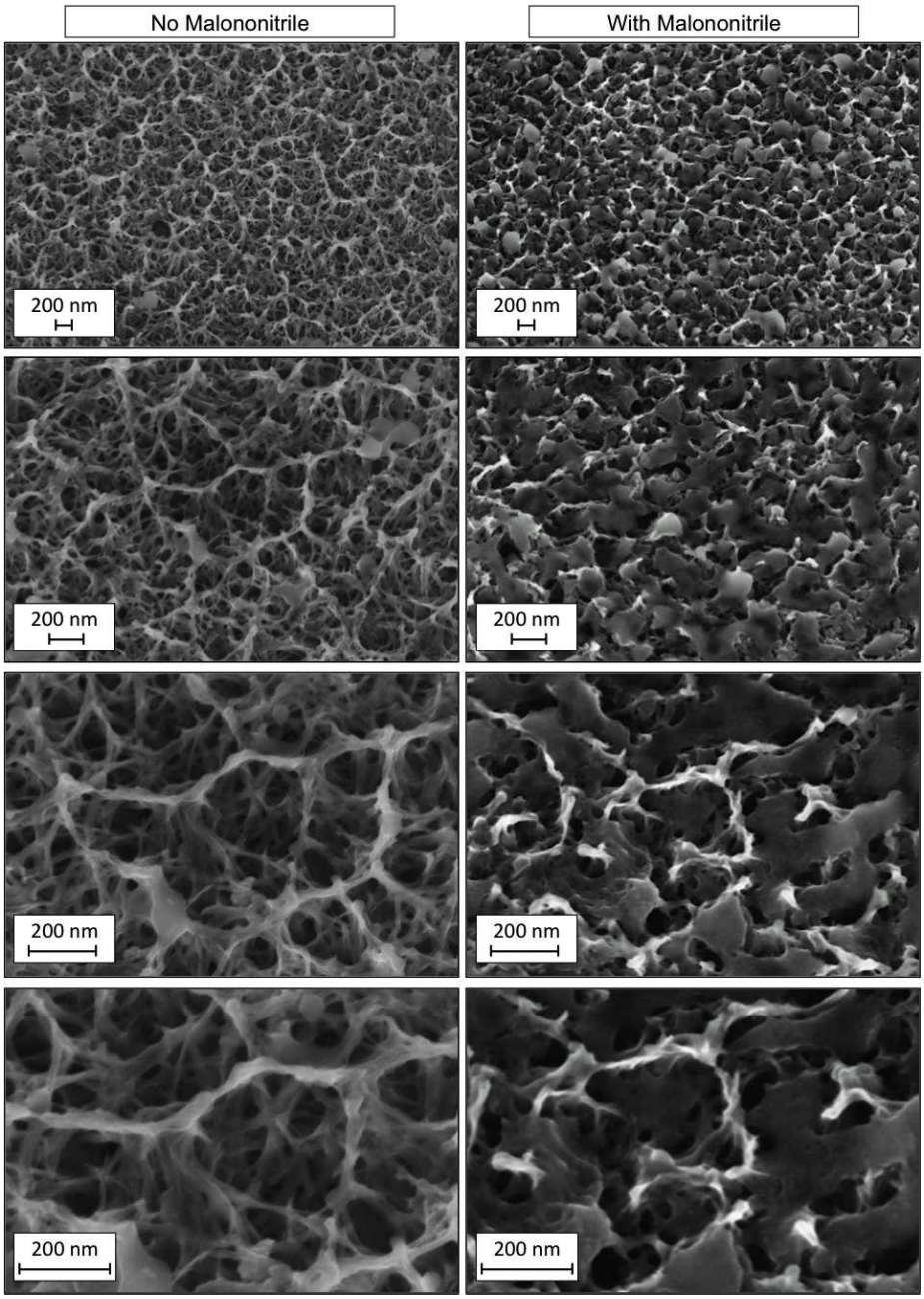

Figure 3.24: SEM micrographs recorded at different magnification of the PMMA layer grown starting from a short-initiator ($C_7H_{30}O_{15}$PBR) modified Ti surface. Left) morphology of the polymer grown without adding malononitrile; right) morphology of the polymer produced by using malononitrile to enhance the polymerization rate.

3.3.4 Estimation of the PMMA layer thickness by TGA

As highlighted in the micrograph reported in Fig. 3.25a it has been noticed that, in certain part of the surface, the polymer undergoes to a preferential growth, producing PMMA richer regions characterized by rounded globules with a higher thickness.

This has been attributed to three main reasons: (*i*) a not uniform spatial distribution of the grafted initiator; (*ii*) a not uniform reaction between the transition metal complex and the malononitrile [17]; and (*iii*) chain confinement effects preventing an uniform growth of adjacent chains [18]. The cross-section analysis (Sec. 3.3.2, Fig. 3.21) allows estimating a local thickness of about 400 nm. In order to get global information from all the surface, TGA experiments have been also performed. This study allows evaluating the average thickness of the PMMA layer. The polymer has been grown on a Ti sheet with a thickness of 0.15 mm, in order to be able to measure a weight loss after the polymer decomposition process.

Firstly, the PMMA-coated Ti sheet has been cut and its initial mass $m_{PMMA/Ti}$ has been measured and found equal to 69.12 mg. Then, its weight variation has been recorded while the temperature has been increased up to 577 °C (see Fig. 3.25b). The sample has been then cooled down to room temperature. In order to verify that the entire polymer has been decomposed, a second recording of the weight variation has been performed on the same sample. As expected, a weight decrease has been only observed during the first heating, whereas it remained constant during the second heating cycle. Thus, from the

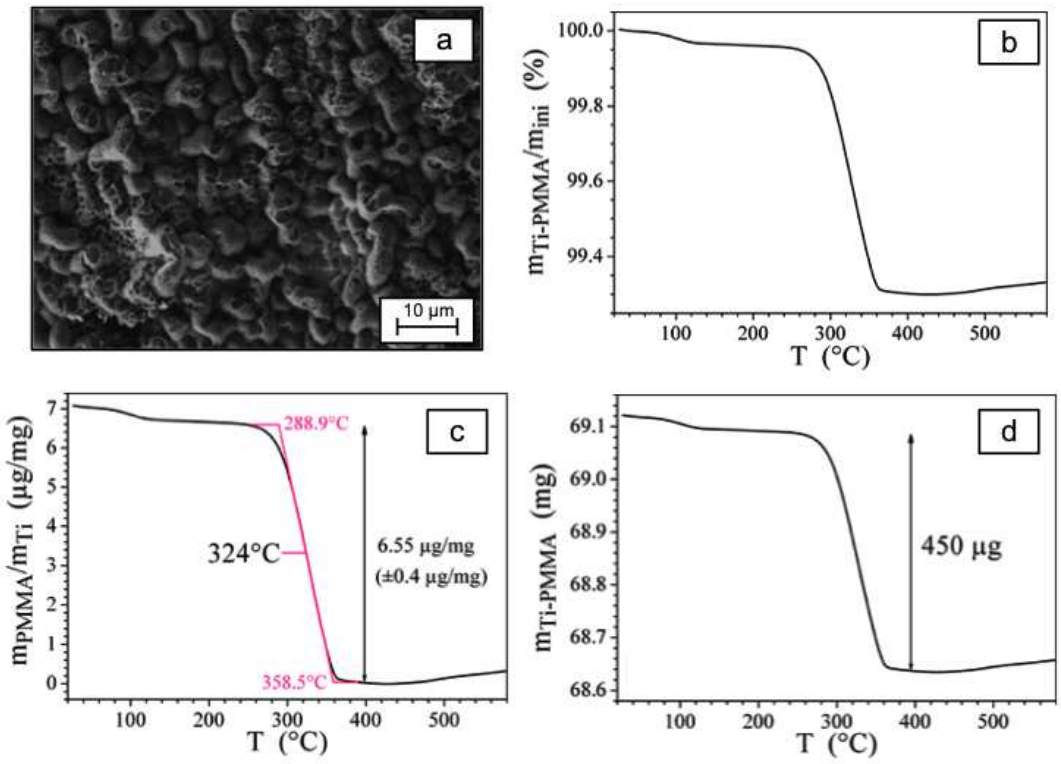

Figure 3.25: a) surface morphology of a PMMA richer zone; b) weight loss recorded on PMMA-coated Ti under air; c) polymer mass in μg by mg of Ti and d) PMMA weight loss.

polymer decomposition (Fig. 3.25c), we obtained a weight loss of 450 μg which corresponds to the PMMA mass (m_{PMMA}), shown in Fig. 3.25d.

Finally, the polymer thickness has been calculated taking into account the Ti and PMMA densities (d_{Ti} = 4.51 g/cm^3 and d_{PMMA} = 1.2 g/cm^3, respectively) and the Ti foil thickness (t_{Ti}), following this procedure:

1. the Ti sheet mass has been evaluated knowing the initial mass of the PMMA-coated Ti ($m_{PMMA/Ti}$) and its weight loss (m_{PMMA}):

$$m_{Ti} = m_{PMMA/Ti} - m_{PMMA} \tag{3.1}$$

2. the area of the Ti sheet (A_{Ti}) has been calculated considering the Ti densitiy and sheet thickness (d_{Ti} and t_{Ti}, respectively):

$$A_{Ti} = \frac{m_{Ti}}{d_{Ti} t_{Ti}} \tag{3.2}$$

3. the polymer thickness has been finally derived:

$$t_{PMMA} = \frac{m_{PMMA}}{d_{PMMA} A_{Ti}} \tag{3.3}$$

Taking into account that the polymer grown on both sides of the Ti sheet, the obtained value has been then divided by 2 and an average thickness of 1.9 $\pm$ 0.3 μm has beens estimated.

3.4 Stability and biological properties of PMMA-coated Ti surfaces

The aim of these analysis is to prove the feasibility of replacing epoxy resins with tethered polymer to design innovative resin-free sandwich material, as described in Chap. 2. Even if, for the application of this thesis PMMA-coated Ti surfaces will not directly interact with body tissues, it is important to check: (*i*) their stability once immersed in a simulated body fluid (SBF) solution and (*ii*) evaluate their cytotoxicity.

3.4.1 Stability of PMMA-coated Ti surfaces soaked in saturated simulated body fluid

Since human body may represent an aggressive environment for implantable materials [19–22], an investigation of its influence on the PMMA-coated Ti surface properties have performed. Indeed, in the presence of the physical and chemical conditions of the human body, the new biomaterial could lose its stability, and may corrode or degrade [22]. Thus, morphological and compositional surface properties of the PMMA-coated Ti have been assessed after soaking them in a supersaturated SBF solution. In particular, a solution with ion concentrations 1.5 times higher than standard c-type SBF (1.5×SBF) was employed. This kind of solution is generally used to promote the apatite formation on bioactive coating [23, 24].

PMMA-coated Ti disks have been soaked in a 1.5×SBF for three different immersion time: 2, 14 and 21 days. FTIR spectra and SEM micrographies of the sample for each

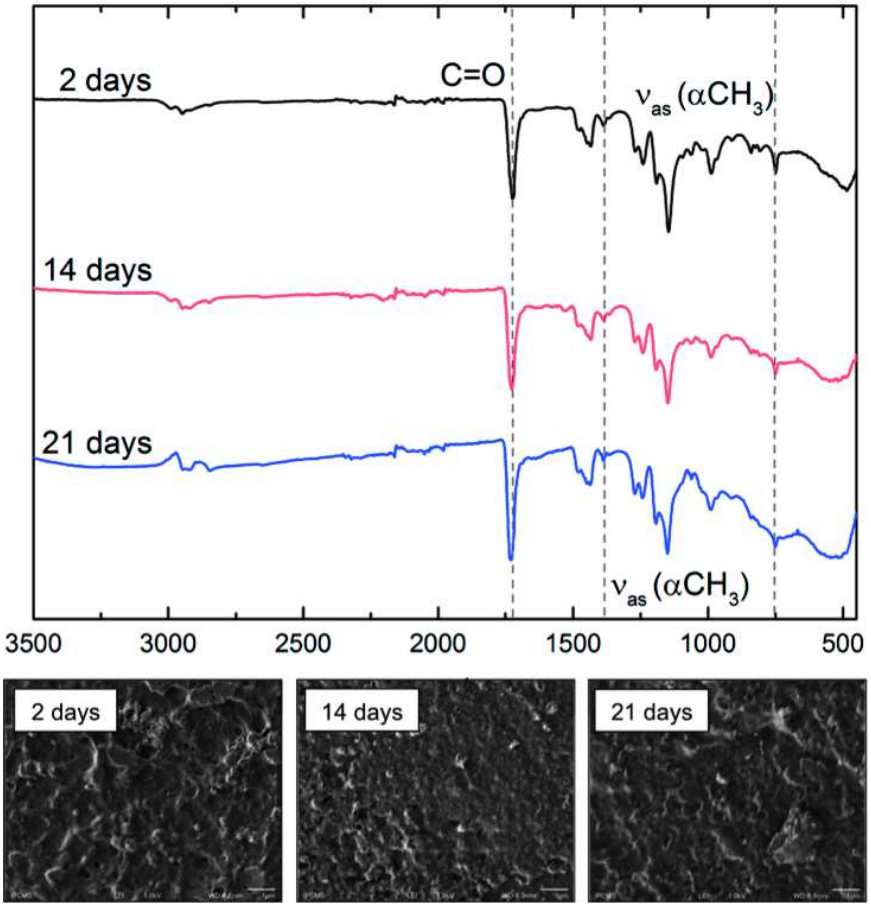

Figure 3.26: Top: FTIR spectra of the PMMA-coated Ti samples soaked in a 1.5×SBF solution for 2 days (black curve), 14 days (red), 21 (blue). Bottom: SEM images of the samples surface morphology after each soaking period.

soaking period are shown in Fig. 3.26. They prove that no significant variation in the surface composition and morphology have been revealed. Indeed, from the SEM images the typical features of the polymer morphology is still visible. Moreover, as highlighted in FTIR spectra both peaks related to the carbonyl group and the bands ascribed to the α-methyl group vibrations are well distinguishable even after a soaking period of 21 days (blue curve).

Once, the samples have been removed from the solutions, the ionic calcium (Ca) and phosphorus (P) concentrations of the residual solutions, after each soaking periods, have been evaluated by inductively coupled plasma atomic emission spectroscopy (ICP-AES) measurements. Tab. 3.1 presents the ionic concentration of the residual solutions compared to the mother 1.5×SBF. As expected, no significant differences in the Ca and P concentrations have been detected. Indeed, being the PMMA an inert material, the deposition of apatite is not promoted [25]. Nevertheless, Ca-P agglomerates have been detected (as reported in Fig. 3.27), and thus slightly increase in the Ca concentration can be attributable to a dissolution of these Ca-P flakes in the renewed solutions. As the P concentration does not increase, it means that the polymer layer does not degrade and that the anchorage between the Ti and the organic initiator, ensured by the Ti−O−P bonds, is stable.

Table 3.1: Calcium (Ca) and phosphorous (P) concentration, evaluated by ICP-AES measurements, of: (*i*) a 1.5×SBF mother solution; (*ii*) a 1.5×SBF solution where PMMA-coated Ti samples where soaked for 2, 14 and 21 days.

1.5×SBF	Ca (mg/L)	P (mg/L)
Mother solution	61±3	22±2
2 days soaking periods	63±3	22±1
14 days soaking periods	71±4	23±2
21 days soaking periods	68±4	22±1

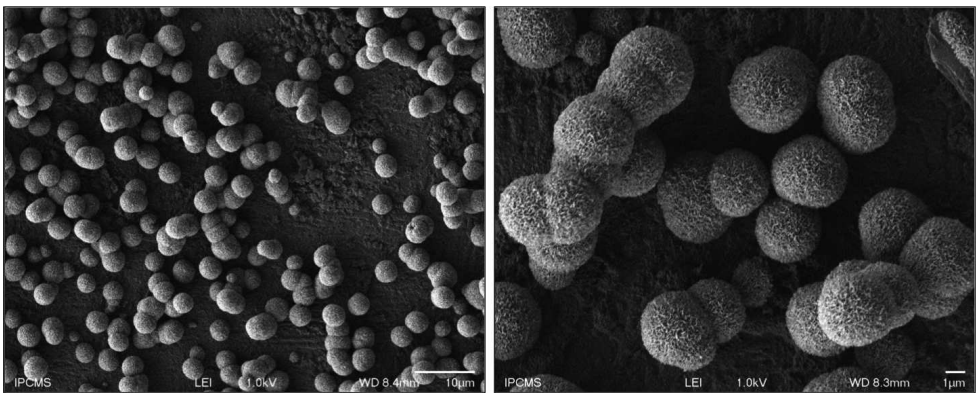

Figure 3.27: Ca-P agglomerates deposited on the PMMA-coated Ti surfaces after a soaking periods of 21 days.

Overall, it has been proved that the chemical structure of the grafted PMMA is not degraded and no delamination occurred between the layers after an incubation of 21 days in a 1.5×SBF, confirming its good stability.

3.4.2 Cytotoxicity evaluation of the PMMA-coated Ti surfaces

In order to prove the biocompatibility of the PMMA layer, human fibroblasts have been seeded and let proliferate on the grown PMMA-modified Ti and on the untreated Ti substrates (used as control samples). The cells morphology and growth on PMMA-coated Ti interface have been compared with the one on the pure Ti. It has been shown, by Alamar Blue assay (Sec. 2.3.5), that the fibroblasts grew on the modified surface over a course of six days (red histogram Fig 3.28).

In particular, it has been observed that cells were able to adhere and spread on both the untreated (Fig. 3.29a and Fig. 3.29c) and PMMA-coated Ti substrates (Fig. 3.29b-d). Furthermore, the areas richer in PMMA promoted the formation of cell clusters and cells with multiple filopodia (Fig. 3.29d). The presence of PMMA resulted in less cell numbers, compared with that obtained on the untreated Ti ((blue histogram in Fig 3.28). Nevertheless, the presence of the PMMA has no detrimental effect on the cells morphology and behavior and consequently on the implant surrounding tissue interface.

In order to prove the possibility to functionalize the PMMA-coated Ti with natural biopolymers (e.g. gelatin), a dilute solution of gelatin (0.1% w:v) has been deposited onto untreated Ti and PMMA-coated Ti and its effect has been investigated.

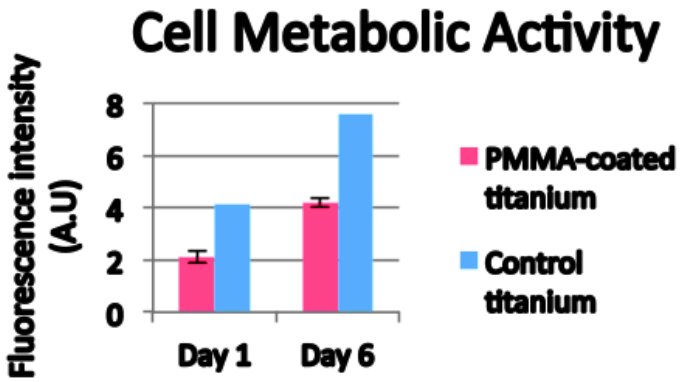

Figure 3.28: Metabolic activity of BJ2 human fibroblast let proliferate on PMMA-coated Ti surfaces over a period of six days (Alamar Blue assay).

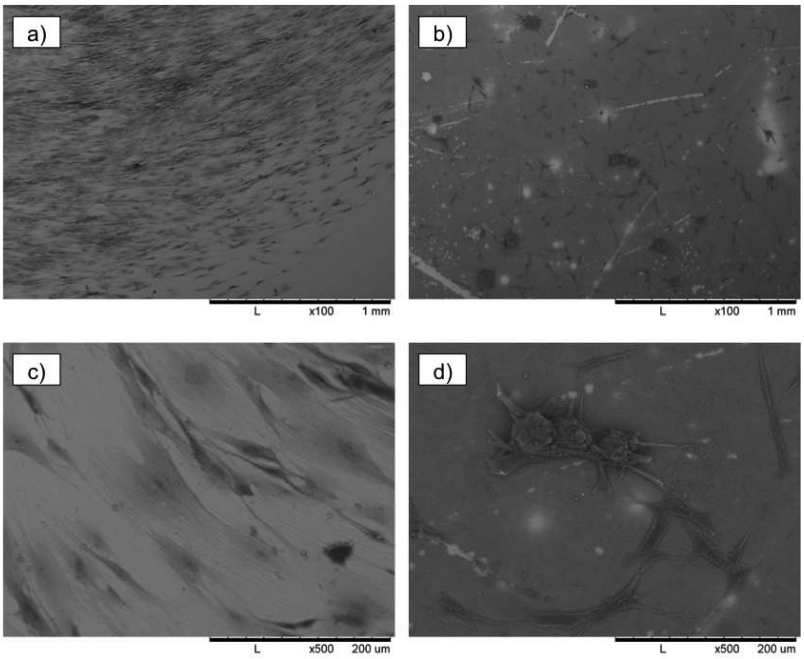

Figure 3.29: SEM images of the cells made adhere to: a) an untreated Ti sample (control); b) a PMMA-coated Ti substrates; c) and d) are higher magnification of a) and b), respectively.

The effect of the gelatin functionalization on the cells behavior has been assessed by Immunofluorescence staining.

Fig. 3.30 shows the fluorescence images of the cells grown on the unmodified Ti (Fig. 3.30a) and on the gelatin-modifed Ti (Fig. 3.30d), as well as those of the PMMA-coated Ti samples (not modified in Fig. 3.30b and functionalized with gelatin in Fig. 3.30d). It has been observed that PMMA-coated surfaces modified with gelatin result in clustering of cells (Fig. 3.30d).

In conclusion, these preliminary tests show that the grown PMMA chains have no cytotoxic effects and the PMMA can also be further functionalized by adsorption of additional

natural polymeric components (such as gelatin).

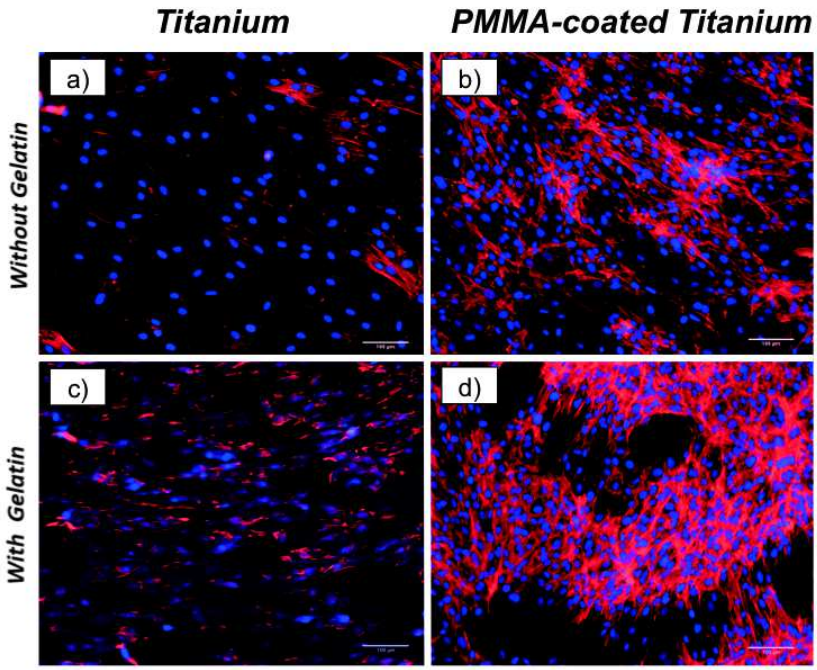

Figure 3.30: Immunofluorescence staining of cells made adhere and spread on: a) an unmodified Ti substrate; b) a PMMA-coated Ti sample; c) a Ti substrate functionalized with gelatin and d) a PMMA-coated Ti sample functionalized with gelatin.

3.5 Further considerations

In this chapter a strategy allowing the development of hybrid-layered structures consisting of thick PMMA and Ti has been described. The key elements of the process are: (*i*) the Ti surfaces activation performed in a basic media (NaOH solution) and (*ii*) the use of malononitrile as a polymerization activator. The former leads to a nanostructured sodium titanate interlayer with an open microporosity. This hierarchical interlayer, acting as a scaffold made of regular pillared and cone-shaped structure, drives the growth of the polymer chains along the pillared structure enhancing the development of the polymer layer. The latter allows producing polymer layers (several hundreds of nanometre thick) covering Ti surfaces of some centimeter square. Moreover, the covalent bond between the organic layer and the metal substrate is ensured by grafting phosphonic acids, used as coupling agents, which, reacting with the hydroxyl groups on the activated Ti surfaces, lead to the creation of strong Ti-O-P bonds.

This study has been completed by investigating how an increase of NaOH concentration affects the polymer morphology and its thickness.

Indeed, as observed in Sec. 3.1.2, the titanate interlayer, produced after an alkali treatment of 1 h in a 5 M concentrated NaOH solution, appears thicker with a higher quantity of interconnected porous and wider pillars. Thus, it has been investigated how this can affect the polymer growth. Fig. 3.31 shows the morphology and the cross section of the PMMA layer obtained after growing the chains from a Ti substrate activated in a 5 M concen-

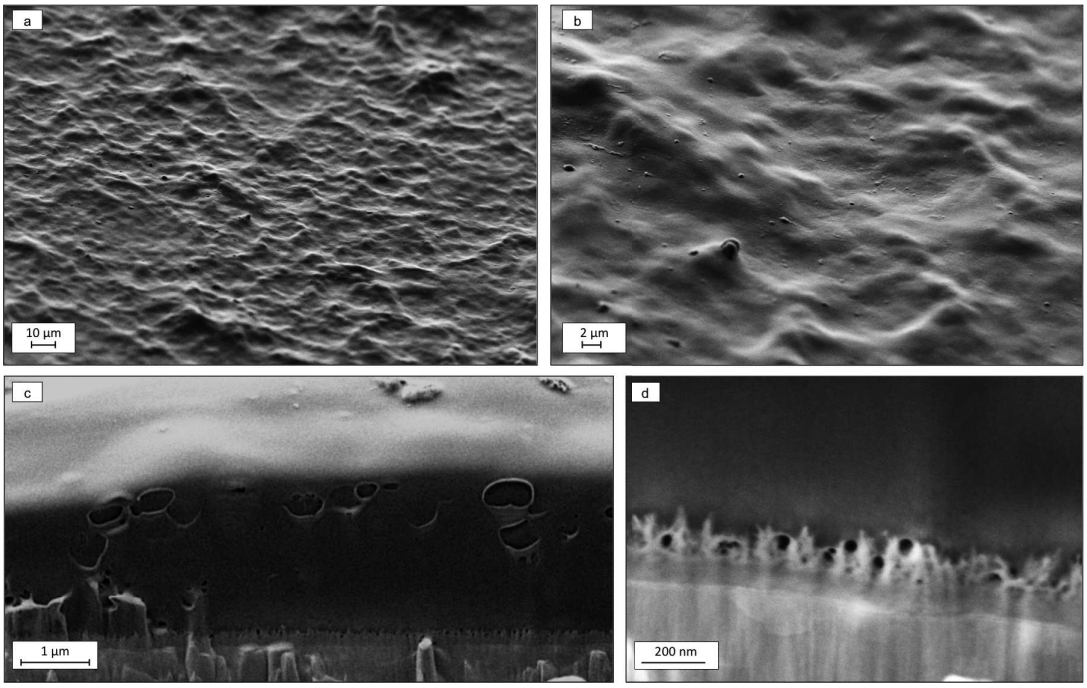

Figure 3.31: a-b) Surface morphology of a polymer layer grown starting from a Ti substrate activated in 5 M concentrated NaOH solution for 1 h and functionalized with the C_{11} ATRP initiator; c) cross-section of the PMMA-coated Ti surfaces produced and d) detail of the interaction between the structure of titanate and the polymer layer grown inside the pillars.

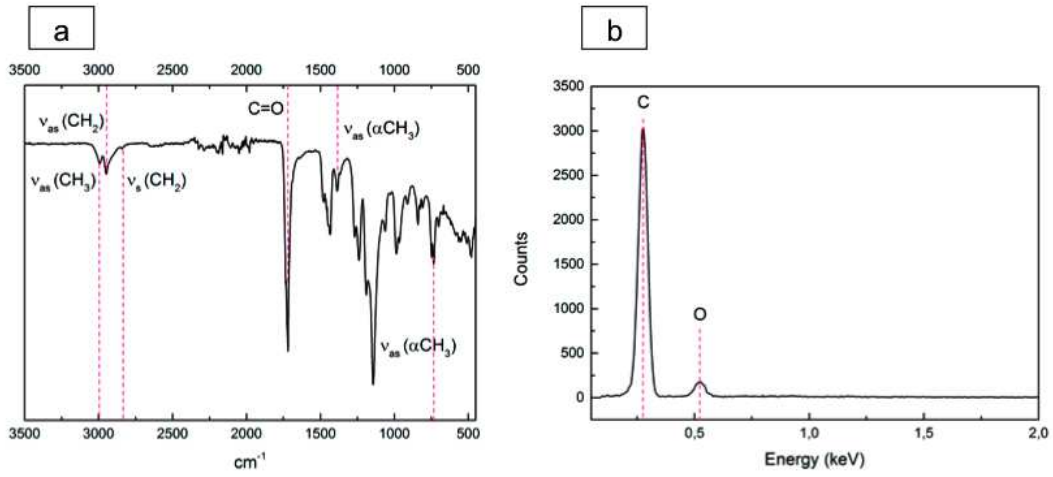

Figure 3.32: a) FTIR spectrum of the PMMA-coated Ti surface and n) EDX spectrum of the PMMA layer grown of a 5 M alkali activated Ti surface.

trated NaOH solution for 1 h and functionalized with the C_{11} ATRP initiator. Fig. 3.31a, and Fig. 3.31b highlight that the surface topography of the PMMA layer (whose FTIR spectrum is reported in Fig. 3.32a) is smoother and denser than that obtained after a 2 M NaOH activation. Moreover, the EDX spectrum (Fig. 3.32b), where only C and O peaks have been detected, reveals that the polymer layer is thicker since the signal from

the Ti substrate cannot be detected. This is also confirmed by the cross-section analysis (Fig. 3.31c), in which a compact layer of of about 2 μm has been observed. Furthermore, it allowes to better visualize the structure of the titanate interlayer and how the polymer has grown inside it pillared structure (Fig. 3.31d).

This study opens new insights for future investigation of this kind of system for the fabrication of sandwich materials. Indeed, we have pointed out that a more homogeneous layer could be obtained and no area with preferential growth of the polymer layer was observed.

Bibliography

[1] S.-i. Tanaka, H. Tobimatsu, Y. Maruyama, T. Tanaki, and G. Jerkiewicz, "Preparation and characterization of microporous layers on titanium," *ACS Applied Materials & Interfaces*, vol. 1, no. 10, pp. 2312–2319, 2009.

[2] K. Zhang, J. A. Li, K. Deng, T. Liu, J. Y. Chen, and N. Huang, "The endothelialization and hemocompatibility of the functional multilayer on titanium surface constructed with type iv collagen and heparin," *Colloids and Surfaces B: Biointerfaces*, vol. 108, pp. 295–304, 2013.

[3] H.-M. Kim, F. Miyaji, T. Kokubo, and T. Nakamura, "Apatite-forming ability of alkali-treated Ti metal in body environment," *Journal of the Ceramic Society of Japan*, vol. 105, no. 1218, pp. 111–116, 1997.

[4] V. Q. Le *et al.*, *Caractérisation et biocompatibilité de dépôts de phosphates de calcium sur Ti-6Al-4V obtenus par chimie douce*. PhD thesis, Strasbourg, 2014.

[5] M. Wei, H.-M. Kim, T. Kokubo, and J. Evans, "Optimising the bioactivity of alkaline-treated titanium alloy," *Materials Science and Engineering: C*, vol. 20, no. 1, pp. 125–134, 2002.

[6] L. Jonášová, F. A. Müller, A. Helebrant, J. Strnad, and P. Greil, "Biomimetic apatite formation on chemically treated titanium," *Biomaterials*, vol. 25, no. 7, pp. 1187–1194, 2004.

[7] G. Guerrero, P. Mutin, and A. Vioux, "Anchoring of phosphonate and phosphinate coupling molecules on titania particles," *Chemistry of Materials*, vol. 13, no. 11, pp. 4367–4373, 2001.

[8] V. Vergnat, *Matériaux hybrides organiques-inorganiques par greffage covalent de polymères sur des oxydes métalliques*. PhD thesis, Strasbourg, 2011.

[9] V. Vergnat, T. Roland, G. Pourroy, and P. Masson, "Effect of covalent grafting on mechanical properties of TiO_2/polystyrene composites," *Materials Chemistry and Physics*, vol. 147, no. 1, pp. 261–267, 2014.

[10] Y. Tanaka, H. Saito, Y. Tsutsumi, H. Doi, H. Imai, and T. Hanawa, "Active hydroxyl groups on surface oxide film of titanium, 316L stainless steel, and cobalt-chromium-molybdenum alloy and its effect on the immobilization of poly (ethylene glycol)," *Materials Transactions*, vol. 49, no. 4, pp. 805–811, 2008.

[11] J. Castle, "The composition of metal surfaces after atmospheric exposure: An historical perspective," *The Journal of Adhesion*, vol. 84, no. 4, pp. 368–388, 2008.

[12] E. Ajami and K.-F. Aguey-Zinsou, "Functionalization of electropolished titanium surfaces with silane-based self-assembled monolayers and their application in drug delivery," *Journal of Colloid and Interface Science*, vol. 385, no. 1, pp. 258–267, 2012.

[13] I. Minet, J. Delhalle, L. Hevesi, and Z. Mekhalif, "Surface-initiated ATRP of PMMA, PS and diblock PS-b-PMMA copolymers from stainless steel modified by 11-(2-bromoisobutyrate)-undecyl-1-phosphonic acid," *Journal of Colloid and Interface Science*, vol. 332, no. 2, pp. 317–326, 2009.

[14] Q. Wang, L. Zhong, J. Sun, and J. Shen, "A facile layer-by-layer adsorption and reaction method to the preparation of titanium phosphate ultrathin films," *Chemistry of Materials*, vol. 17, no. 13, pp. 3563–3569, 2005.

[15] C. Wagner, D. Briggs, and M. Seah, "Practical surface analysis," *Auger and X-ray Photoelectron Spectroscopy*, vol. 1, p. 595, 1990.

[16] G. Duan, C. Zhang, A. Li, X. Yang, L. Lu, and X. Wang, "Preparation and characterization of mesoporous zirconia made by using a poly (methyl methacrylate) template," *Nanoscale Research Letters*, vol. 3, no. 3, p. 118, 2008.

[17] Z. Jiaming, H. Jianying, C. Jiayan, L. Xurong, L. Yutai, Z. Yousi, *et al.*, "A novel rate-accelerating additive for atom transfer radical polymerization of styrene," *Journal of Polymer Science Part A: Polymer Chemistry*, vol. 45, no. 17, pp. 4082–4090, 2007.

[18] C. B. Gorman, R. J. Petrie, and J. Genzer, "Effect of substrate geometry on polymer molecular weight and polydispersity during surface-initiated polymerization," *Macromolecules*, vol. 41, no. 13, pp. 4856–4865, 2008.

[19] J. Y. Wong, J. D. Bronzino, and D. R. Peterson, *Biomaterials: principles and Practices*. CRC Press, 2012.

[20] I. Johnson and H. Liu, "A study on factors affecting the degradation of magnesium and a magnesium-yttrium alloy for biomedical applications," *PLoS One*, vol. 8, no. 6, p. e65603, 2013.

[21] D. Korpas, *Implantable cardiac devices technology*. Springer, 2013.

[22] M. T. Mohammed, Z. A. Khan, and A. N. Siddiquee, "Surface modifications of titanium materials for developing corrosion behavior in human body environment: a review," *Procedia Materials Science*, vol. 6, pp. 1610–1618, 2014.

[23] M. Tanahashi, T. Yao, T. Kokubo, M. Minoda, T. Miyamoto, T. Nakamura, and T. Yamamuro, "Apatite coating on organic polymers by a biomimetic process," *Journal of the American Ceramic Society*, vol. 77, no. 11, pp. 2805–2808, 1994.

[24] A. Yoshio, M. Kawashita, T. Kokubo, and T. Nakamura, "Effects of solution on apatite formation on substrate in biomimetic process," *Journal of the Ceramic Society of Japan*, vol. 109, no. 1266, pp. 106–109, 2001.

[25] H. Varma, K. Sreenivasan, Y. Yokogawa, and A. Hosumi, "In vitro calcium phosphate growth over surface modified PMMA film," *Biomaterials*, vol. 24, no. 2, pp. 297–303, 2003.

Chapter 4

Nanomechanical characterization through AFM-based techniques

In order to characterize emerging micro and nanostructured materials, such as layered interfaces and coatings, the development of techniques able to measure local mechanical properties with a nanoscale resolution is essential. Currently, standard nanoindentation is the most widespread method used to determine the mechanical properties of layered coatings, usually made of soft polymers grown or deposited on hard substrates [1, 2]. However, its applicability is strictly limited by the thickness and the homogeneity of the polymer layer. Indeed, the mechanical properties of the substrate may dramatically affect the measured elastic modulus of the coating as its thickness decreases. Moreover, the presence of porosity within the polymer layer thickness and/or at the polymer-substrate interface may induce local reduction of their "apparent" (i.e. measured) elastic modulus [3–6]. Besides, nanoindentation does not allow the visualization of the surface elastic distribution because of its poor spatial resolution. For this reason alternatives methods, based on the atomic force microscopy (AFM), either quasi-static [7–9] or dynamic [10, 11] methods have been developed. They exploit the high resolution of the AFM as well as the possibility of positioning within a nanometer resolution and probing the surface sample with ultra-low loads using a feedback system to map the sample surface with a controlled applied force. In this way, maps of both the mechanical and viscoelastic properties (such as indentation, storage and loss moduli, damping, adhesion, energy dissipation) of the sample can be achieved [12, 13].

In the work of this thesis, four different AFM-based techniques have been employed to determine the indentation modulus (M) of the layered PMMA-coated Ti sample, synthesized following the procedure described in Chap. 3. For this purpose, these AFM-based techniques have been extensively validated by analyzing both stiff and soft materials. Then, they have been employed for the characterization of our PMMA-coated Ti interfaces.

This chapter is divided in three parts. The first one is devoted to a detailed description of the AFM working principle; in the second, the AFM-based techniques for the surface mechanical characterization are described and their theoretical aspects discussed; at the end, an overview of the results obtained in the characterization of some case studies, which allowed us to validate these techniques, are also shown.

4.1 Atomic force microscopy: working principle

The working principle of AFM is based on the measurement of the interaction forces acting between the sample and a sharp tip with a nominal curvature radius (R_{tip}) generally smaller than 10 nm. The tip is mounted near the free end of a clamped-free cantilever, with a length (L) of about few hundreds microns, width (w) of few tens microns and thickness (t) of few microns. When the tip is brought in close proximity to the surface, an interaction force is produced and the cantilever bends. This cantilever's deflection is generally monitored using an optical lever, the principle of which is illustrated in Fig. 4.1.

A laser beam is focused on the cantilever back side, made reflective by a coating of gold or aluminum. Then, the reflected beam is centered onto a four areas photodiode. By measuring the difference signal between the two upper and two lower segments (i.e. $(A+B)-(C+D)$) the cantilever deflection is determined; instead, the difference between the two left and two right segments (i.e. $(A+C)-(B+D)$) gives the cantilever torsion. Since the deflection signal is proportional to the sample height, it is possible to reconstruct the sample topography by scanning the predetermined surface area, using a system of piezoelectric transducers to move the tip across the surface sample (see Fig. 4.2a).

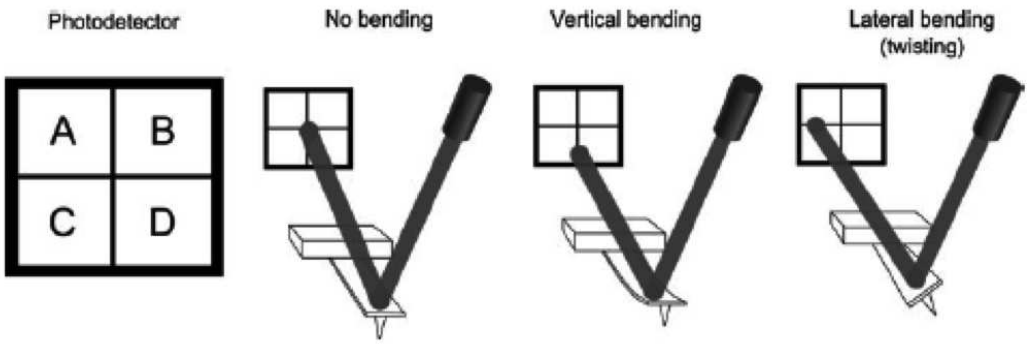

Figure 4.1: Representation of the optical lever working principle. A laser source is focused on the back side of the cantilever and then sent to a four-segments photodetector. By measuring the difference signal between the two upper and the two lower segments, or the the two left and two right segments, the cantilever deflection, or torsion, are respectively determined.

Piezoelectric transducers (generally made of piezo-ceramic tubes) are devices that convert the electrical applied potential in a mechanical strain, allowing the movement of the tip over the sample surface. They are driven by the control electronics so as to keep the tip-sample distance, and thus the interaction forces, at a fixed value.
As depicted in Fig. 4.2b, the size of the scanning area is set by the operator and it is divided in a homogeneous array of points. The scanning direction is also set and it is called *fast scan direction* (red arrows in Fig. 4.2b). The tip moves along this direction and at each point the deflection (or torsion) signal is measured. When the first line is finished, the tip is rapidly brought at the beginning point and it passes at the next line along the so-called *slow scan direction* (blue arrows in Fig. 4.2b).
The detected deflection signal is used by the controller as the input signal of a feedback circuit. It has to maintain the deflection signal at a constant value (namely, the set-point) during the scanning. In order to achieve this task, the feedback loop acts on the piezo-

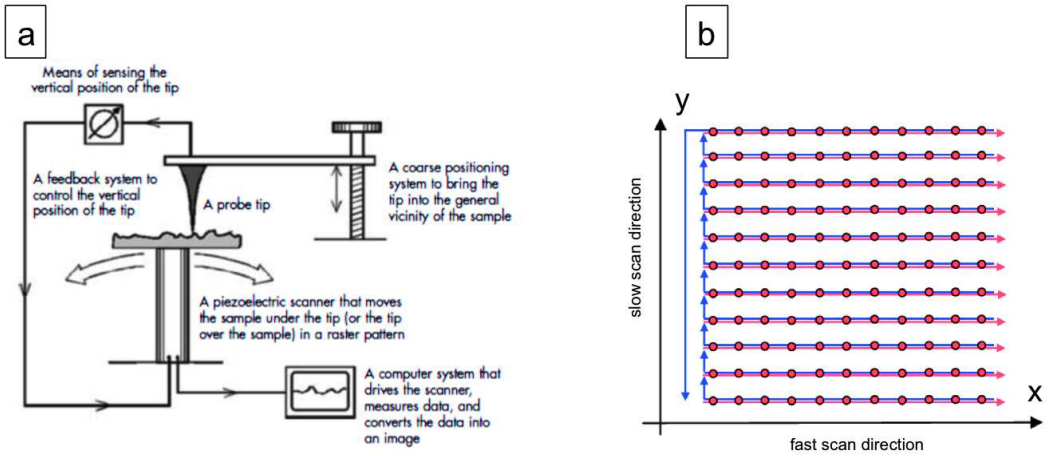

Figure 4.2: a) Schematic representation of the atomic force microscopy set-up and b) of scanning process. Direction of the forward motion of the scanner is indicated by black arrows. Instead, reverse motion of the scanner is indicated by gray arrows.

electric scanner in the vertical direction (z-axes direction) which modifies the tip-sample distance of a quantity equals to the height variation of the surface (see Fig. 4.2a). This value, collected at each point of the scanned area, is then processed by a software for the imaging analysis to visualize a quantitatively map of the sample surface morphology (also called AFM height image). It has to be underlined that the static deflection signal is detected and recorded for those experiments carried out in *contact mode* (see Sec. 4.1.2). In these experiments the tip is held continuously in contact with the surface. Another usual operating mode is the *non-contact mode* in which the tip is made oscillate and the amplitude variations of these oscillations is recorded and used as signal input of the feedback controller (see Sec. 4.1.2).

4.1.1 Interaction forces and force-distance curves

Interatomic forces acting between two atoms or molecules can be repulsive or attractive, short or long range. In equilibrium, typical interatomic distances are between 2 Å and 3 Å. Below these values, the interatomic forces are always repulsive and short range. At larger atomic distances, the long-range interatomic forces become attractive [14]. AFM uses the tip-sample interaction forces (i.e. the interatomic forces acting between the tip atoms and the sample's atoms) to build-up the surface topography images. There are several type of interatomic forces which, acting on the cantilever tip, generate its deflection. They can be classified as follows.

Van der Waals forces are due to the interactions between polar molecules. The polarization of an atom induces a polarization in the nearby atoms and therefore an attractive interaction is established between them.

Repulsive interactions (or exchange interactions) are strong repulsive forces originated by the overlap of the electronic orbitals at interatomic distances (few angstroms).

Capillary forces caused by the liquid film which can be formed on the sample surface when the instrument operates in air.

Adhesion forces generated by tip-sample bonds that may occur during the scanning.

Friction forces occur during the scanning in contact mode and make the cantilever bending laterally.

Magnetic interactions are caused by magnetic dipoles both on the tip and the sample. This interaction is used for Magnetic Force Microscopy to study magnetic domains on the sample surface.

Electrostatic interactions are generated by potential difference between the tip and the sample when both of them are conductive.

For the sake of simplicity hereinafter, only van der Waals and repulsive forces have been considered. They are mainly due to: (*i*) electrostatic interactions between charges or dipoles; (*ii*) polarization forces that arise when a distribution of charges in one molecule generates a dipole in an adjacent molecule; (*iii*) quantum-mechanical forces which give rise to covalent bonding and repulsive interactions (caused by Pauli's exclusion principle) [15]. It has been experimentally found that, if one separates two atoms, the repulsive force falls

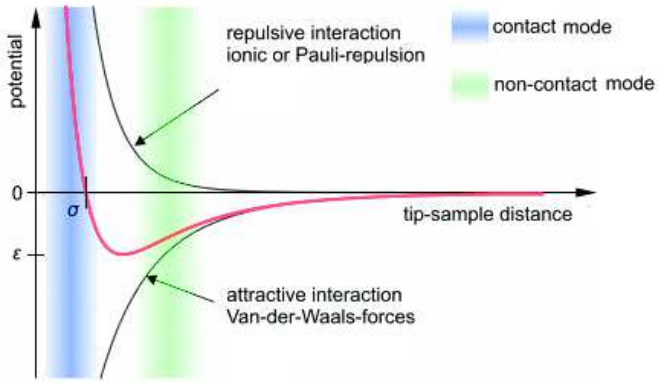

Figure 4.3: Lennard-Jones potential as a function of the distance between two atoms. It is a sum of an attractive and a repulsive contribution.

to zero at a distance of about 3 Å and above which it becomes attractive. These repulsive and attractive van der Waals potential are well modeled by the so-called *Lennard-Jones potential* [16]. It is depicted in Fig. 4.3 as a function of the distance between two atoms. Its expression is given by the following law:

$$U_{LJ} = 4\epsilon \left[\left(\frac{\sigma}{z}\right)^{12} - \left(\frac{\sigma}{z}\right)^{6} \right] \tag{4.1}$$

where σ is the distance at which the energy goes to zero and ϵ is its minimum value obtained at a distance $z = 1.12\sigma$. The first term of Eq. (4.1) describes the long range attraction caused by a dipole-dipole interaction and the second term takes into account the short range repulsion due to the Pauli's exclusion principle. The expression of the force, deduced from Eq. (4.1), is:

$$F_{LJ} = 4\epsilon \left[\left(\frac{-12\sigma^{12}}{z^{13}}\right) + \left(\frac{6\sigma^{6}}{z^{7}}\right) \right] \tag{4.2}$$

As already explained, Lennard-Jones potential model is only a qualitative approximation of the interaction forces existing between the tip and the sample as it does not consider all the forces involved during AFM experiments. Indeed, actually the attractive force goes as $-z^n$ with $n \leq 3$ (and not $n = 7$ as in Eq. (4.2)) and the repulsive part is more complex than that one modeled in Eq. (4.2) [14,17]. Nevertheless, it can be used to well understand how an AFM works, since it maintains the particular feature to be a sum of an attractive and a repulsive contributions.

The local tip-sample interaction forces can be derived performing the so-called force measurements, in which the evolution of the cantilever deflection is recorded as it approaches the sample surface. In this way, deflection curves as function of the tip-sample distance are obtained. By simply multiplying the cantilever deflection by its spring constant (k_c), these curves can be transformed in a plot of the interactions forces versus the tip-sample distances [2, 18]. As illustrated in Fig. 4.4, in a force measurement two plots are obtained as the piezoelectric element along the z-axes is extended and retracted. At the beginning of the experiment (point A) a large tip-sample distance exists. Here, the cantilever doesn't feel the interaction forces and its deflection is set to zero. When a voltage (of the order of mV) is applied, the piezo-element starts to extend and the tip-sample

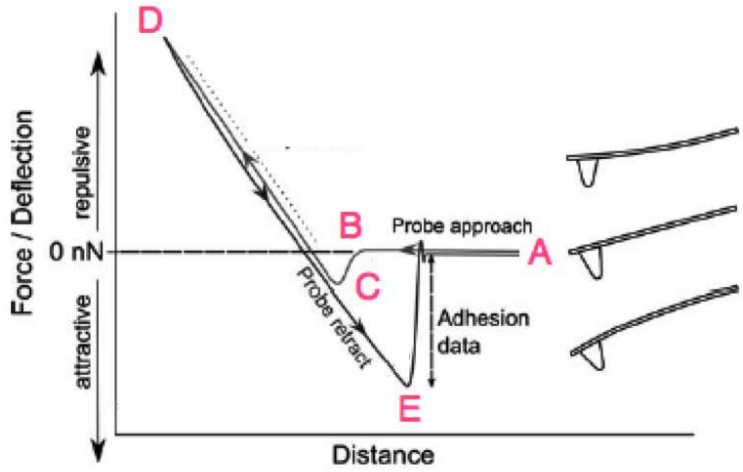

Figure 4.4: Representation of force-distance curve. At point A the probe is far from the surface, at point B van der Waals interactions cause the cantilever bending toward the surface. By decreasing the tip-sample distance, the elastic force cannot balance the attractive forces and the tip jumps into contact with the surface (point C). The force becomes repulsive as the distance continues to diminish and cantilever bends upward (point D). Then the direction of the motion is reversed. At point E pull-off occurs as the force applied to the cantilever overcomes the tip-sample adhesion.

distance decreases. The cantilever deflection maintains a constant value till van der Waals interactions make the cantilever bend toward the surface (point B). At this point, van der Waals forces are balanced by the elastic restoring force of the cantilever. By further decreasing the tip-sample distance, the elastic force cannot balance the attractive forces and the tip jumps into contact with the surface (point C). Since the tip pushes on the surface, the distance continues to decrease and the cantilever bends upward (point D). At this point interactions are dominated by the repulsive forces and the piezo-element begins to retract. Cantilever deflection increases and tip-sample separation occurs when the cantilever elastic force overcomes the adhesion and capillary forces (point E). Measurement of force-distance curves is a very sensitive way to determine tip-sample interactions, and is the basis for several non-topographic AFM modes, i.e. nanoindentation, as explained in Sec. 4.2.1.

4.1.2 Operation modes

Different AFM modes of operation exist depending on the value of the tip-sample distance and the kind of the corresponding forces involved (see Fig. 4.3). If the tip is held at distances smaller than a few angstroms from the surface, the interatomic forces are repulsive and the AFM works in the so-called *contact regime*. Conversely, in *non-contact regime* the tip is held on the order of tens to hundreds angstroms from the surface where the forces are attractive [19]. These topographic modes can be also divided in: (*i*) static modes and (*ii*) dynamic modes. The first one corresponds to the *contact mode* and it measures the static cantilever deflection. Instead, dynamic modes measure the dynamic oscillation of the cantilever and they include non-contact and intermittent-contact mode.

Static modes

Contact mode has been the first and simplest mode developed. In this mode the tip is always kept in contact with the surface and it follows the surface topography. Strong repulsive forces, which induce variation in the cantilever deflection, are used to create the image. There are two contact modes: (*i*) *constant force* and (*ii*) *constant height*.

In the former the feedback loop works to constantly maintain the cantilever deflection at a fixed value (set-point) and therefore at a constant force. For this purpose, during the scanning the piezoelectric elements are moved along the z-axes by the feedback controller. The amount of this motion forms the *height image* which is actually the sample topography.

In the latter the feedback is turned off and the cantilever deflection is measured and related to the surface morphology. This last mode can be used for fast-scan and when the investigated sample surface is very smooth.
The main advantage of contact mode is its high resolution but, since the tip is dragged over the surface, there is always the possibility of surface damaging and it cannot be used to study soft and biological samples without loosing in resolution.

Dynamic modes

Dynamic modes of operations comprise both *non-contact mode* and *intermittent contact mode*. In both of them, a stiff cantilever oscillates in close proximity of its resonance frequency (see Fig. 4.5) and when it approaches the surface, its resonance frequency and consequently also its amplitude and phase change because of the force field existing between the tip and the sample (see Fig. 4.6). For both of them, the amount of these variations can be deduced considering the dynamic behavior of a clamped-free cantilever. In these operation modes a fixed value of the detection signal (generally *oscillation amplitude*) is held constant during the scan. Thus, the feedback controller constantly moves the scanner in the z-direction in order to maintain the oscillation amplitude at the chosen set-point and the topographic image is build-up recording the bias voltage (or current) required to move the z-scanner. The main difference between non-contact and intermittent mode is the distance from the sample at which the cantilever is held, as illustrated in Fig. 4.5.

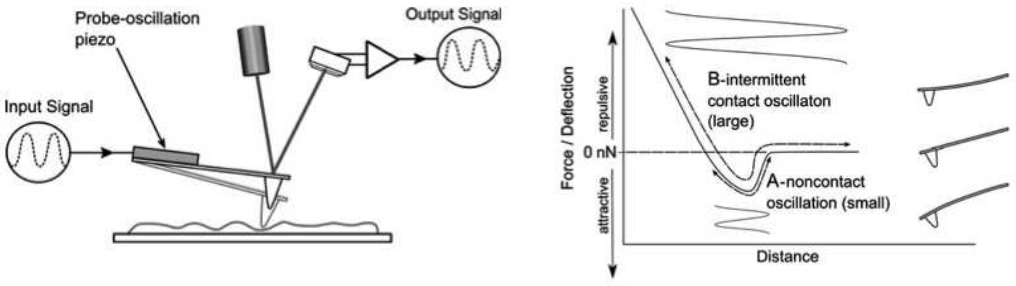

Figure 4.5: In dynamic modes a stiff cantilever oscillates in proximity of its resonance frequency. It is held within a distance of tens to hundreds angstroms from the surface, in the region dominated by the long range van der Waals forces. The main difference between non-contact and intermittent mode is the distance from the sample at which the cantilever is held. In non-contact mode this distance is higher and the tip does not touch the sample. Instead, in intermittent-contact mode the cantilever is held closer to the surface and the tip intermittently touches the surface.

In **non-contact mode** cantilever oscillates close to the sample surface without touching it. It is held within the region dominated by the long range van der Waals forces (i.e. 5-10 nm from the sample surface). Stiff cantilevers are required to prevent the crash of the tip on the surface. This leads to smaller deflection and, therefore, the signal magnitude detected is lower than that in contact mode. This mode has been first introduced in 1987 [20]. Until the invention of the intermittent-contact mode (also known as tapping mode), it has been the favorite mode used to study polymers, biological samples and soft polymeric matter. Nowadays, tapping mode is usually preferred for topographic image of soft samples thanks to the better resolution and non-contact mode is generally used to detects non interatomic forces (such as magnetic forces).

Intermittent-contact mode has been developed in 1993 in order to: (*i*) avoid surface damage, (*ii*) improve non-contact mode lateral resolution and (*iii*) eliminate lateral forces (such as drag) [21]. A stiff cantilever is made oscillate, by a piezo actuator, closer to the surface than in non-contact mode. Part of these oscillations extends untill the region wherein the repulsive forces predominate thus the tip intermittently touches the surface. As shown in Fig. 4.6, the cantilever dynamic behavior is affected by the influence of the interaction forces.

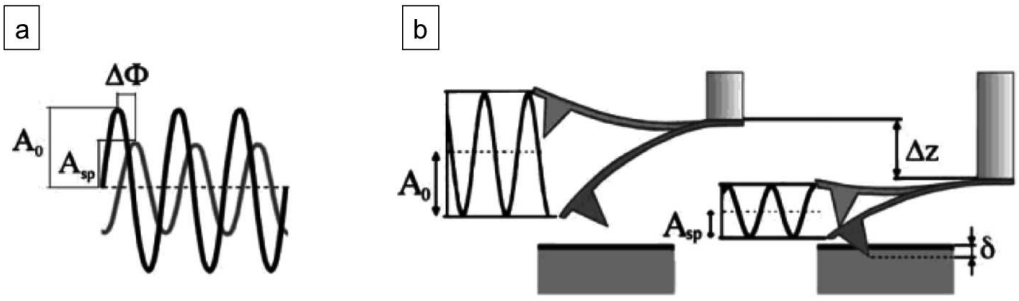

Figure 4.6: a) Shift of resonance frequency, amplitude and phase of the cantilever oscillations occurs when the tip approaches the surface because of the force field existing between the tip and the sample; b) Illustration of the AFM tapping mode working principle.

Far away from the surface it oscillates with a certain amplitude A_0 at or near its resonance frequency f_0 (the black curve in Fig. 4.6a). Its dynamics can be described considering the motion equation of an elastic massless beam, with an elastic constant k_c and a concentrated mass m located at its free end, oscillating with angular frequency ω [14, 22]:

$$m\ddot{z} + \gamma\dot{z} + k_c z = k_c u_0 cos(\omega t) + F_0 \tag{4.3}$$

where γ is the damping coefficient and F_0 any possible constant force acting on the system. Considering that F_0 can only change the equilibrium position of the system without affect frequency, amplitude and phase of the oscillations, Eq. (4.3) can be rewritten as function of the cantilever displacement from its equilibrium position $z_d = z + F_0/k_c$:

$$m\ddot{z} + \gamma\dot{z} + k_c z = k_c u_0 cos(\omega t) \tag{4.4}$$

From Eq. (4.4) an expression of the oscillations amplitude and phase, as function of the angular resonant frequency($\omega_0 = \sqrt{(k_c/m)}$) and the cantilever's quality factor ($Q = \omega_0 m/\gamma$),

can be derived:

$$A(\omega) = \frac{{\omega_0}^2 u_0}{\sqrt{({\omega_0}^2 - \omega^2)^2 + j\frac{\omega\omega_0}{Q^2}}} \tag{4.5}$$

$$\phi(\omega) = arctg\frac{\omega_0\omega}{Q({\omega_0}^2 - \omega^2)} \tag{4.6}$$

Whereas, when the tip approaches the surface, the value of the oscillation amplitude and the phase vary although the piezo actuator excites the cantilever with the same energy, because of the force field existing between the tip and the sample (see Fig. 4.6b). Thus, the cantilever starts tapping the sample surface with a reduced set-point amplitude A_{sp} and with a phase shift $\Delta\phi$ with respect to the cantilever free vibrations. In this phase, the cantilever-sample interaction consists in both the van der Waals forces and the elastic force, added during the tip-sample contact, which change the cantilever's equation of motion, resulting in a shift of the cantilever's oscillations amplitudes and phases. Thus, even though during the scanning the amplitude oscillation tends to vary, the feedback loop maintains it constantly equal to a set-point value (A_{sp}) chosen by the operator. The vertical displacement of the z-scanner, which is needed to maintain the amplitude constant, is displayed as *height images* and the local shift in phase is employed as *phase images*. The height images show the morphological structure of the sample [23]. Whereas, the phase images describes the energy dissipation involved in the contact between the tip and the sample, which depends on several factors such as: (i) adhesion, (ii) friction, (iii) viscoelasticity, (iv) and tip-sample contact area. Thus, if the regions of differing viscoelasticity are encountered on the sample surface, the oscillation phase changes due to different amount of damping sensed by the tip. Since during each oscillation cycle the tip touches the surface for a very short time, intermittent-contact mode is the method mainly involved in the study of the soft materials.

4.2 Mechanical characterization at the nanoscale

4.2.1 AFM-based nanoindentation

AFM nanoindentation is a versatile method used to study the local mechanical properties of polymeric thin films. The working principle of AFM nanoindentation is similar to that of the common DSI technique that uses a nanoindenter as probe. Compared with DSI measurement, AFM nanoindentation is preferably employed to characterize soft materials, since it can operate with smaller force and consequently with smaller deformations [24]. It is based on the acquisition of force-distance curves which, elaborated with a suitable contact-mechanics model, enable the evaluation of the sample elastic modulus (or Young's modulus, E) [2, 25, 26]. These curves describe the evolution of the tip-sample interaction force (F) versus the displacement of the microscope piezoelectric scanner (Δz). As already mentioned in Sec. 4.1.1, they are obtained by recording the cantilever deflection (d) as a function of Δz during the tip approaching and retrying phases. Once that d is measured, it is multiplied by cantilever spring constant (k_c) to be transformed into F. On stiff materials, that exhibit a totally elastic behavior and are not indented by the AFM tip, any variation of Δz results in a variation of d of the same amount (blue curve in Fig. 4.7a). Instead, on soft materials, the tip indents the sample surface. Moreover, in the case of elasto-plastic materials, the curves present an hysteresis between the loading and unloading curves [2]. Thus, for the same value of d, Δz is bigger than that observed on hard materials.

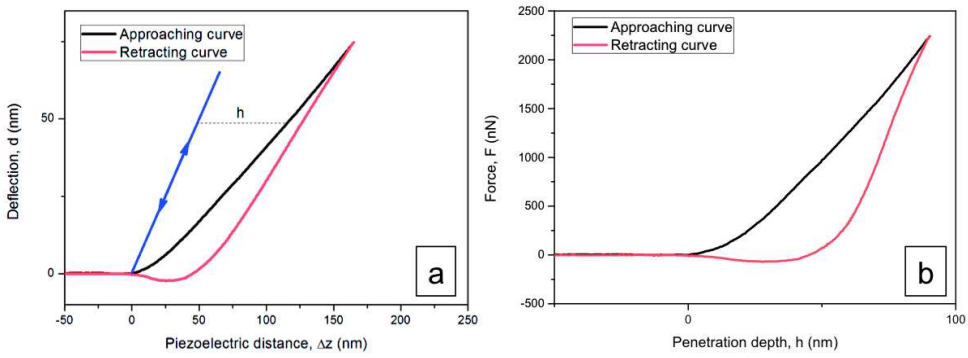

Figure 4.7: a) Deflection versus piezo-displacement curve recorded on a commercial PMMA sheet; b) reconstruction of the indentation curve obtained on the same PMMA sheet.

The difference between Δz of the two materials (at the same deflection value) is called penetration depth, h (see Fig. 4.7a) and can be evaluated as:

$$h = \Delta z - d \tag{4.7}$$

Force-distance curves (Fig. 4.7a) can be transformed into the force-indentation ones (Fig. 4.7b) by calculating h for each point of the deflection curve [2, 25]. From these force-distance curves the mechanical properties of the sample, i.e. the hardness (H) and the indentation modulus (M), can be derived. In particular, the evaluation of M can be determined using well established procedures borrowed from standard DSI measurements [27–29]. When the tip indents the sample both plastic and elastic deformations occur and the value of the penetration h is a sum of two contributions [2]. As schematized in Fig. 4.8, in correspondence of the maximum applied load F_{max}, the indentation depth is $h_{max} = (h_r + h_e)$, where h_e is the recovery of the elastic deformation and h_r is the amount of the residual plastic deformation when the tip is withdrawn from the surface.

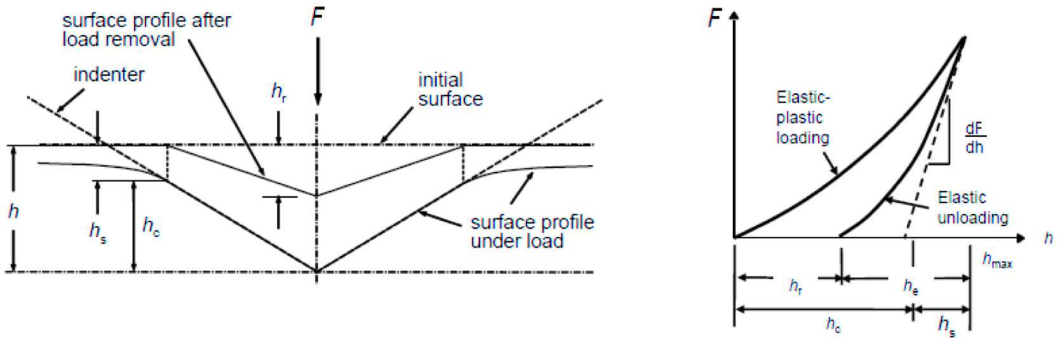

Figure 4.8: Left: Schematic illustration of the indenter. Right: sketch of force-indentation curve of an elasto-plastic material. h_r is the depth of the residual impression, h_{max} is the depth from the original specimen surface at maximum load applied, h_e is the recovery of the elastic deformation and h_s is the distance from the edge of the contact to the specimen surface at full applied load.

The first phenomenon that occurs when the tip is withdrawn is the recovery of the elastic deformation. Thus, the initial slope of the unloading force-indentation curve cor-

responds to the tip-sample contact stiffness (k^*). Using the Sneddon's relation and considering that the indentation modulus of the tip (M_t = 169 GPa) is much higher than that of polymeric samples, the indentation modulus of the sample (M_s) can be obtained as follows [2, 27]:

$$M_s = \frac{\sqrt{\pi}}{2\sqrt{A_c}} k^* \tag{4.8}$$

The values of the contact stiffness k^* and the contact area A_c are determined using the Oliver-Pharr model which describes k^* as a power law [28, 29]:

$$k^* = \left.\frac{dF_n}{dh}\right|_{F_{max}} = m\alpha(h - h_r)^{m-1} \tag{4.9}$$

Instead, the contact area A_c is related to the penetration contact depth h_c:

$$A_c = C(h_c)^2 = C(h_{max} - \varepsilon\frac{F_{max}}{k^*})^2 \tag{4.10}$$

where F_{max} is the maximum value of the applied load and ε as well as C are constant related to the tip shape. For parabolical tips, a ε value equal to 0.75 is assumed; whereas for a flat tip $\varepsilon = 1$ is considered [2]. Thus, from Eq. 4.8, M_s is expressed with the following relation:

$$M_s = \frac{\sqrt{\pi}}{2\sqrt{C}} \left[\frac{k^{*2}}{(k^* h_{max} - \varepsilon F_{max})}\right] = \frac{\sqrt{\pi}}{2\sqrt{C}} f \tag{4.11}$$

The value of $f = k^*/\sqrt{h_c}$ can be easily determined by elaborating the experimental data collected. Instead, the value of the constant C is determined performing a proper calibration on reference materials with known properties [2, 30, 31].

4.2.2 Contact Resonance Atomic Force Microscopy

Contact resonance atomic force microscopy (CR-AFM) has been introduced in 1994 by Rabe et al. in order to investigate the mechanical properties of samples with a non-destructive technique and a resolution on the nanoscale [32–34]. Contrary to AFM nanoindentation, CR-AFM represents a versatile tool to perform not only single point measurements of the elastic modulus, but also to obtain quantitative maps of the sample surface mechanical properties with nanometrical lateral resolution [35, 36].

As schematized in Fig. 4.9, in this technique the sample back side is coupled to a piezoelectric transducer which makes it vibrate with ultrasonic frequencies. By analyzing the deflection signal of the cantilever when the tip is held in contact with the sample surface, the contact resonance frequencies (CRFs) of the sample-tip-cantilever system are determined. CRFs monotonically increase with the tip-sample contact stiffness (k^*). Thus, being k^* related to the M_s by Eq. 4.8, local variations of the M_s, cause a shift of the CRFs. In particular, the higher M_s, the higher the value of CRF of the generic n-th mode (f_n). By recording and analyzing the CRFs through a suitable contact mechanical model, maps of the local elastic properties of the sample are achieved, simultaneously to the conventional topographic images [35–38].
The experimental CR-AFM procedure is a two steps technique.

In the first step, the resonance frequencies of the cantilever oscillating in air, far away from the sample surface, are recorded in order to evaluate a characteristic parameter of the cantilever (c_c) which combines geometrical and material properties [39]. In particular,

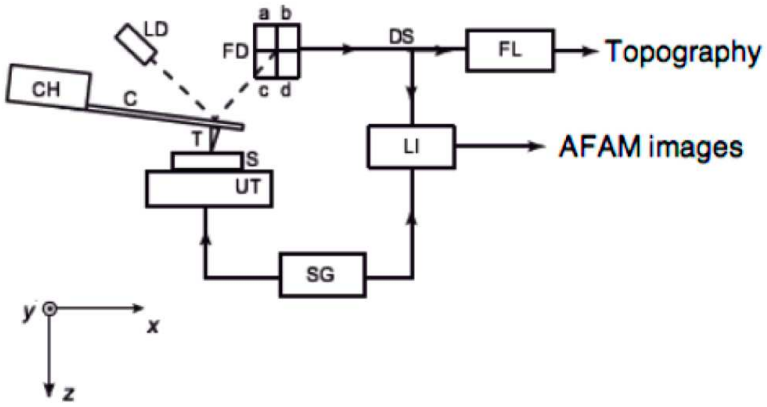

Figure 4.9: Schematic representation of CR-AFM apparatus.

the cantilever is modeled as a flexible clamped-free beam with length L (see Fig. 4.10a), width w, thickness t and Young's modulus E. The value of c_c is obtained inverting the following expression [14]:

$$f_{0n} = \frac{(k_{0n}L)^2}{{c_c}^2} \tag{4.12}$$

Eq. 4.12 comes from the characteristic equation of the beam, where k_{0n} is the wave number of the n-th flexural resonant frequency (f_{0n}) (see Eq. A.7 in Appendix A).

In the second step, the tip is brought in contact with the sample. The tip-sample contact is modeled as a linear spring, the elastic constant of which is the contact stiffness k^* (see Fig. 4.10b) which depends on M_s and determines the values of the CRFs. If the tip is located at position L_1 from the cantilever clamped-end, defined by the parameter $r = L_1/L$, the characteristic equation of the system, allows expressing the k^* as a function of the parameter r, the contact resonance frequency f_n (acquired by the microscope electronics) and the parameter c_c, obtained at the first step of the technique [37, 40] (see Appendix A for more details). The parameter r, generally unknown, is either estimated by SEM characterization or evaluated detecting the CRFs corresponding to two different

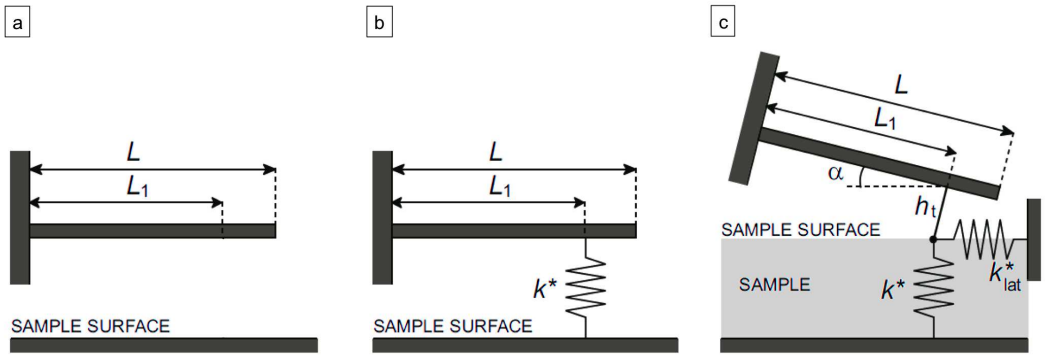

Figure 4.10: Sketch of the models used to analyzed the CR-AFM data: a) clamped-free cantilever; b) clamped spring-coupled cantilever; c) normal and tangential spring-coupled cantilever.

modes (f_n and f_m with $n = m$) and matching the two corresponding contact stiffness: $k^*(f_n, r) = k^*(f_m, r)$. Once, the value of r is estimated, the experimentally determined values of the CRFs are used to calculate the local k^*.

After the experimental session, the data are elaborated to evaluate the M_s. To this aim, the tip-sample contact is described with a suitable contact mechanic model [41], such as the Hertzian one, according to which M_s is calculated after calibration of the radius and the indentation modulus of the tip (R_t and M_t, respectively) using a set of reference materials with known mechanical properties [42, 43]. The Hertzian model describes the contact between two non-conforming elastic bodies, a flat surface and an hemispherical tip, neglecting the adhesive forces between them (see Fig. 4.11). If a normal force (F_n) acts between the tip and the sample, the contact radius (a_c) of a circular contact area is given by:

$$a_c = \sqrt[3]{\frac{3F_n R_t}{4E^*}} \tag{4.13}$$

where E^* is the reduced Young's modulus that comprises the elastic properties of the tip (M_t) and of the sample (M_s): $1/E^* = 1/M_s + 1/M_t$. By substituting Eq. 4.13 in Eq. 4.8, k^* can be related to the sample's indentation modulus:

$$\frac{1}{k^{*3/2}} = \frac{1}{\sqrt{6R_t F_n}} \left(\frac{1}{M_s} + \frac{1}{M_t} \right) \tag{4.14}$$

where F_n is easily calculated from the static cantilever deflection; R_t is generally evaluated by a calibration procedure, using reference samples with known mechanical properties; whereas, M_t is either assumed as the theoretical indentation modulus of the material forming the tip [44, 45] or independently measured using a more accurate approach: the second reference method proposed by Stan et al. [42]. This approach has been demonstrated to overcome the limitation due to neglecting the tip-sample lateral forces, which represent a major source of inaccuracy in CR-AFM measurements especially when characterizing the polymers [43]. Indeed, a more comprehensive model of the system is depicted in Fig. 4.10c, where the cantilever is assumed tilted with respect to the surface of an angle α and the tip height h_t is considered [40, 46]. Moreover, the lateral contact stiffness (k^*_{lat}) is introduced. It accounts for the tip-sample lateral coupling, i.e. the sample shear modulus defined as [46]:

$$G_\mathrm{s} = \frac{1}{2} E_s / (1 + \nu_s) \tag{4.15}$$

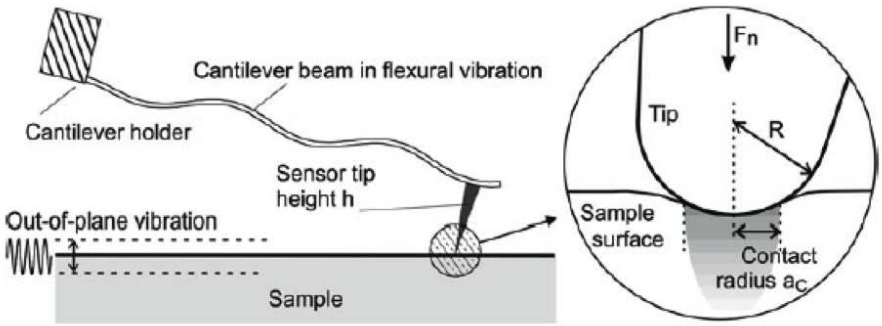

Figure 4.11: Schematic representation of the tip-sample contact described by the Hertzian model used during a CR-AFM experiments.

where, ν_s is the sample Poisson's ratio.
In this way, the chosen CFRs values can be simulated in a wide range of k^*/k_c values, by solving the characteristic equation of the system depicted in Fig. 4.10c, in which k^*_{lat} can be expressed using the following expression:

$$\frac{k^*_{lat}}{k^*} \approx \frac{2(1-\nu_s)}{2-\nu_s} \tag{4.16}$$

having considered the indentation modulus of the tip much higher than those of the polymeric samples ($M_t \gg M_s$). Thus, curves of the CRFs versus the normalized contact stiffness k^*/k_c are obtained. As an example, Fig. 4.12 reports the first and third CRFs as function of k^*/k_c, simulated considering a clamped spring-coupled cantilever (dotted curves) and a normal and tangential spring-coupled cantilever (solid curves).

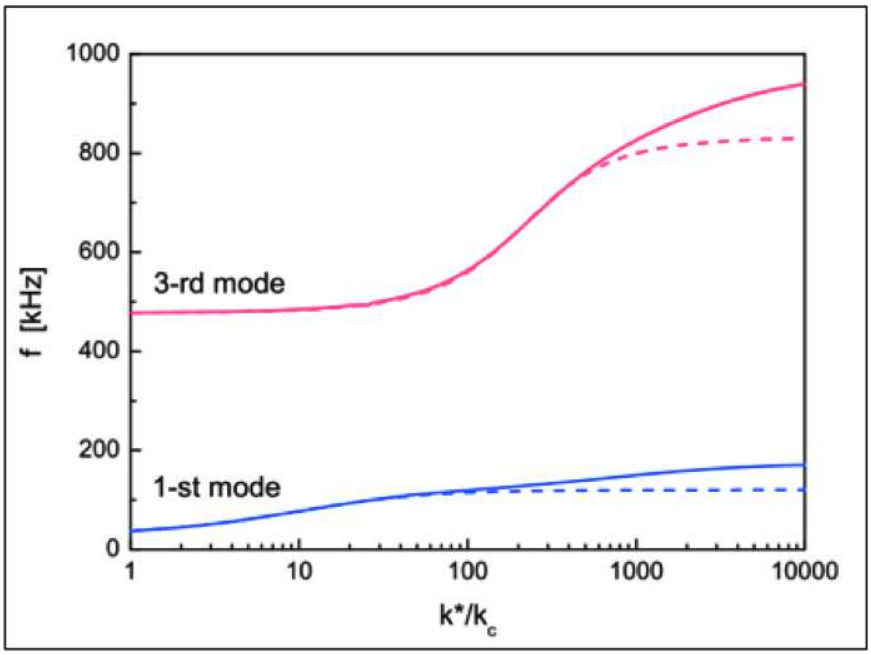

Figure 4.12: First (blue lines) and third (red lines) CRFs as a function of the normalized contact stiffness k^*/k_c. The dotted lines have been calculated considering the simple clamped spring-coupled cantilever (Fig. 4.10b). The solid curves are obtained introducing the contribution of a lateral spring (k^*_{lat}, Fig. 4.10c) [38].

From these curves, in correspondence of the measured CRFs, values of the k^* are extracted and, consequently, M_s calculated using Eq. (4.14).

Furthermore, in the last years, CR-AFM has been proposed as a method able to characterize the viscoelastic properties of materials, i.e. the storage and loss moduli (E' and E'', respectively) and the loss tangent ($\tan\delta$), by acquiring and elaborating the values of CRFs and their corresponding quality factors Q [47–49]. In this case, the tip-sample contact is modeled as the parallel between a spring with elastic constant k^* and a dashpot of damping σ, introduced to describe the effect of the sample viscosity (see Fig. 4.13a). The $n-th$ contact resonance frequency (f_n) and the corresponding quality factor (Q_n) are measured to evaluate both the normalized contact stiffness k^*/k_c and the normalized damping, defined as:

$$\beta = \sigma\sqrt{L_1^2/9EI\rho A} \tag{4.17}$$

where E is the sample Young's modulus, I the cantilever's area moment of inertia, ρ the cantilever density, and A the cantilever cross-sectional area [47,48]. First, the tip position, expressed in terms of the ratio $r = L_1/L$, is determined matching the expression of k^* in correspondence of two different modes ($k^*(f_n, r) = k^*(f_m, r)$), neglecting the damping σ. Then, after a calibration of the tip geometry and mechanical properties, α and β are determined allowing the evaluation of the sample storage and loss moduli, E' and E'', respectively. To avoid the source of uncertainty related to the calibration procedure, viscoelastic properties of the sample can be obtained in terms of the loss tangent ($\tan\delta$) defined as [50]:

$$\tan\delta = \frac{E''}{E'} \tag{4.18}$$

From CR-AFM data, $\tan\delta$ can be calculated as

$$\tan\delta = (\lambda_n r)^2 \frac{\beta}{\alpha} \frac{f_n}{f_{0n}} \tag{4.19}$$

where λ_n is the solution of the characteristic equation for free flexural vibrations of the cantilever ($1 + \cos\lambda_n \cosh\lambda_n = 0$). Thus, according to Eq. 4.19, CR-AFM allows one to acquire accurate quantitative maps of $\tan\delta$ without the explicit calculation of E' and E'' and, thus, without calibration of the tip using reference materials [50, 51].

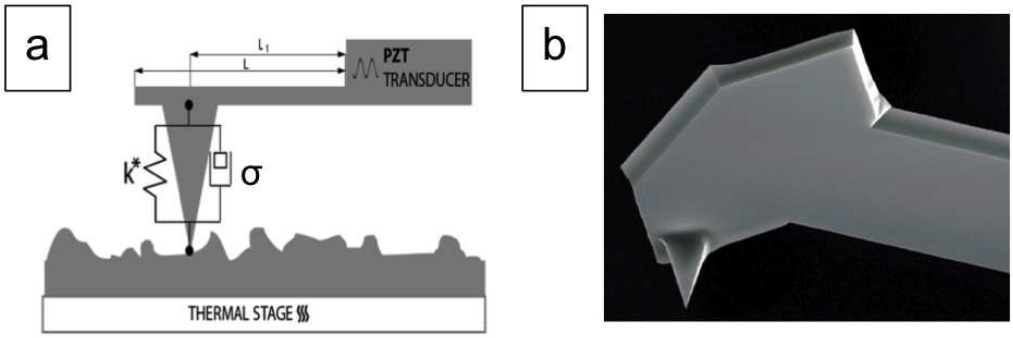

Figure 4.13: a) Sketch of the model used to describe the viscoelastic behavior of the samples in CR-AFM experiments; b) Scanning electron micrograph of a torsional harmonic cantilever.

4.2.3 HarmoniX™ mode

In HarmoniX™ mode, the sample surface is imaged in tapping mode with a T-shaped cantilever with a tip placed out of the cantilever axis, (see Fig. 4.13b) made oscillate close to its first resonant frequency f_{01} [52, 53].

Because of this particular cantilever geometry, tip-sample interaction forces generate a torque around the cantilever axis which excites the torsion of the cantilever. As a result, while tapping over the surface, the cantilever simultaneously moves in flexural and torsional modes.

If the sample under investigation is sufficiently soft, the tip indents the surface during the lower portion of each oscillation cycle. As a consequence, during each oscillation cycle both the cantilever deflection signal and the torsional signal contain a complete loading/unloading force-indentation curve, periodic with period $T = 1/f_{01}$. While flexural

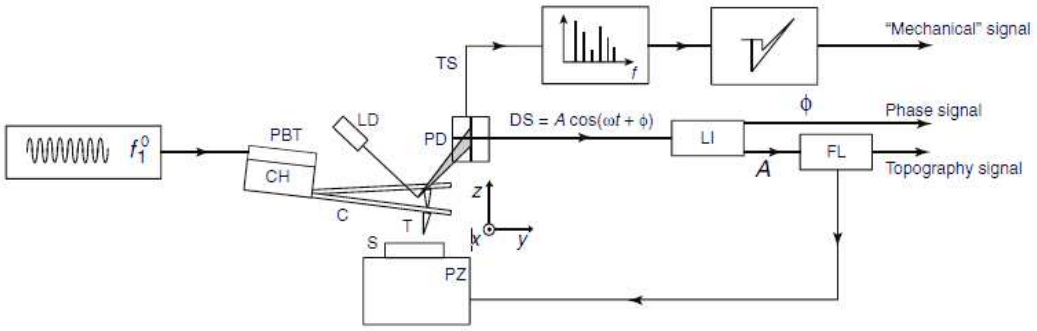

Figure 4.14: Torsional harmonic AFM set-up. The torsional signal (TS) is acquired and analyze by Fourier inverse transform to obtain force-distance curves. Simultaneously, the deflection signal (DS) is used to image the sample in tapping mode.

signal is used to reconstruct the sample surface topography, as in a conventional AFM tapping mode, the torsional one is used to acquire force-indentation curves through inverse Fourier transform analysis (Fig. 4.14). Indeed, the use of the torsional signal ensures a higher signal-to-noise ratio since the first torsional resonance frequency τ_{01} is about 20 times higher than f_{01} and, thus, at least 20 harmonic components of the signal are located in a undistorted spectral region [52, 53]. After a proper calibration of the tip geometry and instrument sensitivity performed using a reference sample, these curves are in real-time analyzed using the Derjaguin-Muller-Toporov (DMT) model [54, 55] in order to built-up maps of the sample indentation modulus. In DMT model, the force acting on a flat surface indented by a spherical tip is expressed by [54]:

$$F(h) = \frac{4}{3} E^* \sqrt{R_t} h^{3/2} + F_{\text{pull-off}} \tag{4.20}$$

where $F_{\text{pull-off}}$ is the maximum force which has to be applied to break the adhesive contact and pull-off the tip from the surface. It can be easily measured from the force-indentation curves. Additional parameters mapped during the scanning are the peak force, the tip-sample adhesion force, and the dissipated energy during each indentation cycle [13].

Being based on AFM tapping mode and thus not requiring the continuous contact between tip and sample, TH-AFM find natural application in the nanomechanical study of soft samples, like the polymers or the biological structures. The materials which have been effectively investigated by TH-AFM have indentation modulus ranging approximately from 10 MPa up to 10 GPa [53], including highly oriented pyrolytic graphite (HOPG) [53], polymers [53, 56], polymer blends [13, 53], polymer-based (nano)composites [38, 57], pigment coatings [58], amyloid fibrils [59], bacterial nanowires [60]. Although, the range of investigable elastic moduli is not as wide as those of other AFM-based techniques, TH-AFM is particularly suitable to acquire simultaneous high resolution and high speed mechanical images of soft samples. Furthermore, TH-AFM probes the sample down to a few tens of nanometers from the surface. As a consequence, mechanical properties of the bulk may be not accessible and the comparison between TH-AFM data and those from techniques which probe the sample down to bigger penetration depths (such as depth sensing indentation) may be misleading. On the other hand, the shallow penetration depth makes TH-AFM particularly suitable for the study of mechanical properties of polymeric ultrathin films.

4.2.4 Peak Force Quantitative Nanomechanical Mapping

The Peak force quantitative nanomechanical mapping (PF-QNM^{TM}) is a recently introduced imaging mode which allows one to map the local elastic properties, tip-sample adhesion, maximum sample deformation, and energy dissipation with lateral nanometer resolution [61–63]. In PF-QNM^{TM}, the cantilever is made oscillate well below its resonance frequency (usually between $1 - 2$ kHz), and the peak force, i.e. the maximum tip-sample force $F_{\max}$, is used as feedback control parameter and kept constant during the scanning. During each interaction cycle, a force curve is collected and analyzed. As in HarmoniX^{TM} experiments, after a proper tip calibration using a reference sample with well-known indentation modulus, the unloading portion of the curves are analyzed using a DMT model (Eq. 4.20) and the indentation modulus in real-time determined. Thus, two-dimensional maps of M_s, the maximum deformation, F_{adh}, and the energy dissipated during each cycle are acquired simultaneously with topographical images [61–63].

4.3 Case studies: validation of the AFM-based techniques

The main goal of this thesis is the synthesis and characterization of layered PMMA-coated Ti interfaces, which are composed of a stiff Ti substrate from which tethered PMMA chains are grown. To this aim, before analyzing the surface mechanical properties of the produced samples, the AFM-based techniques, previously described, have been validated performing the mechanical characterization of both stiff and soft materials. Here, the main results achieved on some interesting case studies will be reported.

4.3.1 Mechanical characterization of stiff samples: CR-AFM on a thermally treated diaspore

In this study, the characterization of a thermally treated diaspore have been performed. This section briefly reports the results integrally presented in [64] (see also Appendix C).

After a heat treatment at 600 °C, the natural diaspore undergoes to a microstructure transformation exhibiting a polycrystalline structure with ordered micrometer-size rectangular grains of uniform crystallographic orientation. It has been demonstrated how CR-AFM can be effectively used to study the mechanical properties of very hard materials. Following the two reference methods proposed by Stan et. al [42], using natural diaspore (M = 300 GPa) and corundum (aluminium oxide Al_2O_3, M=432 GPa) as reference samples, elastic maps of the heated diaspore surfaces have been obtained and an indentation modulus of 390 ± 20 GPa have been derived.

Fig. 4.15 shows the results of the nanomechanical characterization performed. Along with the CR-AFM characterization, the sample morphology has been investigated by AFM (Fig. 4.15a) and SEM analysis Fig. 4.15d. The diaspore morphology is characterized by ordered rectangular grains with sizes on the order of hundreds of nanometers. The first and second CRF maps are presented in Fig. 4.15b and Fig. 4.15c, respectively. They show a network of cracks and single micro-grains. The same CRFs maps have been used to reconstruct the sample's indentation modulus map (Fig. 4.15e) following the procedure described in Sec. 4.2.2. In particular, a variation of the indentation modulus on the surface of the single micro-grain has been highlighted. It reaches a value of (395 ± 400) GPa in the center of the grains, while it decreased to 380 GPa near the edges.

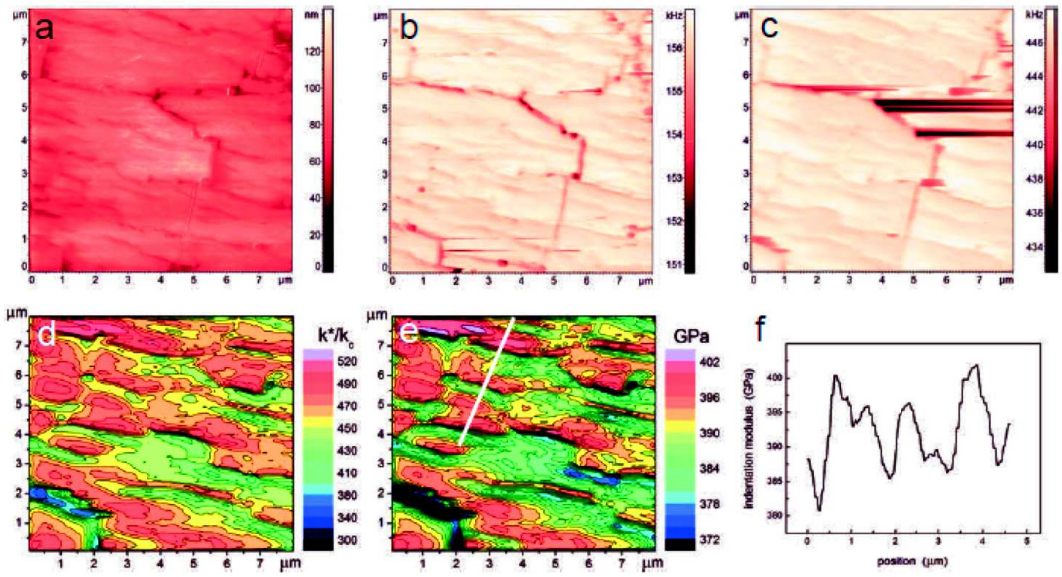

Figure 4.15: Characterization of the thermally heated diaspore. a) AFM height image of the surface topography; b-c) maps of the first an second CRFs acquired with a static normal load of 25 nN; d) SEM micrograph of the thermally heated diaspore; e) map of the indentation modulus and f) profile of the indentation modulus corresponding to the white line in (e).

Overall, by enabling non-destructive quantitative stiffness measurements as well as imaging at the nanometer scale, CR-AFM has been demonstrated to be applicable for the mechanical characterization of hard materials. Besides, it showed that CR-AFM nanomechanical mapping can be used to detect cracks, defects, voids, as well as micro- and nano-inclusions of the sample surface.

4.3.2 Mechanical characterization of soft samples: CR-AFM and HarmoniX™ on polianiline-based nanocomposites

In the present case study (detailed in the work presented in [38] and reported in Appendix C), it has been investigated how the mechanical properties of the single nanostructures (i.e. nanodiamonds) can rule the surface mechanical properties of a macroscale sample. Polyaniline (PANI) and polyaniniline doped with nanodiamond particles (PANI-ND) tablets have been characterized using both CR-AFM and HarmoniX™ to determine how the introduction of detonation nanodiamonds (NDs) modulates the elastic surface properties of the samples. For this purpose, first PANI and PANI-ND have been synthesized by a precipitation method [38, 65], then PANI and PANI-ND tablets have been prepared by a pressing process conducted at 200 bar. In Fig. 4.16a a typical topographical image of PANI, consisting in a granular structure, is reported. Conversely, on the surface of PANI-ND fibrillar features are visible (Fig. 4.16b) which are triggered by the presence of the ND particles, as previously observed by Tamburri et al. [65].

CR-AFM has been performed detecting the first (f_1) and the third (f_3) contact resonance frequencies (CRFs) using as reference material (i.e. material with known mechanical properties) a polymer blend composed of a polystyrene matrix where round-shaped inclusion on polyethylene have been inserted (PS-LDPE). CRFs have been analyzed with the

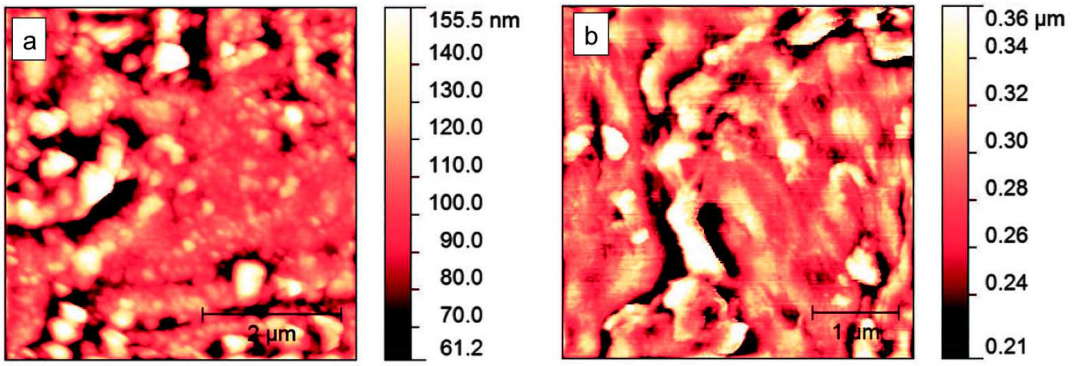

Figure 4.16: Topographical image of PANI (a) and PANI-ND (b).

model depicted in Fig. 4.10, as described in Sec. 4.2.2. Using this model, curves of CRFs versus the normalized contact stiffness k^*/k_c are obtained. From these curves (reported in Fig. 4.12), values of the k^* corresponding to f_1 and f_3, have been extracted and, consequently, M_s calculated using Eq. (4.14) has been calculated. It has been found: $\mathrm{M}_{PANI} = (1.2 \pm 0.1)$ GPa and $\mathrm{M}_{PANI-ND} = (3.1 \pm 0.5)$ GPa.

Then, to validate the results retrieved with CR-AFM, indentation modulus maps of the investigated samples have been obtained performing HarmoniX$^{\mathrm{TM}}$ experiments. The elastic maps have been calibrated on the PS-LDPE reference sample. In particular, the indentation modulus of the PS matrix has been used for the calibration of the technique while the LDPE has been used as a control material. For each sample, the statistics have been calculated on the collected indentation modulus maps to assign the values of the indentation moduli and the corresponding uncertainties. As an example of the typical results of a HarmoniX$^{\mathrm{TM}}$ measurement session, the histograms of the indentation moduli of the investigated and reference samples are reported in Fig. 4.17. It has been obtained:

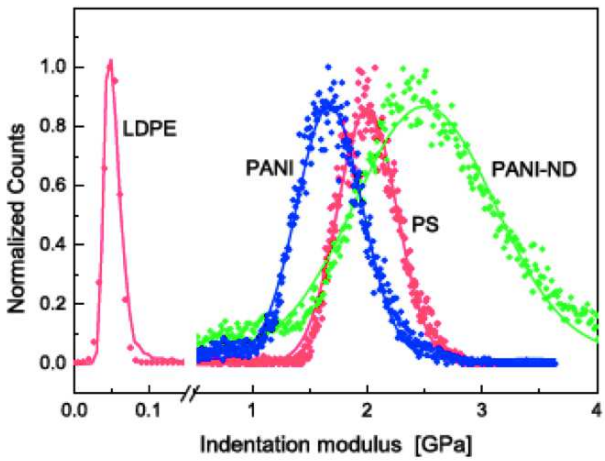

Figure 4.17: Histograms (points) together with the corresponding Gaussian fits (solid lines) of the indentation moduli measured on: the PS-LDPE (red), PANI-ND (green) and PANI (blue) samples.

M_{PANI} = (1.4 ± 0.2) GPa and $M_{PANI-ND}$ = (2.3 ± 0.5) GPa.

This confirms that the results obtained by HarmoniX^{TM} and CR-AFM are in fairly good agreement, which represents a cross-validation of the techniques. Moreover, the surface indentation moduli retrieved with the two AFM-based techniques have been compared with the bulk ones measured by DSI. It has been observed that surface indentation moduli measured with the AFM-based methods are significantly lower than the bulk ones, which can be attributed to the presence of nanometrical surface layers of polymer softer than the bulk.

Overall, the results confirm the importance of methods, such the AFM-based ones, for the mechanical testing at the nanoscale, which are capable of investigating ultrathin films and layers out of the range of standard mechanical tests.

4.3.3 Mechanical characterization of soft samples at variable temperature: AFM nanoindentation and CR-AFM of low density polyethylene (LDPE)

It has been demonstrated that both the quasi-static AFM nanoindentation and the dynamic CR-AFM can be employed for the mechanical characterization of soft materials at variable temperature. A cross-validation of these two techniques has been performed by comparing the results obtained on a low density polyethylene (LDPE) reference material. These results are included in [66] and here shortly presented (for details see Appendix C). The sample has been mounted on a heating stage (SU003, NT-MDT, Russia) and AFM nanoindentation have been carried-out, as described in Sec. 4.2.1, recording force indentation curves. Fig. 4.18a shows examples of deflection curves obtained on the LDPE heated at three different temperatures, i.e. 23 °C (ambient conditions), 50 °C, and 70 °C. The curves highlight that for the same value of Δz (i.e. the displacement of the piezoelectric scanners), the values of the deflection (d) decreases as the temperature increases. According to Eq. 4.7, this indicates a deeper penetration of the tip into the sample and, thus, an increase of the indentation at higher temperature. This result demonstrates the softening of the LDPE when the temperature increases. Moreover, referring to Fig. 4.18b, where the

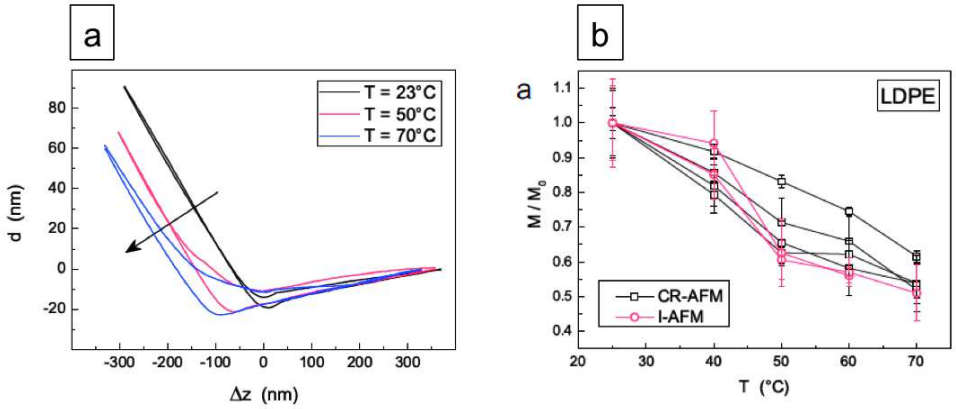

Figure 4.18: a) Deflection (d) versus displacement of the piezoelectric actuator (Δz) curves collected on LDPE at three different temperature values. b) Indentation modulus M normalized by the corresponding value at room temperature M_0 measured using I-AFM (red open circles) and CR-AFM (open black squares) on a LDPE sample.

LDPE indentation modulus values is normalized by the corresponding modulus at room temperature (M_0), it has been noticed that, in a range of temperatures comprises the LDPE glass transition temperature ($\approx -120°C$) and its melting temperature ($\approx 140°C$), as the temperature increase the LDPE indentation modulus roughly linearly decreases down to 50% of M_0, in agreement with results reported in literature [67]. Analogous effects, but less marked, have been observed on a polycarbonate (PC) reference sample, too. To validate these results, CR-AFM analysis has been performed measuring the first and second CRFs. The LDPE values of M/M_0, determined in three different CR-AFM experimental sessions, are shown in Fig. 4.18b (black open squares). The comparison between the data obtained with the two different techniques demonstrates the good agreement between the M/M_0 values retrieved by AFM nanoindentation and CR-AFM, highlighting the accuracy of the two techniques.

In conclusion, quasi-static AFM-nanoindentation and the dynamic CR-AFM techniques have been validated as methods to investigate the temperature dependence of mechanical properties of soft samples. The particular configuration of the experimental setup allows one to perform both AFM-nanoindentation and CR-AFM on the same samples. Thus, the technique to be used can be easily chosen on the basis of sample characteristics, like its thickness, as they probe different volume of the material under the tip, i.e., CR-AFM is more sensitive to the surface while nanoindentation can access to the bulk properties of the sample. Overall, the good agreement between indentation moduli (normalized by the corresponding values at room temperature) retrieved using the two techniques, as well as their compatibility with results obtained using standard macroscopic methods reported in literature, demonstrated their accuracy and validates AFM nanoindentation and CR-AFM for nanometer scale elastic modulus characterization of polymers at variable temperatures.

4.3.4 Viscoelastic characterization of soft samples: CR-AFM on PS-LDPE blends

In this section, some results presented in [49] (and reported in Appendix C) are shown. This study aimed to demonstrate the possibility to perform viscoleastic characterization of polymer blends and polymer-based nanocomposites using CR-AFM. Indeed, the mechanical response of viscoelastic materials is described by a complex modulus: its real part represents the storage modulus (E') and the imaginary part the loss modulus (E''). Thus, in the case of polymeric material, the tip-sample contact can be modeled using a more comprehensive model depicted in Fig. 4.19a, described in Sec. 4.2.2.

To asses the accuracy of the technique, a PS-LDPE reference sample has ben measured. By recording both the CRFs maps and the corresponding quality factors for two different oscillation modes, and elaborating them using the contact model depicted in Fig. 4.19a, the normalized contact stiffness (k^*/k_c) and the normalized damping (β) have been evaluated. Then, according to the Eq. 4.19, $\tan\delta$ has been calculated. Fig. 4.19b and Fig. 4.19c show the maps of the first and second CRFs (i.e. f_1 and f_2) while Q-factor maps of the same modes (i.e. Q_1 and Q_2) are reported in Fig. 4.19d and Fig. 4.19e. The f_1 and f_2 frequency images have been used to determine the parameter r (which describe the tip position). Then, maps of f_1, and Q_1 and the evaluated values of r have been combined to numerically solving the characteristic equation of the system in Fig. 4.19a [47] and the maps of k^*/k_c and β have been thus obtained. Finally using Eq. 4.19, these have been used to achieve the map of $\tan\delta$ relative to the first and second modes are reported in

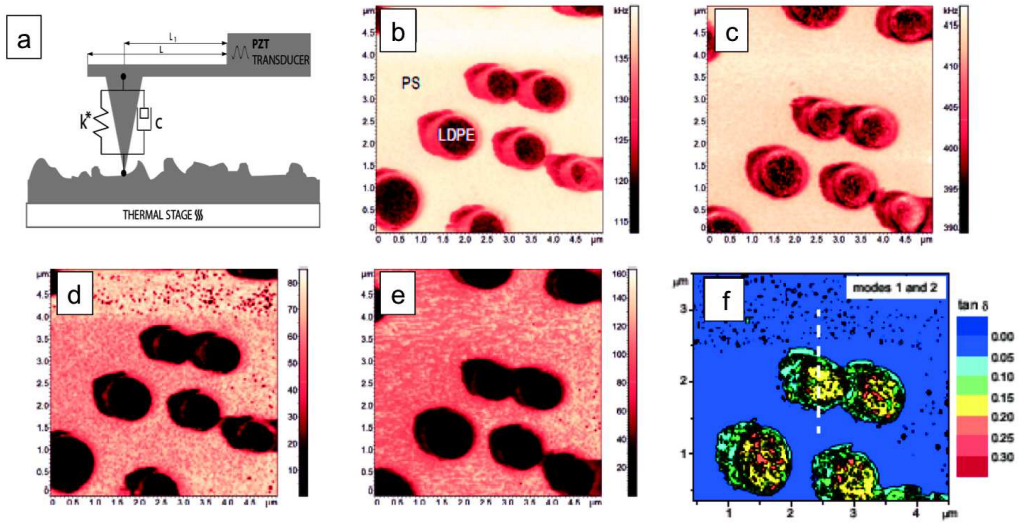

Figure 4.19: a) Sketch of the model used to analyze CR-AFM data; b-c) maps of the first and second contact resonance frequencies (f_1 and f_2, respectively); d-e) maps of the corresponding first and second quality factors (Q_1 and Q_2, respectively); f) maps of tanδ obtained from the analysis of first and second mode.

Fig. 4.19f. The measured values of $\tan\delta$ on LDPE and PS are 0.19 ± 0.01 and 0.025 ± 0.005, in good agreement with data reported in literature [68, 69].

4.3.5 Mechanical characterization of biological samples: CR-AFM as subsurface nanomechanical imaging

Detecting stiff nanoparticles buried in soft biological matrices by AFM-based techniques represents a new frontier in the field of scanning probe microscopies, originally developed as surface characterization methods. This study reports the detection of stiff (magnetic) nanoparticles (NPs) internalized in cells by using CR-AFM employed as a non-destructive subsurface characterization tool [70]. Agglomerates of NPs internalized in cells have been visualized on basis of the local increase in the contact stiffness with respect to the surrounding biological matrix. As expected, the values of CRFs measured on engulfed cells (Fig. 4.20b) are significantly higher than those measured on the empty ones (Fig. 4.20a). This corresponds to significantly larger values of normalized contact stiffness. This can be attributed to a significant presence of Fe_3O_4 NPs in labeled cells resulting in the increase of the effective elastic modulus of the cell. Moreover, in the case of empty cells (Fig. 4.20a), CRF values were constant within the cell and no areas corresponding to higher CRFs have been detected. Conversely, large areas with higher CRFs have been observed in the case of cells labeled with NPs (Fig. 4.20b). This suggests that Fe_3O_4 NPs agglomerate within the structure of the cell, produce some mechanical inhomogeneities detectable by CR-AFM nanomechanical imaging. Furthermore, by considering the contact between the tip and the sample affected by both a vertical (k^*) and a tangential spring (k^*_{lat}), we simulated the f_5 values, for a range of k^*/k_c between 1 and $2{\cdot}10^4$, by numerically solving the characteristic equation of the system [38]. The calculated values of k^*/k_c have be used to

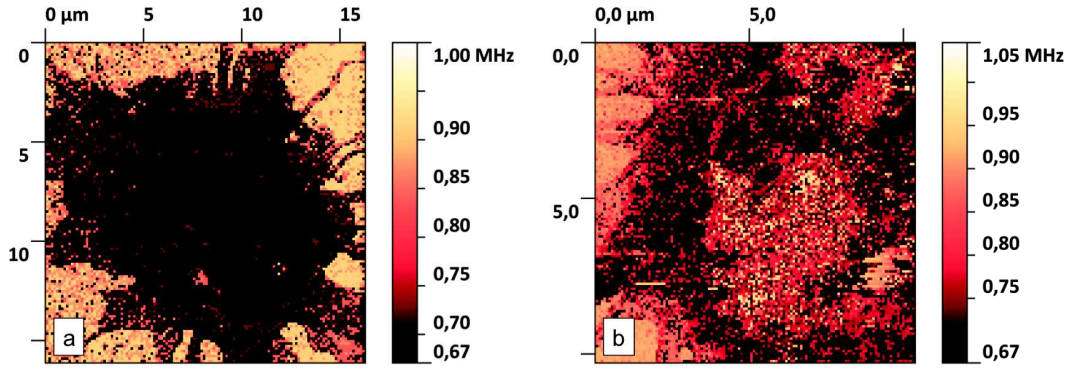

Figure 4.20: a) CRF map of an empty microglia cell; b) CRF map of a microglia engulfed with Fe_3O_4 NPs.

estimate the depth at which the agglomerates are located, adopting the well-established models derived to describe the effective mechanical properties of layered materials during nanoindentation [71].

Overall, Fe_3O_4 NPs agglomerates into microglia cells, located at $\approx$ 100 nm under the sample surfaces, have been detected. This demonstrates that CR-AFM can be used for the subsurface imaging of stiff nanomaterials buried into biological samples (see Appendix C). Although the resolution of the technique must be improved, CR-AFM is a promising tool for studying the fate of NPs into biological tissues.

Bibliography

[1] A. C. Fischer-Cripps, *Nanoindentation*. Springer-Verlag, 2004.

[2] C. Reynaud, F. Sommer, C. Quet, N. El Bounia, and T. M. Duc, "Quantitative determination of young's modulus on a biphase polymer system using atomic force microscopy," *Surface and Interface Analysis*, vol. 30, no. 1, pp. 185–189, 2000.

[3] Y. Xiang, X. Chen, T. Tsui, J. Jang, and J. Vlassak, "Mechanical properties of porous and fully dense low-κ dielectric thin films measured by means of nanoindentation and the plane-strain bulge test technique," *Journal of Materials Research*, vol. 21, no. 02, pp. 386–395, 2006.

[4] X. Chen, Y. Xiang, and J. J. Vlassak, "Novel technique for measuring the mechanical properties of porous materials by nanoindentation," *Journal of Materials Research*, vol. 21, no. 03, pp. 715–724, 2006.

[5] Z. Parlak and F. Levent Degertekin, "Contact stiffness of finite size subsurface defects for atomic force microscopy: Three-dimensional finite element modeling and experimental verification," *Journal of Applied Physics*, vol. 103, no. 11, p. 114910, 2008.

[6] G. S. Shekhawat, S. Avasthy, A. K. Srivastava, S.-H. Tark, and V. P. Dravid, "Probing buried defects in extreme ultraviolet multilayer blanks using ultrasound holography," *IEEE Transactions on Nanotechnology*, vol. 9, no. 6, pp. 671–674, 2010.

[7] B. Bhushan and V. N. Koinkar, "Nanoindentation hardness measurements using atomic force microscopy," *Applied Physics Letters*, vol. 64, no. 13, pp. 1653–1655, 1994.

[8] A. V. Kulkarni and B. Bhushan, "Nanoscale mechanical property measurements using modified atomic force microscopy," *Thin Solid Films*, vol. 290, pp. 206–210, 1996.

[9] K. Miyahara, N. Nagashima, T. Ohmura, and S. Matsuoka, "Evaluation of mechanical properties in nanometer scale using AFM-based nanoindentation tester," *Nanostructured Materials*, vol. 12, no. 5-8, pp. 1049–1052, 1999.

[10] S. S. Asif, K. Wahl, and R. Colton, "Nanoindentation and contact stiffness measurement using force modulation with a capacitive load-displacement transducer," *Review of Scientific Instruments*, vol. 70, no. 5, pp. 2408–2413, 1999.

[11] S. Syed Asif, K. Wahl, R. Colton, and O. Warren, "Quantitative imaging of nanoscale mechanical properties using hybrid nanoindentation and force modulation," *Journal of Applied Physics*, vol. 90, no. 3, pp. 1192–1200, 2001.

[12] D. Passeri, A. Bettucci, and M. Rossi, "Acoustics and atomic force microscopy for the mechanical characterization of thin films," *Analytical and Bioanalytical Chemistry*, vol. 396, no. 8, pp. 2769–2783, 2010.

[13] D. Passeri, M. Rossi, E. Tamburri, and M. L. Terranova, "Mechanical characterization of polymeric thin films by atomic force microscopy based techniques," *Analytical and Bioanalytical Chemistry*, vol. 405, no. 5, pp. 1463–1478, 2013.

[14] D. Sarid, *Scanning force microscopy: with applications to electric, magnetic, and atomic forces*, vol. 5. Oxford University Press on Demand, 1994.

[15] J. N. Israelachvili, *Intermolecular and surface forces*. Colloid Science, Academic Press, 2 ed., 1992.

[16] J. E. Lennard-Jones, "Wave functions of many-electron atoms," *Mathematical Proceedings of the Cambridge Philosophical Society*, vol. 27, pp. 469–480, 6 1931.

[17] B. Cappella and G. Dietler, "Force-distance curves by atomic force microscopy," *Surface Science Reports*, vol. 34, no. 1, pp. 1–104, 1999.

[18] P. Eaton and W. P., *Atomic Force Microscopy*. Oxford University Press USA, 2010.

[19] K. Khulbe, C. Feng, and T. Matsuura, *Synthetic Polymeric Membranes: Characterization by Atomic Force Microscopy*. Springer, 1 ed., 2008.

[20] Y. Martin, C. C. Williams, and H. K. Wickramasinghe, "Atomic force microscope–force mapping and profiling on a sub 100-[a-ring] scale," *Journal of Applied Physics*, vol. 61, no. 10, pp. 4723–4729, 1987.

[21] Q. Zhong, D. Inniss, K. Kjoller, and V. Elings, "Fractured polymer/silica fiber surface studied by tapping mode atomic force microscopy," *Surface Science*, vol. 290, no. 1–2, pp. L688 – L692, 1993.

[22] V. L. Mironov, "Fundamentals of scanning probe microscopy," *Moscow: Technosfera*, p. 144, 2004.

[23] J. Tamayo and R. Garcia, "Deformation, contact time, and phase contrast in tapping mode scanning force microscopy," *Langmuir*, vol. 12, no. 18, pp. 4430–4435, 1996.

[24] H.-J. Butt, B. Cappella, and M. Kappl, "Force measurements with the atomic force microscope: Technique, interpretation and applications," *Surface science reports*, vol. 59, no. 1, pp. 1–152, 2005.

[25] A. L. Weisenhorn, M. Khorsandi, S. Kasas, V. Gotzos, and H. J. Butt, "Deformation and height anomaly of soft surfaces studied with an AFM," *Nanotechnology*, vol. 4, no. 2, p. 106, 1993.

[26] J. Domke and M. Radmacher, "Measuring the elastic properties of thin polymer films with the atomic force microscope," *Langmuir*, vol. 14, no. 12, pp. 3320–3325, 1998.

[27] I. N. Sneddon, "The relation between load and penetration in the axisymmetric boussinesq problem for a punch of arbitrary profile," *International Journal of Engineering science*, vol. 3, no. 1, pp. 47–57, 1965.

[28] G. Pharr, W. Oliver, and F. Brotzen, "On the generality of the relationship among contact stiffness, contact area, and elastic modulus during indentation," *Journal of Materials Research*, vol. 7, no. 03, pp. 613–617, 1992.

[29] W. C. Oliver and G. M. Pharr, "Measurement of hardness and elastic modulus by instrumented indentation: Advances in understanding and refinements to methodology," *Journal of Materials Research*, vol. 19, no. 01, pp. 3–20, 2004.

[30] C. A. Clifford and M. P. Seah, "Quantification issues in the identification of nanoscale regions of homopolymers using modulus measurement via afm nanoindentation," *Applied Surface Science*, vol. 252, no. 5, pp. 1915–1933, 2005.

[31] D. Passeri, A. Bettucci, A. Biagioni, M. Rossi, A. Alippi, E. Tamburri, M. Lucci, I. Davoli, and S. Berezina, "Indentation modulus and hardness of viscoelastic thin films by atomic force microscopy: A case study," *Ultramicroscopy*, vol. 109, no. 12, pp. 1417–1427, 2009.

[32] U. Rabe and W. Arnold, "Acoustic microscopy by atomic force microscopy," *Applied Physics Letters*, vol. 64, no. 12, pp. 1493–1495, 1994.

[33] U. Rabe, K. Janser, and W. Arnold, "Vibrations of free and surface-coupled atomic force microscope cantilevers: theory and experiment," *Review of Scientific Instruments*, vol. 67, no. 9, pp. 3281–3293, 1996.

[34] U. Rabe, V. Scherer, S. Hirsekorn, and W. Arnold, "Nanomechanical surface characterization by atomic force acoustic microscopy," *Journal of Vacuum Science & Technology B: Microelectronics and Nanometer Structures Processing, Measurement, and Phenomena*, vol. 15, no. 4, pp. 1506–1511, 1997.

[35] D. Hurley, M. Kopycinska-Müller, A. Kos, and R. Geiss, "Nanoscale elastic-property measurements and mapping using atomic force acoustic microscopy methods," *Measurement Science and Technology*, vol. 16, no. 11, p. 2167, 2005.

[36] D. Passeri, A. Bettucci, M. Germano, M. Rossi, A. Alippi, A. Fiori, E. Tamburri, S. Orlanducci, M. Terranova, and J. Vlassak, "Local indentation modulus characterization via two contact resonance frequencies atomic force acoustic microscopy," *Microelectronic Engineering*, vol. 84, no. 3, pp. 490–494, 2007.

[37] F. Marinello, D. Passeri, and E. Savio, *Acoustic scanning probe microscopy*. Springer Science & Business Media, 2012.

[38] M. Reggente, M. Rossi, L. Angeloni, E. Tamburri, M. Lucci, I. Davoli, M. L. Terranova, and D. Passeri, "Atomic force microscopy techniques for nanomechanical characterization: A polymeric case study," *JOM*, vol. 67, no. 4, pp. 849–857, 2015.

[39] E. Kester, U. Rabe, L. Presmanes, P. Tailhades, and W. Arnold, "Measurement of young's modulus of nanocrystalline ferrites with spinel structures by atomic force acoustic microscopy," *Journal of Physics and Chemistry of Solids*, vol. 61, no. 8, pp. 1275–1284, 2000.

[40] U. Rabe, "Atomic force acoustic microscopy," in *Applied Scanning Probe Methods II*, pp. 37–90, Springer, 2006.

[41] K. L. Johnson and K. L. Johnson, *Contact mechanics*. Cambridge university press, 1987.

[42] G. Stan and W. Price, "Quantitative measurements of indentation moduli by atomic force acoustic microscopy using a dual reference method," *Review of Scientific Instruments*, vol. 77, no. 10, p. 103707, 2006.

[43] D. Passeri, M. Rossi, and J. Vlassak, "On the tip calibration for accurate modulus measurement by contact resonance atomic force microscopy," *Ultramicroscopy*, vol. 128, pp. 32–41, 2013.

[44] D. Passeri, A. Bettucci, M. Germano, M. Rossi, A. Alippi, S. Orlanducci, M. Terranova, and M. Ciavarella, "Effect of tip geometry on local indentation modulus measurement via atomic force acoustic microscopy technique," *Review of Scientific Instruments*, vol. 76, no. 9, p. 093904, 2005.

[45] S. Jena, R. Tokas, N. Kamble, S. Thakur, D. Bhattacharyya, and N. Sahoo, "Investigation of elastic and optical properties of electron beam evaporated ZrO_2−MgO composite thin films," *Thin Solid Films*, vol. 537, pp. 163–170, 2013.

[46] D. Hurley and J. A. Turner, "Measurement of poisson's ratio with contact-resonance atomic force microscopy," *Journal of Applied Physics*, vol. 102, no. 3, p. 033509, 2007.

[47] P. Yuya, D. Hurley, and J. A. Turner, "Contact-resonance atomic force microscopy for viscoelasticity," *Journal of Applied Physics*, vol. 104, no. 7, p. 074916, 2008.

[48] P. Yuya, D. Hurley, and J. A. Turner, "Relationship between q-factor and sample damping for contact resonance atomic force microscope measurement of viscoelastic properties," *Journal of Applied Physics*, vol. 109, no. 11, p. 113528, 2011.

[49] M. Natali, D. Passeri, M. Reggente, E. Tamburri, M. L. Terranova, M. Rossi, M. Rossi, L. Dini, D. Passeri, M. L. Terranova, *et al.*, "Contact resonance atomic force microscopy for viscoelastic characterization of polymer-based nanocomposites at variable temperature," in *AIP Conference Proceedings*, pp. 020008–1 – 020008–8, AIP Publishing, 2016.

[50] D. C. Hurley, S. E. Campbell, J. P. Killgore, L. M. Cox, and Y. Ding, "Measurement of viscoelastic loss tangent with contact resonance modes of atomic force microscopy," *Macromolecules*, vol. 46, no. 23, pp. 9396–9402, 2013.

[51] A. B. Churnside, R. C. Tung, and J. P. Killgore, "Quantitative contact resonance force microscopy for viscoelastic measurement of soft materials at the solid–liquid interface," *Langmuir*, vol. 31, no. 40, pp. 11143–11149, 2015.

[52] O. Sahin, S. Magonov, C. Su, C. F. Quate, and O. Solgaard, "An atomic force microscope tip designed to measure time-varying nanomechanical forces," *Nature Nanotechnology*, vol. 2, no. 8, pp. 507–514, 2007.

[53] O. Sahin and N. Erina, "High-resolution and large dynamic range nanomechanical mapping in tapping-mode atomic force microscopy," *Nanotechnology*, vol. 19, no. 44, p. 445717, 2008.

[54] B. V. Derjaguin, V. M. Muller, and Y. P. Toporov, "Effect of contact deformations on the adhesion of particles," *Journal of Colloid and Interface Science*, vol. 53, no. 2, pp. 314–326, 1975.

[55] M. E. Dokukin and I. Sokolov, "Quantitative mapping of the elastic modulus of soft materials with HarmoniX and PeakForce QNM AFM modes," *Langmuir*, vol. 28, no. 46, pp. 16060–16071, 2012.

[56] P. Schön, S. Dutta, M. Shirazi, J. Noordermeer, and G. J. Vancso, "Quantitative mapping of surface elastic moduli in silica-reinforced rubbers and rubber blends across the length scales by afm," *Journal of Materials Science*, vol. 46, no. 10, pp. 3507–3516, 2011.

[57] D. Passeri, A. Biagioni, M. Rossi, E. Tamburri, and M. Terranova, "Characterization of polyaniline–detonation nanodiamond nanocomposite fibers by atomic force microscopy based techniques," *European Polymer Journal*, vol. 49, no. 5, pp. 991–998, 2013.

[58] P. Ihalainen, J. Järnström, A. Määttänen, and J. Peltonen, "Nano-scale mapping of mechanical and chemical surface properties of pigment coated surfaces by torsional harmonic atomic force microscopy," *Colloids and Surfaces A: Physicochemical and Engineering Aspects*, vol. 373, no. 1, pp. 138–144, 2011.

[59] K. Sweers, K. Van Der Werf, M. Bennink, and V. Subramaniam, "Nanomechanical properties of α-synuclein amyloid fibrils: a comparative study by nanoindentation, harmonic force microscopy, and peakforce QNM," *Nanoscale Research Letters*, vol. 6, no. 1, p. 270, 2011.

[60] K. M. Leung, G. Wanger, Q. Guo, Y. Gorby, G. Southam, W. M. Lau, and J. Yang, "Bacterial nanowires: conductive as silicon, soft as polymer," *Soft Matter*, vol. 7, no. 14, pp. 6617–6621, 2011.

[61] J. Adamcik, A. Berquand, and R. Mezzenga, "Single-step direct measurement of amyloid fibrils stiffness by peak force quantitative nanomechanical atomic force microscopy," *Applied Physics Letters*, vol. 98, no. 19, p. 193701, 2011.

[62] G. Pletikapić, A. Berquand, T. M. Radić, and V. Svetličić, "Quantitative nanomechanical mapping of marine diatom in seawater using peak force tapping atomic force microscopy1," *Journal of Phycology*, vol. 48, no. 1, pp. 174–185, 2012.

[63] T. Young, M. Monclus, T. Burnett, W. Broughton, S. Ogin, and P. Smith, "The use of the PeakForceTM quantitative nanomechanical mapping afm-based method for high-resolution young's modulus measurement of polymers," *Measurement Science and Technology*, vol. 22, no. 12, p. 125703, 2011.

[64] D. Passeri, M. Reggente, M. Rossi, S. N. Cesaro, V. Guglielmotti, J. J. Vlassak, A. M. De Francesco, R. Scarpelli, M. Hatipoğlu, and D. Ajò, "Contact resonance atomic force microscopy (CR-AFM) in applied mineralogy: the case of natural and thermally treated diaspore," *European Journal of Mineralogy*, vol. 28, no. 2, pp. 273–283, 2016.

[65] E. Tamburri, V. Guglielmotti, S. Orlanducci, M. L. Terranova, D. Sordi, D. Passeri, R. Matassa, and M. Rossi, "Nanodiamond-mediated crystallization in fibers of PANI nanocomposites produced by template-free polymerization: Conductive and thermal properties of the fibrillar networks," *Polymer*, vol. 53, no. 19, pp. 4045–4053, 2012.

[66] M. Natali, M. Reggente, D. Passeri, M. Rossi, M. Rossi, L. Dini, D. Passeri, M. L. Terranova, and M. V. Antisari, "Elastic modulus measurements at variable temperature: Validation of atomic force microscopy techniques," in *AIP Conference Proceedings*, pp. 020007–1 – 020007–7, AIP Publishing, 2016.

[67] A. G. Pedroso and D. d. S. Rosa, "Mechanical, thermal and morphological characterization of recycled LDPE/corn starch blends," *Carbohydrate Polymers*, vol. 59, no. 1, pp. 1–9, 2005.

[68] M. C. G. Rocha, M. E. Leyva, and M. G. d. Oliveira, "Thermoplastic elastomers blends based on linear low density polyethylene, ethylene-1-octene copolymers and ground rubber tire," *Polímeros*, vol. 24, no. 1, pp. 23–29, 2014.

[69] A. Shojaei and G. Li, "Thermomechanical constitutive modelling of shape memory polymer including continuum functional and mechanical damage effects," in *Proceedings of The Royal Society A*, p. 20140199, The Royal Society, 2014.

[70] M. Reggente, D. Passeri, L. Angeloni, F. A. Scaramuzzo, M. Barteri, F. De Angelis, I. Persiconi, M. E. De Stefano, and M. Rossi, "Detection of stiff nanoparticles within cellular structures by contact resonance atomic force microscopy subsurface nanomechanical imaging," *Nanoscale*, pp. –, 2017.

[71] R. King, "Elastic analysis of some punch problems for a layered medium," *International Journal of Solids and Structures*, vol. 23, no. 12, pp. 1657–1664, 1987.

Chapter 5

Multiscale mechanical characterization of layered PMMA-coated Ti surfaces

In the previous Chapter (see Chap. 3) the strategy employed to synthesize PMMA-coated Ti interfaces has been described. Here their mechanical characterization (using the methodologies detailed in Chap. 4) will be reported. Besides the interest in the mechanical study of this particular class of materials, the need for a multiscale characterization is also discussed. Ideed, these polymer layers can be affected by altered surface mechanical properties compared to the bulk ones, because of the higher surface mobility of the polymer chains at the interface [1]. Thus, knowing the surface mechanical properties of the grafted polymers is of primary importance to control the adhesive bond which strongly relies on the physical properties (such as viscoelasticity and wettability) of the brush layer [2, 3]. However, the mechanical characterization of these layered materials using standard techniques is not trivial as they are made of soft polymers grown on hard substrates. They may have nonhomogeneous thickness and can exhibit porosity within the polymer layer thickness and/or at the polymer/metal interface. Indeed, several responses can be obtained performing different mechanical tests due to the material structure, which can be considered homogeneous or not, depending on the investigation length scale. In general, the properties of multilayered materials may dramatically differ when macro-, meso-, micro-, or nanoscopic volumes of material are analyzed. Therefore, for this class of materials, a multiscale mechanical characterization (from the macro- or mesoscale to the micro- or nanoscale), which provides complementary results [4, 5], is generally required. Thanks to its capability of positioning within a nanometer resolution on the sample surface, AFM has been used as a versatile platform to develop advanced mechanical characterization methods. Indeed, either quasi-static [6–8] or dynamic [9, 10] AFM-based techniques have been developed taking advantage of: (*i*) the positioning capability, (*ii*) the nanometer lateral resolution, (*iii*) the possibility of probing the sample with ultralow loads, and (*iv*) the capability of using a feedback system to map the sample surface with a controlled applied force. These characteristics make AFM-based methods advantageous over standard methods, in particular to study soft thin films on hard substrates [11, 12].

In this Chapter, the characterization of PMMA-coated Ti substrates using standard nanoindentation as well as different AFM-based techniques will be presented. In particular, AFM-based nanoindentation, contact resonance AFM (CR-AFM), HarmoniX^{TM}, and PeakForce quantitative nanomechanical mapping (PF-QNM^{TM}), which are characterized by different penetration depths and tip-sample contact radii, have been employed (see

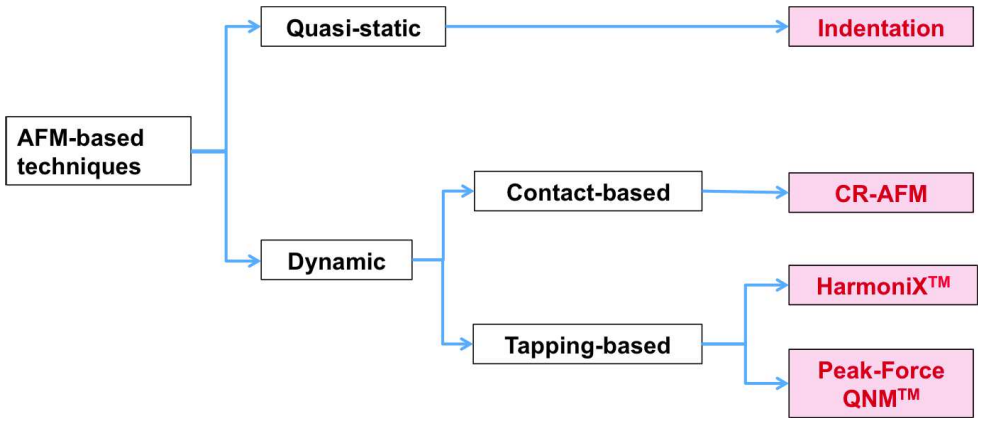

Figure 5.1: Sketch of the AFM-based techniques used to mechanical characterized the PMMA-coated Ti surfaces.

Fig. 5.1). In Sec. 5.3 a comparison of the results obtained with these different techniques will be provided. In each of the mechanical characterizations reported in this work, the PMMA-coated Ti substrates have been probed using a different tips (Berkovich indenters or AFM tips). The response of the material during mechanical tests depends on the volume of probed material, i.e. the portion of material affected by the stress field induced by the tip, which in turns depends on the tip-sample contact radius a_c [13, 14]. Thus, in order to compare results of mechanical tests on layered materials obtained with different indenters, the measured indentation modulus should be plotted versus the corresponding value of $a_t extrmc$ normalized by the film thickness [15, 16]. Since, in the present case, the PMMA thickness is difficult to be accurately determined (see the cross-section in Fig. 5.2), the indentation modulus values resulting from the different mechanical characterizations have been analyzed by plotting them versus the (not normalized) a_c.

Before making the mechanical characterization, the PMMA-coated Ti sample morphology have been deeply investigated. SEM micrograph in Fig. 5.2a confirms that the Ti surface is completely covered by a PMMA layer characterized by a non-uniform thickness. The PMMA surface shows the presence of rough spherical agglomerates of polymer. Moreover, the cross-section of the PMMA-coated Ti interface (Fig. 5.2b) reveals a complex porous structure with voids at the polymer-substrate interface. The thickness of the PMMA layer ranges from about 100 nm to 1 μm. As explained in Sec. 3.1, this complex structure is assigned to the particular Ti activation which leads to a microporous oxide layer from which the polymer is grown.

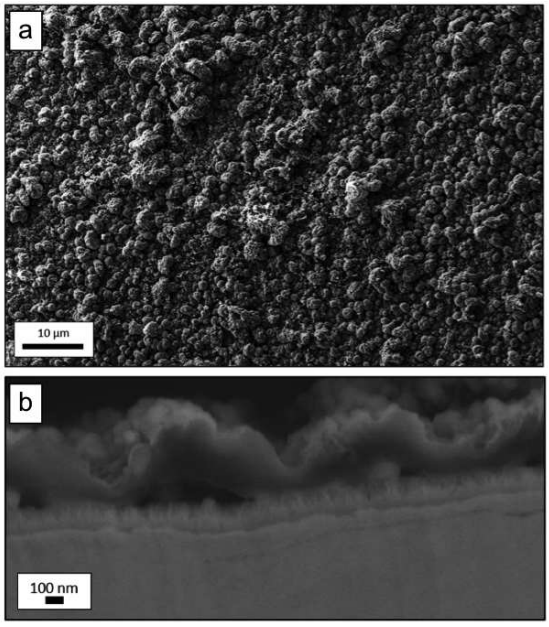

Figure 5.2: a) SEM micrograph of the PMMA-coated Ti sample's morphology. b) Cross-section of the PMMA-coated Ti interfaces highliting the porous structure underneath the polymer layer.

5.1 Standard methods: depth sensing nanoindentation

First, the indentation modulus of the PMMA-coated TI surface has been determined using DSI. Force-distance curves have been retrieved applying different values of maximum load

(0.2 mN, 0.4 mN, 0.6 mN, 1 mN, 3 mN, and 5 mN). Thus, also different values of penetration depth have been reached, from 70 nm to 850 nm. The obtained values of the sample indentation modulus (M_{DSI}) have been calculated for each applied load, using the data taken from the slope of the tangent to the unloading curve. The M_{DSI} values so obtained have been compared with the indentation moduli achieved with different AFM-based techniques, each of them characterized by different tip-sample contact radii. In Fig. 5.3 the (M_{DSI}) values are shown with green points. The results obtained with the AFM-based techniques are also shown and discussed in the following sections. As previously explained, for a fair comparison the evaluated indentation moduli of the PMMA-coated TI surface are plotted as a function the tip-sample contact radius (a_{c}). At smaller contact radius, i.e. up to 4 μm, the measured average value of indentation modulus is $M_{\mathrm{DSI}} = (2.2 \pm 0.2)$ GPa. At larger values of a_{c}, either the same values of indentation modulus or significantly larger ones are obtained depending on the actual point on the surface. The bigger values of indentation modulus can be rationalized invoking a more severe effect of the Ti substrate on DSI measurements. Therefore, the presence of dramatic variation of M in correspondence of $a_{\mathrm{c}} > 4$ μm suggests that the polymer layer thickness is not uniform. Conversely, the value $M_{\mathrm{DSI}} = (2.2 \pm 0.2)$ GPa obtained for $a_{\mathrm{c}} < 4$ μm is significantly lower than that measured on the commercial bulk PMMA sheet ($M_{\mathrm{DSI}} = (4.1 \pm 0.4)$ GPa). In principle, this is not surprising as it is well known that mechanical properties of polymers may significantly vary depending on the actual synthesis procedure as well as on the shaping of the polymer. Nevertheless, we think that the actual reduction of indentation modulus is ascribable to the voids at the polymer-substrate interface. Indeed, a reduction of the indentation modulus values caused by voids has been already measured with DSI [17, 18] as well as with AFM-based techniques such as CR-AFM [19] or scanning near-field ultrasound holography [20]. Also, AFM-based methods, such as CR-AFM, have been demonstrated to be sensitive to delaminations and lack of adhesion at buried film-substrate interfaces [21, 22]. Thus, the

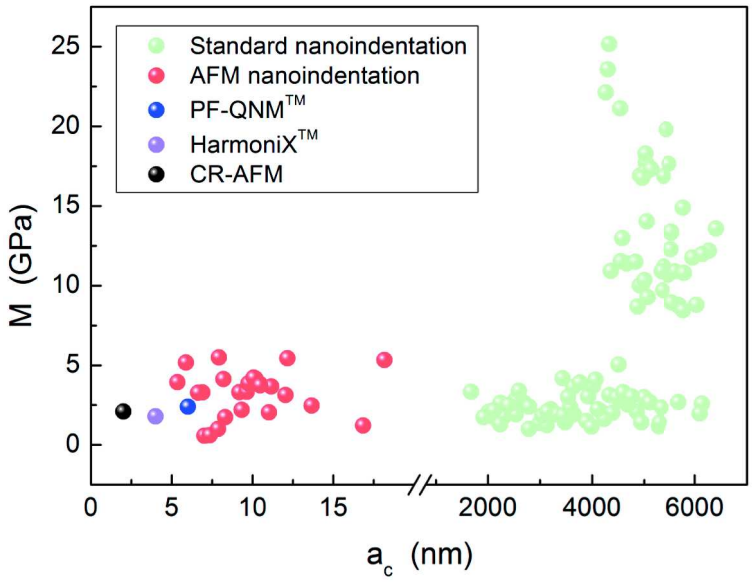

Figure 5.3: Measured values of indentation modulus (M) of the PMMA-coated Ti sample measured using standard nanoindentation (green), AFM nanoindentation (red), CR-AFM (black), PF-QNM™ (blue), and HarmoniX™ (pink) as a function of the tip-sample contact radius (a_{c}).

value of indentation modulus retrieved using DSI describes the mechanical response of the 'porous film' for $a_c < 4$ μm and of the system constituted by the 'porous film' plus the stiff substrate for $a_c > 4$ μm.

5.2 AFM-based methods

AFM-based experiments have been then performed in order to obtain results from shallower indentation tests, i.e. with values of a_c in the range of $5 - 20$ nm. In the following sections the elastic modulus of the PMMA-coated Ti samples evaluated employing quasi-static AFM nanoindentation and three different dynamic AFM-based techniques (namely, CR-AFM, PF-QNM^{TM}, and HarmoniX^{TM}) are shown and discussed. Accurate mechanical measurements of the PMMA-coated Ti sample were carried out using different reference materials to calibrate the AFM-based methods: a polystyrene-low density polyethylene blend (PS-LDPE, Bruker) and a commercial 0.5 mm thick PMMA sheet (Goodfellow). The former, consisting of a PS matrix in which round-shaped regions of LDPE are dispersed, in form of a film on a Si substrate, has been used as the calibration reference for CR-AFM, HarmoniX^{TM} and PF-QNM^{TM} experiments. The indentation modulus of the PS-LDPE reference sample has been characterized using dynamic nanoindentation. A Hysitron TI-950 has been used to perform the nanoindentation experiments with a Berkovich indenter probe. The tip area function has been calibrated on a fused quartz standard sample prior to the experiment. The depth profiles of hardness and reduced modulus have been determined using a CMX load function (where, CMX refers to the continuous measurement of the "X" property; X = hardness, modulus, etc.) in which a quasistatic force is superimposed with an oscillating force. The harmonic frequency used was 110 Hz and the displacement amplitude was around 1 nm. The PS matrix has been found to have an indentation modulus (M_{PS}) equal to 2.3 ± 0.1 GPa, while the indentation modulus of the LDPE regions (M_{LDPE}) is about 150 MPa. Instead, the PMMA sheet, has been used to calibrate the AFM nanonindentaton and CR-AFM measurements. Its indentation modulus (M_{PMMA}) has been determined by standard nanoindentation and found equal to (4.1 ± 0.4) GPa.

5.2.1 AFM nanoindentation

This section is referred to the data plotted as red points in Fig. 5.3 obtained by the AFM-nanoindentation techniques whose basic principle have been explained in Sec. 4.2.1. AFM nanoindentation measurements have been carried out by performing single point force measurements with a commercial AFM setup (Solver, NT-MDT, Russia) equipped with a stiff silicon tip (NSC16, MikroMasch). Both the commercial PMMA sheet and the synthesized PMMA-coated Ti samples have been characterized collecting several indentations curves (following the procedure described in Sec. 4.2.1).

First of all, to overcome the uncertainty connected to the tip shape in AFM nanoindentation measurements (see Eq. 4.8 in Chapter 4), the tip radius (R_{tip}) and the tip-sample contact area (A_c) has been calibrated recording deflection curves (namely, the evolution of the cantilever deflection, caused by tip-sample interaction force (F), versus the displacement (Δz) of the microscope piezoelectric scanner) on the commercial PMMA sheet.

Afterwards, several deflections curves, recorded increasing the indentation depth from 65 nm to 150 nm, have been collected on the PMMA-coated Ti interfaces and the corresponding values of the indentation modulus (M_{IND}) have been derived according to the

following procedure. Since the deflection of the cantilever is expressed in nA^{-1} by the instrument, an estimation of the instrument sensitivity (k_A) has been computed in order to express the deflection signal in nm. To this end, 6 force-distance curves on a hard silicon substrate have been performed. Then, from the slope of the unloading curve, which is properly the instrument sensitivity, a value of k_A equal to (0.0188 ± 0.0002) nA/nm, has been extrapolated. Furthermore, using the nominal value of the cantilever spring constant ($k_c = 30$ N/m), deflection curves have been then transformed into indentation curves using Eq. 4.7. From the indentation curves recorded on the PMMA sheet, an example of which is reported in Fig. 5.4, values of the maximum tip penetration depth, h_{max}, cantilever deflection, d_{max}, and contact stiffness k^* (i.e., slope of the retrying curve), were extracted and the penetration contact depth h_c derived according to Eq. 4.10. This allowed to estimate the value of the constant C related to the tip shape, which has been successively employed to quantitatively determined the PMMA-coated Ti indentation modulus from the corresponding indentation curves using Eq. 4.11. Moreover, the contact stiffness (k^*) and PMMA-coated Ti indentation modulus (M_{IND}) have been used to evaluate the corresponding tip-sample contact radius a_c, using the Sneddon's relation (Eq. 4.8) [23, 24] . In Fig. 5.3 values of the estimated M_{IND} as function of the contact radius a_c are depicted (red points).

As clearly visible, data obtained using AFM indentation are more scattered than those obtained by DSI (green points). This results in a bigger relative uncertainty in the mean value of indentation modulus retrieved with AFM nanoindentation, $M_{\mathrm{IND}} = (3.3 \pm 0.6)$ GPa. This was expectable as the smaller R_{t}, and thus the smaller a_{c}, enables one to perform indentations of the sample more local than those obtained with DSI. Indeed, referring to the topography reported in Fig. 5.2a, the values of a_{c} as high as some microns, typical of DSI measurements, imply that several agglomerates of polymer are probed during a single indentation. Thus, the sub-micron structures in Fig. 5.2b are not mechanically resolved. Therefore, the variations in the value of M measured with DSI, reflecting the

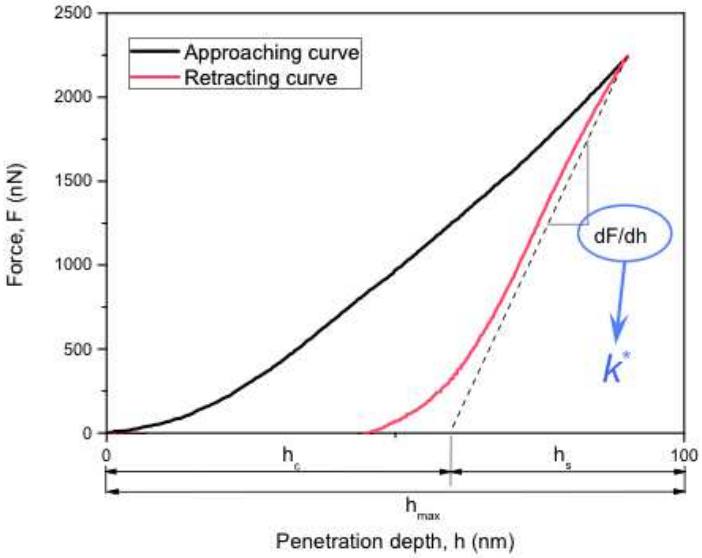

Figure 5.4: Indentation curve obtained on a PMMA commercial sheet. The black one is the approaching curve whereas the red one expresses the retracting.

effect of the substrate, are due to variations in the average value of the film thickness. On the contrary, the values of a_c in AFM nanoindentation enable us to resolve the local variations in film thickness observable in Fig. 5.2b. In other words, AFM nanoindentation could be affected (even if partially) by the effect of the substrate mechanical properties in correspondence of the valleys between two adjacent agglomerates where the thickness is smaller [25]. Conversely, it could probe the mechanical response of the PMMA film, unaffected by the presence of voids, in correspondence of the peaks of the agglomerates. In the latter case, the measured value of M is compatible, within the experimental uncertainty, with the indentation modulus of bulk PMMA measured with DSI.

5.2.2 Contact Resonance Atomic Force Microscopy

This section referred to the data plotted as black point in Fig. 5.3. CR-AFM experiments have been performed, following the procedure explained in Sec. 4.2.2 using an AFM setup (Solver, NT-MDT, Russia) equipped with a commercial Si cantilever (CSG10, NT-MDT, Russia) with nominal dimensions $L = 250$ μm (length), $w = 35$ μm (width), $t = 1$ μm (thickness) and nominal spring constant $k_c = 0.1$ N/m. The commercial PMMA sheet and the PS regions of the PS-LDPE sample have been used as reference materials for calibration purposes.

As explained in Chapter 4 (Sec. 4.2.2), the first step of the technique, consists in the measurement of the resonance frequencies of the cantilever vibrating in air (f_{0n}) in order to determine the characteristic parameters of the cantilever, c_c. In particular, in the present study, the first and second resonance frequencies (namely, f_{01} and f_{02}) have been measured. Thus, the characteristic c_c parameter of the cantilever, in this phase modeled as a clamped-free cantilever, has been determined using Eq. 5.1:

$$f_{0n} = \frac{(k_{0n}L)^2}{{c_c}^2} \tag{5.1}$$

where $k_{0n}L$ represents the n-th eigenvalues of a clamped-free cantilever and can be easily found in literature [26].

In Tab. 5.1, the first four measured flexural resonance frequencies are reported and compared with those calculated numerically solving the characteristic equation of a cantilever, described as a uniform rectangular beam; the difference between calculated and measured values of the frequencies is attributed to a deviation of the actual geometrical parameters of the cantilever from the nominal ones used in the calculation. Thus, as previously noted [27], their ratio remained constant for each oscillation mode.

Table 5.1: Calculated and measured values of the first four flexural resonance frequencies of the CSG10 (NT-MDT) cantilever used in CR-AFM experiments.

Frequency	Calculated [kHz]	Measured [kHz]
f_{01}	19	26.7 ± 0.2
f_{02}	120	173.5 ± 0.7
f_{03}	341	499.1 ± 0.7
f_{04}	664	995.2 ± 1.1

In the second step, the AFM tip has been brought in contact with the sample surface which is made oscillate by the piezoelectric transducer coupled with its back side. In this

way, the sample vibrations have been coupled to the AFM cantilever through the tip and detected. The tip-sample interactions change the boundary conditions of the system which, in this phase has been modeled as a spring-coupled cantilever, resulting in an increase of the contact resonance frequencies (CRFs, f_n) with respect to the corresponding natural frequencies of the cantilever oscillating in air (f_{0n}). CRFs are related to the sample contact stiffness by Eq. A.11. For each material, e.g. the PMMA-coated Ti investigated sample and the PS and PMMA references, the first and the second modes have been analyzed by mapping f_1 and f_2, in order to have enough probed points on the sample surfaces needed for statistics. Indeed, averaged values of f_1 and f_2 have been used to calculate k^*, of each sample.

At the beginning, f_1 and f_2 maps have been acquired on the PMMA sheet, which was expected to be the stiffer sample; then f_1 and f_2 of the PMMA-coated Ti specimens have been mapped and finally those of the PS reference material have been also recorded. In addition, PMMA sheet has been further measured after the PS to ensure the stability of the procedure and to verify the absence of drift due to the increase of the tip radius as the result of tip wear [28]. Different zones of the samples have been investigated and the entire experimental cycle has been repeated twice under the same conditions. As an example, Fig. 5.5 shows the f_1 maps recorded on the PMMA-coated Ti (Fig. 5.5a) and on the two references (Fig. 5.5b-c) and the corresponding statistics (Fig. 5.5d).

Values of f_1 of PMMA-coated Ti are lower than those of the two references, indicating that these latter are stiffer than the investigated sample. Moreover, the relative standard deviation of its Gaussian distribution is bigger than those of the reference samples. This is partially attributable to topography-induced artifacts caused by local inclination of the surface [29] and to the modulation of the contact area in presence of grains and agglomerates [30]. Besides, the more dispersed values of CRF can be related to the mechanical

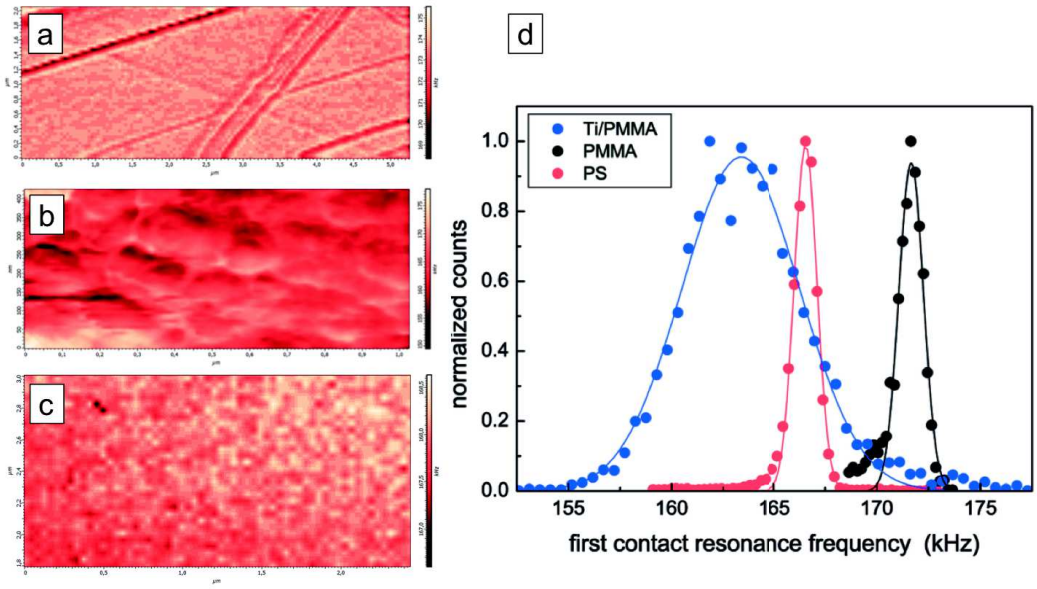

Figure 5.5: Maps of the first Contact Resonance Frequency measured on: a) commercial PMMA sheet; b) PMMA-coated Ti substrate; c) PS reference sample. d) Histograms (symbols) and corresponding Gaussian fit (solid lines) of the values of the first CRFs.

properties of the PMMA-coated Ti interface less homogeneous than those of the two reference materials due to the presence of subsurface voids at the substrate-polymer interface. Indeed, it has been demonstrated, that although CR-AFM is a 'surface' characterization technique, it is sensitive to buried mechanically nonhomogeneous features (like voids or stiff nanoparticles in polymer-based nanocomposites) typically located a few hundreds of nanometers below the surface [19, 31] (see Sec. 4.3.5 in Chap. 4).

Successively, the f_1 and f_2 maps recorded have been post-processed and their statistics used to determine k^* for all the samples. Finally, indentation modulus of the PMMA-coated Ti sample has been evaluated using the dual reference method proposed by Stan et al. [32] considering a flat tip-sample contact. A representative indentation modulus map of the PMMA-coated Ti and its corresponding AFM topography are shown in Fig. 5.6 in which the modulation of the indentation modulus on the PMMA-coated Ti surface is evident. From statistics on the indentation modulus maps, the indentation modulus retrieved with CR-AFM have been evaluated as $M_{\text{CR-AFM}}$= (2.1 ± 0.3) GPa (black point in Fig. 5.3) and the corresponding value of a_c is 2 nm, which has been calculated using the Sneddon approach (Eq. 4.8) [23, 24]. Although the value of $M_{\text{CR-AFM}}$ is compatible with that obtained with AFM nanoindentation, the contact radius suggests that CR-AFM is not sensitive to the presence of buried voids which, therefore, cannot be invoked to justify the value of $M_{\text{CR-AFM}}$ lower than that obtained with AFM indentation. The reduction of the modulus can be attributed to the effect of the very first layers of polymer, which have been reported to be softer with respect of the bulk [33–36].

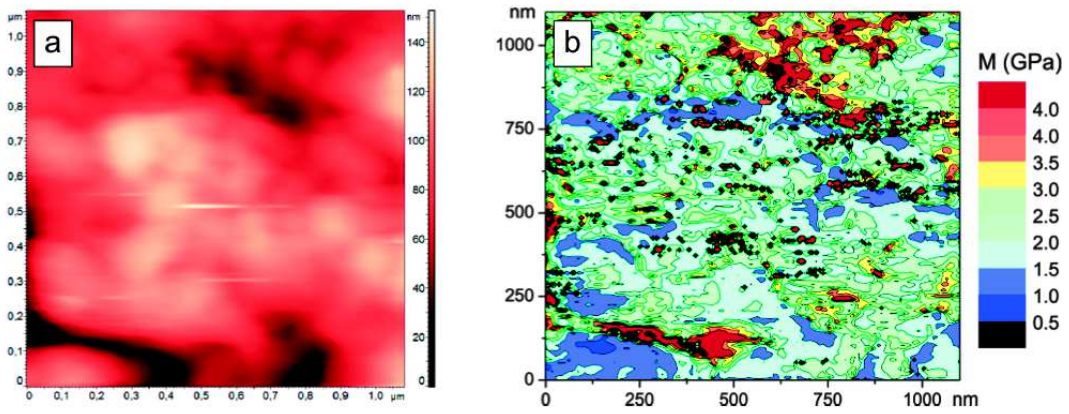

Figure 5.6: Example of CR-AFM nanomechanical characterization. a) Topography of the PMMA-coated Ti surface; b) Map of the indentation modulus map reconstructed from the first and the second CRFs images acquired on the surface of the PMMA-coated Ti sample.

5.2.3 Torsional-harmonic AFM

This section referred to the data plotted as pink point in Fig. 5.3, obtained by torsional-harmonic AFM (see Sec. 4.2.3). Shallower indentations have been attained using torsional-harmonic AFM, also known with its commercial name HarmoniX$^{\text{TM}}$, carried out with a Dimension Icon AFM system (Bruker) equipped with commercial Si T-shaped cantilevers (HMX10, Bruker). As explained in Chapter. 4 (Sec. 4.2.3), HarmoniX$^{\text{TM}}$ is a dynamic

technique based on tapping mode in which, because of the peculiar cantilever geometry, torsional vibration are coupled to the standard flexural ones and used to map the local mechanical properties of the surface sample. During the scanning, the tip periodically indents the surface and force curves (i.e. force versus piezo displacement curves) have been in real-time acquired and used to obtain maps of the sample indentation modulus (using the Derjaguin-Muller-Toporov model described by Eq. 4.20). An example of topography and corresponding indentation modulus map retrieved with this technique are shown in Fig. 5.7a and 5.7b, respectively. From the latter, the indentation modulus values of M_{HMX}= (1.8 ± 0.5) GPa is obtained (pink point in Fig. 5.3). Clearly distinguishable topography-induced mechanical artifacts are responsible for the apparent modulation of the indentation modulus measured on the PMMA-coated Ti sample. Statistics of the modulus maps (Fig. 5.7c) indicate that the Gaussian distribution of the PMMA-coated Ti sample is broader than that corresponding to the PS sample, used as reference material. We attribute this result to the sole effect of modulation of the tip-sample contact area. Indeed, although HarmoniX$^{\mathrm{TM}}$ has been reported to be sensitive to subsurface variation of elastic modulus in case of ultra-thin samples [37], in the present case even the thinnest areas of the PMMA layer are too big compared to the contact radius (calculated as $a_c = 4$ nm using the DMT model, Eq. 4.13) to allow one to detect buried voids or the substrate-film interface. Again, the reduction ascribable to the effect of the very first layers of polymer invoked discussing CR-AFM results can be considered, also in this case, to rationalize the value of M lower than the bulk one.

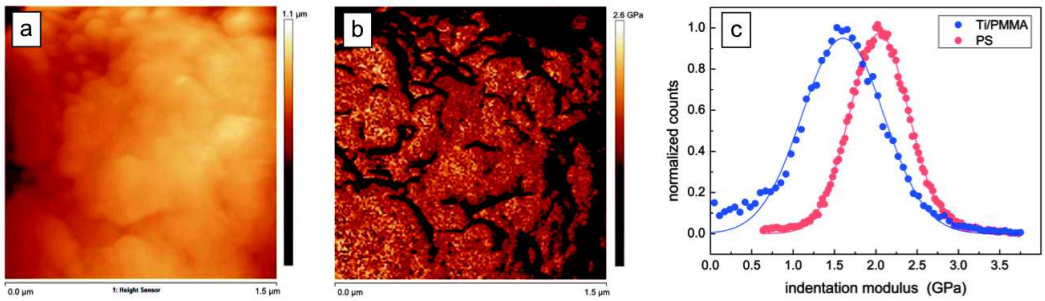

Figure 5.7: Example of HarmoniX$^{\mathrm{TM}}$ nanomechanical characterization. a) PMMA-coated Ti topography; b) Indentation modulus map of the PMMA-coated Ti surface; c) Histograms of the indentation modulus values (symbols) and corresponding Gaussian fit (solid lines) obtained on PMMA-coated Ti and PS.

5.2.4 Peak-force quantitative nanomechanical mapping

This section referred to the data plotted as blue point in Fig. 5.3 evaluated performing Peak-force quantitative nanomechanical mapping (PF-QNM) experiments, as detailed in Sec. 4.2.4 Peak-Force taping mode, is based on the detection of fast force curves at each pixel of the AFM image. The cantilever is made oscillate far away its resonant frequency and a map of the surface mechanical properties, with the same resolution of height images, is provided. Since the sample deformation depths are smaller than in the other techniques, the effect of the substrate on the measured modulus is decreased. In this study, PF-QNM$^{\mathrm{TM}}$ experiments have been carried out with a commercial AFM system (Dimension

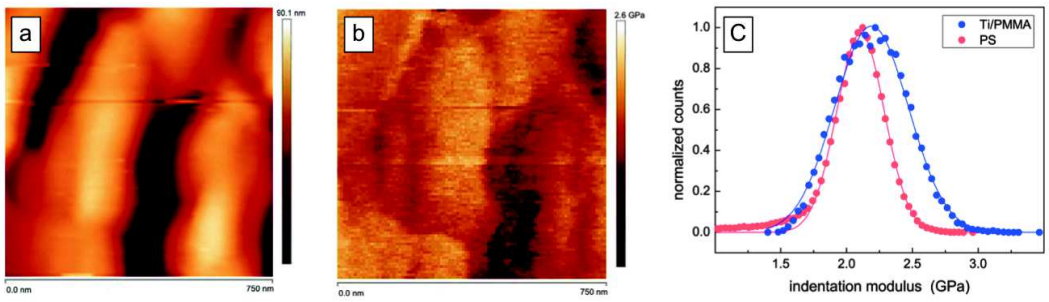

Figure 5.8: Example of PF-QNM^{TM} nanomechanical characterization. a) PMMA-coated Ti topography; b) Indentation modulus map of the PMMA-coated Ti surface; c) Histograms of the indentation modulus values (symbols) and corresponding Gaussian fit (solid lines) obtained on Ti/PMMA and PS.

Icon, Bruker) equipped with Si tips (RTESP, Bruker), using a F_{max} value of 80 nN. Calibration was performed using the PS-LDPE reference sample. PF-QNM^{TM} results confirm those obtained using CR-AFM and HarmoniX^{TM}. An example of topography and the corresponding indentation modulus map retrieved with this technique is shown in Fig. 5.8a and Fig. 5.8b, respectively. While, statistics of the measured indentation modulus are reported in Fig. 5.8c. The measured indentation modulus (2.4 ± 0.3) GPa (blue point in Fig. 5.3) is compatible with the values retrieved with CR-AFM and HarmoniX^{TM}. Further, the tip-sample contact radius has been estimated as small as 6 nm (using the DMT model, i.e. Eq. 4.13), which is similar to the value obtained with the other two techniques. Also in this case, the lower indentation modulus can be caused by the presence of a softer layer of polymer on the sample surface.

5.3 Comparison and further considerations

The results obtained with the different techniques are summarized in Tab. 5.2. Except for the measurements performed with standard DSI at larger penetration depths, i.e. larger contact radii, which are obviously affected by the substrate properties, the comparison of the results obtained using the different techniques clearly shows compatible results. The smaller contact radii of AFM techniques allowed us to perform local mechanical measurements which are, therefore, more sensitive to the local polymer thickness and homogeneity

Table 5.2: Average value of the indentation modulus of the PMMA-coated Ti sample $M_{Ti/PMMA}$ measured with the different techniques and the corresponding values of contact radius a_c.

Technique	$M_{Ti/PMMA}$ (GPa)	a_c (nm)
Standard nanoindentation	2.2 ± 0.2	$2000 - 4000$
AFM nanoindentation	3.3 ± 0.6	$5 - 20$
CR-AFM	2.1 ± 0.3	8
PF-QNM^{TM}	2.4 ± 0.3	7
HarmoniX^{TM}	1.8 ± 0.5	4

and more affected by topography-induced artifacts. In addition, due to the different tip-sample contact radii, the measured mechanical properties reflect the properties of different portions of surface volumes.

A schematic representation of the possible scenario is depicted in Fig. 5.9 (compare with Fig. 5.2 where the real sample cross-section is shown). Red areas represent the portion of the surface volume affecting the measurements. Standard nanoindentation probes the whole system formed by the PMMA matrix and the subsurface voids (points A and B in Fig. 5.9). Conversely, AFM nanoindentation data are more scattered as the technique locally probes the sample surface and the average indentation modulus reflects more the properties of the bulk PMMA matrix without being affected by the subsurface voids (point C in Fig. 5.9). Whereas, dynamic AFM methods like CR-AFM, PF-QNM^{TM}, and HarmoniX^{TM}, are more affected by the very superficial nanomechanical properties of the investigated sample (point D in Fig. 5.9) and, thus, are the most suitable to study the effect of surface treatments of polymers.
Finally, it is worth mentioning that AFM-based methods can be used to map other mechanical parameters besides indentation modulus which may be of interest for the applications of this polymer-metal layered materials. For example, PF-QNM^{TM} and HarmoniX^{TM} allow collecting maps of tip sample adhesion forces. Preliminary characterization of the adhesion using PF-QNM^{TM} with the same AFM tip seems to indicate that the tip-sample adhesion on the PMMA-coated Ti is about 140% of that on the commercial PMMA, which may indicate differences in the adhesion and/or in the hydrophobicity/hydrophilicity. Furthermore, the viscoelastic properties of the PMMA-coated Ti sample have been assessed using CR-AFM. For this purpose, the values of f_1 and f_2 and the corresponding quality factors Q_1 and Q_2 on both the PMMA-coated Ti and on the commercial bulk PMMA have been acquired in order to evaluate $\tan\delta$, as detailed in Sec 4.2.2 [38]. For the commercial bulk PMMA, it has been found $\tan\delta = 0.024$, which is in good agreement with results obtained in the same range of frequencies reported in literature [39]. Conversely, $\tan\delta = 0.043$ has been measured for the PMMA-coated Ti sample, indicating a material with a more viscoelastic response with respect to the commercial PMMA, which shows

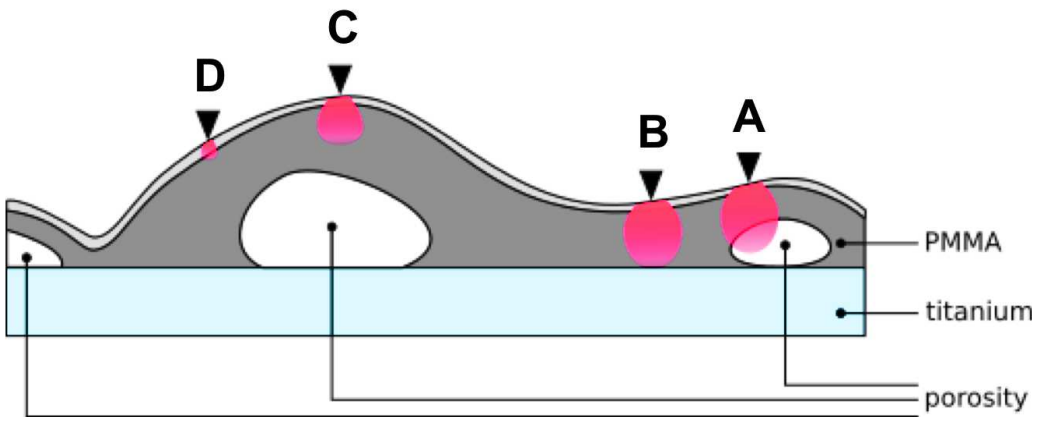

Figure 5.9: Schematic representation of the subsurface volume portion affecting the surface mechanical properties characterized by: A: DSI measurements; B: DSI and AFM indentation measurements; C: AFM indentation measurement; D: CR-AFM, HarmoniX^{TM} and PF-QNM^{TM} measurements.

a more elastic response. Although these results requires more detailed studies, adhesion mapping using PF-QNM^{TM} or HarmoniX^{TM} and viscoelastic mapping using CR-AFM may represent a useful tool for the characterization of nanoscale properties of polymer-metal layered materials to be related to mesoscopic and macroscopic properties.

Overall, the combined approach, resulting from the synergistic use of the different methods, allowed to investigate the sample mechanical properties varying the tip-sample contact radius from a few nanometers to ten microns. Depending on the contact radius, each technique enabled us to investigate specific aspects of the mechanical response of these materials, which represent complex systems formed by a 'porous' polymeric film on a stiff metal substrate.

5.3.1 Evaluation of the adhesion strength: preliminary results

This study has been completed investigating the adhesion properties between the Ti and the grafted PMMA layer. Indeed, as described in Chap. 1, coatings must exhibit sufficient adhesion to the underlying substrate to prevent delamination, that, especially in the case of implantable materials, could severely limit their effectiveness. It is therefore important to carefully determine the adhesion between the coating and the substrate which is not always easy to be achieved. Indeed, it has been shown that pull-off test, the most widespread method, can give distorted results for porous and thin coatings caused by bonding agents [40]. In this test, the coating that has to be tested is prepared on the surface of a cylinder and stuck, with a glue or an epoxy resin, to an uncoated cylinder. Thus, in case of porous coating, the glue can penetrate the coating and therefore affect the results [40].

An alternative and simpler method is the scratch testing which can give semi-quantitative results measuring the adhesion strength of several type of coatings [41]. In scratch testing measurements, a normal load to the surface is applied while the indenter is displaced through the sample surface. The critical load (p_c), defined as the load at which the coating fails (either for cohesive failures or delaminations) is generally used as a comparative test of the adhesion strength [42–44].

The coating failure mechanism may result from different phenomena, such as spalling, buckling, chipping, and conformal cracking [43, 45–47]. For this reason it is generally coupled with imaging techniques which, allowing the measurements of the width imprints (w_i), enable the determination of failure mechanism [41,46] and the detection of the critical load:

$$p_c = \frac{Fn}{\pi(w_i/2)^2} \tag{5.2}$$

In this study, the adhesion between the Ti substrate and the PMMA layer has been qualitatively evaluated performing scratch tests with a spherical indenter made of sapphire and a radius of 1000 μm. It has been scratched, 10 times, across the PMMA-coated Ti surface at a constant velocity. All the 10 scratches have been performed with a constant applied normal force (F_n), which has been increased at each scratch, varying from 0.6 N to 9 N. As shown by Bull et al. [43], the failure mode established between the brittle PMMA coating and the ductile Ti substrate is the buckling. This consists of crack formation at the coating-sample interfaces which spreads along the scratch direction resulting in the delimitation of the coating.

Referring to SEM micrographs of the scratches reported in Fig. 5.10, it can be noticed that for an applied force of 1.6 N (F_2 in Fig. 5.10), cohesive cracks (i.e. crack formed within the coating and not at coating-substrate interface) propagate through the coating. Conformal micro-cracks, generated in the direction of scratch in order to adapt to the fissure, have been observed at a force of 2.5 N (F_3 in Fig. 5.10). Whereas, a further increase of the force (F_4=3.5 N in Fig. 5.10), corresponding to a critical load of 270 MPa, results in larger cracks in which the coated is separated from the substrates. For higher applied forces (from 4.5 N to 8.3 N in Fig. 5.11) wider areas of polymer missing appears throughout the entire wear imprints. The final total delimitation has been observed for an applied load of ≈280 MPa. This preliminary study allowed confirming the good adhesion existing between the grown PMMA layer and the Ti substrate, ensured by the covalent immobilization of the polymeric chains on the substrate.

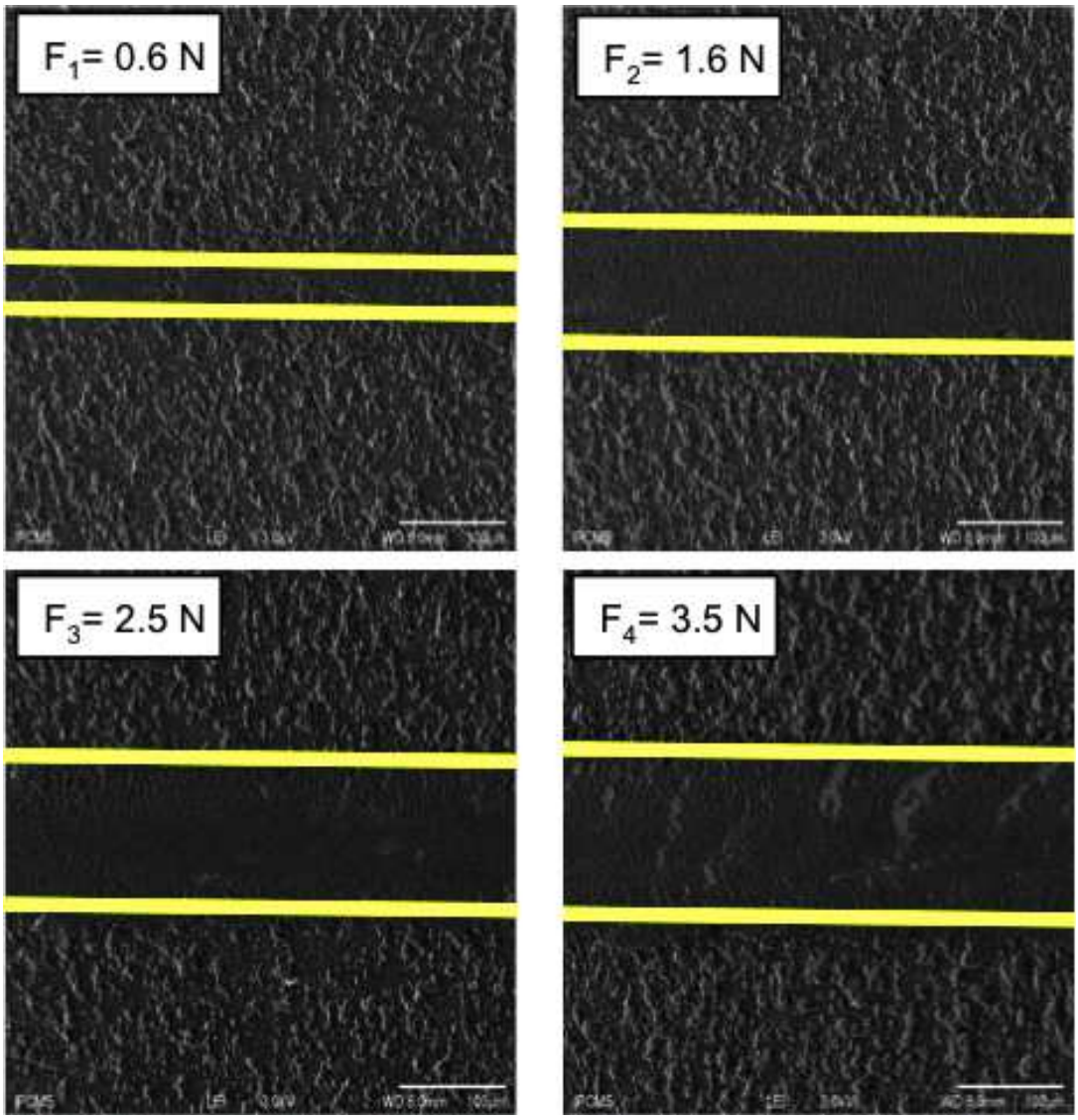

Figure 5.10: SEM micrographs of scratch tests on PMMA-coated Ti samples performed with an indenter of 1000 μm of radius. The applied normal load was increased from 0.6 N to 3.5 N.

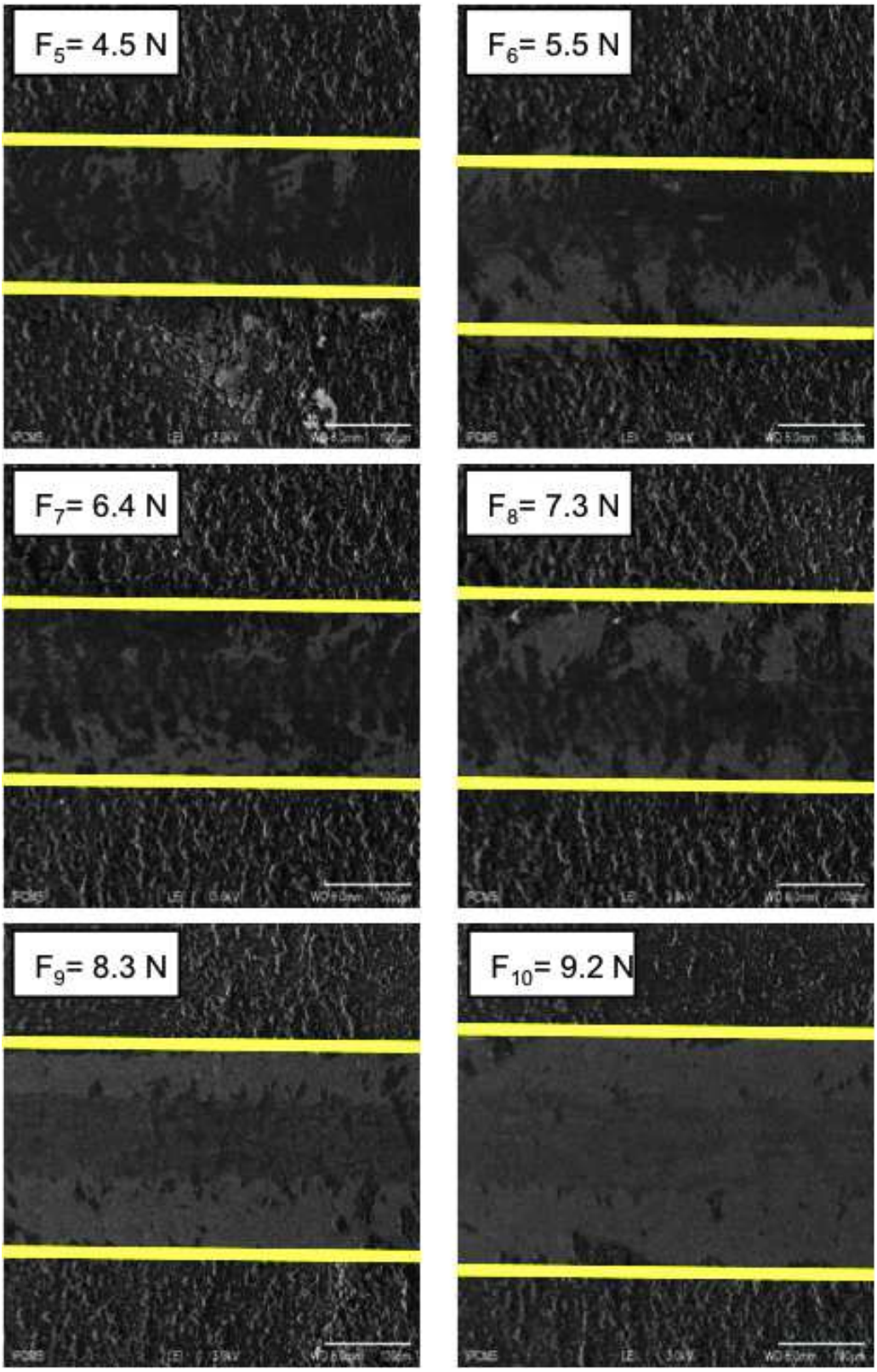

Figure 5.11: SEM micrographs of scratch tests on PMMA-coated Ti samples performed with an indenter of 1000 μm of radius. The applied normal load was increased from 4.5 N to 9.2 N.

Bibliography

[1] B. Zhao and W. J. Brittain, "Polymer brushes: surface-immobilized macromolecules," *Progress in Polymer Science*, vol. 25, no. 5, pp. 677–710, 2000.

[2] D. Julthongpiput, M. LeMieux, and V. Tsukruk, "Micromechanical properties of glassy and rubbery polymer brush layers as probed by atomic force microscopy," *Polymer*, vol. 44, no. 16, pp. 4557–4562, 2003.

[3] W. S. Gutowski, S. Li, C. Filippou, P. Hoobin, and S. Petinakis, "Interface/interphase engineering of polymers for adhesion enhancement: Part ii. theoretical and technological aspects of surface-engineered interphase-interface systems for adhesion enhancement," *The Journal of Adhesion*, vol. 79, no. 5, pp. 483–519, 2003.

[4] P. Schön, S. Dutta, M. Shirazi, J. Noordermeer, and G. J. Vancso, "Quantitative mapping of surface elastic moduli in silica-reinforced rubbers and rubber blends across the length scales by AFM," *Journal of Materials Science*, vol. 46, no. 10, pp. 3507–3516, 2011.

[5] K. Sweers, K. Van Der Werf, M. Bennink, and V. Subramaniam, "Nanomechanical properties of α-synuclein amyloid fibrils: a comparative study by nanoindentation, harmonic force microscopy, and peakforce QNM," *Nanoscale Research Letters*, vol. 6, no. 1, p. 270, 2011.

[6] B. Bhushan and V. N. Koinkar, "Nanoindentation hardness measurements using atomic force microscopy," *Applied Physics Letters*, vol. 64, no. 13, pp. 1653–1655, 1994.

[7] A. V. Kulkarni and B. Bhushan, "Nanoscale mechanical property measurements using modified atomic force microscopy," *Thin Solid Films*, vol. 290, pp. 206–210, 1996.

[8] K. Miyahara, N. Nagashima, T. Ohmura, and S. Matsuoka, "Evaluation of mechanical properties in nanometer scale using AFM-based nanoindentation tester," *Nanostructured Materials*, vol. 12, no. 5-8, pp. 1049–1052, 1999.

[9] S. S. Asif, K. Wahl, and R. Colton, "Nanoindentation and contact stiffness measurement using force modulation with a capacitive load-displacement transducer," *Review of Scientific Instruments*, vol. 70, no. 5, pp. 2408–2413, 1999.

[10] S. Syed Asif, K. Wahl, R. Colton, and O. Warren, "Quantitative imaging of nanoscale mechanical properties using hybrid nanoindentation and force modulation," *Journal of Applied Physics*, vol. 90, no. 3, pp. 1192–1200, 2001.

[11] D. Passeri, A. Bettucci, and M. Rossi, "Acoustics and atomic force microscopy for the mechanical characterization of thin films," *Analytical and Bioanalytical Chemistry*, vol. 396, no. 8, pp. 2769–2783, 2010.

[12] D. Passeri, M. Rossi, E. Tamburri, and M. L. Terranova, "Mechanical characterization of polymeric thin films by atomic force microscopy based techniques," *Analytical and Bioanalytical Chemistry*, vol. 405, no. 5, pp. 1463–1478, 2013.

[13] K. L. Johnson and K. L. Johnson, *Contact mechanics*. Cambridge university press, 1987.

[14] M. Kopycinska-Müller, R. Geiss, J. Müller, and D. Hurley, "Elastic-property measurements of ultrathin films using atomic force acoustic microscopy," *Nanotechnology*, vol. 16, no. 6, p. 703, 2005.

[15] H. Li, N. X. Randall, and J. J. Vlassak, "New methods of analyzing indentation experiments on very thin films," *Journal of Materials Research*, vol. 25, no. 04, pp. 728–734, 2010.

[16] H. Li and J. J. Vlassak, "Determining the elastic modulus and hardness of an ultrathin film on a substrate using nanoindentation," *Journal of Materials Research*, vol. 24, no. 03, pp. 1114–1126, 2009.

[17] Y. Xiang, X. Chen, T. Tsui, J. Jang, and J. Vlassak, "Mechanical properties of porous and fully dense low-κ dielectric thin films measured by means of nanoindentation and the plane-strain bulge test technique," *Journal of Materials Research*, vol. 21, no. 02, pp. 386–395, 2006.

[18] X. Chen, Y. Xiang, and J. J. Vlassak, "Novel technique for measuring the mechanical properties of porous materials by nanoindentation," *Journal of Materials Research*, vol. 21, no. 03, pp. 715–724, 2006.

[19] Z. Parlak and F. Levent Degertekin, "Contact stiffness of finite size subsurface defects for atomic force microscopy: Three-dimensional finite element modeling and experimental verification," *Journal of Applied Physics*, vol. 103, no. 11, p. 114910, 2008.

[20] G. S. Shekhawat, S. Avasthy, A. K. Srivastava, S.-H. Tark, and V. P. Dravid, "Probing buried defects in extreme ultraviolet multilayer blanks using ultrasound holography," *IEEE Transactions on Nanotechnology*, vol. 9, no. 6, pp. 671–674, 2010.

[21] A. Sarioglu, A. Atalar, and F. Degertekin, "Modeling the effect of subsurface interface defects on contact stiffness for ultrasonic atomic force microscopy," *Applied Physics Letters*, vol. 84, no. 26, pp. 5368–5370, 2004.

[22] D. Hurley, M. Kopycinska-Müller, E. Langlois, A. Kos, and N. Barbosa III, "Mapping substrate/film adhesion with contact-resonance-frequency atomic force microscopy," *Applied Physics Letters*, vol. 89, no. 2, p. 021911, 2006.

[23] I. N. Sneddon, "The relation between load and penetration in the axisymmetric boussinesq problem for a punch of arbitrary profile," *International Journal of Engineering science*, vol. 3, no. 1, pp. 47–57, 1965.

[24] G. Pharr, W. Oliver, and F. Brotzen, "On the generality of the relationship among contact stiffness, contact area, and elastic modulus during indentation," *Journal of Materials Research*, vol. 7, no. 03, pp. 613–617, 1992.

[25] D. Passeri, A. Alippi, A. Bettucci, M. Rossi, E. Tamburri, and M. Terranova, "Indentation modulus and hardness of polyaniline thin films by atomic force microscopy," *Synthetic Metals*, vol. 161, no. 1, pp. 7–12, 2011.

[26] B. Bhushan and H. Fuchs, *Applied scanning probe methods VII*. Springer, 2007.

[27] M. Reggente, M. Rossi, L. Angeloni, E. Tamburri, M. Lucci, I. Davoli, M. L. Terranova, and D. Passeri, "Atomic force microscopy techniques for nanomechanical characterization: A polymeric case study," *JOM*, vol. 67, no. 4, pp. 849–857, 2015.

[28] S. Amelio, A. Goldade, U. Rabe, V. Scherer, B. Bhushan, and W. Arnold, "Measurements of elastic properties of ultra-thin diamond-like carbon coatings using atomic force acoustic microscopy," *Thin Solid Films*, vol. 392, no. 1, pp. 75–84, 2001.

[29] D. Passeri, M. Rossi, and J. Vlassak, "On the tip calibration for accurate modulus measurement by contact resonance atomic force microscopy," *Ultramicroscopy*, vol. 128, pp. 32–41, 2013.

[30] G. Stan and R. Cook, "Mapping the elastic properties of granular au films by contact resonance atomic force microscopy," *Nanotechnology*, vol. 19, no. 23, p. 235701, 2008.

[31] J. P. Killgore, J. Y. Kelly, C. M. Stafford, M. J. Fasolka, and D. C. Hurley, "Quantitative subsurface contact resonance force microscopy of model polymer nanocomposites," *Nanotechnology*, vol. 22, no. 17, p. 175706, 2011.

[32] G. Stan and W. Price, "Quantitative measurements of indentation moduli by atomic force acoustic microscopy using a dual reference method," *Review of Scientific Instruments*, vol. 77, no. 10, p. 103707, 2006.

[33] K. F. Mansfield and D. N. Theodorou, "Molecular dynamics simulation of a glassy polymer surface," *Macromolecules*, vol. 24, no. 23, pp. 6283–6294, 1991.

[34] A. V. Zaitseva, V. M. Rudoy, O. V. Dement'eva, and M. E. Kartseva, "Study of polystyrene surface local mechanical properties by the atomic force microscopy," *Materials Science*, vol. 20, no. 3, pp. 37–43, 2002.

[35] J. M. Torres, C. M. Stafford, and B. D. Vogt, "Elastic modulus of amorphous polymer thin films: relationship to the glass transition temperature," *Acs Nano*, vol. 3, no. 9, pp. 2677–2685, 2009.

[36] J. M. Torres, C. M. Stafford, and B. D. Vogt, "Manipulation of the elastic modulus of polymers at the nanoscale: Influence of UV-ozone cross-linking and plasticizer," *ACS Nano*, vol. 4, no. 9, pp. 5357–5365, 2010.

[37] D. Passeri, E. Tamburri, M. L. Terranova, and M. Rossi, "Polyaniline–nanodiamond fibers resulting from the self-assembly of nano-fibrils: a nanomechanical study," *Nanoscale*, vol. 7, no. 34, pp. 14358–14367, 2015.

[38] M. Natali, D. Passeri, M. Reggente, E. Tamburri, M. L. Terranova, M. Rossi, M. Rossi, L. Dini, D. Passeri, M. L. Terranova, *et al.*, "Contact resonance atomic force microscopy for viscoelastic characterization of polymer-based nanocomposites at variable temperature," in *AIP Conference Proceedings*, pp. 020008–1 – 020008–8, AIP Publishing, 2016.

[39] J. Capodagli and R. Lakes, "Isothermal viscoelastic properties of PMMA and LDPE over 11 decades of frequency and time: a test of time–temperature superposition," *Rheologica Acta*, vol. 47, no. 7, pp. 777–786, 2008.

[40] Y. Tsui, C. Doyle, and T. Clyne, "Plasma sprayed hydroxyapatite coatings on titanium substrates part 1: Mechanical properties and residual stress levels," *Biomaterials*, vol. 19, no. 22, pp. 2015–2029, 1998.

[41] D. Barnes, S. Johnson, R. Snell, and S. Best, "Using scratch testing to measure the adhesion strength of calcium phosphate coatings applied to poly (carbonate urethane) substrates," *Journal of the Mechanical Behavior of Biomedical Materials*, vol. 6, pp. 128–138, 2012.

[42] J. Valli, U. Mäkelä, A. Matthews, and V. Murawa, "Tin coating adhesion studies using the scratch test method," *Journal of Vacuum Science & Technology A: Vacuum, Surfaces, and Films*, vol. 3, no. 6, pp. 2411–2414, 1985.

[43] S. Bull, "Failure modes in scratch adhesion testing," *Surface and Coatings Technology*, vol. 50, no. 1, pp. 25–32, 1991.

[44] S. Bull, "Failure mode maps in the thin film scratch adhesion test," *Tribology International*, vol. 30, no. 7, pp. 491–498, 1997.

[45] B. Feddes, P. González, J. Serra, J. Pou, S. Chiussi, J. G. Wolke, and C. Jäger, "Characterization of thin calcium phosphate coating," in *Thin Calcium Phosphate Coatings for Medical Implants*, pp. 25–66, Springer, 2009.

[46] J. Sekler, P. Steinmann, and H. Hintermann, "The scratch test: Different critical load determination techniques," *Surface and Coatings Technology*, vol. 36, no. 1-2, pp. 519–529, 1988.

[47] K. Suresh, "Advanced scratch testing for evaluation of coatings," 2012.

Chapter 6

Towards biocompatible Ti/PMMA/Ti sandwich materials

This chapter reports a brief "state of the art" about sandwich materials, made of Ti and polyolefin (Ti/PP-PE/Ti), as a means to prevent the stress shielding in implants. Ti Gr. 1 sheets and a PP-PE core have been chosen for their biocompatibility even if an epoxy resin has been used to stuck them in the first step. Then, as proof of concept, some preliminary results, concerning the fabrication of biocompatible resin-free sandwich materials will be described. The epoxy resin has been replaced by surface-confined polymer chains and the adhesion between the tethered chains and those of the core material has ben achieved by exploiting their miscibility, i.e. following the diffusion theory [1–6]. As described in Chap. 1, the "grafting from" method allows synthesizing more stable polymer layers than those obtained by the "grafting to" one. Thus, since PP-PE layers could not be grown by "grafting from", to prove the feasibility of our approach it has been substituted by PMMA that can be easily synthesized by SI-ATRP. In the following sections the production of resin-free Ti/PMMA/Ti sandwich, as well as their mechanical characterization aiming at the evaluation of the bonding strength, will also be illustrated.

6.1 State of the art: sandwich materials as a means to reduce stress-shielding in implants

In a previous study [7], the possibility to employ layered sandwich structures for the fabrication of innovative prostheses has been investigated. In particular, the mechanical properties and forming behavior of a model system (see Fig. 6.1a) composed of two Ti sheets (0.5 mm thick) and a polyolefin core (PP-PE, 0.6-1 mm thick) stuck together using an epoxy resin (Köratac FL201, Kömmerling Chemische Fabrik GmbH) have been analyzed (Tab. 6.1).

Table 6.1: Ultimate tensile stress (UTS) and stiffness (E) of: Ti Grade 1, commercial polyethylene-polypropylene (PP-PE), cortical bone and Ti/PP-PE/Ti sandwich materials [7].

Material	Thickness [mm]	YS [MPA]	UTS [MPa]	E [GPa]
Ti Gr. 1	0.5	170 ± 3	321 ± 2	93.2 ± 0.5
PP-PE	0.6	27 ± 1	31 ± 1	1.5 ± 0.2
Cortical bone [8, 9]	-	30-100	70-150	15-30
Ti/PP-PE/Ti	0.5/0.6/0.5	114 ± 2	221 ± 2	52 ± 2
Ti/PP-PE/Ti	0.5/1/0.5	100 ± 2	170 ± 2	42 ± 2

Two main characteristics, that make them suitable candidates for biomedical applications, have been pointed out:

1. the adjustment of their mechanical properties varying the thickness of each component, to reach values comparable to that of the bones (Tab. 6.1) and

2. their good formability, essential to build up complex shapes required for prosthesis reconstruction (Fig. 6.2).

Performing standard tensile tests (Fig. 6.1b), it has been observed that depending on the thickness ratio of the mono-materials (Ti and PP-PE), it is possible to design the

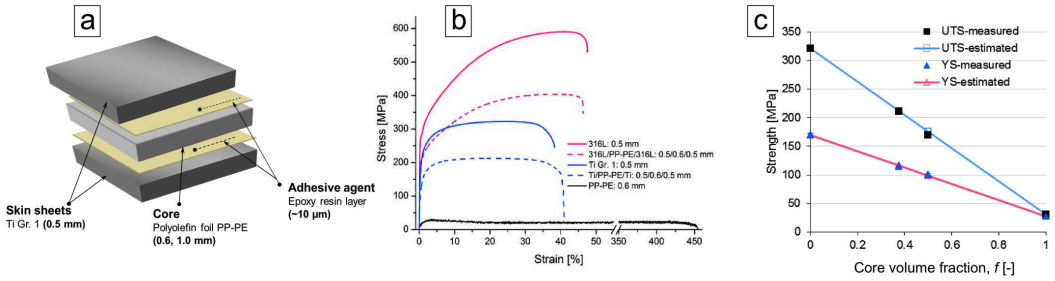

Figure 6.1: a) Schematization of the Ti/PP-PE/Ti sandwich material configuration; b) Stress-strain curves for Ti Gr. 1, PP-PE foil (0.5 thick) as well as Ti/PP-PE/Ti sandwich structure; c) verification of the measured and estimated values according to the rule of mixture (Eq. 6.1) [7].

mechanical properties of the hybrid system Fig. 6.1c). As an example, with a high ratio of polymer one can reduce the yield and ultimate tensile stresses (YS and UTS) as well as the Young's modulus (E), in order to reach properties close to the bones ones. This result is obtained according to the rule of mixture:

$$P_{sandwich} = \frac{P_{Ti} \cdot f_{Ti} + P_{PP-PE} \cdot f_{PP-PE}}{f_{Ti} + f_{PP-PE}} \tag{6.1}$$

where f is the volume fraction of the core sheet and P is the sandwich's property to be calculated, i.e. YS, UTS, or E.

Indeed, the chosen Ti and commercial PP-PE have a Young's modulus equal to (93.2 ± 0.5) GPa and (1.5 ± 0.2) GPa respectively, the Ti/PP-PE/Ti sandwich one has a value of (52 ± 2) GPa. This results in a decrease of the bio-mechanical impairment existing between the bone and the implant. Moreover, using a 1 mm thick polymer core, following the rule of mixture [7], these values can be further designed to match the properties required for the specific application (Tab. 6.1). Vice versa, the same result can be achieved reducing the metal thickness on one or both sides.

The forming behavior (delamination) of the sandwich has been investigated performing bending and torsion tests (Fig. 6.2). It has been shown that failure occurs by cracking and never by delamination. Moreover, performing deep drawing tests it has been observed that their ductility is comparable with that of the metal involved [7].

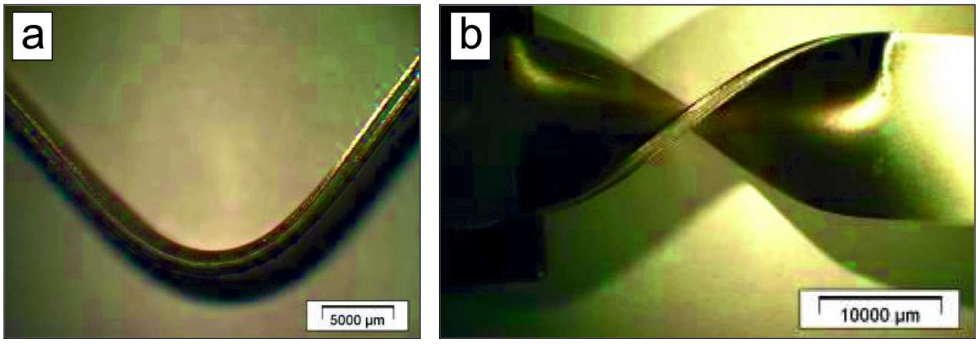

Figure 6.2: Ti/PP-PE/Ti sandwich structure after: a) a bending test of 90 degrees and torsion of 180 degrees (b).

Although this system seems obviously promising for the construction of complex prostheses, the presence of the epoxy resin, commonly employed as adhesive agent to stick the polymer onto the metal surfaces, represents the main drawback of this system because of its toxicity.

6.2 Fabrication and characterization of Ti/PMMA/Ti sandwich

With respect to the procedure described in Chap. 2 and Tab. 2.2, PMMA-coated Ti sheets have been fabricated changing the Ti polishing pretreatment. Indeed, because of the low thickness of the Ti sheet substrates (0.5 mm) and the higher surface required to test the mechanical behavior of the system (60×20 mm^2 or 100×25 mm^2), mechanical polishing could not be applied. Thus, an electrochemical polishing procedure has been developed to prepare the surfaces which have been then modified with PMMA brushes following the strategy previously presented (Chap. 2).

The surface morphology and chemical composition achieved after the electropolishing are shown in Fig. 6.3a. In particular, in the AFM image (Fig. 6.3a) the Ti grains structure is visible and the roughness has been estimated equal to R_a= (5.6 ± 3.0) nm. Whereas, the XPS spectrum (Fig. 6.3b) highlights that the surface was composed of C (34.5%), O (49.3%), Ti (13.7%). Moreover, a slight contamination of Cl (1.1 %) from the solution has also been observed.

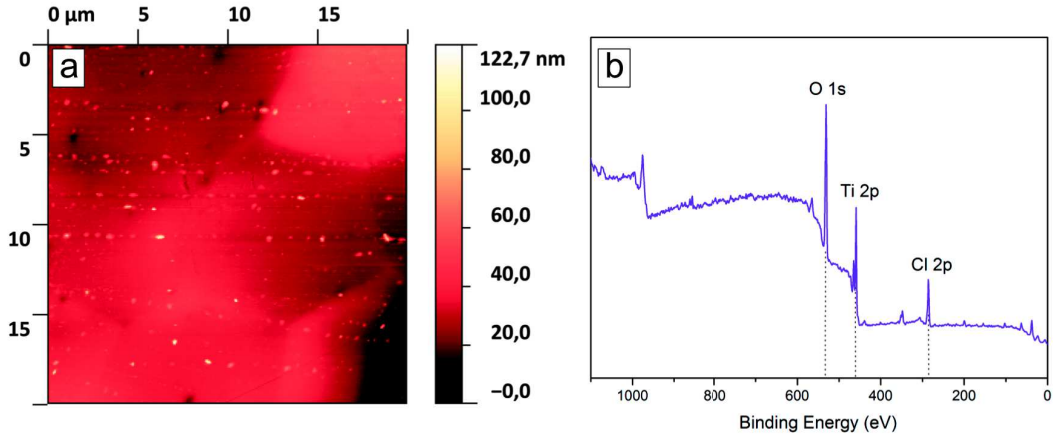

Figure 6.3: a-b) AFM topography of the Ti surface after the electrochemical polishing; c) XPS survey spectrum of the electropolished Ti.

Afterwards, electropolished Ti sheets have been activated in a 2M NaOH solution (heated at 80 °C) for 1h and then transferred in the reactor assigned to the grafting reaction (see Sec. 2.2.2 for details). They have been modified with the long C_{11} ATRP initiator, following the protocol reported in Sec. 2.2.3. Finally, the polymerization reaction took place according to the procedure described in Sec. 2.2.4.

Two different geometries have been prepared, as schematized in Fig. 6.4:

- a two layered half sandwich (Ti/PMMA, Fig. 6.4a), for testing the shear resistance of the bonding;
- a complete three layered sandwich (Ti/PMMA/Ti, Fig. 6.4b-c), for standard tensile and three-points bending tests. They have been performed in the complete Ti/PMMA/Ti material to investigate the pull-off strength of the bond and its formability behavior. The Ti/PMMA/Ti sandwich has been developed in two different sizes and geometries: a squared form (20×20 mm^2, Fig. 6.4b) and a rectangular one (60×20 mm^2, Fig. 6.4c).

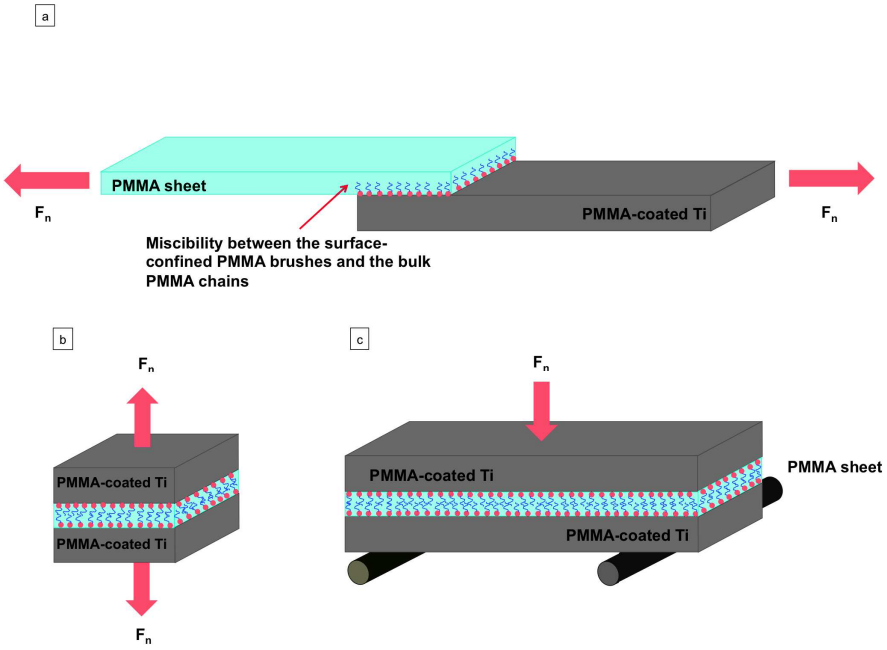

Figure 6.4: Schematization of the sample geometries and testing methods.

6.2.1 Mechanical behavior of PMMA sheet

Prior to prepare the sandwich structure, the mechanical behavior of the commercial PMMA sheet, as core material, has been tested in order to evaluate its mechanical resistance. In Fig. 6.5, a representative PMMA stress-strain curve is presented. The measured UTS was found equal to (40 ± 1) MPa, which is in good agreement with the values reported in literature [10].

In order to determine the glass transition temperature (T_g) of the PMMA sheet, DSC measurements have been performed (see Appendix B). Then, to find a proper temperature to enable the diffusion of the polymer chains, the behavior of the PMMA heated above its $T_g = 116$°C, has been investigated. The behavior of the PMMA heated for 1 h at 140 °C, 160 °C and 180 °C, respectively, has been tested. It has been observed that in the range of 160-180 °C, the PMMA started to soften and visibly melt. In particular, since at 180 °C the polymer shrank, the temperature for the preparation of the half sandwich has been set at 160 °C. Indeed, if the polymer shrank during the heating the sample width would vary not allowing quantitative mechanical testing. Whereas, a temperature of 180

°C was set to fabricate the complete three-layered sandwiches. Indeed, the sample holder kept the polymer pressed between the two modified Ti sheets preventing it to spread out. This support has been provided of recess with the same sandwich's geometry, where the samples have been arranged.

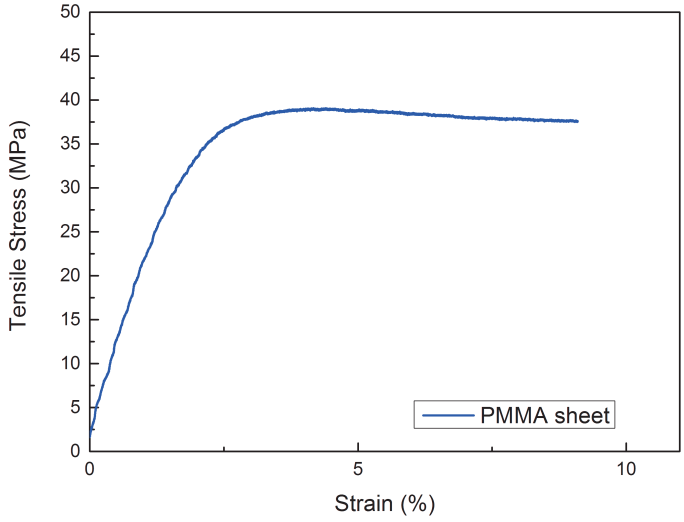

Figure 6.5: Representative stress-strain curve of a PMMA commercial sheet (0.5 mm thick).

6.2.2 Ti/PMMA half sandwich production

The shear strength of the Ti/PMMA bond has been tested preparing half sandwiches, as schematized in Fig. 6.4a. 25×100 mm^2 PMMA-coated Ti sheet have been arranged on a metallic holder. The adhesion between the two grafted and bulk polymers is driven by the interpenetration of the polymer chains into the bulk polymer creating entanglement points [5]. Thus, in order to improve the bonding, a 7 kg load has been put above the overlapped area and heated at 160 °C for 1 h. Afterwards, the half sandwich has been produced by roll-bonding, as described in [11].

6.2.3 Ti/PMMA bonding strength characterization: shear tests

The shear tests have been performed on Ti/PMMA half sandwiches. Using a universal tensile testing machine a force has been applied on the specimen until the rupture occurs (as schematized in Fig. 6.4). Thanks to the sample geometry, this force is transferred on the Ti/PMMA overlapped area which generates shear stresses inducing a debonding between the Ti and PMMA. Thus, the applied force has been monitored until failure occurred in order to evaluate the ultimate shear strength of the bonding.

First Ti/PMMA samples have been fabricated with an overlapping area of 12.5×25 mm^2 (according to ASTM D3165-00). It has been observed that failure occurred in the PMMA sheet and not at the Ti/PMMA interface at an ultimate applied force of (235 ± 26) N. This indicates that the shear strength of the PMMA-coated Ti/PMMA interface is higher than the tensile strength of the PMMA sheet. Therefore, the overlapping area was

reduced. Two different Ti/PMMA systems have been prepared with overlapping area of: (*i*) 5×25 mm^2; (*ii*) 3×25 mm^2.

For all these samples, the fracture occurred within the PMMA sheet and not at the PMMA-coated Ti/PMMA interface. The ultimate shear stress (USS) has been calculated dividing the ultimate applied force (F_{n}) by the overlapping area. For the structures with an overlapped area of 5×25 mm^2 the USS was equal to (1.56 ± 0.22) MPa. For those with a 3×25 mm^2 overlapping area the USS was (1.86 ± 0.62) MPa. It is important to note that since the failure has been taken place inside the PMMA (and not in the bonding area), these values have to be considered as "fictitious". Nevertheless, it can be stated that the bonding strength is better than the strength of the PMMA.

In order to cross-check that the registered strength has been actually related to the PMMA failure, the real rupture stress has been estimated. To this end F_{n} has been divided by the transversal area of the PMMA (equal to 25×0.25 mm^2), where the force really acted. Thus, an ultimate strength of (33 ± 5) MPa, which is comparable to that obtained in the single PMMA sheet with (40 ± 1) MPa, has been determined.

Since no failure occurred in the bonding area, only qualitatively results can be discussed. The shear resistance of Ti/PMMA half sandwich at the interface is higher than the mechanical resistance of the bulk PMMA. Thus, it can be expected that under these load conditions failure will occur in the PMMA and not in the interface.

6.2.4 Ti/PMMA/Ti sandwich production

Square (20×20 mm^2) and rectangular (20×60 mm^2) three layered Ti/PMMA/Ti sandwiches (0.5 mm thick Ti Gr. 2 sheets and 0.25 mm thick PMMA core) have been produced by hot-pressing.

First, sample holders consisting of a stainless steel mask with square or rectangular shaped dips have been prepared. The dip depth has been chosen equal to the height of the three components (1.5 mm) and their surface dimension equal to the dimensions of the two sized sandwiches. Then, the sandwiches have been arranged in the mask and heated at 180 °C for 1 h under a load of 7 kg.

6.2.5 Ti/PMMA/Ti bonding strength characterization: rupture tests

In order to perform the rupture tests on the Ti/PMMA/Ti sandwiches, their external surfaces have been stuck on a parallelepiped stainless steel support sufficiently high to be inserted in the universal test machine, using a two components adhesive (3M Scotch-Weld DP490 Structural Adhesive Epoxy).
At the beginning, the cure conditions of the two components adhesive have been optimized: it has been heated at 60 °C for 24 h. After this, the sample has been slowly cooled down, by turning off the oven and leaving the sample there for 24 h. Then the steel surfaces and the external sandwich ones has been roughened using a 120 grit sandpaper. Its mechanical resistance has been determined equal to (24 ± 7) MPa. Afterwards the samples have been tested; the results of four tested samples are reported in Fig. 6.6. The PMMA-coated Ti/PMMA bonding strength is higher than (16 ± 8) MPa, which represents the average value to break the interface between the steel surface and the external sandwich one. Thus, since failure occurred at the sandwich/steel interface, leaving the PMMA-coated Ti/PMMA interface unaltered, the PMMA-coated Ti/PMMA bonding is stronger than the adhesion between Ti-steel.

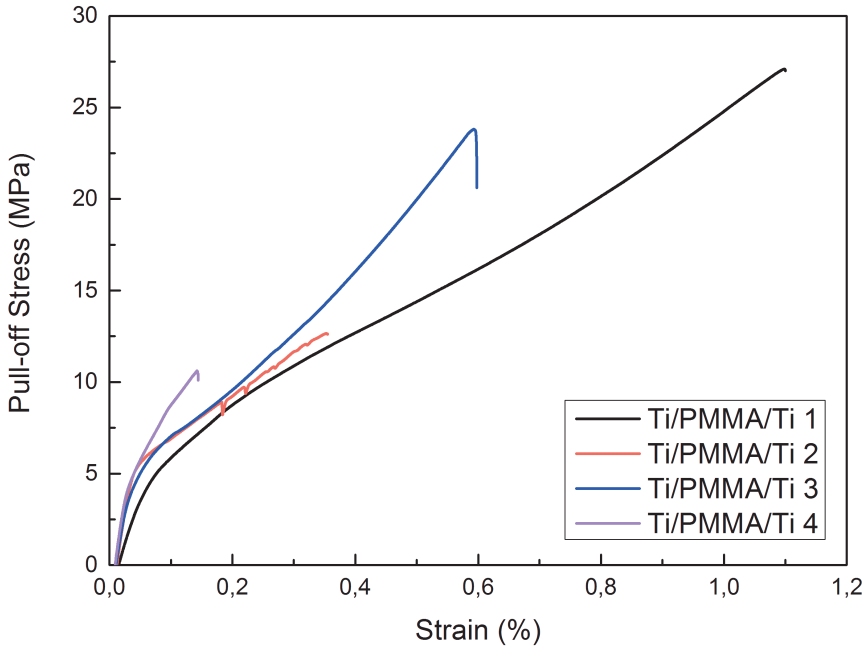

Figure 6.6: Stress-Strain curves obtained performing rupture tests of four Ti/PMMA/Ti sandwich structures.

6.2.6 Ti/PMMA/Ti formability behavior: bending tests

The formability behavior of the Ti/PMMA/Ti sandwich structures - an important aspect for shaping cranioplastic prostheses - has been preliminarily investigated performing three-

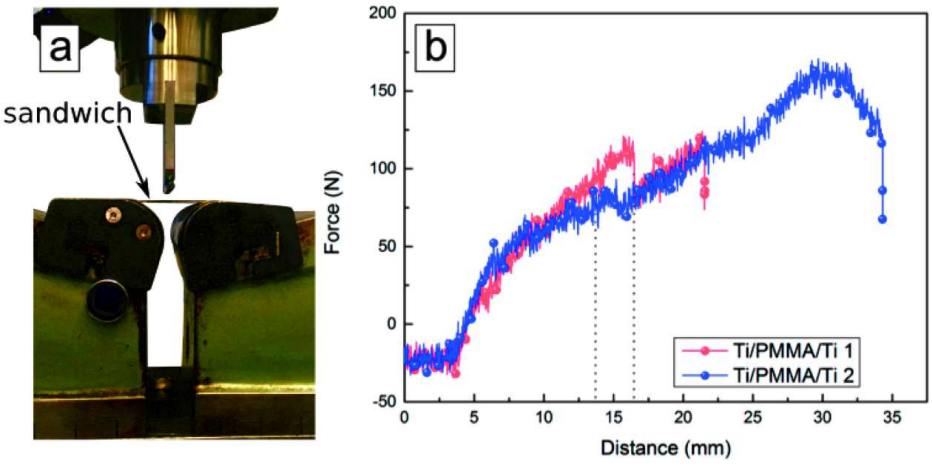

Figure 6.7: Force-distance curves obtained performing three-points bending tests of two Ti/PMMA/Ti sandwiches.

point bending tests, according to the schematization reported in Fig. 6.4. 60×20 mm^2 sandwiches have been tested with a punch with a diameter of 6 mm to determine the ultimate flexural load and the bending fracture stress (see experimental set-up shown in Fig. 6.7a).

Fig. 6.7 shows the results obtained by the analysis of the two sandwiches. It has been observed that no rupture occurred while delamination took place (Fig. 6.8) at an applied force of (101 $\pm$ 13) N corresponding to a bending fracture stress equal to (290 $\pm$ 40) MPa. These results show that the adhesion between the PMMA-coated Ti and the PMMA core has to be optimized to improve their formability.

Figure 6.8: Ti/PMMA/Ti sandwich structure after a bending with an angle of approximately 90°.

6.3 Further considerations

These preliminary tests show that confined-polymers can actually be employed as adhesive layers to replace epoxy resins in the fabrication of biocompatible sandwich structures. These new systems would open new insights of paramount interest in the field of polymer science and engineering applied to the biomedical industrial sector. They allow a development of hybrid-layered structures as a means to control stress shielding in implants. Indeed, their mechanical properties can be tailored by varying the volume fraction of the two components reaching values closer to that of the target bone [7].

Bibliography

[1] H. Arita, K. Mitamura, M. Kobayashi, N. L. Yamada, H. Jinnai, and A. Takahara, "Chain-mixing behavior at interface between polystyrene brushes and polystyrene matrices," *Polymer Journal*, vol. 45, no. 1, pp. 117–123, 2013.

[2] H. Lee, S. Jo, T. Hirata, N. L. Yamada, K. Tanaka, E. Kim, and D. Y. Ryu, "Interpenetration of chemically identical polymer onto grafted substrates," *Polymer*, vol. 74, pp. 70–75, 2015.

[3] S. W. Sides, G. S. Grest, M. J. Stevens, and S. J. Plimpton, "Effect of end-tethered polymers on surface adhesion of glassy polymers," *Journal of Polymer Science Part B: Polymer Physics*, vol. 42, no. 2, pp. 199–208, 2004.

[4] W. S. Gutowski, S. Li, C. Filippou, P. Hoobin, and S. Petinakis, "Interface/interphase engineering of polymers for adhesion enhancement: Part ii. theoretical and technological aspects of surface-engineered interphase-interface systems for adhesion enhancement," *The Journal of Adhesion*, vol. 79, no. 5, pp. 483–519, 2003.

[5] K. Shimizu, K. Malmos, A. H. Holm, S. U. Pedersen, K. Daasbjerg, and M. Hinge, "Improved adhesion between PMMA and stainless steel modified with PMMA brushes," *ACS Applied Materials & Interfaces*, vol. 6, no. 23, pp. 21308–21315, 2014.

[6] O. Alageel, M.-N. Abdallah, Z. Y. Luo, J. Del-Rio-Highsmith, M. Cerruti, and F. Tamimi, "Bonding metals to poly (methyl methacrylate) using aryldiazonium salts," *Dental Materials*, vol. 31, no. 2, pp. 105–114, 2015.

[7] M. Harhash, A. Carradò, and H. Palkowski, "Lightweight titanium/polymer/titanium sandwich sheet for technical and biomedical application," *Materialwissenschaft und Werkstofftechnik*, vol. 45, no. 12, pp. 1084–1091, 2014.

[8] J. Y. Rho, R. B. Ashman, and C. H. Turner, "Young's modulus of trabecular and cortical bone material: ultrasonic and microtensile measurements," *Journal of Biomechanics*, vol. 26, no. 2, pp. 111–119, 1993.

[9] P. K. Zysset, X. E. Guo, C. E. Hoffler, K. E. Moore, and S. A. Goldstein, "Elastic modulus and hardness of cortical and trabecular bone lamellae measured by nanoindentation in the human femur," *Journal of Biomechanics*, vol. 32, no. 10, pp. 1005–1012, 1999.

[10] M. Koleva, "Poly (methyl methacrylate)(PMMA)," *Injection Moulding Materials*, 2005.

[11] O. Sokolova, A. Carradó, and H. Palkowski, "Production of customized high-strength hybrid sandwich structures," in *Advanced Materials Research*, vol. 137, pp. 81–128, Trans Tech Publ, 2010.

Conclusion and perspectives

The work of this thesis is the preliminary part of a wider project aiming at the development of innovative sandwich materials for the fabrication of craniofacial and mandibular implants. With respect to the materials currently employed, these layered structures possess mechanical properties which can be tailored by varying the thickness of the sandwich components (i.e the skin metal sheets and/or the polymer core), to reach values comparable to those of the cortical bone. Therefore, the mechanical impairment, generally existing between the implant and the bone, can be decreased preventing stress-shielding phenomena. Nevertheless, the toxic epoxy resin, commonly used as an adhesive agent to stick the polymer onto the skin metal surfaces, makes sandwich materials inappropriate for the fabrication of medical prostheses.

The objective of this thesis was to replace the epoxy resin with tethered polymer grown directly on the surface of the sandwiches' skin metal sheets and use them as adhesive layers. In particular, it has been shown that, by exploiting the miscibility between the tethered polymer chains and the chains of a bulk polymer foil, the sandwich polymer core can be stuck onto our modified metal sheets without using epoxy resins. Therefore, in principal biocompatible sandwich material have been designed.

To test the feasibility of our approach, the most widely employed materials for biomedical applications have been used: Ti sheets as substrates where PMMA chains have been grown. The hybrid PMMA-coated Ti system has been built-up by developing a three-step methodology based on SI-ATPR coupled with the "grafting from" method. Firstly, Ti substrates have been activated with an alkali treatment in order to increase the hydroxyl groups on the surface. Secondly, phosponate-containing ATRP initiators have been covalently anchored on the activated Ti surfaces making interact the P−OH groups of the phosphonic acid, with the surface hydroxyl groups Ti−OH. Thirdly, PMMA chains have been grown starting from the initiator-modified Ti surfaces using the SI-ATRP method. This procedure allowed to:

- establish a Ti-PMMA link consisting in an oxide-polymer graduated structure which possesses both a covalent and an interlocking nature.
  The polymer is covalently immobilized on the substrates through the formation of Ti−O−P bonds and, simultaneously, mechanically interlocked in the nanostructured network produced by the alkali treatment.

- obtain biocompatible tethered PMMA layers, up to 1-2 μm thick, grown on alkali-activated titanium substrates, whose chemical structure remains stable and unaltered after an incubation of 21 days in a saturated SBF.

- obtain a satisfying bonding strength between a PMMA foil and a Ti sheet stuck together using PMMA-tethered chains as innovative adhesives.

In particular, the key elements of the process are: (*i*) the Ti surfaces activation performed in a basic media (NaOH solution) and (*ii*) the use of malononitrile as a polymerization activator. The former leads to a nanostructured sodium titanate interlayer with an open microporosity. This hierarchical interlayer, acting as a scaffold made of regular pillared and cone-shaped structure, drives the growth of the polymer chains along the pillared structure enhancing the development of the polymer layer. The latter allows producing polymer layers (several hundreds of nanometre thick) covering Ti surfaces of some centimeter square.

Moreover, in order to analyze the surface mechanical properties of the synthesized PMMA-coated Ti surface, different AFM-based techniques have been employed and compared with the standard DSI test. This allowed performing an accurate multiscale characterization of the layered material made of the soft PMMA grown on the harder Ti substrates. Indeed, being the PMMA layer heterogeneous, with a thickness ranging from 100 nanometers to 1-2 micron and small voids confined at the polymer/metal interface, its characterization is affected by the different portion of measured volumes. In particular, it has been pointed out that complementary results are achieved performing some mechanical characterization from the macro- or mesoscale to the micro- or nanoscale. It has been found that:

- the indentation modulus measured by DSI exhibits a bimodal distribution dependent upon the contact radii. Measurements performed with large contact radii ($>$ 4000 nm) are affected by the substrate properties; whereas, for smaller contact radii (in the range of 2000-4000 nm), the measured values are influenced by the presence of the underneath voids.
- AFM-nanoindentation reflects more the properties of the bulk PMMA matrix without being affected by the subsurface voids because of the smaller portion of surface volume probed.
- emerging and advanced AFM based techniques (i.e. CR-AFM, HarmoniX and PF-QNM) display the mechanical properties of the very superficial polymer layer.

Furthermore, the adhesion between the PMMA and the Ti substrates was preliminary evaluated performing scratch tests. Due to the heterogeneity of the polymer layer, preliminary adhesion tests were performed using a macro-sized indenter (with a radius of 1000 μm). This allowed the measurement of the average PMMA/Ti adhesion without being affected by the sample's heterogeneity.

Finally, as proof of concept, the Ti/PMMA half sandwich and the Ti/PMMA/Ti complete one have been fabricated by sticking the PMMA-coated Ti interfaces on a PMMA sheets. Their adhesion has been achieved by exploiting the miscibility between the tethered PMMA chains and the bulk PMMA ones. Both their mechanical properties and formability behavior have been investigated. In particular, shear tests have been performed on the Ti/PMMA half sandwich whereas rupture (or pull-off) tests have been used to investigate the bonding properties of the complete Ti/PMMA/Ti sandwich. While formability behavior has been assessed by three-point bending testing. It has been shown that:

- during the shear tests, the PMMA sheets broke always before the Ti/PMMA interface. It can be deduced that the Ti/PMMA shear resistance is higher than the mechanical resistance of the PMMA foil.
- the pull-off resistance has been found to be approximately equal to 20 MPa. These tests, were performed by glueing the external parts of the sandwich onto a metal support (required to arranged the sample in the tension machine). Since, the failure occurred at the glue/support interface, we can state that at least a resistance greater than that of the glue is aspected.

Besides, even though the preparation of greater sandwich sizes has to be developed and optimized, preliminary three-points bending tests have shown that PMMA can sustain

bending deformation up to 90°. Indeed, the complete Ti/PMMA/Ti sandwiches, bended up to 90°, fails because of delamination but both the components did not undergo rupture.

These preliminary results show that surface confined-polymers can be actually employed as adhesive layers to replace epoxy resins for the production of biocompatible sandwich materials. These new systems would open new insights of paramount interest in the field of polymer science and engineering applied to the biomedical sector because they allow the development of hybrid-layered structures as a means to control stress shielding in implants. Moreover, the specific choice of working with Ti substrates and PMMA may contribute to enlarge the potential application of these kind of systems (i.e. PMMA-coated Ti) which could be of interest for the fabrication of other biomedical devices requiring a strong bond between Ti and the PMMA, (such as dental implants and Ti/PMMA bone cements).

Moreover, this synthesis methodology is very versatile and by modifying the experimental conditions other type of homopolymers or even copolymers, of the polymethacrylates or polyacrylates series, bonded on Ti flat surface can be obtained.

Further investigations will involve:

- the analysis of the stability and durability of the Ti/PMMA/Ti sandwiches in aqueous and SBF solutions;
- the optimization of the Ti/PMMA/Ti sandwich production in order to increase the size of the system;
- the study of the Ti/PMMA/Ti formability performing “small punch-tests”;
- the quantitative evaluation of the TI/PMMA bonding strength.

Conclusion et perspectives

Ce travail de thèse est la première partie d'un projet plus large dont le but est la fabrication d'implants mandibulaires, faciaux ou cr âniens à base de nouveaux matériaux sandwichs de type métal/polymère/métal. Comparés aux matériaux généralement utilisés, les structures sandwichs ou en couches possèdent des propriétés mécaniques adaptables. En effet, en modifiant les épaisseurs des composants du sandwich, c'est- à-dire de la peau métallique et du c¡ur polymère, on peut atteindre des caractéristiques mécaniques proches de celles de l'os. La diminution de l'écart entre les propriétés mécaniques de l'os et celle de l'implant permet de réduire le phénomène de "stress shielding" ou de mauvaises répartition des contraintes mécaniques. Néanmoins, la toxicité de la résine epoxy couramment utilisée pour coller le métal au polymère rend les matériaux sandwichs inutilisables pour la fabrication de prothèses médicales. L'objectif de cette thèse a été de mettre au point une technique de greffage et de croissance de polymère directement sur la surface du métal qui est un des constituants du sandwich. La miscibilité entre les chaines de polymère greffé et les chaînes polymères de la feuille de polymère introduite entre les feuilles de métal a permis l'adhésion entre les différents constituants du matériau sandwich sans utilisation de colle epoxy.

Pour valider cette approche, les matériaux les plus employés dans les applications biomédicales ont été utilisés: à savoir le PMMA et le titane. Le système hybride constitué par du PMMA greffé sur Ti a été élaboré par un processus en trois étapes fondé sur une méthode SI-ATRP. Dans une première étape, les substrats de Ti ont été activés par un traitement alcalin de manière à augmenter le nombre de groupes hydroxyles en surface. Ensuite, l'amorceur de polymérisation qui est un acide alkylphosphonique a été fixé de manière covalente par réaction de ses groupements P−OH avec les fonctions hydroxyles Ti−OH présentes à la surface du titane. Dans une troisième étape, nous avons fait cro ître les cha înes de PMMA en utilisant une polymérisation par transfert d'atomes à partir de l'initiateur. Cette procédure a permis:

- de créer un lien covalent entre Ti et PMMA à travers une structure dont la composition varie graduellement de l'oxyde au polymère, cette structure conduit à un enchev êtrement entre les deux matériaux. Le polymère est lié de manière covalente sur les substrats par les liaisons TiOP et est mécaniquement bloqué dans le réseau nanostructuré produit par le traitement alcalin

- d'obtenir des couches de PMMA dont l'épaisseur peut atteindre jusqu' à 1-2 μm, fixées sur du Ti activé. Cette structure est stable et n'est pas détériorée après un séjour de 21 jours dans une solution saturée de fluide corporel artificiel.

- d'obtenir une forte force de liaison entre une feuille de PMMA et une feuille de Ti collée ensemble en utilisant des chaînes de PMMA comme adhésifs innovants.

De plus, de nouvelles techniques d'AFM ont été utilisées pour analyser les propriétés mécaniques de surface et les résultats obtenus ont été comparés à ceux d'un test standard d'indentation (DSI). Ceci a permis d'avoir une caractérisation multi-échelle précise du PMMA greffé (matériau mou) sur un substrat de Ti qui est un matériau plus dur. Les résultats des caractérisations dépendent de la portion de volume mesurée par la technique utilisée car la couche de PMMA est hétérogène, en effet son épaisseur varie de 100 nm à 1-2 μm et des vides sont présents à l'interface entre le polymère et le titane. Nous avons mis en évidence que les différentes techniques conduisent à des résultats complémentaires des échelles macro ou méso aux échelles micro ou nano. Nous avons montré que:

- le module d'indentation mesuré par DSI est caractérisé par une distribution bimodale et dépend du rayon de contact. Les mesures faites avec un rayon de contact élevé (>4000 nm) sont affectées par le substrat en titane alors que pour des rayons de contact plus petits (entre 2000 et 4000 nm) ces mesures sont sensibles à un défaut d'adhérence du polymère sur le substrat (présence de vides).

- la nanoindentation par AFM permet de bien caractériser les propriétés de la couche de PMMA car les résultats ne sont pas affectés par la présence de vides. En effet, cette technique n'est sensible qu'aux parties externes de la couche du polymère.

- les techniques avancées et perfectionnées, fondées sur l'AFM (i.e. CR-AFM, HarmoniX and PF-QNM) fournissent une caractérisation des propriétés mécaniques de la couche de polymère très superficielle.

De plus, l'adhésion entre le PMMA et le Ti a été évaluée par des scratch tests. A cause de l'hétérogénéité de la couche de polymère, des tests préliminaires d'adhésion ont été réalisés en utilisant un indenteur ayant un rayon de 1000 μm. Ceci a permis d'obtenir une valeur moyenne de l'adhésion malgré l'hétérogénéité des échantillons.

Enfin, comme preuve du concept, un demi-sandwich Ti/PMMA et un sandwich complet Ti/PMMA/Ti ont été fabriqués en collant le Ti greffé par du PMMA sur une feuille de PMMA. L'adhésion a été obtenue gr âce à la miscibilité des chaines de PMMA entre elles. Les propriétés mécaniques et le comportement au formage ont été étudiés. En particulier, le comportement des demi-sandwichs en cisaillement et des sandwichs en rupture a permis d'étudier la force de l'adhésion entre les différentes parties du sandwich. Letest de flexion en trois points a permis d'évaluer la capacité de formage. Nous avons montré que :

- au cours d'un test de cisaillement, une fissure apparait dans la feuille de PMMA alors que l'interface Ti/PMMA n'est pas affectée, ce qui nous a permis de conclure que la résistance en cisaillement de l'interface Ti/PMMA est plus élevée que la résistance mécanique de la feuille de PMMA.

- la résistance en rupture est d'environ 20 MPa. Les parties externes du sandwich ont été collées par une colle époxy sur un support métallique adapté à la machine de traction. Lors des essais, la fracture s'est produite à l'interface entre le support et le sandwich. Nous en avons conclu que la résistance du sandwich et donc de l'interface Ti/PMMA est plus élevée que l'interface faite de cette colle.

En outre, bien que des tests préliminaires de flexion en trois points aient montré que le PMMA peut supporter des déformations jusqu' à 90°, les sandwichs Ti/PMMA/Ti présentent des délaminations après une flexion de 90°. Cependant, aucune rupture n'a été constatée. La préparation de sandwich de grandes tailles doit être optimisée pour permettre une bonne caractérisation de la tenue en flexion.

Ces résultats montrent que les polymères greffés sur des surfaces peuvent être employés comme couche adhésive pour remplacer la colle époxy dans la production de matériaux sandwichs biocompatibles. Ces systèmes ouvrent de nouvelles perspectives dans le domaine de la science des polymères et de l'ingénierie pour les applications biomédicales. Le développement de ce type d'architectures stratifiées hybrides permet d'envisager un contr ôle du "stress shielding" provoqué par les implants. De plus, l'étude que nous avons conduite sur le système Ti-PMMA peut contribuer à envisager d'autres applications nécessitant une liaison forte entre Ti et PMMA, par exemple pour des implants dentaires ou des ciments osseux.

Cette méthode d'élaboration est très versatile. En effet, d'autres polymères ou copolymères de type polymethacrylate ou polyacrylate peuvent être greffés à la surface du Ti en modifiant les conditions expérimentales de l'ATRP,.

L'étude des sandwichs Ti/PMMA/Ti pourrait se poursuivre par:

- l'analyse de leur stabilité et durabilité en solution aqueuse ou dans du SBF.
- l'optimisation de la production pour pouvoir augmenter leur taille.
- l'étude de leur formabilité par un test au pointeau.
- l'évaluation quantitative de la force de liaison entre le polymère et le titane.

Appendix A

Contact resonance atomic force microscopy

A.1 Analytical model of the cantilever oscillating in air

As explained in Sec. 4.2.2, the first step of the CR-AFM technique consists in the measurement of the resonance frequencies of the system in order to calculate the value of the characteristic parameter of the cantilever, c_c. To do this the cantilever is made oscillate far away from the sample surface. It can be model as a flexible clamped-free beam with length L, width w, thickness t and Young's modulus E (see Fig. A.1).

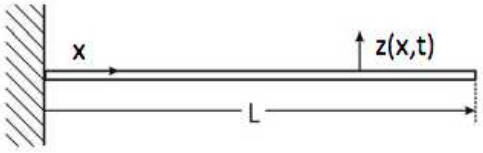

Figure A.1: Mechanical model of an AFM clamped-free cantilever

If the cross-section of the cantilever is constant for its entire length, the flexural vibrations can be determined by considering the Euler-Bernoulli equation [1, 2]

$$EI\frac{\partial^4 z(x,t)}{\partial z^4} + \rho_c \frac{\partial^2 z(x,t)}{\partial t^2} = 0 \tag{A.1}$$

where $A = wt$ and $I = wt^3/12$ are respectively the area of the cross section and the area moment of inertia of a beam with a rectangular section. By applying a separation of variables, the general solution of the Eq. (A.1) can be found as follows [1, 2]:

$$z(y,t) = (A_1 e^{kx} + A_2 e^{-kx} + A_3 e^{jkx} + A_4 e^{-jkx}) e^{-j\omega t} \tag{A.2}$$

where A_1, A_2, A_3, A_4 are constants, j is the imaginary unit and $\omega = 2\pi f$ is the angular frequency. By substituting the Eq. (A.2) in the equation of motion Eq. (A.1), an expression of the wave number k is derived:

$$EIk^4 - \rho_c A\omega^2 = 0 \Rightarrow \; k = \sqrt[4]{\frac{\rho_c A}{EI}\omega^2} \tag{A.3}$$

from which follows also the espression of the resonance frequency of the system [1, 2]:

$$f = \frac{(kL)^2}{2\pi}\frac{1}{L^2}\sqrt{\frac{EI}{\rho_c A}} \tag{A.4}$$

In order to find the effective motion of the cantilever, the boundary conditions at the clamped end (e.g. $x = 0$) and at the free end (e.g. $x = L$) of the cantilever have to be applied. They are the following:

$$x = 0 : \begin{cases} z(x) = 0 \\ \\ \frac{\partial z(x)}{\partial x} = 0 \end{cases} \qquad x = L : \begin{cases} \frac{\partial^2 z(x)}{\partial x^2} = 0 \\ \\ \frac{\partial^3 z(x)}{\partial x^3} = 0 \end{cases} \tag{A.5}$$

By substituting the general solution Eq. (A.2) into the boundary conditions Eq. (A.5), the characteristic equation of the resonant modes of the system is determined [1, 2]:

$$\cos(k_{0n}L)\cosh(k_{0n}L) + 1 = 0 \tag{A.6}$$

where k_{0n}, is the wave number of the nth flexural resonant frequency f_{0n}. The roots of the Eq. (A.6) are well known in literature and related to the resonance frequencies of the clamped-free cantilever:

$$f_{0n} = \frac{(k_{0n}L)^2}{{c_c}^2} \tag{A.7}$$

where c_c is the cantilever parameter that combines its geometrical and material properties.

$$c_c = L\sqrt{2\pi}\sqrt[4]{\frac{12\rho_c}{Ew^2}} \tag{A.8}$$

A.2 Analytical model of the cantilever oscillating in contact with the sample surface

In the second step of the procedure the tip is brought in contact with the sample and the tip-sample interaction change the boundary condition of the system. For small oscillation amplitudes, tip-sample interactions, such as elastic forces, adhesion forces and viscoelastic forces can be modeled by linear springs and dashpots (see Fig. A.3). Forces acting normal at the surface are represented by the normal contact stiffness k^* and the contact damping γ, forces lateral to the surface are schematized by the lateral contact stiffness k^*_{Lat} and lateral contact damping γ_{Lat}.

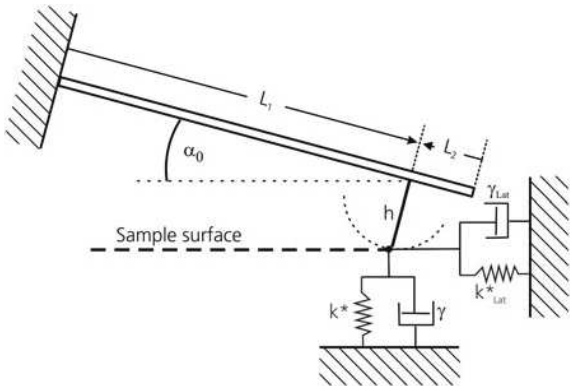

Figure A.2: Schematic representation of an AFM cantilever oscillating in contact with a sample surface

For sake of simplicity a simpler version of the model, reported in Fig. A.3, is considered. The tip is located at position L_1 from the clamped end and the total length of the cantilever is $L = L_1 + L_2$ [3]. The boundary conditions of this system can be found by defining two solutions for the two parts of the cantilever. At the clamped end and at the free end the

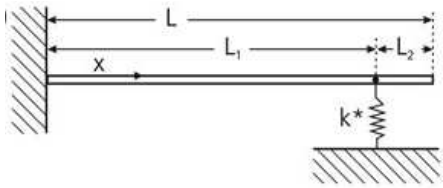

Figure A.3: Mechanical model of a clamped spring-coupled cantilever.

conditions are those reported in Eq. (A.5). At the tip position (e.g in $x = L_1$) additional conditions have to be taken into account. These are due to the tip-sample interactions and have to ensure the continuity of the cantilever displacement and slope in $x = L_1$. These considerations lead to a different characteristic equation from which the contact stiffness is determined [3]:

$$\begin{aligned} k^* = \; & \tfrac{2}{3}k_c(k_nLr)^3(1+\cos k_nL\cosh k_nL) \\ & /[-(\cosh k_nLr\sin k_nLr-\sin k_nLr\cos k_nL) \\ & \times(1+\cos(1-r)k_nL\cosh(1-r)k_nLr) \\ & +(\cosh(1-r)k_nL\sin(1-r)k_nL \\ & -\sinh(1-r)k_nL\cos(1-r)k_nL) \\ & \times(1-\cos k_nLr\cosh k_nLr)] \end{aligned} \tag{A.9}$$

where $r = L_1/L$ is a useful parameter indicating the tip position and k_c is the cantilever spring constant. As in the case of the cantilever free oscillations, the wave number k_n is related to the contact resonance frequenciy f_n by the expression:

$$f_n = \frac{(k_nL)^2}{{c_c}^2} \tag{A.10}$$

Thus the Eq. (A.9) can be rewritten as a function of f_n:

$$\begin{aligned} k^* = \; & \tfrac{2}{3}k_c(c_c\sqrt{f_n}r)^3(1+\cos c_c\sqrt{f_n}\cosh c_c\sqrt{f_n}) \\ & /[-(\cosh c_c\sqrt{f_n}r\sin c_c\sqrt{f_n}r-\sin c_c\sqrt{f_n}r\cos c_c\sqrt{f_n}r) \\ & \times(1+\cos(1-r)c_c\sqrt{f_n}\cosh(1-r)c_c\sqrt{f_n}) \\ & +(\cosh(1-r)c_c\sqrt{f_n}\sin(1-r)c_c\sqrt{f_n} \\ & -\sinh(1-r)c_c\sqrt{f_n}r\cos(1-r)c_c\sqrt{f_n}r) \\ & \times(1-\cos c_c\sqrt{f_n}r\cosh c_c\sqrt{f_n}r)] \end{aligned} \tag{A.11}$$

The parameter c_c is known because it derives from the measurement of the free cantilever resonance frequencies (i.e., first step of the technique). The contact resonance frequencies of the cantilever clamped-spring coupled (f_n) are higher than that of the cantilever clamped-free (f_{0n}). In particular the following relation exists between them:

$$f_{0n} < f_n < f_{0n+1} \tag{A.12}$$

The value of r is necessary in order to determine the contact stiffness k^* by the Eq. (A.11). It can be either estimated by SEM characterization or used as fitting parameter and numerically or graphically evaluated using two different contact-resonance frequencies (f_n and f_m). This is generally carried out by matching the Eq. (A.11) calculated for the two different frequencies f_n and f_m [3]:

$$k^*(f_n, r) = k^*(f_m, r) \tag{A.13}$$

Once, the value of the parameter r is estimated, the experimentally determined values of the CRFs are used to calculate the local contact stiffness k^*.

Bibliography

[1] D. Sarid, *Scanning force microscopy: with applications to electric, magnetic, and atomic forces*, vol. 5. Oxford University Press on Demand, 1994.

[2] U. Rabe, K. Janser, and W. Arnold, "Vibrations of free and surface-coupled atomic force microscope cantilevers: theory and experiment," *Review of Scientific Instruments*, vol. 67, no. 9, pp. 3281–3293, 1996.

[3] F. Marinello, D. Passeri, and E. Savio, *Acoustic scanning probe microscopy*. Springer Science & Business Media, 2012.

Appendix B

Differential Scanning Calorimetry measurement

Differential Scanning Calorimetry (DSC) measurement of a PMMA sheet

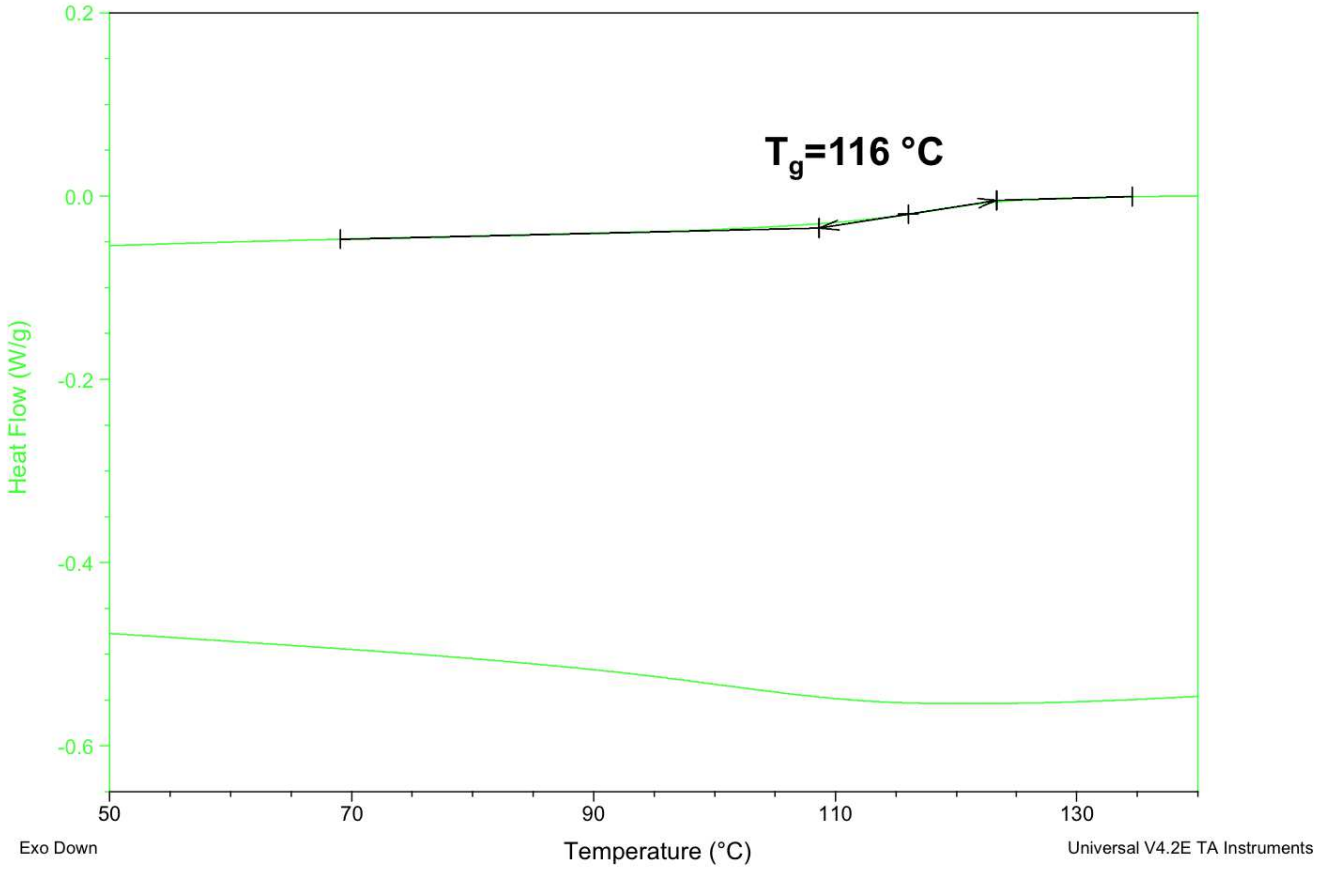

Appendix C

Publications

Nanoscale

PAPER

Cite this: *Nanoscale*, 2017, **9**, 5671

Detection of stiff nanoparticles within cellular structures by contact resonance atomic force microscopy subsurface nanomechanical imaging

Melania Reggente,[a,b] Daniele Passeri, *[a] Livia Angeloni,[a,c] Francesca Anna Scaramuzzo,[a] Mario Barteri,[d] Francesca De Angelis,[e,f] Irene Persiconi,[g] Maria Egle De Stefano[g] and Marco Rossi[a,h]

Received 14th February 2017,
Accepted 24th March 2017

DOI: 10.1039/c7nr01111c

rsc.li/nanoscale

Detecting stiff nanoparticles buried in soft biological matrices by atomic force microscopy (AFM) based techniques represents a new frontier in the field of scanning probe microscopies, originally developed as surface characterization methods. Here we report the detection of stiff (magnetic) nanoparticles (NPs) internalized in cells by using contact resonance AFM (CR-AFM) employed as a potentially non-destructive subsurface characterization tool. Magnetite (Fe_3O_4) NPs were internalized in microglial cells from cerebral cortices of mouse embryos of 18 days by phagocytosis. Nanomechanical imaging of cells was performed by detecting the contact resonance frequencies (CRFs) of an AFM cantilever held in contact with the sample. Agglomerates of NPs internalized in cells were visualized on the basis of the local increase in the contact stiffness with respect to the surrounding biological matrix. A second AFM-based technique for nanomechanical imaging, *i.e.*, HarmoniX™, as well as magnetic force microscopy and light microscopy were used to confirm the CR-AFM results. Thus, CR-AFM was demonstrated as a promising technique for subsurface imaging of nanomaterials in biological samples.

The capability of detecting nanoparticles (NPs) buried in soft biological samples represents one of the main challenges in bio-nanoscience, as it would allow the monitoring of the interactions between cells and NPs at the nanoscale. Developing innovative and nondestructive imaging techniques for the visualization of NPs embodied into cells with nanometer resolution is a challenging task of primary importance in several applications, from drug delivery to nanotoxicology.[1–4] The most common techniques currently used to analyze intracellular structures are based on light, confocal and electron (both scanning and transmission) microscopies, which nevertheless have limited resolution and/or are destructive techniques that require several steps for sample preparation, such as dehydration, fixation, metallization, or cross-section cutting.[5–8] Even though atomic force microscopy (AFM) was originally developed as a surface characterization platform,[9] it potentially represents a useful alternative to develop nondestructive subsurface imaging techniques. In AFM, a sharp probe, *i.e.*, the tip at the free-end of the cantilever, interacts with the surface of the investigated sample. The cantilever static deflection (in contact mode) and the amplitude of the oscillating cantilever (in tapping mode) are measured to reconstruct a map of the surface heights, *i.e.*, the sample topography. Furthermore, since the probe physically interacts with the surface sample, different types of interaction forces can be monitored. Thus, several techniques have been developed to map local magnetic,[10] mechanical,[11] electrical,[12] thermal[13] and chemical[14] properties of the sample surface, with nanometer spatial resolution, together with the standard AFM topography. In these techniques, the probed tip–sample forces are the result of the interaction between the tip and a small volume of material below the surface of the sample with dimensions generally comparable to those of the tip. Therefore, they are sensitive not only to physical inhomogeneities on the surface, but also under the surface, within the sample probed volume, thus allowing the detection of buried

[a]*Department of Basic and Applied Sciences for Engineering, SAPIENZA University of Rome, Rome, Italy. E-mail: daniele.passeri@uniroma1.it*
[b]*Institute of Physics and Chemistry of Materials of Strasbourg, UMR 7504-CNRS, Strasbourg University, Strasbourg, France*
[c]*Lab. for Biomaterials and Bioengineering (CRC-I), Dept. Min-Met-Materials Eng. & University Hospital Research Center, Laval University, Quebec City, Canada*
[d]*Department of Chemistry, SAPIENZA University of Rome, Rome, Italy*
[e]*Department of Anatomy, Histology, Forensic Medicine and Orthopaedics, SAPIENZA University of Rome, Rome, Italy*
[f]*Center for Life Nano Science@Sapienza, Istituto Italiano di Tecnologia, Rome, Italy*
[g]*Department of Biology and Biotechnology 'Charles Darwin', SAPIENZA University of Rome, Laboratory affiliated to Istituto Pasteur-Fondazione Cenci Bolognetti, Italy*
[h]*Research Center for Nanotechnology applied to Engineering of SAPIENZA University of Rome (CNIS), Rome, Italy*

nanostructures with properties different from those of the host matrix. For instance, magnetic force microscopy (MFM), electric force microscopy (EFM), and conductive AFM (C-AFM) derived techniques, such as dc-biased amplitude modulated AFM and Kelvin probe AFM, have been successfully employed for subsurface imaging of composite materials made of polymer matrices filled with Fe_3O_4 nanoparticles[15] and carbon nanotubes,[16,17] or for the detection of magnetic NPs in biological matrices.[18–20] Since the presence of harder (softer) inclusions inside a softer (harder) matrix as well as voids beneath the sample surface causes local variations in the sample stiffness, subsurface imaging can be performed probing the different elastic properties of the host and guest systems. Thus, some of the different AFM based techniques which allow nanomechanical characterization have been already used for subsurface imaging of samples. Recently, Roduit *et al.*[21,22] have proposed a method to analyze quasi-static indentation curves acquired by AFM to obtain 3D stiffness tomography reconstructions. Moreover, the synergistic use of AFM and ultrasound testing resulted to be particularly effective for subsurface feature detection with nanometer lateral resolution. In particular, Yamanaka *et al.* used ultrasonic force microscopy (UFM) for subsurface imaging on highly oriented pyrolytic graphite (HOPG).[23] In addition to this, subsurface imaging of void defects in interconnections[24] has been successfully performed by using scanning near field ultrasound holography (SNFUH).[25,26] To the best of our knowledge, this is the only AFM based technique which has been used for the visualization of single nanostructures, *i.e.*, SiO_2 NPs and carbon nanohorns, embodied within a cell.[27,28] Finally, contact resonance AFM (CR-AFM) has been demonstrated to be a very versatile technique, which can be used to study materials with a wide range of mechanical properties, *i.e.*, from stiff coatings and gemstones[29–32] to soft polymers[33–35] and biological samples.[36] CR-AFM was used to study nanocomposite samples constituted by stiff nanomaterials incorporated into soft polymeric matrices, in which the presence of the nanomaterials was confirmed by the analysis of the variation of the indentation modulus and its spatial distribution.[37–39] CR-AFM provided subsurface imaging by using *ad hoc* designed test samples, detecting voids generated by means of a focused ion beam (FIB) under the surface of a Si single crystal,[40] as well as visualizing SiO_2 NPs buried beneath a smooth and thin polystyrene film.[41] However, to the best of our knowledge, CR-AFM has never been used to detect NPs internalized in cells.

Here we report, for the first time, the use of CR-AFM for the detection of stiff NPs embodied in cells. Because of their high phagocytic activity, microglia cells were used to produce model samples of cells engulfed with magnetic NPs, the presence of which was revealed by MFM.

Magnetite NPs were synthesized starting from Mohr salt ($(NH_4)_2Fe(SO_4)_2{\cdot}6H_2O$) and $Fe_2(SO_4)_3$ in ammonia solution containing 2% (w/v) of polyvinylpyrrolidone (PVP), following the Massart's co-precipitation method[42] that we modified as previously described.[20] Microglia cells were taken from cerebral cortices of 18 days old mouse embryos, dissociating the tissue at 37 °C with trypsin 0.1% and DNAse (100 mg mL^{-1}) in a suitable salt solution. A rather pure population of microglia (less than 2% of contamination) was obtained suspending them in Dulbecco's Modified Eagle's Medium (DMEM) containing 10% fetal bovine serum (FBS), by placing them in a culture flask and leaving them in culture for 18 days. Subsequently, cells were made adhere onto glass slides pre-treated with poly-lysine (10^5 cells per slide). An example of a microglia cell on a glass substrate is shown in Fig. 1. Fe_3O_4 NPs were then added to the culture medium and internalized by endocytosis into the cytoplasm of microglia cells.[43] The process of phagocytosis required 5 hours of incubation in DMEM at 37 °C under an air atmosphere with 5% CO_2. After having removed the culture medium, the glass slide with the adherent cells was washed several times with a phosphate buffered saline (PBS) solution (pH = 7.4) to remove non-phagocytized NPs, and fixed for 15 min at room temperature in PBS with 4% formaldehyde. This fixation process, which implied the polymerization of cell membrane's proteins, altered the elastic properties of the cells making them stiffer, but still significantly softer than the NPs, allowing us to obtain a detectable contrast in the CR-AFM images.

Light microscopy images collected with 40× magnification (Fig. 2) highlighted the presence of NP aggregates in close proximity to the cells, likely inside the cytoplasm.

Massive internalization of Fe_3O_4 NPs in microglia cells was assessed by MFM imaging, which confirmed the presence of a significant magnetic signal from labeled cells. An example is shown in Fig. 3, in which standard MFM apparatus (Solver, NT-MDT, Russia) equipped with magnetic coated tips (MESP, Bruker Inc.) was used to acquire the topography of a microglia cell (Fig. 3a) and the corresponding magnetic phase image (Fig. 3b). The dark contrast at the center of the MFM phase image indicates the presence of a massive agglomerate of magnetite NPs at the center of the cell (see for comparison Fig. 2a), although we made no attempts to improve the quality of the image by removing electrostatic artifacts from the magnetic signal.[44,45]

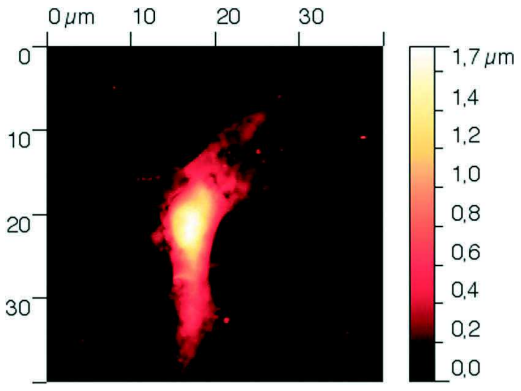

Fig. 1 Topography of a microglia cell on a glass substrate recorded in tapping mode.

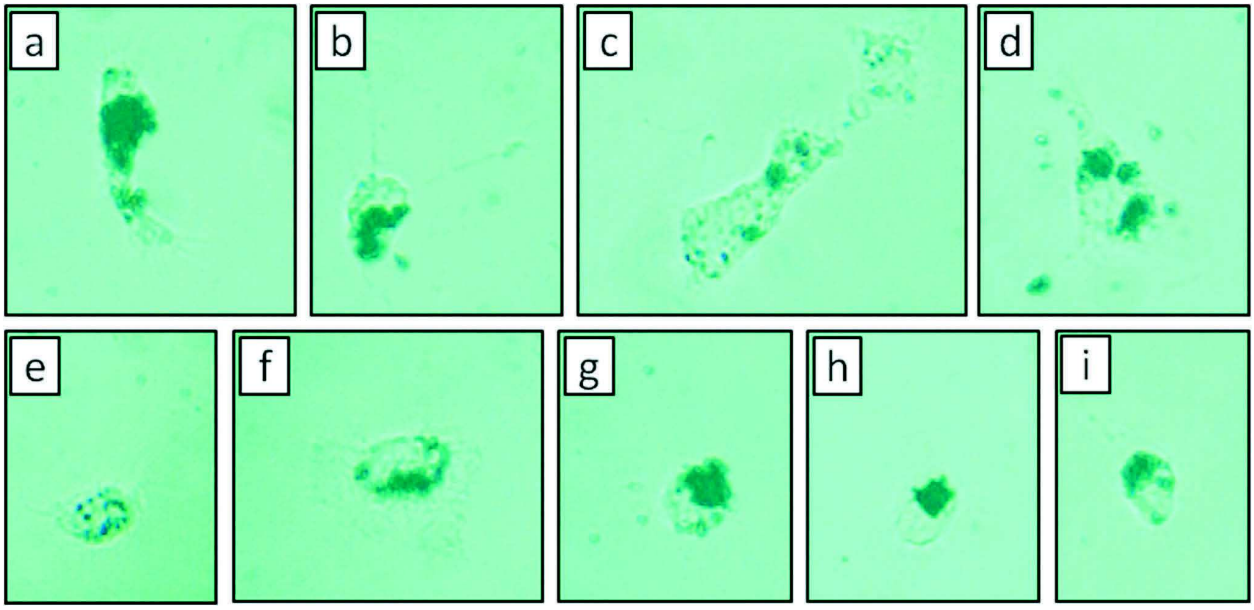

Fig. 2 Light microscopy images (original magnification 40×) of microglia cells incubated with magnetite NPs.

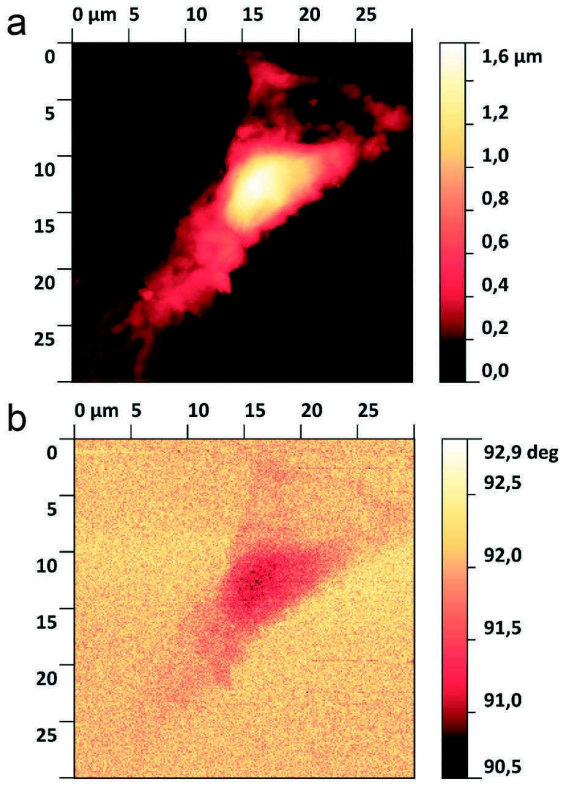

Fig. 3 (a) Topography of a microglia cell engulfed with NPs and (b) the corresponding magnetic phase image obtained by magnetic force microscopy.

CR-AFM is a contact mode based technique in which the back of the sample is mounted on an ultrasonic transducer, which excites out-of-plane oscillation of the sample surface. Spectra of the cantilever flexural vibrations are recorded and resonance frequencies of the cantilever-tip–sample system, namely the contact resonance frequencies (CRFs), are measured at each point of the scanned area and thus mapped on the sample surface simultaneously to the topography. The values of CRFs reflect the local elastic properties of the sample, *i.e.*, the stiffer the sample, the higher the CRFs, and can be used to evaluate the sample indentation modulus. Therefore, CRF maps can be considered as semi-quantitative nanomechanical images of the sample surface. Our AFM experimental setup (Solver, NT-MDT, Russia), the detailed description of which can be found elsewhere,[46] was equipped with commercial Si cantilevers (CSC17, MikroMasch, Estonia) chosen on the basis of their low spring constant (nominal value k_c = 0.18 N m^{-1}) to minimize surface modification and sample damaging during CR-AFM experiments. CR-AFM experiments were conducted using a static normal force applied between the tip and the sample of about 20 nN. Under these conditions, we observed neither irreversible modifications of the imaged cells between two subsequent images nor tip contamination. This indicated the non-destructiveness of CR-AFM under our actual experimental conditions. The measured first free resonance frequencies of the cantilever used to acquire the images shown in this work were: f_1^0 = 9.5 kHz; f_2^0 = 65 kHz; f_3^0 = 185 kHz; f_4^0 = 372 kHz; f_5^0 = 626 kHz.

Additionally, the chosen cantilevers are characterized by relatively low values of CRFs allowing their detection up to the sixth eigenmode. CR-AFM performed at higher eigenmodes

has been demonstrated to have the maximum sensitivity to subsurface variations in the mechanical properties.[41,47] As expected, the values of CRFs measured on the engulfed cells are significantly higher than those measured on the empty ones. This corresponds to significantly larger values of normalized contact stiffness. Conversely, subsurface features in engulfed cells could be observed in CRF images obtained using higher modes. In Fig. 4, the fifth eigenmode CRF maps of an empty cell (Fig. 4a) and of a cell engulfed with NPs (Fig. 4b) are shown. Images were obtained by searching the resonance in the range from 660 kHz to 1100 kHz, *i.e.*, between the fifth and the sixth eingenmodes of the free cantilever in air. As expected, CRF values corresponding to the cells are much lower than those corresponding to the stiff substrate. In addition to this, CRF values corresponding to empty cells are lower than those corresponding to the engulfed ones. This can be attributed to a significant presence of Fe_3O_4 NPs in labeled cells resulting in the increase of the effective elastic modulus of the cell. Moreover, in the case of empty cells (Fig. 4a), CRF values were constant within the cell and no areas corresponding to higher CRFs were detected. Conversely, large areas with higher CRFs were observed in the case of cells labeled with NPs (Fig. 4b). This suggests that Fe_3O_4 NPs agglomerate within the structure of the cell, producing mechanical inhomogeneities detectable by CR-AFM nanomechanical imaging (see for comparison Fig. 2a, b, g–i).

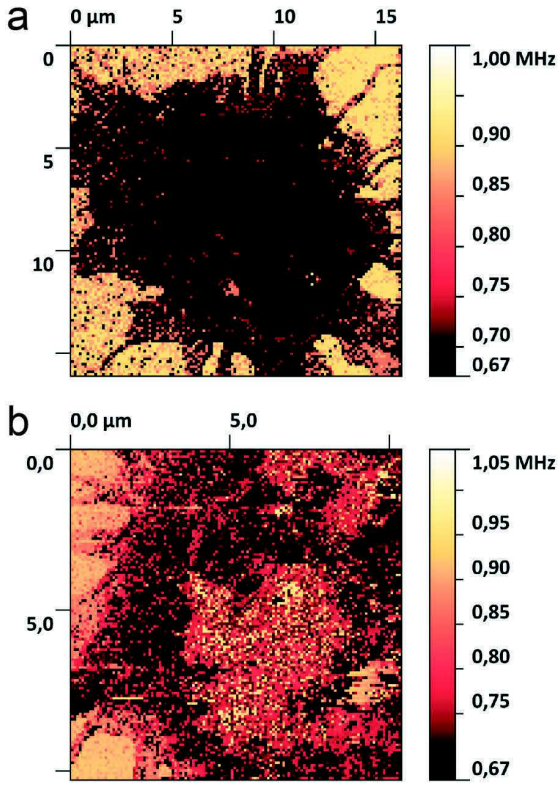

Fig. 4 (a) CRF map of an empty microglia cell; (b) CRF map of a microglia engulfed with NPs.

To gain deeper insight into this phenomenon, several NP labeled cells were investigated. Fig. 5a shows a labeled cell in which two distinct sub-micrometer spherical agglomerates are visible (see the details in Fig. 5b, which can be compared to Fig. 2c–f). Overall, the CR-AFM images revealed the presence of a single huge agglomerate like that shown in Fig. 4 or of one or more smaller agglomerates distributed in the cell volume like those shown in Fig. 5. In order to compare the capabilities of CR-AFM to detect stiff nanomaterials buried in cells with that of other AFM based techniques for nanomechanical imaging, we performed HarmoniX™ (Dimension Icon, Bruker Inc.) on the same sample of microglia cells engulfed with NPs. HarmoniX™ takes advantage of the use of an out-of-axis tip to set into torsional vibration a T-shaped cantilever during tapping.[48,49] The analysis of the cantilever torsional signal allows one to map the elastic modulus of polymers[50–53] and biological materials.[54–56] However, we generally could not detect any subsurface structure in the engulfed microglia cells. Only in a few cases we observed localized agglomerates, like in the case of the cell shown in Fig. 6 (see for comparison Fig. 2g and h).

Without any relation to the topography (Fig. 6a), the stiffness map (Fig. 6b) shows an agglomerate (marked with the arrow), the stiffness of which is comparable to that of the glass substrate. The scarcity of agglomerates detected by HarmoniX™ can be rationalized considering that this technique probes the sample down to penetration depths smaller than CR-AFM. Indeed, we demonstrate that HarmoniX™ can

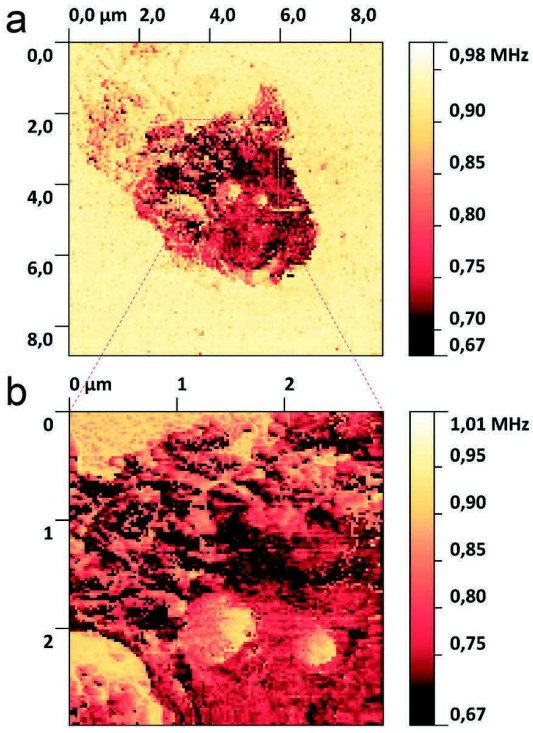

Fig. 5 (a) CRF map and (b) details of a microglia cell engulfed with NPs.

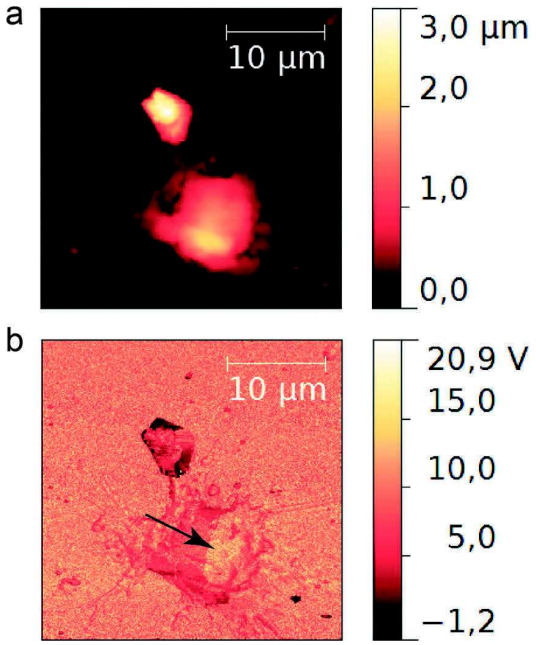

Fig. 6 (a) Topography of a microglia cell engulfed with NPs and (b) the corresponding stiffness map obtained in Harmonix™ mode.

be used on ultrathin soft samples, while we revealed the presence of stiff nanodiamond particles only in the case they emerge from the surface or are buried immediately under the surface.[57] Due to the absence of contrast in the phase image, the agglomerate shown in Fig. 6 is likely to be buried under an ultrathin layer of biological material. Being more affected by the properties of the underlying layers, CR-AFM is more sensitive to buried stiff NPs. Notably, we could not detect isolated NPs using CR-AFM, but only massive agglomerates. This, however, does not necessarily indicate the absence of single NPs but may result from the presently limited resolution of CR-AFM.

Furthermore, the measured CRFs have been analyzed to calculate the apparent contact stiffness of each sample k^*.[38] In particular, by considering the contact between the tip and the sample affected by both a vertical and a tangential spring (with spring constants defined by k^* and k^*_{lat}, respectively), we simulated the f_5 values, for a range of k^*/k_c between 1 and 2×10^4, by numerically solving the characteristic equation of the system,[38] considering the nominal dimensions of the cantilever supplied by the manufacturer and the beam inclined by an angle of 11° with respect to the sample surface. The values of k^* calculated in this way for each sample are reported in Table 1. As expected, the values of CRFs measured on engulfed cells are significantly higher than those measured on the empty ones corresponding to significantly larger values of normalized contact stiffness.

Table 1 Fifth eigenmode contact resonance frequencies (f_5) and normalized contact stiffness k^*/k_c values of empty and NP-engulfed microglia

Sample	f_5 (kHz)	k^*/k_c
Empty cell	670 ± 6	501 ± 56
Cell + NPs	802 ± 7	1698 ± 98

The calculated values of k^*/k_c can be eventually used to estimate the depth at which the agglomerates are located. For this purpose, we assumed well-established models derived for the effective mechanical properties of layered materials during nanoindentation[58] in the realistic approximation that the indentation moduli of the tip (M_{tip}) and of the Fe_3O_4 nanoparticles (M_{NPs}) are much bigger than those of the microglia cells (M_{cell}). The effective indentation modulus measured on the surface of NP-engulfed cells ($M_{cell+NPs}$) in which NP agglomerates are buried under a layer of a cellular matrix with thickness t can be evaluated as

$$\frac{1}{M_{cell+NPs}} = \frac{1}{M_{cell}}(1 - \exp(-\alpha t/a)) \quad (1)$$

in which a is the radius of the contact area between the tip and the sample and α is a geometry-related parameter.[58] In order to obtain a rough estimation of t from the data reported in Table 1, exploiting the proportionality between the evaluated contact stiffness k^* and the sample indentation modulus, we assumed a flat contact between the tip and the sample with radius a = 200 nm, estimated by scanning electron microscopy analysis, and α = 0.5.[58] Thus, eqn (1) allows us to estimate that the agglomerates of NPs are approximately located at t = 100 nm under the sample surfaces. Even though these preliminary results do not provide the exact location of the nanoparticles, they demonstrate the feasibility of our approach for the detection of buried objects underneath the surface.

In conclusion, by detecting Fe_3O_4 NP agglomerates in microglia cells, we demonstrated that CR-AFM can be a suitable technique for subsurface imaging of stiff nanomaterials, either magnetic or not, buried in biological samples. Although the resolution of the technique must be improved, CR-AFM is a promising tool for studying the fate of NPs in biological tissues.

References

1 R. D'Aquino, *Chem. Eng. Prog.*, 2004, **100**, 15S–17S.
2 D. Peer, J. M. Karp, S. Hong, O. C. Farokhzad, R. Margalit and R. Langer, *Nat. Nanotechnol.*, 2007, **2**, 751–760.
3 L. Zhang, F. X. Gu, J. M. Chan, A. Z. Wang, R. S. Langer and O. C. Farokhzad, *Clin. Pharmacol. Ther.*, 2008, **83**, 761–769.
4 B. Chertok, B. A. Moffat, A. E. David, F. Yu, C. Bergemann, B. D. Ross and V. C. Yang, *Biomaterials*, 2008, **29**, 487–496.
5 C.-C. Wang, C.-W. Lee, C.-Y. Huang, J.-Y. Lin, P.-K. Wei and C.-H. Lee, *Appl. Opt.*, 2008, **47**, 2458–2464.
6 E. A. Gibbs-Flournoy, P. A. Bromberg, T. P. Hofer, J. M. Samet and R. M. Zucker, *Part. Fibre Toxicol.*, 2011, **8**, 1.
7 D. van der Zwaag, N. Vanparijs, S. Wijnands, R. De Rycke, B. G. De Geest and L. Albertazzi, *ACS Appl. Mater. Interfaces*, 2016, **8**, 6391–6399.

8 A. E. Porter, M. Gass, K. Muller, J. N. Skepper, P. A. Midgley and M. Welland, *Nat. Nanotechnol.*, 2007, **2**, 713–717.
9 G. Binnig, C. F. Quate and C. Gerber, *Phys. Rev. Lett.*, 1986, **56**, 930–933.
10 U. Hartmann, *Annu. Rev. Mater. Sci.*, 1999, **29**, 53–87.
11 U. Rabe, J. Janser and W. Arnold, *Rev. Sci. Instrum.*, 1996, **67**, 3281–3293.
12 P. Girard, *Nanotechnology*, 2001, **12**, 485–490.
13 A. Majumdar, *Annu. Rev. Mater. Sci.*, 1999, **29**, 505–585.
14 A. Noy, D. V. Vezenov and C. M. Lieber, *Annu. Rev. Mater. Sci.*, 1997, **27**, 381–421.
15 G. Cordova, S. Attwood, R. Gaikwad, F. Gu and Z. Leonenko, *Nano Biomed. Eng.*, 2014, **23**, 31–39.
16 M. J. Cadena, R. Misiego, K. C. Smith, A. Avila, B. Pipes, R. Reifenberger and A. Raman, *Nanotechnology*, 2013, **24**, 135706.
17 H. T. Thompson, F. Barroso-Bujans, J. G. Herrero, R. Reifenberger and A. Raman, *Nanotechnology*, 2013, **24**, 135701.
18 Y. Zhang, M. Yang, M. Ozkan and C. S. Ozkan, *Biotechnol. Prog.*, 2009, **25**, 923–928.
19 Z. Wang and A. Cuschieri, *Int. J. Mol. Sci.*, 2013, **14**, 9111–9125.
20 D. Passeri, C. Dong, M. Reggente, L. Angeloni, M. Barteri, F. A. Scaramuzzo, F. De Angelis, F. Marinelli, F. Antonelli, F. Rinaldi, C. Marianecci, M. Carafa, A. Sorbo, D. Sordi, I. W. C. E. Arends and M. Rossi, *Biomatter*, 2014, **4**, e29507.
21 C. Roduit, S. Sekatski, G. Dietler, S. Catsicas, F. Lafont and S. Kasas, *Biophys. J.*, 2009, **97**, 674–677.
22 C. Roduit, G. Longo, I. Benmessaoud, A. Volterra, B. Saha, G. Dietler and S. Kasas, *J. Mol. Recognit.*, 2012, **25**, 241–246.
23 K. Yamanaka, H. Ogiso and O. V. Kolosov, *Appl. Phys. Lett.*, 1994, **64**, 178–180.
24 G. Shekhawat, A. Srivastava, S. Avasthy and V. P. Dravid, *Appl. Phys. Lett.*, 2009, **95**, 263101.
25 G. S. Shekhawat and V. P. Dravid, *Science*, 2005, **310**, 89–92.
26 A. C. Diebold, *Science*, 2005, **310**, 61–62.
27 L. Tetard, A. Passian, K. T. Venmar, R. M. Lynch, B. H. Voy, G. Shekhawat, V. Dravid and T. Thundat, *Nat. Nanotechnol.*, 2008, **3**, 501–505.
28 L. Tetard, A. Passian, R. H. Farahi and T. Thundat, *Ultramicroscopy*, 2010, **110**, 586–591.
29 S. Amelio, A. V. Goldade, U. Rabe, V. Scherer, B. Bhushan and W. Arnold, *Thin Solid Films*, 2001, **392**, 75–84.
30 U. Rabe, M. Kopycinska, S. Hirsekorn, J. Muñoz Saldaña, G. A. Schneider and W. Arnold, *J. Phys. D: Appl. Phys.*, 2002, **35**, 2621–2635.
31 D. Passeri, A. Bettucci, M. Germano, M. Rossi, A. Alippi, V. Sessa, A. Fiori, E. Tamburri and M. L. Terranova, *Appl. Phys. Lett.*, 2006, **88**, 121910.
32 D. Passeri, M. Reggente, M. Rossi, S. Nunziante Cesaro, V. Guglielmotti, J. J. Vlassak, A. M. De Francesco, R. Scarpelli, M. Hatipoğlu and D. Ajò, *Eur. J. Mineral.*, 2016, **28**, 273–283.
33 J. P. Killgore, D. G. Yablon, A. H. Tsou, A. Gannepalli, P. A. Yuya, J. A. Turner, R. Proksch and D. C. Hurley, *Langmuir*, 2011, **27**, 13983–13987.
34 D. G. Yablon, A. Gannepalli, R. Proksch, J. Killgore, D. C. Hurley, J. Grabowski and A. H. Tsou, *Macromolecules*, 2012, **45**, 4363–4370.
35 D. C. Hurley, S. E. Campbell, J. P. Killgore, L. M. Cox and Y. Ding, *Macromolecules*, 2013, **46**, 9396–9402.
36 A. Ebert, B. R. Tittmann, J. Du and W. Scheuchenzuber, *Ultrasound Med. Biol.*, 2006, **32**, 1687–1702.
37 D. Passeri, M. Rossi, A. Alippi, A. Bettucci, M. L. Terranova, E. Tamburri and F. Toschi, *Physica E*, 2008, **40**, 2419–2424.
38 M. Reggente, M. Rossi, L. Angeloni, E. Tamburri, M. Lucci, I. Davoli, M. L. Terranova and D. Passeri, *JOM*, 2015, **67**, 849–857.
39 M. Natali, D. Passeri, M. Reggente, E. Tamburri, M. L. Terranova and M. Rossi, *AIP Conf. Proc.*, 2016, **1749**, 020008.
40 Z. Parlak and F. L. Degertekin, *J. Appl. Phys.*, 2008, **103**, 114910.
41 J. P. Killgore, J. Y. Kelly, C. M. Stafford, M. J. Fasolka and D. C. Hurley, *Nanotechnology*, 2011, **22**, 175706.
42 R. Massart, *IEEE Trans. Magn.*, 1981, **17**, 1247–1248.
43 F. De Angelis, G. Berardi, F. A. Scaramuzzo, M. Liberatore and M. Barteri, *Int. J. Nanotechnol.*, 2016, **13**, 659–666.
44 M. Jaafar, O. Iglesias-Freire, L. Serrano-Ramón, M. R. Ibarra, J. M. de Teresa and A. Asenjo, *Beilstein J. Nanotechnol.*, 2011, **2**, 552–560.
45 L. Angeloni, D. Passeri, M. Reggente, D. Mantovani and M. Rossi, *Sci. Rep.*, 2016, **6**, 26293.
46 D. Passeri, A. Bettucci, M. Germano, M. Rossi, A. Alippi, A. Fiori, E. Tamburri, M. L. Terranova and J. J. Vlassak, *Microelectron. Eng.*, 2007, **84**, 490–494.
47 J. P. Killgore and D. C. Hurley, *Nanotechnology*, 2012, **23**, 055702.
48 O. Sahin, S. Magonov, C. Su, C. F. Quate and O. Solgaard, *Nat. Nanotechnol.*, 2007, **2**, 507–514.
49 O. Sahin and N. Erina, *Nanotechnology*, 2008, **19**, 445717.
50 P. Schön, K. Bagdi, K. Molnár, P. Markus, B. Pukánszky and G. J. Vancso, *Eur. Polym. J.*, 2011, **47**, 692–698.
51 M. E. Dokukin and I. Sokolov, *Langmuir*, 2012, **28**, 16060–16071.
52 D. Passeri, M. Rossi, E. Tamburri and M. L. Terranova, *Anal. Bioanal. Chem.*, 2013, **405**, 1463–1478.
53 D. Passeri, A. Biagioni, M. Rossi, E. Tamburri and M. L. Terranova, *Eur. Polym. J.*, 2013, **49**, 991–998.
54 K. M. Leung, G. Wanger, Q. Guo, Y. Gorby, G. Southam, W. M. Laue and J. Yang, *Soft Matter*, 2011, **7**, 6617–6621.
55 K. Sweers, K. van der Werf, M. Bennink and V. Subramaniam, *Nanoscale Res. Lett.*, 2011, **6**, 270.
56 M. Rossi, F. Cubadda, L. Dini, M. L. Terranova, F. Aureli, A. Sorbo and D. Passeri, *Trends Food Sci. Technol.*, 2014, **40**, 127–148.
57 D. Passeri, E. Tamburri, M. L. Terranova and M. Rossi, *Nanoscale*, 2015, **7**, 14358–14367.
58 R. B. King, *Int. J. Solids Struct.*, 1987, **23**, 1657–1664.

JOM, Vol. 67, No. 4, 2015
DOI: 10.1007/s11837-015-1340-9

Atomic Force Microscopy Techniques for Nanomechanical Characterization: A Polymeric Case Study

MELANIA REGGENTE,[1] MARCO ROSSI,[1,4] LIVIA ANGELONI,[1] EMANUELA TAMBURRI,[2] MASSIMILIANO LUCCI,[3] IVAN DAVOLI,[3] MARIA LETIZIA TERRANOVA,[2] and DANIELE PASSERI[1]

1.—Department of Basic and Applied Sciences for Engineering, Sapienza University of Rome, Via A. Scarpa 16, 00161 Rome, Italy. 2.—Dipartimento di Scienze & Tecnologie Chimiche - MinimaLab, University of Rome Tor Vergata, Via Della Ricerca Scientifica, 00133 Rome, Italy. 3.—Department of Physics, University of Rome Tor Vergata, Via Della Ricerca Scientifica, 00133 Rome, Italy. 4.—e-mail: marcorossi@uniroma1.it

Atomic force microscopy (AFM) is a versatile tool to perform mechanical characterization of surface samples at the nanoscale. In this work, we review two of such methods, namely contact resonance AFM (CR-AFM) and torsional harmonics AFM (TH-AFM). First, such techniques are illustrated and their applicability on materials with elastic moduli in different ranges are discussed, together with their main advantages and limitations. Then, a case study is presented in which we report the mechanical characterization using both CR-AFM and TH-AFM of polyaniline and polyaniniline doped with nanodiamond particles tablets prepared by a pressing process. We determined the indentation modulus values of their surfaces, which were found in fairly good agreement, thus demonstrating the accuracy of the techniques. Finally, the determined surface elastic moduli have been compared with the bulk ones measured through standard indentation testing.

INTRODUCTION

In the field of nanotechnology, the development of innovative and nondestructive characterization techniques plays a crucial role. Indeed, the characterization of nanostructured hybrid materials (e.g., thin films and nanocomposites) and devices requires the capability of acquiring maps of the local mechanical properties at the nanoscale. Nanoindentation is the most common method for determining the mechanical properties of thin films. However, its applicability is strictly limited by the thickness of the sample. Furthermore, its poor spatial resolution does not allow the reconstruction of an accurate distribution of the sample surface mechanical properties. For this reason, alternative methods, based on atomic force microscopy (AFM), have been developed. By exploiting the high resolution of the AFM, maps of the surface mechanical properties (i.e., indentation modulus) can be achieved. Among these techniques, AFM nanoindentation[1] is the simplest method used to evaluate the local mechanical properties of both stiff and soft samples.[2–5] AFM nanoindentation consists in locally recording force-indentation (FI) curves. If the FI curves are collected at each point of the scanning area, then a stiffness map of the sample is obtained in the so-called force volume mode.[6] Due to the low of resolution and the long acquisition time required by this technique, different AFM-based methods have been established. In particular, contact resonance AFM (CR-AFM) and torsional harmonics AFM (TH-AFM) can be used to perform both qualitative and quantitative maps of the mechanical properties of the sample surfaces with nanometric lateral spatial resolution. CR-AFM is a well-established technique for the characterization of hard elastic materials.[7–9] Furthermore, recently it has been employed to investigate the indentation moduli and the viscoelastic properties (i.e., storage and loss moduli)[10–13] of soft polymeric films. Instead, TH-AFM is one of the latest AFM mode specifically developed to characterize soft matters. It operates in tapping mode using a T-shaped cantilevers with an out-of-axis tip that periodically indents the surface during the scanning. By collecting the FI curves produced by

(Published online March 6, 2015)

the periodical indentation of the tip into the sample, maps of the mechanical properties of the surface sample are achieved.[14–17]

In previous studies, by adopting the above-mentioned AFM techniques (i.e., AFM nanoindentation, CR-AFM, and TH-AFM), we deeply analyzed the mechanical properties of hybrid nanocomposite materials based on conductive polymers, i.e., polyaniline (PANI) and poly(3,4-ethylenedioxythiophene) (PEDOT) filled with nanodiamond (ND) particles.[5,17–22] In particular, we have pointed out that ND is able to induce a high structural order of the polymerchains that organize themselves in the form of nanofibrils, nanoglobules, or nanoparticles depending on the experimental conditions of the synthesis. On such materials, we performed accurate material characterizations at the nanoscale.[5,17,18,21,22]

Considering the results obtained so far, in the current study we investigated how the mechanical properties of the single nanostructures can rule the surface mechanical properties of a macroscale sample, especially when it consists of a dense and forced packing of the individual nanostructures. For this purpose, we first synthesized PANI and polyaniline doped with nanodiamond particles (PANI-ND) by a precipitation method, and then we prepared PANI and PANI-ND tablets by a pressing process conducted at 200 bar. Thus, we have investigated the effect of the compression of the polymer chains on both the bulk and surface mechanical properties of the two final tablets by using standard nanoindentation for the bulk properties and both TH-AFM and CR-AFM for the surface ones.

TECHNIQUES

Torsional Harmonics Atomic Force Microscopy

In TH-AFM, the sample surface is imaged in tapping mode. The cantilever is oscillating at (a frequency close to) its first free flexural resonance f_{01}. In case of compliant samples, during a portion of each oscillation cycle, the tip indents the sample surface. As a consequence, during each oscillation cycle the cantilever deflection signal contains a complete loading/unloading force versus penetration curve, which is repeated with period $T = 1/f_{01}$. Therefore, the periodic force versus penetration curve could be reconstructed through inverse Fourier transform from the harmonic components at frequencies $N \times f_{01}$ of the deflection signal. Nevertheless, such a procedure is limited by to the poor signal-to-noise ratio due to the presence of the higher flexural modes of the cantilever.[23,24] To overcome this practical limitation, a T-shaped cantilever with out-of-axis tip is used. The tip-sample contact produces a torque that excites the torsion of the cantilever, enhanced by its geometry. Analogously to the deflection signal, the cantilever torsional signal contains a complete loading/unloading force versus penetration curve, periodic with period $T = 1/f_{01}$, which can be reconstructed through inverse Fourier transform analysis. In this case, the use of the torsional signal ensures a higher signal-to-noise ratio because the first torsional resonance frequency t_{01} is about 20 times higher than f_{01} and thus at least 20 harmonic components of the signal are located in an undistorted spectral region.[23,24] As a result, during the tapping, force-distance curves are obtained at each point of the scanned area. After proper calibrations, such curves are analyzed to map the sample indentation modulus (M_s) through the fitting of the unloading portion of the curve with the Derjaguin–Muller–Toporov (DMT) model.[25] Additional parameters mapped during the scanning are the peak force, the tip-sample adhesion force, and the dissipated energy during each indentation cycle.[17] In particular, the quantitative mapping of M_s requires the knowledge of R_t. Alternatively, a sample with known elastic modulus can be used as a reference, which is the approach used in this work.

Because it is based on AFM tapping mode and thus not requiring the continuous contact between tip and sample, TH-AFM finds natural application in the nanomechanical study of soft samples, like polymers or biological structures. The materials that have been effectively investigated by TH-AFM have indentation modulus ranging approximately from 10 MPa up to 10 GPa,[24] including highly oriented pyrolytic graphite (HOPG),[24] polymers,[15,24] polymer blends,[17,24] polymer-based (nano) composites,[14,21] pigment coatings,[26] amyloid fibrils,[27] and bacterial nanowires.[28] Although the range of investigable elastic moduli is not as wide as those of other AFM-based techniques, TH-AFM is particularly suitable to acquire simultaneous high-resolution (i.e., 256 × 256 or 512 × 512 points) and high-speed (e.g., a few minutes) mechanical images of soft samples, which conversely may represent challenging materials for other AFM-based methods, mainly for those working in contact mode. Also, TH-AFM probes the sample down to a few tens of nanometers from the surface. As a consequence, the mechanical properties of the bulk may be not accessible and the comparison between TH-AFM data and those from techniques that probe the sample down to bigger penetration depths (such as depth sensing indentation) may be misleading. On the otherhand, the shallow penetration depth makes TH-AFM particularly suitable for the study of mechanical properties of polymeric ultrathin films.

Contact Resonance Atomic Force Microscopy

The CR-AFM technique has been extensively described in previous works.[29,30] Briefly, the AFM experimental apparatus is equipped with a piezoelectric transducer that is coupled to the back of the sample. The piezoelectric transducer excites out-of-plane oscillation at ultrasonic frequencies of the

sample surface. When the AFM tip becomes in contact with the sample surface, such oscillation results in the high-frequency modulation of both the cantilever deflection and the tip-sample penetration depth. By analyzing the high-frequency components of the cantilever deflection signal through the AFM electronics, one can measure the resonance frequencies of the sample-tip-cantilever system, namely, the contact resonance frequencies (CRFs) $f_n's$, where the subscript n indicates the nth mode. The experimentally determined values of $f_n's$ can be used to evaluate the elastic properties of the surface of the sample. In particular, the indentation modulus of the samples (M_s) can be obtained, which is defined as $M_s = E_s/(1-\upsilon_s^2)$ for isotropic materials, where E_s and υ_s are the Young's modulus and the Poisson ratio of the sample, respectively. To this aim, the experimentally measured values of $f_n's$ are analyzed assuming a suitable modelfor the cantilever, the most commonly used of which is depicted in Fig. 1a. The cantilever is approximated as a uniform beam with length L and rectangular cross section with thickness t and width w, with its main axis parallel to the sample surface. The tip is placed at distance L_1 from the cantilever clamped end, so that the ratio $r = L_1/L$ can be defined. The tip-sample contact is modeled as a linear spring, the elastic constant of which is the contact stiffness k^*, which accounts for the mechanical properties of the sample surface, i.e., M_s. The damping and the effect of tip-sample lateral forces are neglected. The characteristic equation of the system in Fig. 1a, whose explicit analytical expression is easily obtained and can be found elsewhere,[29] shows that the values of $f_n's$ are fixed by r, k^* and a geometrical parameter c_c characteristic of each cantilever. In particular, it is observed that for fixed values of r and c_c, the higher k^* the higher $f_n's$. Such a characteristic equation can be inverted so that $k^* = k^*(f_n, r)$ is obtained as a function of both the generic f_n and r. To evaluate r that is generally unknown, the CRFs corresponding to two different modes are measured (say f_n and f_m, with $n \neq m$). r is obtained as the value in correspondence of which the two CRFs give the same contact stiffness, i.e., by solving $k^*(f_n, r) = k^*(f_m, r)$. Thus, k^* is determined and can be used to evaluate M_s, assuming that the values of the indentation modulus of the tip M_t, the tip radius R_t, and the normal load applied by the cantilever F_N are known. Indeed, in case of parabolical tip, M_s is evaluated from k^* using the relation

$$\frac{1}{k^{*3/2}} = \frac{1}{\sqrt{6R_tF_N}}\left(\frac{1}{M_s} + \frac{1}{M_t}\right) \quad (1)$$

F_N can be easily calculated from the static cantilever deflection. R_t is generally evaluated by calibration of the technique using a reference sample with known mechanical properties. M_t is either assumed as the theoretical indentation modulus of the material forming the tip[30,31] or independently measured using a second reference material.[32] The latter approach has been demonstrated to overcome also the limitation due to neglecting the tip-sample lateral forces, which represents a major source of inaccuracy in CR-AFM measurements especially when characterizing polymers.[33] Indeed, a more comprehensive model of the system is depicted in Fig. 1b, where the cantilever is assumed tilted with respect to the surface of an angle α and the tip height h_t is considered.[34–36] Moreover, the lateral contact stiffness k^*_{lat} is introduced, which accounts for the tip-sample lateral coupling, i.e., the sample shear modulus $G_s = \frac{1}{2}E_s/(1+\upsilon_s)$.[36] For practical purposes, it has been demonstrated that k^*_{lat} can be neglected and experimental data can be analyzed through the model in Fig. 1a provided that fictitious values of M_t and r are assumed.[33] Conversely, including lateral coupling in the model allows one to analyze experimental data assuming the real values of such parameters. In this case, the values of all the parameters in the model are fixed and $k^*(f_n, r) = k^*(f_m, r)$ is not imposed. As a consequence, different values of k^* may be obtained in correspondence of different modes.[11,13] This may represent an artifact originated from approximation in the model

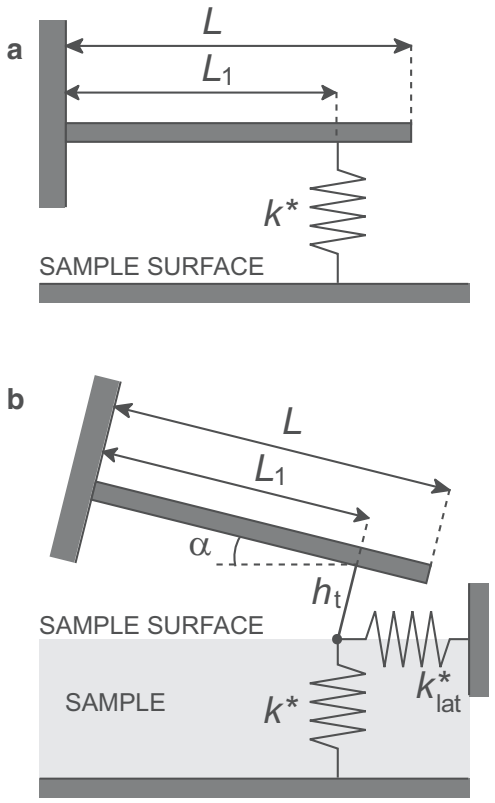

Fig. 1. Sketch of two models used to analyze CR-AFM data: (a) normal spring coupled cantilever, where lateral forces, tip height, and cantilever tilt angle are neglected; (b) normal and tangential spring coupled cantilever.

as well as a real effect reflecting frequency-dependent mechanical parameters of the sample. Based on AFM contact mode, CR-AFM is particularly suitable for the nanomechanical characterization of relatively stiff materials, including diamond-like carbon coatings,[7,9] ultrathin films,[10] piezoelectric materials,[37] single crystals,[30] nanobelts and nanotubes,[38,39]and epoxy-based nanocomposites.[40–42] Recently, CR-AFM has been extended to softer samples, i.e., polymers. In particular, CR-AFM allows one to determine the storage and loss moduli of viscoelastic materials from the analysis of the contact resonance frequencies and the corresponding quality factors.[11,13] Finally, such parameters have been mapped on the surface of polymeric blends.[12,43]Notwithstanding these results, the application of CR-AFM to soft materials still remains challenging because it involves the continuous tip sample contact during all the image acquisition, which is actually quite timeconsuming even for not too-high-resolution images (e.g., 10–20 min for 128 × 128 points images). Moreover, some difficulties in the quantitative analysis of CR-AFM data may arise from the need for more accurate models in which lateral forces or dissipation are not neglected.

CASE STUDY: POLYANILINE AND POLYANILINE-NANODIAMOND COMPOSITES

In this section, we report the results of the functional characterization of PANI and PANI-ND. The aim of the study is to determine how the introduction of detonation NDs modulates the elastic surface properties of the samples when they are prepared by a pressing process. To this end, the indentation moduli of PANI and PANI-ND samples have been calculated by employing two different AFM-based techniques, i.e., TH-AFM and CR-AFM previously described.

Materials

PANI and PANI-ND materials were synthesized following a protocol optimized in previous studies. Namely, a precipitation polymerization of aniline monomer was carried out in acidic aqueous solution using an anionic surfactant, i.e., sodium dodecyl sulfate, as a dopant and dispersing agent of ND particles in the case of the PANI-ND composite. The complete characterization of the obtained PANI and PANI-ND samples was performed using optical microscopy, both transmission and scanning electron microscopy, Raman spectroscopy, reflection high-energy electron diffraction, X-ray diffraction, and thermogravimetric analysis, which can be found elsewhere.[18] Tablet samples 1 mm thick were prepared by pressing, at 200 bar, 100 mg of PANI and PANI-ND.

Equipment

CR-AFM experiments have been performed using an AFM setup (Solver; NT-MDT, Moscow, Russia) equipped with a silicon cantilever (CSG10; NT-MDT). The cantilever used in the experiments has a length of 250 μm, width of 35 μm, thickness of 1 μm, and nominal spring constant k_c = 0.1 N/m. The cantilever has been used after extensive scanning of the surface of hard samples to severely wear the tip, as large tip radius and thus large tip-sample contact radius values reduce the stress under the tip and consequently diminish the damaging of soft samples during AFM contact mode imaging. For TH-AFM measurements, a standard AFM apparatus (Dimension Icon, Bruker Inc., Madison, WI) has been employed that was equipped with T-shaped cantilevers (HMX10; Bruker Inc.) with nominal spring constant k_c = 4 N/m. Brand-new cantilevers have been used after some preliminary scans of the polymeric samples to allow the tip radius to stabilize. Both CR-AFM and TH-AFM experiments have been performed in air and at room temperature. In both the techniques, quantitative measurements have been performed using a blend of polystyrene (PS) and low-density polyethylene (LDPE) reference sample (PS-LDPE; Bruker Inc.) with known mechanical properties for calibration purposes. The PS-LDPE sample consists of a matrix of PS in which round-shaped regions of LDPE are dispersed, deposited onto a silicon substrate. The PS matrix has an indentation modulus equal to 2 GPa, while that of LDPE regions is about 100 MPa.

The indentation modulus and hardness measurements have been performed by Nano Test Micro Materials Ltd. (Wrexham, U.K.), using a diamond Berkovitch tip. For each sample, an array of 10 × 10 points have been probed, covering a surface of a few microns squared, by applying a maximum load of 5 mN, holding time of 10 s, indentation depth doing range between 500 nm and 1200 nm, penetration speed/load control of 0.2 mN/s. The instrumental uncertainty of the indenter is approximately 2%.[44,45]

RESULTS AND DISCUSSION

Preliminarily to the mechanical characterization of the samples, the morphology of the samples has been characterized in standard AFM tapping mode. In Fig. 2a and b two typical topographical images of PANI are reported at two different magnifications after subtraction of polynomial background in order to emphasize the different nanoscale features, which show a granular structure. Conversely, on the surface of PANI-ND fibrillar features are visible (Fig. 2c and d) which are triggered by the presence of the ND particles, as already observed by Tamburri et al.[18]

To validate the results retrieved with TH-AFM, by verifying the stability and the accuracy of the technique, several preliminary measurement sessions have been carried out under different operating conditions (i.e., different cantilevers of the same type and set-point values). In each experiment, the

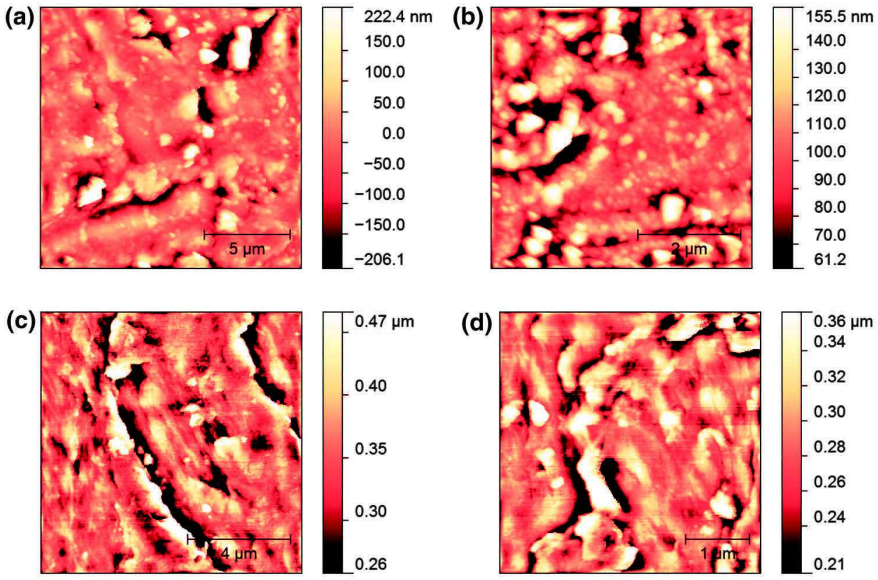

Fig. 2. Topographical images of PANI (a and b) and PANI-ND (c and d). Polynomial background has been subtracted to highlight the nanoscale features of the surfaces.

characterization of the PS-LDPE reference sample has been performed twice, before and after the measurement on the investigated samples. In each experimental session, all the samples have been scanned under the same operating conditions (i.e., same set-point, drive-frequency and drive-amplitude values). The acquired indentation modulus maps, initially expressed in arbitrary units, have been calibrated on the PS-LDPE reference sample according to the procedure supplied by the producer. In particular, the indentation modulus of the PS matrix has been used for the calibration of the technique while the LDPE has been used as a control material. For each sample, the statistics were calculated on the collected indentation modulus maps to assign the values of indentation moduli and corresponding uncertainties. As an example of the typical results of a TH-AFM measurement session, the histograms of the indentation moduli of the investigated and reference samples are reported in Fig. 3. It should be noted that the obtained value of the indentation modulus of the LDPE is in fairly good agreement with the expected one even though slightly lower, indicating a not perfect calibration for low modulus values. Nevertheless, since the moduli of the investigated PANI and PANI-ND samples are of the same order of magnitude of those of the PS, the calibration can be considered accurate enough in the range of interest. The obtained indentation modulus values of PANI and PANI-ND are reported in Table I.

CR-AFM is a two steps technique. In the first step, the free resonance frequencies of the cantilever oscillating in air (f_{0n}) are measured to experimentally determine the characteristic parameters of the

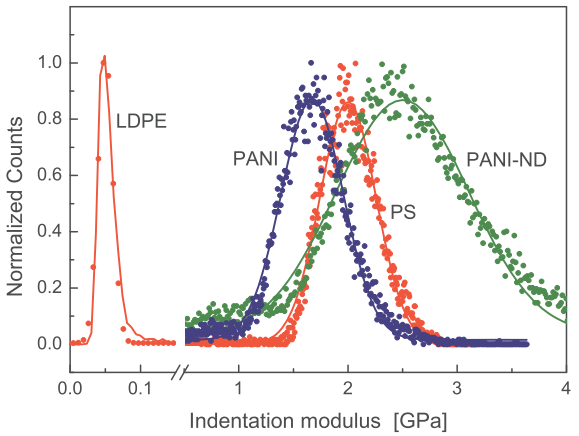

Fig. 3. Histograms of the indentation moduli measured on the PS-LDPE (red), PANI-ND (green) and PANI (blue) samples (symbols) together with the corresponding Gaussian fits (solid lines) (Color figure online).

cantilever (i.e., the c_c parameter). In Table II, the first four measured natural frequencies are reported and compared with those calculated supposing the cantilever as a uniform rectangular beam.[29] It should be noted that the ratio between the calculated and the measured values of the frequencies keeps constant for each mode of the cantilever. Indeed, the used cantilever is rectangular and the differences between measured and calculated free resonance frequencies result from the deviation of the actual geometrical parameters from the nominal ones. The ratio between calculated and experimental free resonance frequencies can be used to indi-

Table I. Indentation modulus (M_S) of PANI and PANI-ND measured through TH-AFM, CR-AFM, and standard nanoindentation and nanoindentation hardness (H_S)

Samples	TH-AFM M_S (GPa)	CR-AFM M_S (GPa)	Nanoindentation M_S (GPa)	Nanoindentation H_S (MPa)
PANI	1.4 ± 0.2	1.2 ± 0.1	4.3 ± 1.4	130 ± 60
PANI-ND	2.3 ± 0.5	3.1 ± 0.5	12.0 ± 5.0	300 ± 200

viduate the correct free flexural resonances in case of the presence of multipeaks. In this work, CR-AFM nanomechanical measurements have been performed using only the first and the third resonance frequencies. The parameter c_c was determined from the values of the first (f_{01}) and third (f_{03}) free resonance frequencies through the relation

$$c_c = \frac{k_n L}{\sqrt{f_{0n}}} \quad (2)$$

where $k_n L$ are eigenvalues of each mode which are well known from the literature.[29] In particular, the value of c_c was determined for each mode, so that c_{c1} and c_{c3} were calculated from f_{01} and f_{03}, respectively.

In the second step of the procedure, the tip is brought in contact with the sample surface, which is set into oscillation through a piezoelectric transducer coupled with the sample back side. Maps of the first and third CRFs (f_1, f_3) of the investigated samples are recorded and semiquantitative maps of the samples stiffness were achieved. To extract quantitative information about the indentation modulus of the investigated samples and eliminate the uncertainty related to the mechanical (M_t) and geometrical (R_t) properties of the tip, calibration has been performed on the PS-LDPE reference sample. Furthermore, to guarantee the stability of the experimental session, it has been tested twice, before and after the two investigated samples. As en examples, in Fig. 4 a typical CR-AFM map of f_1 on PS-LDPE is reported, together with a profile of the first CRF extracted from the map in correspondence of the line. As expected, in correspondence of the LDPE regions the values of the frequencies decrease, as a result of the lower value of indentation modulus and thus of k^*. To reduce the possibility of tip damaging between the two investigated samples, we purposely investigated the samples following the decreasing order of expected stiffness, i.e., starting from the sample which we expected to be the stiffer one. In this way, we were able to monitor the performances of our technique during the whole experimental session. Furthermore, to prevent tip wear, we avoided long scans of the surfaces limiting the acquisition to a number of lines, which ensured enough points to make a significant statistics of the results. For all the reference and investigated samples, f_1 and f_3 have been measured by main-

Table II. Calculated and measured values of the first four flexural resonance frequencies of the cantilever used in CR-AFM

Frequency	Calculated (kHz)	Measured (kHz)
f_{01}	19	26.7
f_{02}	120	169.8
f_{03}	341	477.3
f_{04}	664	933.0

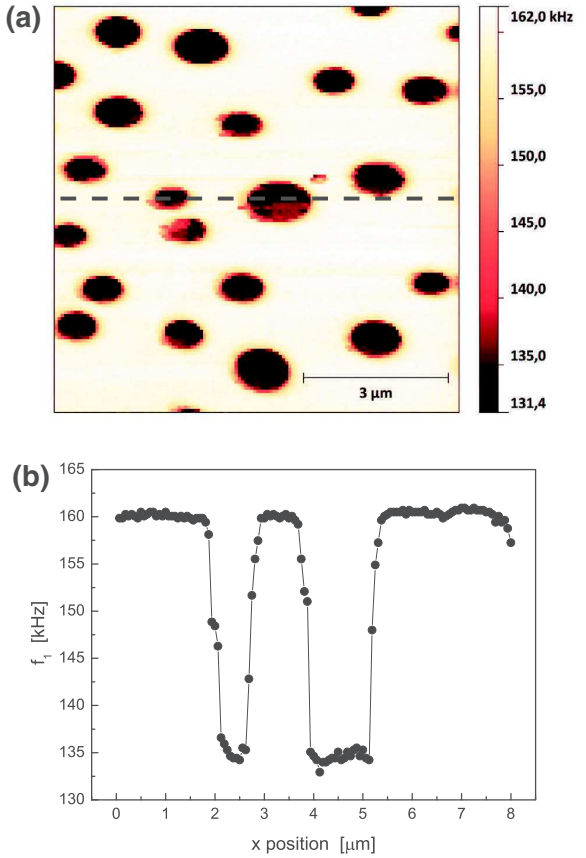

Fig. 4. (a) CR-AFM map of the first contact resonance frequency acquired on the PS-LDPE reference sample and (b) profile extracted in correspondence of the dashed line.

taining constant the cantilever deflection set point, i.e., thus the applied load. Statistics of the CRFs maps have been used to determine mean values and corresponding uncertainties of the indentation modulus of the samples. As expected, CRFs measured on the PANI-ND samples are higher than that measured on the undoped PANI, indicating that the former is stiffer than the latter.

In the post experiment data analysis, CRFs have been analyzed with a suitable method to calculate the contact stiffness of each sample (k_s^*) and to quantitative determine the value of their indentation modulus (M_s). To this aim, the simplest model depicted in Fig. 1a is the most widespread one to analyze CR-AFM data. Nevertheless, it has been recently shown that on polymeric materials the presence of tangential spring constant k_{lat}^*, which is related to the reduced sample shear modulus,[36] may dramatically affect the calibration procedure.[33] Thus, we analyzed our CR-AFM experimental data by modeling the contact between the tip and the sample by considering both a vertical and a tangential spring (with spring constant defined by k^* and k_{lat}^*, respectively), i.e., assuming the model depicted in Fig. 1b. In particular, considering realistic or experimentally determined values for the parameters of the model in Fig. 1b, we simulated the f_1 and f_3 values in a wide range of k^*/k_c values, to determine the values of k_s^* for each sample from the measured values of CRFs. In details, since the $M_t \gg M_s$, the ratio k_{lat}^*/k_*, was determined by the following expression:[34]

$$\frac{k_{lat}^*}{k^*} \approx \frac{2(1-\upsilon_s)}{2-\upsilon_s} \tag{3}$$

The value of the Poisson ratio υ_s has been approximated to 0.4 for all the measured samples. The dimensions of the cantilever have been assumed as the nominal ones supplied by the manufacturer, and the beam was inclined by an angle $\alpha = 11°$ with respect to the sample surface. The tip, with nominal height h = 15 μm, was placed at a distance L_1 from the cantilever clamped end, and its position was defined by the $r = L_1/L = 0.985$, experimentally evaluated by scanning electron microscopy analysis. The first and third CRFs have been determined by numerically solving the characteristic equation of the system (reported in Ref. 36) for values of k^*/k_c ranging between 1 and 10^4. In this way, curves of the f_1 and f_3 CRFs versus the normalized contact stiffness k^*/k_c are obtained, which are reported in Fig. 5 (solid line). For comparison, for the same values of k^*/k_c the CRFs determined using the simplest model, which neglects k_{lat}^*, are reported (dotted lines). It should be explicitly observed that the simple model is unable to predict the experimental CRFs, as the well-known saturation of the CRFs for large stiffness k^*/k_c[29] corresponds to frequency values lower than those measured on the

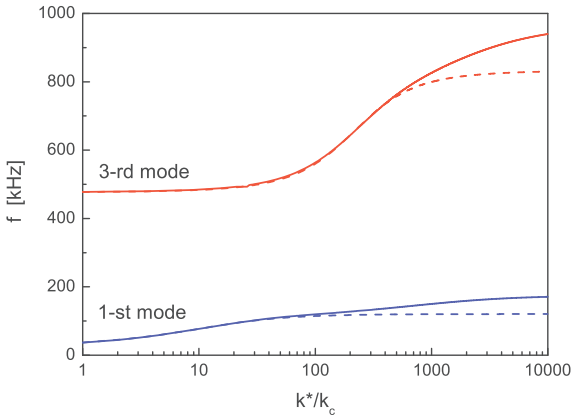

Fig. 5. First (blue lines) and third (red lines) contact resonance frequencies as a function of the normalized contact stiffness k^*/k_c. The dotted lines were calculated considering the simple clamped spring-coupled cantilever, i.e., the model in Fig. 1a. The solid curves are obtained introducing the contribution of a lateral spring (k_{lat}^*), i.e., the model in Fig. 1b (Color figure online).

stiffer samples. Conversely, the CRFs experimentally determined on all the samples are predicted using the model (Fig. 1b), which takes into account lateral tip sample coupling. From these curves, two values of the k^*, one for each CRFs recorded, have been extracted for each samples. From the values of k^*/k_c those of M_s have been calculated. As the inclusion of k_{lat}^* in the model allows one to consider the real values of the parameters,[33] being $M_t \gg M_s$, Eq. 1 can be approximated as

$$(k^*)^{3/2} = \sqrt{6R_tF_N}M_s = AM_s \tag{4}$$

indicating a direct proportionality between $k^{*3/2}$ and M_s (for both the two chosen vibration modes). The proportionality coefficient A has been determined on the PS sample, independently for each of the analyzed modes, and the moduli of the LDPE control materials and of PANI and PANI-ND are finally retrieved. We want to explicitly report that the indentation modulus of the LDPE control material retrieved using f_1 (M_{LDPE} = 130 MPa) fairly matches the reference value, whereasthe one retrieved using f_3 (M_{LDPE} = 660 MPa) is significantly higher. This result can be rationalized considering that the LDPE islands are tens of nanometers thick and are surrounded by PS. In TH-AFM, the indentation depth and the contact radius are a few nanometers, and therefore, the technique is sensitive to the mechanical properties in a volume under the surface with a depth usually not exceeding a few tens of nanometers. Conversely, as CR-AFM is performed using worn tips with large radius, larger tip-sample contact radii are involved. In the case of PS, the contact radius can be evaluated as large as some tens of nanometers. In addition, in CR-AFM higher modes are more sensitive to buried features due to the in-

creased effective stiffness.[46] Therefore, the third CRF is more sensitive to the presence of PS under the LDPE islands. Averaging the data obtained for the two modes, the indentation moduli of PANI and PANI-ND are retrieved and reported in Table I.

We observe that the results obtained by TH-AFM and CR-AFM are in fairly good agreement, which represents a cross-validation of the techniques. Surface indentation moduli retrieved with the two AFM-based techniques have been compared withthe bulk ones measured by standard nanoindentation. The latter are reported together with the measured indentation hardness (H_s) in Table I, which is obtained with penetration depth varying between 500 nm and 1.2 μm, where the experimental uncertainties arerelated to the inhomogeneity of the samples. Bulk indentation moduli are significantly higher for both samples, although the relative variation of modulus due to the introduction of NDs is almost the same for all the three techniques. In particular, bulk indentation modulus of PANI is in good agreement with the value we have previously determined by AFM nanoindentation.[5] It is well known that the mechanical properties of the surface of polymers are decreased by the presence of a softer layer (a few nanometers thick) with reduced density.[17] Thus, our results indicate that, different from standard indentation, which is sensitive to bulk mechanical properties, both TH-AFM and CR-AFM can probe the actual surface elastic modulus. This represents a further confirmation of the importance of AFM-based techniques to measure mechanical properties at the nanoscale especially in case of two-dimensional materials such as thin films and layers.

CONCLUSION

We have described two AFM-based techniques for the characterizations of the surface indentation modulus of materials at the nanoscale, namely, TH-AFM and CR-AFM. They operating principles, the range of measurable sample indentation moduli, the main advantages and limitations have been discussed. Then, such techniques have been demonstrated in a particular case study, i.e., the nanomechanical characterization of polyaniline and polyaniniline doped with nanodiamond particles tablets prepared by a pressing process. The agreement between surface indentation moduli obtained with the two techniques represented a cross-validation of the methods. When compared with bulk indentation moduli retrieved with standard nanoindentation, we observed an almost constant ratio between the data for PANI and PANI-ND. Moreover, surface indentation moduli measured with the AFM-based methods are significantly lower than the bulk ones measured with nanoindentation, which can be attributed to the presence of nanometrical surface layers of polymer softer than the bulk. Overall, the results confirm the importance of methods such the AFM-based ones for the mechanical testing at the nanoscale, which are capable of investigating ultrathin films and layers out of the range of standard mechanical tests.

REFERENCES

1. C. Reynaud, F. Sommer, C. Quet, N. El Buonia, and D.T. Minh, *Surf. Interface Anal.* 30, 185 (2000).
2. T. Kocourek, M. Růžek, M. Landa, M. Jelínek, J. Mikšovský, and J. Kopeček, *Surf. Coat. Tech.* 205, S67 (2011).
3. Y.H. Ding, X.H. Deng, X. Jiang, P. Zhang, J.R. Yin, and Y. Jiang, *J. Mater. Sci.* 48, 3479 (2013).
4. D. Passeri, A. Bettucci, A. Biagioni, M. Rossi, A. Alippi, E. Tamburri, M. Lucci, I. Davoli, and S. Berezina, *Ultramicroscopy* 109, 1417 (2009).
5. D. Passeri, A. Alippi, A. Bettucci, M. Rossi, A. Alippi, E. Tamburri, and M.L. Terranova, *Synth. Met.* 161, 7 (2011).
6. S.N. Magonov and D.H. Reneker, *Annu. Rev. Mater. Sci* 27, 175 (1997).
7. S. Amelio, A.V. Goldade, U. Rabe, V. Scherer, B. Bhushan, and W. Arnold, *Thin Solid Films* 392, 75 (2001).
8. M. Prasad, M. Kopycinska, U. Rabe, and W. Arnold, *Geophys. Res. Lett.* 29, 1172 (2002).
9. D. Passeri, A. Bettucci, M. Germano, M. Rossi, A. Alippi, V. Sessa, A. Fiori, E. Tamburri, and M.L. Terranova, *Appl. Phys. Lett.* 88, 121910 (2006).
10. M. Kopycinska-Müller, R.H. Geiss, J. Müller, and D.C. Hurley, *Nanotechnology* 16, 703 (2005).
11. P.A. Yuya, D.C. Hurley, and J.A. Turner, *J. Appl. Phys.* 104, 074916 (2008).
12. J.P. Killgore, D.G. Yablon, A.H. Tsou, A. Gannepalli, P.A. Yuya, J.A. Turner, R. Proksch, and D.C. Hurley, *Langmuir* 27, 13983 (2011).
13. P.A. Yuya, D.C. Hurley, and J.A. Turner, *J. Appl. Phys.* 109, 113528 (2011).
14. P. Schön, S. Dutta, M. Shirazi, J. Noordermeer, and G.J. Vancso, *J. Mater. Sci.* 46, 3507 (2011).
15. P. Schon, K. Bagdi, K. Molńar, P. Markus, B. Pukánszky, and G.J. Vancso, *Eur. Polym. J.* 47, 692 (2011).
16. M.E. Dokukin and I. Sokolov, *Langmuir* 28, 16060 (2012).
17. D. Passeri, M. Rossi, E. Tamburri, and M.L. Terranova, *Anal. Bioanal. Chem.* 405, 1463 (2013).
18. E. Tamburri, V. Guglielmotti, S. Orlanducci, M.L. Terranova, D. Sordi, D. Passeri, R. Matassa, and M. Rossi, *Polymer* 53, 4045 (2012).
19. E. Tamburri, V. Guglielmotti, S. Orlanducci, M.L. Terranova, D. Passeri, M. Rossi, and D. Sordi, *MRS Proceedings*, vol. 1452 (Cambridge, U.K.: Cambridge UniversityPress, 2012), pp. mrss12–1452–ff05–06.
20. M.L. Terranova, E. Tamburri, V. Guglielmotti, F. Toschi, S. Orlanducci, D. Passeri, and M. Rossi, *AIP Conf. Proc.* 1459, 111 (2012).
21. D. Passeri, A. Biagioni, M. Rossi, E. Tamburri, and M.L. Terranova, *Eur. Polym. J.* 49, 991 (2013).
22. E. Tamburri, V. Guglielmotti, R. Matassa, S. Orlanducci, S. Gay, G. Reina, M.L. Terranova, D. Passeri, and M. Rossi, *J. Mater. Chem. C* 2, 3703 (2014).
23. O. Sahin, S. Magonov, C. Su, C.F. Quate, and O. Solgaard, *Nat. Nanotechnol.* 2, 507 (2007).
24. O. Sahin and N. Erina, *Nanotechnology* 19, 445717 (2008).
25. B.V. Derjaguin, V.M. Muller, and Y.P. Toporov, *J. Colloid Interface Sci.* 53, 314 (1975).
26. P. Ihalainen, J. Järnström, A. Määttänen, and J. Peltonen, *Colloid Surf. A* 373, 138 (2011).
27. K. Sweers, K. van der Werf, M. Bennink, and V. Subramaniam, *Nanoscale Res. Lett.* 6, 270 (2011).
28. K.M. Leung, G. Wanger, Q. Guo, Y. Gorby, G. Southam, W.M. Laue, and J. Yang, *Soft Matter* 7, 6617 (2011).
29. U. Rabe, J. Janser, and W. Arnold, *Rev. Sci. Instrum.* 67, 3281 (1996).
30. D. Passeri, A. Bettucci, M. Germano, M. Rossi, A. Alippi, S. Orlanducci, M.L. Terranova, and M. Ciavarella, *Rev. Sci. Instrum.* 76, 093904 (2005).

31. S. Jena, R.B. Tokas, N. Kamble, S. Thakur, D. Bhattacharyya, and N.K. Sahoo, *Thin Solid Films* 537, 163 (2013).
32. G. Stan and W. Price, *Rev. Sci. Instrum.* 77, 103707 (2006).
33. D. Passeri, M. Rossi, and J.J. Vlassak, *Ultramicroscopy* 128, 32 (2013).
34. U. Rabe, *Applied Scanning Probe Methods II*, ed. B. Bhushan andH. Fuchs (New York: Springer, 2006), pp. 37–90.
35. U. Rabe, M. Kopycinska-Müller, S. Hirsekorn, *Acoustic Scanning Probe Microscopy*, ed. by F. Marinello, D. Passeri, and E. Savio (Berlin: Springer, 2012), chap. 5, pp. 123–153.
36. D.C. Hurley and J.A. Turner, *J. Appl. Phys.* 102, 033509 (2007).
37. M. Kopycinska, C. Ziebert, H. Schmitt, U. Rabe, S. Hirsekorn, and W. Arnold, *Surf. Sci.* 532, 450 (2003).
38. Y. Zheng, R.E. Geer, K. Dovidenko, M. Kopycinska-Müller, and D.C. Hurley, *J. Appl. Phys.* 100, 124308 (2006).
39. G. Stan, C.V. Ciobanu, T.P. Thayer, G.T. Wang, J.R. Creighton, K.P. Purushotham, L.A. Bendersky, and R.F. Cook, *Nanotechnology* 20, 035706 (2009).
40. M. Preghenella, A. Pegoretti, and C. Migliaresi, *Polym. Test.* 25, 443 (2006).
41. D. Passeri, M. Rossi, A. Alippi, A. Bettucci, M.L. Terranova, E. Tamburri, and F. Toschi, *Physica E* 40, 2419 (2008).
42. W. Zhao, R.P. Singh, and C.S. Korach, *Compos. Part A.* 40, 675 (2009).
43. D.G. Yablon, A. Gannepalli, R. Proksch, J. Killgore, D.C. Hurley, J. Grabowski, and A.H. Tsou, *Macromolecules* 45, 4363 (2012).
44. A. Fava, M. Lucci, D. Faso, A. Luzzi, M. Salvato, A. Vecchione, R. Fittipaldi, I. Ottaviani, I. Colantoni, M. Tomellini, and I. Davoli, *J. Electrochem. Soc.* 161, D540 (2014).
45. S.K. Balijepalli, I. Colantoni, R. Donnini, S. Kaciulis, M. Lucci, R. Montanari, N. Ucciardello, and A. Varone, *La Metallurgia Italiana* 1/2013, 42 (2013).
46. J.P. Killgore, J.Y. Kelly, C.M. Stafford, M.J. Fasolka, and D.C. Hurley, *Nanotechnology* 22, 175706 (2011).

Eur. J. Mineral.
2016, **28**, 273–283
Published online 5 January 2016

Contact resonance atomic force microscopy (CR-AFM) in applied mineralogy: the case of natural and thermally treated diaspore

DANIELE PASSERI[1,*], MELANIA REGGENTE[1], MARCO ROSSI[1,2], STELLA NUNZIANTE CESARO[3,4], VALERIA GUGLIELMOTTI[5], JOOST JOHAN VLASSAK[6], ANNA MARIA DE FRANCESCO[7], ROBERTA SCARPELLI[7], MURAT HATIPOĞLU[8] and DAVID AJÒ[4,9]

[1] Department of Basic and Applied Sciences for Engineering, SAPIENZA University of Rome, Via A. Scarpa 16, 00161 Rome, Italy
*Corresponding author, e-mail: daniele.passeri@uniroma1.it
[2] Research Center for Nanotechnology applied to Engineering of SAPIENZA University of Rome (CNIS), Piazzale A. Moro 5, 00185 Rome, Italy
[3] ISMN-CNR c/o Department of Chemistry, University of Rome Sapienza, Piazzale A. Moro 5, 00185 Rome, Italy
[4] SMATCH Italia (Scientific Methodologies Applied to Cultural Heritage), Largo U. Bartolomei 5, 00136 Rome, Italy
[5] Department of Chemical Sciences and Technologies, University of Rome Tor Vergata and Micro and Nano-structured Systems Laboratory (MINASlab), Via della Ricerca Scientifica, 00133 Rome, Italy
[6] School of Engineering and Applied Sciences, Harvard University, 29 Oxford Street, Cambridge, MA 02138, USA
[7] Department of Biology, Ecology and Earth Sciences, University of Calabria, Via P. Bucci, cubo 15b, 87036 Rende (Cosenza), Italy
[8] Dokuz Eylul University, Izmir Multidisciplinary Vocational School, Department of Technical Programs, Gemology and Jewelry Program, BUCA-IZMIR, Turkey
[9] Dipartimento di Scienze Chimiche, Università degli Studi di Padova, Padova, Italy

Abstract: Contact resonance atomic force microscopy (CR-AFM) is a nondestructive technique based on atomic force microscopy (AFM) that allows one to perform single-point measurements as well as surface mapping of the indentation modulus of a material. In this work, we demonstrate the potential of CR-AFM in applied mineralogy research. As a case study, we report the characterization of natural and thermally treated diaspore. Natural diaspore samples from the Ilbirdagi diasporic metabauxite (diasporite) deposit in the Milas (Muğla) region in Turkey were heat treated in a muffle furnace causing them to transform from diaspore to corundum. After the treatment, the samples had a polycrystalline structure with ordered micrometer-size rectangular grains of uniform crystallographic orientation. Nanomechanical characterization by CR-AFM allowed us to visualize inclusions with different mechanical properties and to determine the average indentation modulus of the surface of the thermally treated diaspore. Quantitative maps of the indentation modulus reveal the variation of the indentation modulus on the surface of single micro-grains with nanometer spatial resolution.

Key-words: diaspore; thermal treatment; contact resonance atomic force microscopy; elastic modulus; nanomechanical imaging.

1. Introduction

Apart from their optical characteristics, minerals are differentiated most notably by their mechanical properties. The mechanical behavior of minerals is not only of fundamental interest in Earth science and mineralogy, but is also of remarkable importance in geology. Knowledge of storage and dissipation moduli, for instance, allows measurement of the attenuation of seismic waves (Klumbach & Schilling, 2014). Mechanical properties are also among the most important characteristics of minerals in terms of their commercial and industrial applications. Thus, the availability of techniques to quantitatively characterize the mechanical behavior of minerals is of great importance for a number of fields related to Earth science and mineralogy (Angel *et al*., 2009). Originally, minerals were classified on the basis of an empirical hardness scale proposed by Friedrich Mohs in the early 1800s and named after him (Tabor, 1953). Since then, a number of instrumented techniques have been developed for the analysis of mechanical properties of materials. Among them, depth-sensing indentation (DSI) refers to a family of well-established methodologies widely used in materials science. By combining DSI with optical microscopy, it is possible to perform mechanical measurements at selected locations on the sample surface with micrometer spatial resolution.

DOI: 10.1127/ejm/2016/0028-2520
0935-1221/16/0028-2520 $ 4.95

Depending on the tested material and the applied loads, however, the indenter makes permanent imprints with lateral dimensions from a few to some tens of micrometers in the sample surface. Although the presence of such imprints does not alter the physical properties of the tested materials, it nevertheless may represent a serious drawback when applied to valuable materials such as gems. Other methods are based on the measurement of wave velocities (including ultrasound travel time measurement and interferometry or Brillouin, laser, neutron or X-ray scattering) and allow measurement of individual elements of the stiffness tensor and/or their combination (Angel *et al*., 2009; Lin & Chen, 2011). These techniques are nondestructive and highly accurate. The retrieved information is an average over the probed volume of the sample, with dimensions ranging from tens of micrometers to centimeters (*i.e.,* from the mesoscopic to the macroscopic range), depending on the technique. However, both natural and artificial materials may be inhomogeneous over a range of length scales and may contain cracks or inclusions, the dimensions of which can vary from the macroscopic to the nanometer scale (Broska *et al*., 2014; Shatskiy *et al*., 2015). This inhomogeneity highlights a limitation of this type of measurement techniques, because the accuracy of the measurements depends on the dimensions of the defects compared to the volume of material probed. Therefore, local properties of polycrystalline and/or composite materials cannot be easily assessed and issues may arise when mechanical tests are performed across different length scales (Gouldstone *et al*., 2007). The study of such materials and in particular the visualization of these nano-inclusions is currently possible only with transmission electron microscopy (TEM) after a time-consuming and destructive sample preparation process (Viti & Ferrari, 2006; Khisina *et al*., 2008). These nano-inclusions, however, have elastic behavior that is different from that of the host material. Therefore, the inhomogeneity in the elastic response can be used to image nano-inclusions in a mineral with a technique that is capable of mapping the local elastic properties of a sample. In addition, since the local elastic response of a material is affected by the presence of cracks, defects, voids, or delamination at buried interfaces, these features can also be visualized (Yamanaka, 1996; Tsuji & Yamanaka, 2001; Sarioglu *et al*., 2004; Hurley *et al*., 2006; Parlak & Degertekin, 2008, 2012). A significant advance in this field would be the the development of a truly nondestructive technique capable of providing single-point measurements at selected locations and of mapping the local mechanical properties of a surface with sub-micrometer resolution. In this scenario, contact resonance atomic force microscopy (CR-AFM) is a promising technique as it combines the imaging capability typical of AFM with the possibility of quantitatively measuring and mapping the elastic modulus on the surface of a sample (Hurley *et al*., 2005; Passeri *et al*., 2006; Kumar *et al*., 2008). CR-AFM probes the sample surface by applying ultra-low loads (down to a few nanonewtons) using a tip with a radius of a few nanometers placed at the end of a microfabricated cantilever. As such, CR-AFM is a truly nondestructive technique in which the local value of the indentation modulus of the sample is determined from the mechanical resonance frequencies of the cantilever. CR-AFM was originally demonstrated on relatively stiff materials. As discussed below, quantitative determination of the indentation modulus of a sample requires knowledge of the geometry and elastic properties of the tip. In the 'standard' CR-AFM procedure, the indentation modulus of the tip is assumed equal to theoretical value of the tip material, *e.g.,* in the most common case that of a perfect (100) Si single crystal, ignoring the finite dimensions of the tip and the presence of any oxide or amorphization of the material at the apex. Conversely, the tip geometry is calibrated using a reference material with known mechanical properties (Passeri *et al*., 2005). In recent years, CR-AFM has been extended to polymers (Killgore *et al*., 2011; Yablon *et al*., 2012) and the lowest indentation moduli that can be measured are on the order of a few hundreds of megapascals. While the use of CR-AFM for the study of materials with 'medium-low' indentation modulus values can be considered relatively widely reported, its use for very stiff materials is almost unexplored. To the best of our knowledge, high indentation moduli have been explored only by Rabe *et al.* (2002). While CR-AFM has been proposed as a tool for the characterization of materials of interest in different fields, *e.g.,* from nanomaterials (Zheng *et al*., 2006; Stan *et al*., 2009), nanocrystalline thin films (Kester *et al*., 2000; Amelio *et al*., 2001; Kopycinska-Müller *et al*., 2005, 2008; Passeri *et al*., 2008b) and nanocomposites (Preghenella *et al*., 2006; Passeri *et al*., 2008c; Reggente *et al*., 2015) to piezoelectric materials (Rabe *et al*., 2002; Kopycinska *et al*., 2003), polymers (Yablon *et al*., 2012) to biological samples (Ebert *et al*., 2006; Nair *et al*., 2010; Campbell *et al*., 2012), CR-AFM has been hardly used on materials with Earth science, mineralogical, or gemological interest. Indeed, to the best of our knowledge CR-AFM has been used only in the study of clay minerals (Prasad *et al*., 2002) with indentation moduli than 10 GPa. Many materials encountered in mineralogy and gemology are much stiffer than clay minerals and have indentation moduli ranging from at least some tens to some hundreds of gigapascals. In particular, the indentation moduli of many gems are at the opposite extreme of the range, *e.g.,* diamond (indentation modulus larger than 1000 GPa) or corundum (indentation modulus about 430 GPa). Therefore, although interesting for the application of CR-AFM to relatively soft minerals, clay minerals cannot be considered as fully representative of materials commonly encountered in mineralogy and gemology.

In this work, we demonstrate how CR-AFM can be effectively used to study the mechanical properties of minerals at the nanoscale using two materials, one natural and one synthetic, as case studies. Among the endless materials we could chose, we selected a natural Turkish diaspore and a synthetic polycrystalline corundum (alumina) obtained by thermal treatment of natural diaspore. Several considerations led to this choice:

(i) We were interested in a natural material with an 'artificial' counterpart, obtained using an easy and well known treatment to avoid focusing attention on

the treatment rather than the measurement technique. Diaspore meets this requirement as its thermal behavior has been investigated by several authors, across three centuries (Haüy, 1801; Shoval *et al*., 2003; Hatipoğlu *et al*., 2010a);

(ii) To emphasize the potential of the technique, we needed materials with well known 'bulk' elastic properties that had not yet been characterized at the nanometer scale. The diaspore-corundum transition is quite widely studied and the bulk mechanical properties of both corundum and natural diaspore are well known, while the properties at the micro- and nanoscale of thermally treated diaspore have never been studied (Jiang *et al*., 2008; Tsuchiya & Tsuchiya, 2009);

(iii) As discussed above, the novelty of this work lies in the extension of CR-AFM to very hard materials. To this purpose, natural diaspore (indentation modulus of about 300 GPa) and corundum (indentation modulus of about 430 GPa) represented good choices;

(iv) We wanted to explore the implications at the nanometer scale of a phenomenon (the transition from diaspore to corundum) described in 'historical' treatises of mineralogy (Haüy, 1801) and extensively studied in terms of structural modifications of the elemental cells, but not from a microscopic/nanoscopic point of view;

(v) As detailed below, the particular Turkish diaspore we chose is a unique mineral that is purer than common diaspore and that has attracted gemological interest, but has not yet been extensively studied.

Overall, both natural and thermally treated diaspore can be considered representative of broader classes of minerals and gemstones because of their stiffness and microstructure. In the following, the natural diaspore and its thermal treatment are described. Both the natural and synthetic materials were characterized using well established techniques, including X-ray diffraction (XRD), Fourier transform infrared (FTIR) spectroscopy, photoluminescence (PL), and scanning electron microscopy (SEM). Finally, the results of the CR-AFM nanomechanical studies (both single point and mapping of indentation modulus) are presented for both materials.

2. Experimental procedure

2.1. Materials

2.1.1. Natural diaspore

Diaspore is an aluminium oxide hydroxide mineral, AlO(OH), with orthorhombic crystal symmetry that is a relatively common component in metamorphic bauxite deposits. Despite being a relatively well-known material, the elastic properties of diaspore were determined only recently in a number of theoretical and experimental studies (Jiang *et al*., 2008; Tsuchiya & Tsuchiya, 2009). The diaspore used in this study was taken from the Ilbirdagi diasporic metabauxite (diasporite) deposit in the Milas (Muğla) region in South-West Turkey (Hatipoğlu *et al*., 2010b), which originates gem-quality crystals trademarked as 'zultanite'. In nature, diaspore is considered one of the precursors of natural alumina (Garcia-Guinea *et al*., 2001, 2005; Hatipoğlu *et al*., 2010c). Turkish diaspore is the product of hydrothermal circulation and shows important differences from the more common diaspore of metamorphic origin (Hatipoğlu *et al*., 2010d). It is of higher purity and has fewer inclusions, and therefore is well suited as a reference material in quantitative CR-AFM.

2.1.2. Thermally treated diaspore

The natural diaspore sample was cut into slices about 2 mm thick, some of which were thermally treated in a muffle furnace using the following procedure. The samples were placed in the muffle furnace set at an initial temperature of 150°C. The temperature was maintained for 30 minutes and then increased to 300°C over a period of approximately 10 minutes. After reaching 300°C the temperature was again kept constant for 30 minutes and then increased by 150°C. The whole procedure was repeated until a final temperature of 600°C was reached. The samples were then kept at 600°C for 2 hours, after which they were allowed to cool inside the muffle over a period of approximately 20 hours.

2.1.3. Other materials

In addition to natural and thermally treated diaspore, natural corundum single crystals were used as reference samples to rationalize the FTIR results. A synthetic (0001) corundum single crystal was used as an additional reference material for quantitative mechanical characterization with CR-AFM.

2.2. Methods and instrumentations

X-ray diffraction. Mineralogical characterization of the samples was carried out by powder X-ray diffraction analysis (PXRD) using a Bruker D8 Advance diffractometer with Cu$K\alpha$ radiation. Samples were carefully powdered by hand grinding in an agate mortar to produce particles with average diameter smaller than 10 μm. XRD spectra were acquired by varying 2θ in the range 5–65 ° with a step size of 0.02 ° and a step time of 1 s/step. In addition, diffraction measurements were performed on the samples characterized by CR-AFM to determine the crystallographic orientations of the exposed surfaces. A MiniFlex II X-ray diffractometer (Rigaku Corporation, Tokyo, Japan) was used to acquire XRD spectra by varying 2θ in the range 15–90 ° with a step size of 0.05 ° and a scan rate of 0.5 °/min. Several spectra were obtained for each crystal by rotating the crystals over 45 ° and 90 ° around an axis perpendicular to the crystal surface.

Fourier-transform infrared spectroscopy. Fourier-transform infrared (FTIR) spectra of corundum, natural, and

thermally treated diaspore samples were recorded using an Alpha FT-IR spectrometer (Bruker Inc.), equipped with an external reflection module, in the spectral range 7500–375 cm^{-1} with a resolution of 2 cm^{-1} accumulating at least 200 scans.

Scanning electron microscopy. A field-emission gun (FEG) scanning electron microscope (SEM) Quanta 200 with an acceleration voltage of 20 kV was used to perform the morphological analysis of the samples without metallizing the surfaces.

Photoluminescence. Photoluminescence (PL) spectra were recorded at 77 K, using a helium-flux cryostat (TBT, Air Liquide), by means of a custom-made apparatus (Institute of Inorganic Chemistry and surfaces-CNR, Padua, Italy, former position of one of the authors) equipped with a frequency-doubled Nd:YAG LASER, $\lambda = 532$ nm (Casix CDPL-1100T), a monochromator (Jobin Yvon HR640) having a reciprocal dispersion of 24 Å/mm and a photomultiplier tube (Hamamatsu R6357).

Contact resonance atomic force microscopy. Morphological and mechanical characterization of the samples was performed using an AFM apparatus (Solver, NT-MDT, Russia) capable of making contact resonance AFM (CR-AFM) measurements. The AFM apparatus was equipped with standard Si cantilevers (CSG10, NT-MDT, Russia) with a spring constant k_c in the range of 0.1 N/m to 0.2 N/m. We explicitly point out that, while in early works we used stiff ('tapping mode') cantilevers to increase the sensitivity of CR-AFM (Passeri *et al.*, 2005, 2006), here soft ('contact mode') cantilevers were used to reduce the static load applied between tip and sample to reduce tip wear. A piezoelectric transducer coupled to the backside of the sample was used to excite high-frequency out-of-plane oscillations of the sample surface, the latter scanned by the AFM tip in contact mode. The resonance frequencies f_n's of the system, generally referred to as the cantilever contact resonance frequencies (CRFs), were used to characterize the local mechanical properties of the sample. The data analysis procedure, which is described in details in the Supplementary Material S3 'freely available online, linked to this article on the GSW website of the journal, HYPERLINK http://eurjmin.geoscienceworld.org/http://eurjmin.geoscienceworld.org/, can be summarized as follows: (i) the resonance frequencies, $f_{0,n}$, of the free cantilever were measured and used to calculate the characteristic geometrical parameters, c_n, of the cantilever; (ii) the position of the tip on the cantilever was determined from the CRF values and was expressed by the ratio $r = L_1/L$ between the tip position on the cantilever (L_1) and the cantilever length (L); (iii) the tip-sample contact stiffness k^* was calculated from the values of r and the resonance frequencies; (iv) the indentation modulus of sample, M_s, was determined after a calibration procedure to evaluate the tip-sample contact radius and the tip indentation modulus (M_t).

3. Results

3.1. Standard characterizations

The natural diaspore crystal (see Fig. 1a) shows perfect cleavage in the [010] direction and good cleavage in the [110] direction. The corundum, produced by dehydration of the diaspore ($2AlO(OH) \rightarrow Al_2O_3 + H_2O$) is characterized by an opaque white color (see Fig. 1b) and fracture occurs by brittle cleavage.

Morphological analysis of the natural diaspore by SEM shows significant heterogeneity (Fig. 2a). SEM micrographs of the diaspore heated at 600°C for 2 hours (Fig. 2b) display splinters and cracks formed during the heat treatment as a result of the transformation strains and the associated loss of water (Löffler & Mader, 2003). In particular, a network of fractures is observed corresponding to crystalline domains with sizes on the order of hundreds of nanometers.

The PXRD spectra of the natural diaspore sample before and after heat-treatment are shown in Fig. S1 in the

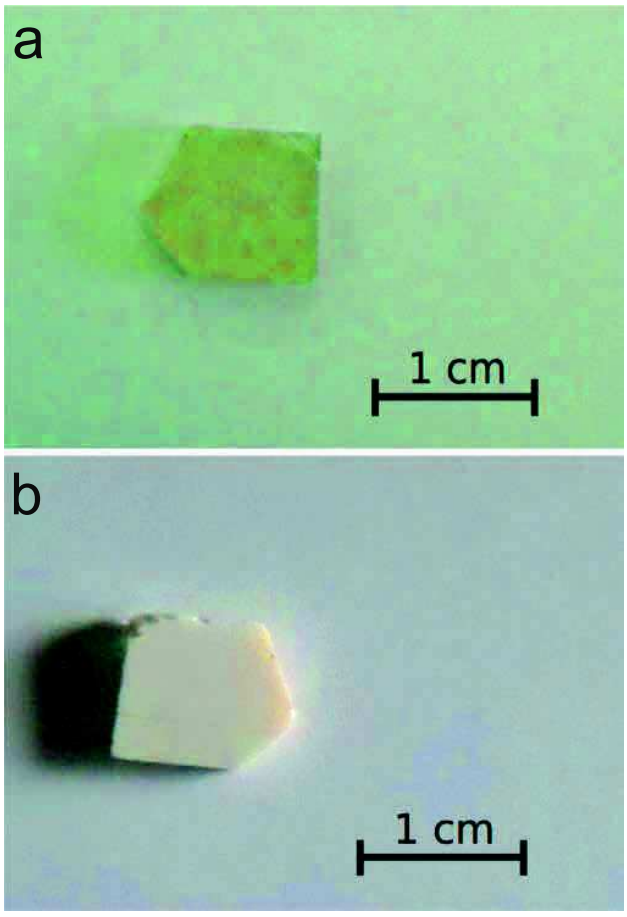

Fig. 1. Photograph of a sample of natural (a) and thermally treated (b) diaspore. (online version in color)

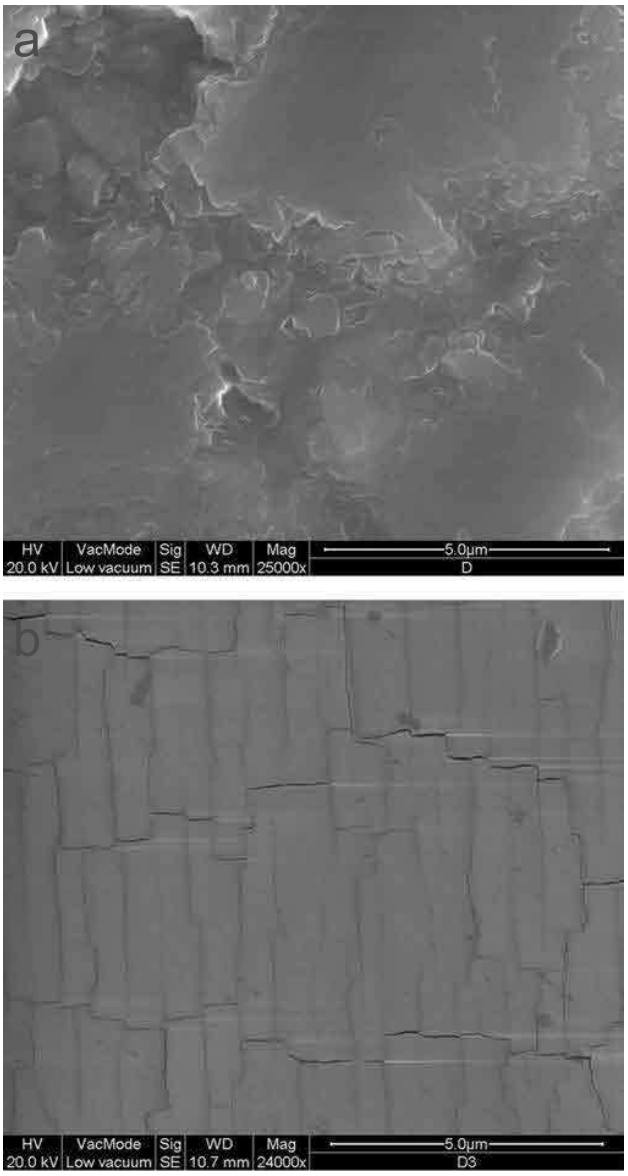

Fig. 2. SEM micrograph of a sample of natural (a) and thermally treated (b) diaspore.

Supplementary Material; they confirm complete reaction to corundum. In Fig. S2, the FTIR spectrum of thermally treated diaspore (a) is reported and compared to the spectra of corundum and natural diaspore (b and c, respectively), showing again complete transformation, as does the non-superposition of the Cr^{+3} peaks (Shoval *et al*., 2003; Gaft *et al*., 2005) in the PL spectra of natural and treated diaspore (not shown).

3.2. Contact resonance atomic force microscopy characterization

3.2.1. Quantitative modulus measurement

The results of the CR-AFM measurements on the natural and treated diaspore, and on the (0001) Al_2O_3 single crystal are summarized in Table 1. As the indentation modulus in anisotropic crystals depends on the crystallographic direction, XRD analysis was performed on the natural and thermally treated diaspore samples to determine the orientations of the exposed surfaces. An example of the spectra collected on natural diaspore is reported in Fig. 3a, in which the most evident peaks are those that can be assigned to AlO(OH). These peaks belong to the same family of reflections, *i.e*., (020) and multiples. This indicates that the exposed surface of the crystal is perpendicular to the [010] crystallographic direction. Conversely, the most pronounced peaks in the XRD spectra of the thermally treated diaspore sample (one of which is reported in Fig. 3b) can be assigned to Al_2O_3. These peaks belong to the same family of reflections, *i.e*., (110) and multiples, indicating that all crystallites have the same orientation and that the exposed surface is perpendicular to the [110] crystallographic direction. Therefore, the thermally treated diaspore can be described as a highly textured polycrystalline corundum. The theoretical indentation modulus values (M_{calc}) of the three samples were calculated from the elements of the stiffness tensors reported in literature (Vlassak *et al*., 2003; Jiang *et al*., 2008) and are listed in Table 1. In the first step of the experimental procedure, the resonance frequencies of the cantilever $f_{0,n}$ in air were acquired and the corresponding values of c_n were calculated. Depending on the vibration mode, a certain variability in the

Table 1. Results of CR-AFM nanomechanical characterization of corundum, natural and thermally treated diaspore, the crystallographic orientations of which are indicated. For each mode (the second or the third), the measured contact resonance frequency (CRF) and the corresponding normalized tip-sample contact stiffness (k^*/k_c), the calculated anisotropic indentation modulus (M_{calc}), and the measured indentation modulus (M_{meas}). The uncertainty in the CRFs is reported between brackets as it was not used in the subsequent data analysis. Also, M_{calc} of treated diaspore is reported between brackets as is was not used as a reference for calibration (like natural diaspore and corundum), but only for comparison.

Sample	Surface	Mode	CRF (kHz)	k^*/k_c	M_{calc} (GPa)	M_{meas} (GPa)
Corundum	(0001)	2	398(±5)	1033	432	–
		3	806(±4)	1102		–
Natural diaspore	(010)	2	389(±1)	470	302	–
		3	786(±3)	755		–
Thermally treated diaspore (corundum)	(110)	2	395 ± 1	761 ± 84	(432)	389 ± 18
		3	801 ± 3	970 ± 60		386 ± 22

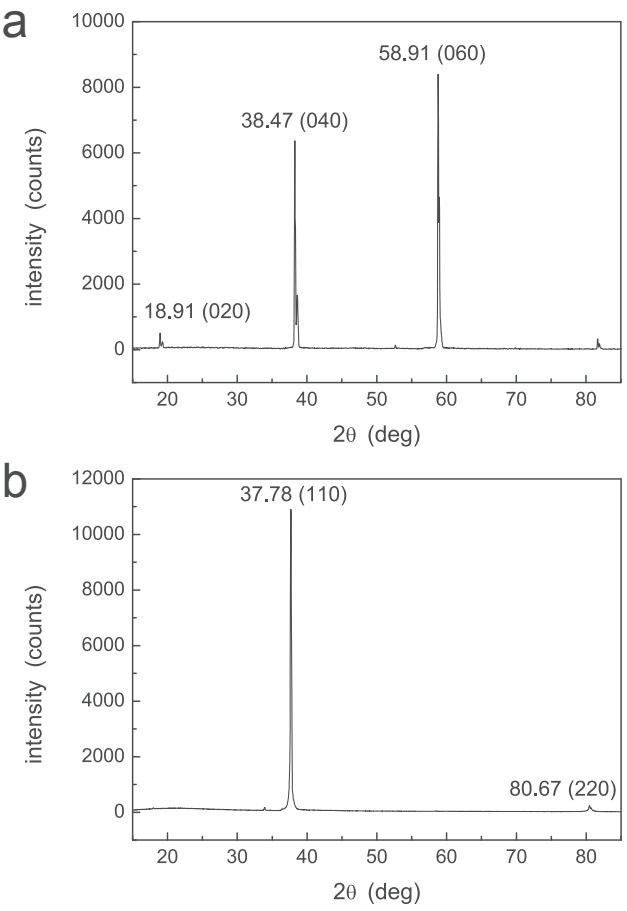

Fig. 3. Examples of XRD spectra of the crystalline sample used in CR-AFM: (a) spectrum of natural diaspore, showing the peaks corresponding to the (020) family of reflections of AlO(OH); (b) spectrum of thermally treated diaspore, showing the peaks corresponding to the (110) family of reflections α-Al_2O_3.

calculated values of c_n is observed, which is mainly due to unavoidable approximations in the model of the cantilever. In our previous work, we performed quantitative measurements of the indentation modulus using a constant value for all modes by averaging the values of c_n obtained for different modes (Passeri *et al.*, 2007, 2008b and c). This procedure results in a larger uncertainty in the value of c_n, which in turn increases the uncertainty in the value of the indentation modulus. In this study, the resonance frequencies were analyzed using the values of c_n obtained from the $f_{0,n}$ values for the corresponding modes. The CRFs of the second and third contact modes were acquired for each of the three materials with a static normal load of 30 nN, low enough to perform nondestructive measurements with a stable tip radius. CRFs values from about 1000 points were collected over areas with a lateral dimension of 8 μm that were selected to ensure that the surfaces were flat and did not contain any obvious inclusions. These values were then averaged to obtain the frequency values reported in Table 1. In order to evaluate the contact stiffness k^*, the value of r needs to be determined. This value can be obtained by independent measurements of the dimensions of the cantilever (*e.g.,* using electron microscope images of the cantilever) or by matching the values of k^* obtained for two different modes. In the latter method, which was widely used in early work (Passeri *et al.*, 2005), the contact stiffness is assumed to be constant for different modes and thus independent of frequency. Here, we follow an alternative approach, in which we assume a constant value of r. The indentation modulus is then evaluated independently for each of the vibration modes, thus providing an estimate of the uncertainty of the method. Although the value of r determined from a SEM characterization of the cantilever ($r = 0.984$) would be a natural choice, neglecting the lateral tip-sample coupling leads to 'effective' values of r that are significantly lower than the 'real' value, especially when the samples are much stiffer or compliant than the cantilever (Passeri *et al.*, 2013c). Thus, r was calculated for each sample by matching the values of k^* for the two modes. Then the values obtained for the three different samples were averaged, and this average value ($r = 0.951$) was used for the samples to determine the values of k^*/k_c for each mode reported in Table 1. In our data analysis procedure, natural diaspore and corundum were used as references to evaluate the geometrical and mechanical properties of the tip. In particular, the mean values of the CRFs were used to determine the parameters of the calibration curve (bias and slope), which are related to the geometrical and mechanical parameters of the tip (Passeri *et al.*, 2013c). The uncertainty in the CRFs values measured on the treated diaspore was used to evaluate the corresponding errors in the k^*/k_c for each mode, which are reported in Table 1. Finally, the indentation modulus of the treated diaspore was evaluated for each mode, while the corresponding error was calculated from that of k^*/k_c. The results of this procedure are reported in Table 1.

3.2.2. Nanomechanical imaging

In order to rationalize the mechanical behavior of the thermally treated diaspore, nanomechanical mapping was performed on natural and treated diaspore. Figure 4a shows a typical topographical reconstruction of the surface of natural diaspore, while CRF maps of the first and third contact modes of the cantilever are reported in Fig. 4b and c, respectively.

The topographical reconstruction of the surface of the heat-treated diaspore is reported in Fig. 5a, while the CRF maps of the first and second contact mode of the cantilever are reported in Fig. 5b and c, respectively. The two CRF images can be used to reconstruct the map of the local contact stiffness reported in Fig. 5d. It is worth noting that a map of r values was obtained (image not shown), which varied over the surface as a result of approximations in the analytical model (Passeri *et al.*, 2013c). The average value of r is approximately 0.85, significantly lower than the value obtained from SEM micrographs. This indicates

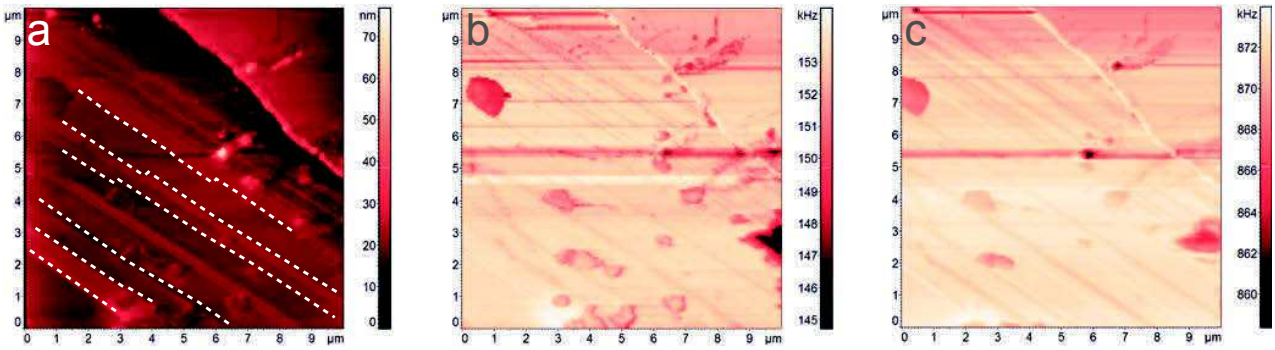

Fig. 4. CR-AFM nanomechanical characterization of the surface of natural diaspore: (a) topography and maps of the first (b) and third (c) CRFs acquired with a static normal load of 25 nN. (online version in color)

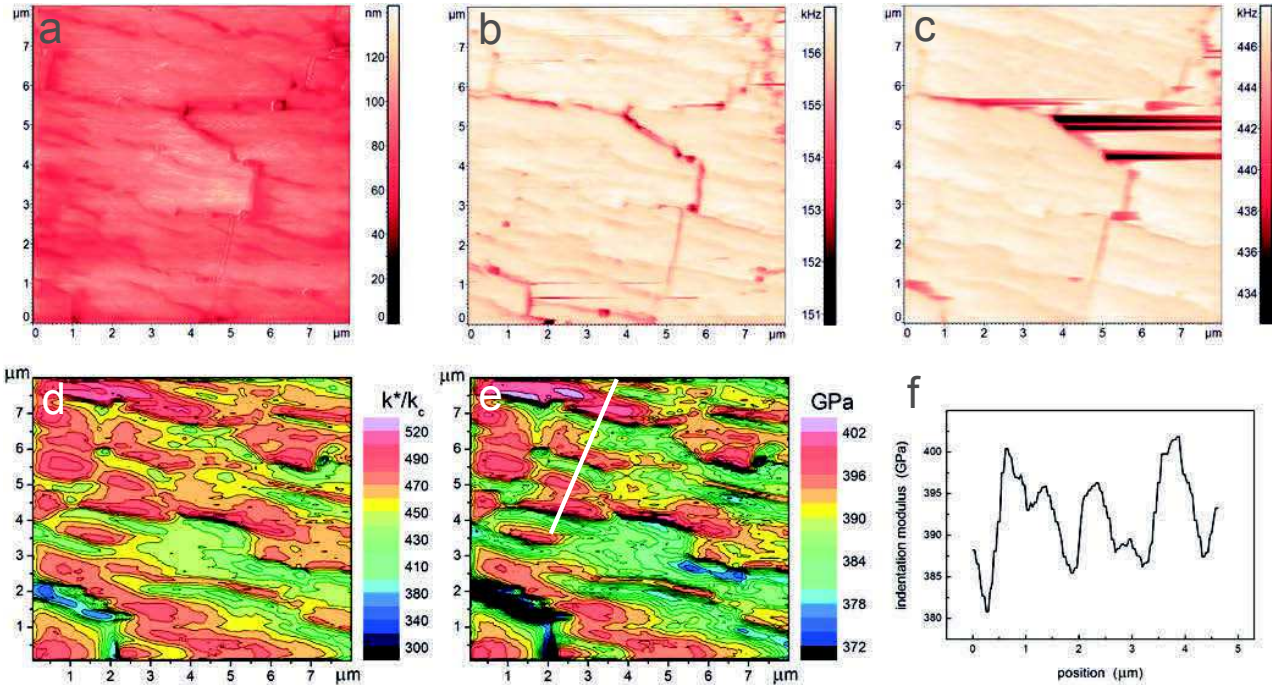

Fig. 5. CR-AFM nanomechanical characterization of the surface of thermally treated diaspore: (a) topography and maps of the first (b) and second (c) CRFs acquired with a static normal load of 25 nN; (d) map of the normalized tip-sample contact stiffness k^*/k_c; (e) map of the indentation modulus and (f) profile of the indentation modulus corresponding to the white line in (e). (online version in color)

that two reference materials are required to obtain accurate maps of the indentation modulus, because the indentation modulus of the tip is not necessarily equal to the theoretical indentation modulus for Si (Passeri *et al.*, 2013c). The (010) natural diaspore sample was used as the first reference. The average contact stiffness of the sample was $k^*/k_c = 270 \pm 60$ and this value was assumed to correspond to the indentation modulus of 302 GPa reported in Table 1. The heat-treated diaspore was used as the second reference, following a procedure of 'self-calibration': the average value of k^*/k_c from Fig. 5d was calculated ($k^*/k_c = 460 \pm 20$) and assumed to correspond to the value of the indentation modulus (390 ± 20 GPa) measured on the treated diaspore as previously discussed.

4. Discussion

4.1. Indentation modulus

The CRF values measured on the thermally treated diaspore are significantly higher than those measured on the natural diaspore (see Table 1). In fact, they are closer to the values obtained for corundum. The indentation moduli obtained for each of the two modes are in good agreement with each other and rather independent of the chosen modes, their relative difference being much smaller than that of the corresponding values of k^*. This observation, which we also reported earlier (Passeri *et al.*, 2010), provides further justification of the data analysis used in this

study. An indentation modulus of 390 ± 20 GPa was found for thermally treated diaspore. The uncertainty was calculated by propagating the error in the CRFs, and can be attributed mainly to the surface roughness of the sample, which modulates the local tip-sample contact area. Also, an inclination of the sample may produce a bias in the measurements (Passeri *et al*., 2013c). The minimal uncertainty of our technique can be estimated as high as ±3 % from the measurement reproducibility for a set of single-crystal reference materials (Passeri *et al*., 2007, 2005, 2015). The roughness of the natural and treated diaspore samples is higher than that of the references and increases the uncertainty. Nevertheless, our CR-AFM approach ensures a relatively low error due to the use of two reference materials (Passeri *et al*., 2013c). Overall, we consider that an error of ± 5% quite realistically represents the uncertainty of our method for this kind of samples. Although several techniques have been developed to perform quantitative elastic modulus measurements at the nanoscale, most of them rely on the indentation of the sample surface using an AFM tip, *e.g.,* AFM indentation (Domke & Radmacher, 1998; Passeri *et al*., 2008a, 2009), torsional harmonics AFM (Sahin *et al*., 2007), or PeakforceQNM™ (Adamcik *et al*., 2011). Therefore, only soft materials like polymers or biological samples can be investigated, while the presence of stiff materials (*e.g.,* substrates) leads to a rapid loss of sensitivity and saturation of the value of the measured indentation modulus (Passeri *et al*., 2011, 2013a). Conversely, the results reported in this work demonstrate that CR-AFM can be used effectively to study almost all stiff materials of interest in mineralogy and gemology.

Finally, the modulus of thermally treated diaspore is lower than the theoretical indentation modulus of a (110) corundum single crystal, *i.e*., 432 GPa. Considering that the result is averaged over an area of several square micrometers, the reduction in the indentation modulus can be attributed to the microcrystalline structure of the material and to the presence of grain boundaries with reduced modulus, which justifies a more detailed investigation through mechanical imaging at the nanometer scale.

4.2. Nanomechanical maps

The topographical reconstruction of the surface of natural diaspore (Fig. 4a) shows well-defined edges of crystalline planes (some of them marked with a white dashed line). Also, inclusions are visible with dimensions ranging from hundreds of nanometers to a few micrometers. CRF maps of the first (Fig. 4b) and third (Fig. 4c) contact modes of the cantilever demonstrate the uniformity of the elastic properties of the sample which is expected for a single crystal. An exception is the reduction of the CRF values corresponding to inclusions and to edges of the crystalline planes, which reduce the tip-sample contact area and thus also the CRF values. This reduction, which enhances the topographical contrast in the CRF images, must nevertheless be considered a topography-induced artifact (Passeri *et al*., 2013b). Conversely, the decrease in the CRF as a result of inclusions suggests that the inclusions have a lower stiffness. The capability of CR-AFM nanomechanical mapping to distinguishing inclusions in the nano- to micrometer range on the basis of their elastic properties may be used to study the nanoscale features that characterize the unique physical properties of both natural and artificial materials, *e.g.,* inclusions responsible for asterism in gemstones (Viti & Ferrari, 2006), 'wet' inclusions (Khisina *et al*., 2008), or ancient glasses (Barber & Freestone, 1990; Wagner *et al*., 2000; Rossi *et al*., 2014).

The topographical reconstruction of the surface of the treated diaspore (Fig. 5a) shows a network of fractures analogous to that observed in the SEM micrographs. The CRF maps of the first (Fig. 5b) and second (Fig. 5c) contact mode of the cantilever indicate that the grains have the same mechanical characteristics, *i.e*., the center is stiff while the indentation modulus decreases in the vicinity of the edges. As evidenced by the indentation modulus map (Fig. 5e) and the example of profile (Fig. 5f), the indentation modulus reaches a value of 395–400 GPa in the center of the grains and decreases to 380 GPa in the vicinity of the edges.

It is worth noting that we obtained nanomechanical maps up to 400 GPa using soft cantilevers (k_c = 0.1–0.2 N/m) by applying static loads lower than 30 nN. An analogous (but lower) range of indentation moduli has been exploited by Rabe *et al*. (2002), who mapped the modulus of barium titanate ceramics up to 350 GPa using diamond-coated tips to reduce tip wear and stiff cantilevers (k_c of about 50 N/m) to apply static loads of several hundreds of nanonewtons. Through use of softer cantilevers and lower loads, our approach ensures the nondestructiveness of the measurements and, in combination with the use of uncoated tips, avoids the loss of lateral resolution due to the increased tip radius.

5. Conclusion

This study demonstrated the potential of CR-AFM, a non-destructive AFM based technique in applied mineralogy by reporting the results obtained for natural and thermally treated diaspore. Thermal treatment at 600°C resulted in the transformation of diaspore to corundum. The SEM analysis of the thermally treated diaspore showed a polycrystalline structure with ordered rectangular grains, approximately a few μ by 500 nm in size. XRD analysis further showed that the thermally treated diaspore had a strong crystallographic texture. Thus the structure can be described as 'partially ordered alumina', which may have potential in several applied fields, possibly as by-product of diaspore mined for gems. CR-AFM allows one to perform quantitative single point indentation modulus measurements as well as quantitative nanomechanical mapping of the sample surface. For natural diaspore, CRF images allowed us to identify sub-micrometer

inclusions with a lower indentation modulus. For thermally treated diaspore, CRF images showed a network of cracks and single micro-grains. The indentation modulus of the treated diaspore was measured to be 390 ± 20 GPa. Moreover, indentation modulus maps revealed that the indentation modulus reached a value of 395–400 GPa in the center of the grains, while it decreased to 380 GPa near the edges. Overall, by enabling nondestructive quantitative stiffness measurements as well as imaging at the nanometer scale, CR-AFM has been demonstrated to have great potential in Earth sciences, mineralogy, and gemology. Beside the nondestructive quantitative evaluation of materials elastic modulus, CR-AFM nanomechanical mapping can be used to nondestructively detect cracks, defects, voids, as well as micro- and nano-inclusions. We are convinced that the use of CR-AFM in these research fields may stimulate new applications of this technique.

References

Adamcik, J., Berquand, A., Mezzenga, R. (2011): Single-step direct measurement of amyloid fibrils stiffness by peak force quantitative nanomechanical atomic force microscopy. *Appl. Phys. Lett.*, **98**, 193701.

Amelio, S., Goldade, A. V., Rabe, U., Scherer, V., Bhushan, B., Arnold, W. (2001): Measurement of elastic properties of ultra-thin diamond-like carbon coatings using atomic force acoustic microscopy. *Thin Solid Films*, **392**, 75–84.

Angel, R. J., Jackson, J. M., Reichmann, H. J., Speziale, S. (2009): Elasticity measurements on minerals: a review. *Eur. J. Mineral.*, **21**, 525–550.

Barber, D. J. & Freestone, I. C. (1990): An investigation of the origin of the colour of the Lycurgus cup by analytical transmission electron microscopy. *Archaeometry*, **32**, 33–45.

Broska, I., Krogh Ravna, E. J., Vojtko, P., Janák, M., Konečný, P., Pentrák, M., Bačík, P., Luptáková, J., Kullerud, K. (2014): Oriented inclusions in apatite in a post-UHP fluid-mediated regime (Tromsø Nappe, Norway). *Eur. J. Mineral.*, **26**, 623–634.

Campbell, S. E., Ferguson, V. L., Hurley, D. C. (2012): Nanomechanical mapping of the osteochondral interface with contact resonance force microscopy and nanoindentation. *Acta Biomater.*, **8**, 4389–4396.

Domke, J. & Radmacher, M. (1998): Measuring the elastic properties of thin polymer films with the atomic force microscope. *Langmuir*, **14**, 3320–3325.

Ebert, A., Tittmann, B. R., Du, J., Scheuchenzuber, W. (2006): Technique for rapid in vitro single-cell elastography. *Ultrasound Med. Biol.*, **32**, 1687–1702.

Gaft, M., Reisfeld, R., Panczer, G. (2005): Modern luminescence spectroscopy of minerals and materials. Springer-Verlag, Berlin Heidelberg, 96–97 p.

Garcia-Guinea, J., Rubio, J., Correcher, V., Valle-Fuentes, F. J. (2001): Luminescence of α-Al_2O_3 α-AlOOH natural mixture. *Radiat. Meas.*, **33**, 653–658.

Garcia-Guinea, J., Correcher, V., Rubio, J., Valle-Fuentes, F. J. (2005): Effects of preheating on diaspore: Modifications in colour centres, structure and light emission. *J. Phys. Chem. Solids*, **66**, 1220–1227.

Gouldstone, A., Chollacoop, N., Dao, M., Li, J., Minor, A. M., Shen, Y.-L. (2007): Indentation across size scales and disciplines: Recent developments in experimentation and modeling. *Acta Mater.*, **55**, 4015–4039.

Hatipoğlu, M., Can, N., Karali, T. (2010a): Effects of heating on fire opal and diaspore from Turkey. *Physica B*, **405**, 1729–1736.

Hatipoğlu, M., Helvacı, C., Chamberlain, S. C., Babalık, H. (2010b): Mineralogical characteristics of unusual ''anatolian'' diaspore (zultanite) crystals from the Ilbirdağı diasporite deposit, Turkey. *J. Afr. Earth Sci.*, **57**, 525–541.

Hatipoğlu, M., Türk, N., Chamberlain, S. C., Akgün, A. M. (2010c): Gem-quality transparent diaspore (zultanite) in bauxite deposits of the ilbir Mountains, Menderes Massif, SW Turkey. *Miner. Deposit.*, **45**, 201–205.

Hatipoğlu, M., Türk, N., Chamberlain, S. C., Akgün, A. M. (2010d): Metabauxite horizons containing remobilized-origin gem diaspore and related mineralization, Milas-Muğla province, SW Turkey. *J. Asian Earth Sci.*, **39**, 359–370.

Haüy, R. J. 1801. Traité de Minéralogie. Vol. 4. Chez Louis, Paris, Ch. VII, Diaspore. p. 358–360.

Hurley, D. C., Kopycinska-Müller, M., Kos, A. B., Geiss, R. H. (2005): Nanoscale elastic-property measurements and mapping using atomic force acoustic microscopy methods. *Meas. Sci. Technol*, **16**, 2167–2172.

Hurley, D. C., Kopycinska-Müller, M., Langlois, E. D., Barbosa, N, III. (2006): Mapping substrate/film adhesion with contact-resonance-frequency atomic force microscopy. *Appl. Phys. Lett.*, **89**, 021911.

Jiang, F., Majzlan, J., Speziale, S., He, D., Duffy, T. S. (2008): Single-crystal elasticity of diaspore, AlOOH, to 12 GPa by Brillouin scattering. *Phys. Earth Planet. Int.*, **170**, 221–228.

Kester, E., Rabe, U., Presmanes, L., Tailhades, P., Arnold, W. (2000): Measurement of Young's modulus of nanocrystalline ferrites with spinel structures by atomic force acoustic microscopy. *J. Phys. Chem. Solids*, **61**, 1275–1284.

Khisina, N., Wirth, R., Matsyuk, S., Koch-Müller, M. (2008): Microstructures and OH-bearing nano-inclusions in ''wet'' olivine xenocrysts from the Udachnaya kimberlite. *Eur. J. Mineral.*, **20**, 1067–1078.

Killgore, J. P., Yablon, D. G., Tsou, A. H., Gannepalli, A., Yuya, P. A., Turner, J. A., Proksch, R., Hurley, D. C. (2011): Viscoelastic property mapping with contact resonance force microscopy. *Langmuir*, **27**, 13983–13987.

Klumbach, S. & Schilling, F. R. (2014): Elastic and anelastic properties of α-and *β*-quartz single crystals. *Eur. J. Mineral.*, **26**, 211–220.

Kopycinska, M., Ziebert, C., Schmitt, H., Rabe, U., Hirsekorn, S., Arnold, W. (2003): Nanoscale imaging of elastic and piezoelectric properties of nanocrystalline lead calcium titanate. *Surf. Sci.*, **532**, 450–455.

Kopycinska-Müller, M., Geiss, R. H., Müller, J., Hurley, D. C. (2005): Elastic-property measurements of ultrathin films using atomic force acoustic microscopy. *Nanotechnology*, **16**, 703–709.

Kopycinska-Müller, M., Caron, A., Hirsekorn, S., Rabe, U., Natter, H., Hempelmann, R., Birringer, R., Arnold, W. (2008): Quantitative evaluation of elastic properties of nano-crystalline nickel using atomic force acoustic microscopy. *Z. Phys. Chem.*, **222**, 471–498.

Kumar, A., Rabe, U., Arnold, W. (2008): Mapping of elastic stiffnes in an $\alpha + \beta$ Titanium alloy using atomic force acoustic microscopy. *Jpn. J. Appl. Phys.*, **47**, 6077–6080.

Lin, C.-C. & Chen, C.-C. (2011): Elasticity of tephroite (α-Mn_2SiO_4) and a comparison of the elastic properties of silicate olivines. *Eur. J. Mineral.*, **23**, 35–43.

Löffler, L. & Mader, W. (2003): Transformation mechanism of the dehydration of diaspore. *J. Am. Ceram. Soc.*, **86**, 534–540.

Nair, S. S., Wanga, S., Hurley, D. C. (2010): Nanoscale characterization of natural fibers and their composites using contact-resonance force microscopy. *Compos. Part a - Appl. S*, **41**, 624–631.

Parlak, Z. & Degertekin, F. L. (2008): Contact stiffness of finite size subsurface defects for atomic force microscopy: Three-dimensional finite element modeling and experimental verification. *J. Appl. Phys.*, **103**, 114910.

Parlak, Z. & Degertekin, F. L. (2012): Quantitative subsurface imaging by acoustic AFM techniques. *in* ''Acoustic scanning probe microscopy'', F. Marinello, D. Passeri, E. Savio, Eds. Springer (Berlin, Heidelberg), Ch. 15, 417–436.

Passeri, D., Bettucci, A., Germano, M., Rossi, M., Alippi, A., Orlanducci, S., Terranova, M. L., Ciavarella, M. (2005): Effect of tip geometry on local indentation modulus measurement via atomic force acoustic microscopy technique. *Rev. Sei. Instrum.*, **76**, 093904.

Passeri, D., Bettucci, A., Germano, M., Rossi, M., Alippi, A., Sessa, V., Fiori, A., Tamburri, E., Terranova, M. L. (2006): Local indentation modulus characterization of diamond-like carbon films by atomic force acoustic microscopy two contact resonance frequencies imaging technique. *Appl. Phys. Lett.*, **88**, 121910.

Passeri, D., Bettucci, A., Germano, M., Rossi, M., Alippi, A., Fiori, A., Tamburri, E., Terranova, M. L., Vlassak, J. J. (2007): Local indentation modulus characterization via two contact resonance frequencies atomic force acoustic microscopy. *Microelectr. Eng.*, **84**, 490–494.

Passeri, D., Bettucci, A., Biagioni, A., Rossi, M., Alippi, A., Lucci, M., Davoli, I., Berezina, S. (2008a): Quantitative measurement of indentation hardness and modulus of compliant materials by atomic force microscopy. *Rev. Sci. Instrum.*, **79**, 066105.

Passeri, D., Rossi, M., Alippi, A., Bettucci, A., Manno, D., Serra, A., Filippo, E., Lucci, M., Davoli, I. (2008b): Atomic force acoustic microscopy characterization of nanostructured Selenium-Tin thin films. *Superlattices Microstruct.*, **44**, 641–649.

Passeri, D., Rossi, M., Alippi, A., Bettucci, A., Terranova, M. L., Tamburri, E., Toschi, F. (2008c): Characterization of epoxy/single-walled carbon nanotubes composite samples via atomic force acoustic microscopy. *Physica E*, **40**, 2419–2424.

Passeri, D., Bettucci, A., Biagioni, A., Rossi, M., Alippi, A., Tamburri, E., Lucci, M., Davoli, I., Berezina, S. (2009): Indentation modulus and hardness of viscoelastic thin films by atomic force microscopy: A case study. *Ultramicroscopy*, **109**, 1417–1427.

Passeri, D., Bettucci, A., Rossi, M. (2010): Acoustic and atomic force microscopy for the mechanical characterization of thin films. *Anal. Bioanal. Chem.*, **396**, 2769–2783.

Passeri, D., Alippi, A., Bettucci, A., Rossi, M., Alippi, A., Tamburri, E., Terranova, M. L. (2011): Indentation modulus and hardness of polyaniline thin films by atomic force microscopy. *Synth. Met.*, **161**, 7–12.

Passeri, D., Biagioni, A., Rossi, M., Tamburri, E., Terranova, M. L. (2013a): Characterization of polyaniline-detonation nanodiamond nanocomposite fibers by atomic force microscopy based techniques. *Eur. Polym. J.*, **49**, 991–998.

Passeri, D., Rossi, M., Tamburri, E., Terranova, M. L. (2013b): Mechanical characterization of polymeric thin films by atomic force microscopy based techniques. *Anal. Bioanal. Chem.*, **405**, 1463–1478.

Passeri, D., Rossi, M., Vlassak, J. J. (2013c): On the tip calibration for accurate modulus measurement by contact resonance atomic force microscopy. *Ultramicroscopy*, **128**, 32–41.

Passeri, D., Tamburri, E., Terranova, M. L., Rossi, M. (2015): Polyaniline-nanodiamond fibers resulting from the self-assembly of nano-fibrils: a nanomechanical study. *Nanoscale*, **7**, 14358–14367.

Prasad, M., Kopycinska, M., Rabe, U., Arnold, W. (2002): Measurement of Young's modulus of clay minerals using atomic force acoustic microscopy. *Geophys. Res. Lett.*, **29**, 1172–1179.

Preghenella, M., Pegoretti, A., Migliaresi, C. (2006): Atomic force acoustic microscopy analysis of epoxy-silica nanocomposites. *Polym. Test*, **25**, 443–451.

Rabe, U., Kopycinska, M., Hirsekorn, S., Muñoz Saldaña, J., Schneider, G. A., Arnold, W. (2002): High-resolution characterization of piezoelectric ceramics by ultrasonic scanning force microscopy techniques. *J. Phys. D*, **35**, 2621–2635.

Reggente, M., Rossi, M., Angeloni, L., Tamburri, E., Lucci, M., Davoli, I., Terranova, M. L., Passeri, D. (2015): Atomic force microscopy techniques for nanomechanical characterization: A polymeric case study. *JOM*, **67**, 849–857.

Rossi, M., Cubadda, F., Dini, L., Terranova, M. L., Aureli, F., Sorbo, A., Passeri, D. (2014): Scientific basis of nanotechnology, implications for the food sector and future trends. *Trends Food Sci. Tech.*, **40**, 127–148.

Sahin, O., Magonov, S., Su, C., Quate, C. F., Solgaard, O. (2007): An atomic force microscope tip designed to measure time-varying nanomechanical forces. *Nat. Nanotechnol.*, **2**, 507–514.

Sarioglu, A. F., Atalar, A., Degertekin, F. L. (2004): Modeling the effect of substrate interface defects on contact stiffness for ultrasonic atomic force microscopy. *Appl. Phys. Lett.*, **84**, 5368–5370.

Shatskiy, A., Gavryushkin, P. N., Litasov, K. D., Koroleva, O. N., Kupriyanov, I. N., Borzdov, Y. M., Sharygin, I. S., Funakoshi, K., Palyanov, Y. N., Ohtani, E. (2015): Na-Ca carbonates synthesized under upper-mantle conditions: Raman spectroscopic and X-ray diffraction studies. *Eur. J. Mineral.*, **27**, 175–184.

Shoval, S., Gaft, M., Panczer, G. (2003): Luminescence of Cr^{3+} in natural and calcined diaspore. *J. Therm. Anal.*, **71**, 699–706.

Stan, G., Ciobanu, C. V., Thayer, T. P., Wang, G. T., Creighton, J. R., Purushotham, K. P., Bendersky, L. A., Cook, R. F. (2009): Elastic moduli of faceted aluminum nitride nanotubes measured by contact resonance atomic force microscopy. *Nanotechnology*, **20**, 035706.

Tabor, D. (1953): Mohs's hardness scale - a physical interpretation. *Proc. Phys. Soc.*, **67**, 249–257.

Tsuchiya, J. & Tsuchiya, T. (2009): Elastic properties of δ-AlOOH under pressure: First principles investigation. *Phys. Earth Planet. Int.*, **174**, 122–127.

Tsuji, T. & Yamanaka, K. (2001): Observation by ultrasonic atomic force microscopy of reversible displacement of subsurface dislocations in highly oriented pyrolytic graphite. *Nanotechnology*, **12**, 301–307.

Viti, C. & Ferrari, M. (2006): The nature of Ti-rich inclusions responsible for asterism in Verneuil-grown corundums. *Eur. J. Mineral.*, **18**, 823–834.

Vlassak, J. J., Ciavarella, M., Barber, J. R., Wang, X. (2003): The indentation modulus of elastically anisotropic materials for indenters of arbitrary shape. *J. Mech. Phys. Solids*, **51**, 1701–1721.

Wagner, F. E., Haslbeck, S., Stievano, L., Calogero, S., Pankhurst, Q. A., Martinek, K.-P. (2000): Before striking gold in gold-ruby glass. *Nature*, **407**, 691–692.

Yablon, D. C., Gannepalli, A., Proksch, R., Killgore, J., Hurley, D. C., Grabowski, J., Tsou, A. H. (2012): Quantitative viscoelastic mapping of polyolefin blends with contact resonance atomic force microscopy. *Macromolecules*, **45**, 4363–4370.

Yamanaka, K. (1996): UFM observation of lattice defects in highly oriented pyrolytic graphite. *Thin Solid Films*, **273**, 116–121.

Zheng, Y., Geer, R. E., Dovidenko, K., Kopycinska-Müller, M., Hurley, D. C. (2006): Quantitative nanoscale modulus measurements and elastic imaging of SnO_2 nanobelts. *J. Appl. Phys.*, **100**, 124308.

Received 16 March 2015
Modified version received 9 July 2015
Accepted 3 December 2015

Elastic modulus measurements at variable temperature: Validation of atomic force microscopy techniques

Marco Natali*, Melania Reggente*, Daniele Passeri* and Marco Rossi*,†

*Department of Basic and Applied Sciences for Engineering, SAPIENZA University of Rome, Via A. Scarpa 16, 00161, Rome, Italy
†Research Center for Nanotechnology applied to Engineering of SAPIENZA University of Rome (CNIS), Piazzale A. Moro 5, 00185, Rome, Italy

Abstract. The development of polymer-based nanocomposites to be used in critical thermal environments requires the characterization of their mechanical properties, which are related to their chemical composition, size, morphology and operating temperature. Atomic force microscopy (AFM) has been proven to be a useful tool to develop techniques for the mechanical characterization of these materials, thanks to its nanometer lateral resolution and to the capability of exerting ultra-low loads, down to the piconewton range. In this work, we demonstrate two techniques, one quasi-static, i.e., AFM-based indentation (I-AFM), and one dynamic, i.e., contact resonance AFM (CR-AFM), for the mechanical characterization of compliant materials at variable temperature. A cross-validation of I-AFM and CR-AFM has been performed by comparing the results obtained on two reference materials, i.e., low-density polyethylene (LDPE) and polycarbonate (PC), which demonstrated the accuracy of the techniques.

Keywords: Elastic modulus; temperature; polymer; atomic force microscopy (AFM); indentation; contact resonance atomic force microscopy (CR-AFM)
PACS: 68.37.Ps; 68.37.Tj; 62.20.de; 68.47.Mn

INTRODUCTION

Nowadays, polymer-based nanocomposites and nanomaterials are increasingly proposed for in applications involving critical thermal environments [1–3]. In order to control and enhance their performances, it is important to characterize, among their other properties, their mechanical behavior at the operating temperatures. This requires the development of suitable methodologies, possibly nondestructive, to overcome the limitations of conventional well-established tools, such as depth sensing micro- and nano-indentation (DSI) or ultrasound-based testing [4, 5] and to enable accurate mechanical characterization of compliant materials at the nanometer scale.

Due to both its nondestructive nature and its high spatial resolution, atomic force microscopy (AFM) has been extensively used for the morphological characterization of compliant samples. In addition, the contrast in phase images retrieved in AFM intermittent contact mode (also referred to as tapping mode) is related to the energy dissipation during tip-sample interaction cycles and, thus, provides some qualitative information on viscoelastic properties of samples [6]. Moreover, different AFM based techniques which enable one to quantitatively map the surface mechanical properties of samples have been developed [7–9]. Among these, AFM based indentation (I-AFM) has been extensively used for two decades for the mechanical characterization of soft materials like polymers or biological samples [10–12]. In I-AFM, force-distance curves are collected and analyzed to evaluate the sample Young's modulus using an approach similar to that used in standard DSI tests [13–16]. In CR-AFM, the resonance frequencies of the AFM cantilever in contact with the sample surface are measured and used to determine the local (visco)elastic properties of the sample [17–20]. Moreover, a CR-AFM setup has been recently proposed for mapping the elastic modulus of polymers, with Young's modulus values from a few megapascals to a few gigapascals, at controlled temperature ranging from room conditions to 150°C [21].

In this work, I-AFM and CR-AFM have been mutually validated by comparing the corresponding results obtained on two commercial thick polymeric samples used as reference materials, i.e., low-density polyethylene (LDPE) and polycarbonate (PC), at variable temperature. The reference samples have been selected on the basis of their different Young's modulus and their different glass transition temperature, as LDPE is in rubber-like state and PC in glassy-state but close to the glass transition in the investigated range of temperature.

NanoItaly 2015
AIP Conf. Proc. 1749, 020007-1–020007-7; doi: 10.1063/1.4954490
Published by AIP Publishing. 978-0-7354-1406-8/$30.00

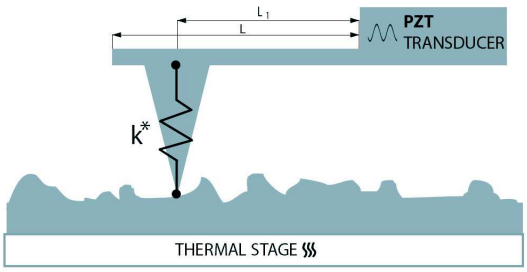

FIGURE 1. Sketch of the model for the cantilever-tip-sample system used to analyze CR-AFM data.

METHODS

Atomic force microscopy based indentation. In I-AFM, force-distance curves are acquired and used to evaluate indentation modulus (M) of the sample. Briefly, at selected locations of the sample surface, the AFM cantilever deflection (d) is recorded as a function of the vertical displacement of the piezoelectric actuator (Δz) when the AFM tip is approached to and then retracted from the sample surface. The collected curves can be used to obtain a force-indentation curves which are analogous to those obtained in standard DSI, the approaching and retracting phases in I-AFM corresponding to the loading and unloading ones in DSI [22, 23]. By varying the range of Δz, different penetration depths can be achieved from a few to several tens or even a few hundreds of nanometers, which represents a key capability in the study of polymeric thin films on stiff substrates [24, 25]. The cantilever deflection is related to the tip-sample interaction force (F_N) by the Hooke's law $F_N = k_c d$, where k_c is the cantilever spring constant. In case of stiff materials, the tip does not indent the surface and, after the contact, any increase of the piezoactuator extension results in an equal increase of the cantilever deflection, so that $d - \Delta z = 0$. Conversely, in case of compliant materials the tip indents the sample surface. In this case, the indentation depth h can be calculated as $h = d - \Delta z$, having assumed $d = 0$ and $\Delta z = 0$ in correspondence of the contact (snap-in) point [22, 23]. The surface elastic modulus of compliant samples can be calculated from the initial slope of the retracting curves, also referred to as the tip-sample contact stiffness k^*, as the unloading phase is affected by plastic effects [26]. k^* is related to the sample elastic modulus through the equation

$$k^* = \frac{2E^*}{\sqrt{\pi}}\sqrt{A_c} \ , \tag{1}$$

where A_c is the contact area, which depends on the tip radius R_t, and E^* is the reduced Young's modulus given by

$$E^* = \left(M^{-1} + M_t^{-1}\right)^{-1} \ , \tag{2}$$

being M and M_t the indentation moduli of the sample and the tip, respectively. For isotropic materials, $M = E/(1-\nu^2)$, where E represents the Young's modulus and ν the Poisson ratio of the investigated sample. In case of samples much more compliant than the tip ($M_t >> M$), $E^* \approx M$. The contact area depends on the geometry of the tip, which has to be calibrated using a set of reference materials [22].

Contact Resonance Atomic Force Microscopy. In CR-AFM, the tip is in contact with the sample surface. The system composed by the cantilever, the tip, and a volume of sample under the tip is set into oscillation at ultrasonic frequencies through a piezoelectric transducer coupled either with the back of the sample or the cantilever chip. The former configuration is sometimes referred to as atomic force acoustic microscopy (AFAM) [27–29] while the latter as ultrasonic AFM (UAFM) [30, 31]. These oscillations result in the high-frequency modulation of both the cantilever deflection and the tip-sample penetration depth. When the probe is not approached to the sample surface, the cantilever can be regarded as a beam clamped at one end while the other one can freely vibrate. In this configuration, the cantilever resonance frequencies f_n^0's depend on the geometry and the mechanical properties of the cantilever [27]. Once engaged to the sample, the tip-sample contact can be modeled by a spring with elastic constant equal to the tip-sample contact stiffness k^*, as sketched in Fig. 1. The modified boundary conditions result in the change in the

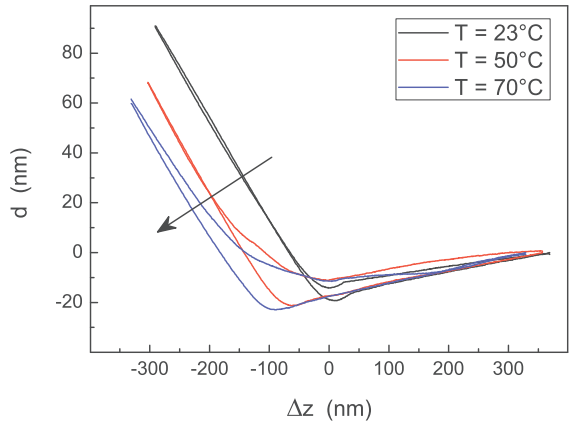

FIGURE 2. I-AFM deflection d versus displacement of the piezoelectric actuator Δz curves collected on LDPE at three different temperature values.

cantilever flexural vibration modes and in the corresponding resonance frequencies. The latter are referred to as the contact resonance frequencies (CRFs) f_n's of the system, where the subscript n refers to the n-th mode. By analyzing the high-frequency components of the cantilever deflection signal through the AFM electronics, we can experimentally measured the CRFs, which are shifted upward with respect to those of the corresponding free modes ($f_n > f_n^0$) [27]. The experimentally determined values of CRFs can be used to evaluate k^* and thus the indentation modulus of the samples M [32]. Indeed, using the characteristic equation of the system depicted in Fig. 1, k^* can be evaluated from f_n and a geometrical parameter $r = L_1/L$ (which is not to be confused with the tip radius R_t) where L is the cantilever length and L_1 is the distance between the tip and the cantilever clamped end. Thus $k^* = k^*(f_n, r)$. To evaluate r, generally unknown, the CRFs corresponding to two different modes are measured (f_n and f_m, with $n \neq m$) and r is obtained as the value in correspondence of which the two CRFs give the same contact stiffness, i.e, $k^*(f_n, r) = k^*(f_m, r)$. Once k^* is obtained, M is determined through Eq. (1) after calibration of the geometry and indentation modulus of the tip using at least two reference samples [33].

EXPERIMENTAL

The experiments have been performed using a standard AFM apparatus (Solver P47H, NT-MDT, Russia), in air and at room conditions. The samples are mounted on a heating stage (SU003, NT-MDT, Russia), consisting of a holder (15×17 mm^2), a temperature sensor (semiconducting diode), an a heating device (resistance) controlled by the AFM electronics with a voltage of 5 V and a maximum power of 4 W to reach a maximum temperature as high as 130°C. As described below, however, the whole temperature range of the device could not be fully exploited due to significant reduction of cantilever deflection signal above 70°C and thus. Thus the temperature range of our experiments was from room temperature to 70°C. The sample and the holder were coupled using a silver-based thermally conductive paste. Although the pre-set temperature of the holder is reached in a few seconds, before carrying out CR-AFM or I-AFM measurements, we have to wait until the surface of the sample has reached the desired temperature so as to avoid thermal drift during the experiment [34, 35]. The time required for reaching the thermal equilibrium depends on the sample thermal conductivity and thickness. With the materials used in this work, i.e., two commercial low-density polyethylene (LDPE) and polycarbonate (PC) sheets 1 mm thick (Goodfellow Cambridge Ltd.), both with surface roughness of about 50 nm measured by AFM topographic images, experiments were performed waiting at least 5 minutes to let the system reach the thermal equilibrium.

I-AFM experiments have been performed using commercial Si cantilevers (NSG-10, NT-MDT, Russia). Cantilevers employed in I-AFM experiments had been previously already used for standard AFM imaging in tapping mode and the tips were blunted, the radius R_t being generally larger than $100 - 200$ nm, thus larger that that of a brand-new

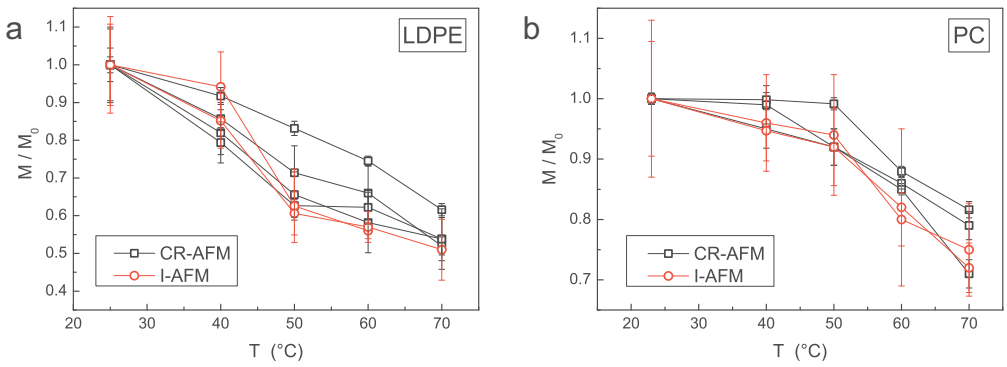

FIGURE 3. Indentation modulus M normalized by the corresponding value at room temperature M_0 measured using I-AFM (red open circles) and CR-AFM (open black squares) on (a) LDPE and (b) PC.

tip (about 10 nm). For each sample and at each temperature value, from 5 to 10 force curves have been recorded at different points of the sample surface (one force curve at each point), analyzed and the obtained results averaged for statistical purposes.

In CR-AFM experiments, we used configuration in which the ultrasonic piezoelectric transducer is coupled with the cantilever chip, in order to obtain detectable oscillations and to avoid possible depolarization of the piezoelectric transducer [21]. This configuration, however, is responsible for an reduction in the signal-to-noise ratio in the cantilever oscillation spectrum [36]. CR-AFM was performed using new commercial Si cantilevers (CSG-10, NT-MDT, Russia) with $R_t = 10$ nm according to the producer. For statistical purposes, CRFs maps on sufficiently wide areas (about 6 μm in length) were recorded and the values of f_n were calculated by averaging the CRFs data. When needed to calculate r, single-point spectra were acquired to measure f_m to avoid excessively time-consuming measurement sessions.

During both I-AFM and CR-AFM experiments, we noticed a significant reduction in the reproducibility of our results above 70°C, in correspondence of which we observed a dramatic lowering of the cantilever deflection signal, preventing the immediate re-use of the probe. This is ascribable to the presence of a Au reflective layer on the cantilever back. Given the different thermal expansion coefficients Si (3.0×10^{-6} °C^{-1}) and Au (14.3×10^{-6} °C^{-1}), the increase of the temperature may lead to the bending of the cantilever, bringing it out from the focusing conditions. Also, the temperature gradient between top and bottom cantilever sides could be responsible for the bending of the cantilever and the loss of focusing conditions. Furthermore, above 70°C even after the subsequent cooling, the initial conditions in the cantilever deflection signal are no longer obtained. This is probably due to a delamination of the Au reflective layer. Therefore, each set of measurements (from room temperature to 70°C) was performed using a new cantilever and the same cantilever could not be used for two different set of measurements. As different cantilevers were used on different samples, the comparison of the elastic moduli would require the calibration of every tip. To avoid excessive lengthening of the measurement session, thus, in this work we compare the elastic modulus values after normalization by the corresponding value at room temperature.

RESULTS AND DISCUSSION

Figure 2 shows examples of $d(\Delta z)$ curves obtained on LDPE at three different temperatures, i.e., 23°C (ambient conditions), 50°C, and 70°C. The curves evidence the reduction of the values of d for the same values of Δz as the temperature increases. In other words, at higher temperatures the same values of F_N are obtained at larger (negative) values of Δz, which indicates a deeper penetration of the tip into the sample and thus the increase of the indentation at higher temperature. This result demonstrates the softening of the LDPE when the temperature increases. Also, the widening of the hysteresis between the approach and retraction curves is observed, which indicates that plastic effects more severely affect indentation curves on LDPE as temperature increases. Analogous effects, but less marked, are observed on PC sample, too (curves not shown).

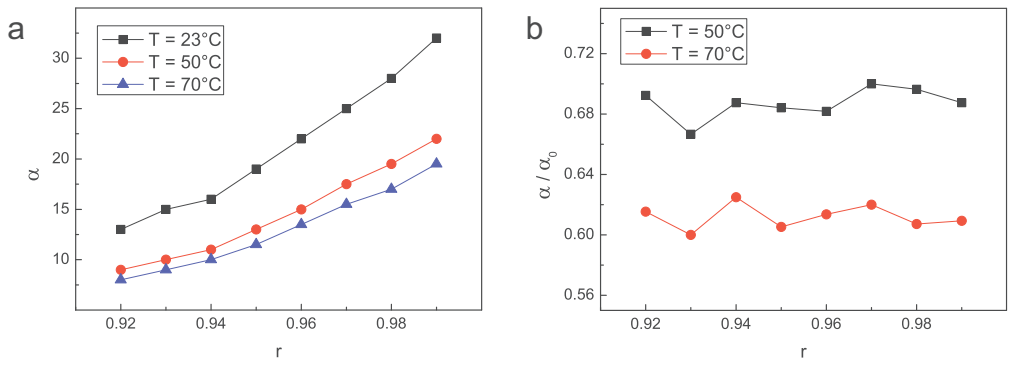

FIGURE 4. (a) Normalized contact stiffness α calculated from the first CRF measured on LDPE at three different temperature as a function of the used value of r. (b) Values of α normalized by the corresponding values at room temperature α_0 as a function of r.

To quantitatively evaluate the indentation modulus of the samples, the geometry of the tip should be calibrated using a set of reference materials [22–24, 37]. In this work, however, indentation modulus values M at different temperatures were compared after normalization by the corresponding value at room temperature M_0, in order to avoid the time-consuming calibration step. In Fig. 3a and b, two series of independent I-AFM indentation modulus measurements (red open circles) on LDPE and PC are shown, respectively. The comparison between the two series of data for each material demonstrates the repeatability of the technique. As temperature increases in the analyzed range, which is comprised between the LDPE glass transition and melting temperatures (around -120°C and 100-140°C, respectively), LDPE indentation modulus roughly linearly decreases down to 50% of M_0, in agreement with results reported in literature [38–40]. For temperature ranging from room condition to 50°C, an almost negligible decrease of indentation modulus is observed on PC, while a slightly more significant reduction down to $75-80\%$ of the corresponding M_0 is observed as temperature increases to 70°C, which is well below the PC glass transition temperature (about 140°C). The relative variation of indentation modulus of PC, less marked than that for LDPE, is compatible with results previously reported in literature [41, 42].

In order to perform CR-AFM measurements, first we measured the first two free resonance frequencies of each cantilever, typical values of which were $f_1^0 = 25$ kHz and $f_2^0 = 130$ kHz. These values were used to calibrate the characteristic geometrical constants of the cantilevers, as detailed elsewhere [43–46]. In the second step of the CR-AFM experimental procedure the first two CRFs were acquired. In particular, f_1 was obtained from statistics on an image and used to evaluate the sample indentation modulus. Conversely, f_2 was obtained from single point contact resonance spectroscopy to evaluate r in combination with f_1. Then, r and f_1 were used to evaluate the normalized contact stiffness $\alpha = k^*/k_c$, which is generally a mode-dependent parameter [47]. According to Eq. (1), α depends on R_t and thus its actual absolute value is strictly related on the experimental conditions and can hardly compared with results on the same materials retrieved in different experiments and with literature data. However, α can be related to M after calibration of M_t and R_t using at least two reference samples [33]. Indeed, R_t is likely to increase during scanning due to tip wear [48, 49], while it has been shown that neglecting the lateral tip-sample coupling in the model in Fig. 1 results in an apparent value of M_t much lower than the real one and comparable with the indentation modulus of the polymers [50]. Therefore, in case of CR-AFM measurements on polymers the approximation $E^* \approx M$ could be no longer valid. Nevertheless, as M_t is comparable with M, we can assume $M_t = \chi M$ where χ is expected to be approximately equal to 1 and independent on temperature. With this assumption, $E^* = M\chi/(\chi+1)$ and Eq. (1) can be rewritten as

$$k^* = \frac{\chi}{\chi+1}\frac{2M}{\sqrt{\pi}}\sqrt{A_c} \ . \tag{3}$$

Therefore, as in this work we are interested in the sample indentation modulus normalized with respect to its room temperature value, from Eq. (3) we can find that $M/M_0 = \alpha/\alpha_0$, which can be thus determined without any calibration

on reference samples. As for r, its determination using f_2 is required since neglecting lateral forces results in apparent values of r lower than the real one [50]. Indeed, in our experiments we determined r in the range $0.93 - 0.98$. Given the same value of f_1, the calculated value of α is dramatically affected by r. This is demonstrated by the curves reported in Fig. 4a, which show the values of α calculated from f_1 measured at three different temperatures on the LDPE sample as a function of the assumed value of r. Nevertheless, when α/α_0 is considered, its value is rather independent on r, as demonstrated by the curves in Fig. 4b where the values of α at 50°C and 70°C reported in Fig. 4a are shown after normalization by α_0 at 23°C (room temperature). Therefore, the analysis of CRFs was conducted assuming $r = 0.95$. The values of M/M_0 (evaluated as α/α_0) determined in three different CR-AFM experimental sessions on LDPE and PC are shown in Fig. 3a and b, respectively (black open squares). The comparison between the two series of data for each material demonstrates the repeatability of CR-AFM. Moreover, CR-AFM results are in good agreement with the I-AFM ones. Notably, the absolute values of M retrieved by the two techniques on each sample are expected to be different, since I-AFM and CR-AFM probe volumes of the sample with different depths, i.e., CR-AFM is more affected than I-AFM by the properties of the first surface layer of the sample. Assuming that the increase of temperature equally affects the surface and the bulk of the sample, and thus that the temperature dependence of the measured indentation modulus does not depend on the used technique, however, the good agreement between the M/M_0 values retrieved by I-AFM and CR-AFM on both the samples demonstrates the accuracy of the two techniques.

CONCLUSIONS

In conclusion, one quasi-static (I-AFM) and one dynamic (CR-AFM) AFM-based techniques have been validated as methods to investigate the temperature dependence of mechanical properties of compliant samples like polymers. The particular configuration of the experimental setup allows one to perform both I-AFM and CR-AFM on the same samples. Thus, the technique to be used can be easily chosen on the basis of sample characteristics, like its thickness, as I-AFM and CR-AFM probe different volume of the material under the tip, i.e., CR-AFM is more sensitive to the surface while I-AFM can access to the bulk properties of the sample. The good agreement between indentation moduli (normalized by the corresponding values at room temperature) retrieved using the two techniques, as well as their compatibility with results obtained using standard macroscopic methods reported in literature, demonstrated their accuracy and validates I-AFM and CR-AFM for nanometer scale elastic modulus characterization of polymers at variable temperatures.

REFERENCES

1. C. Zweben, *JOM* **50**, 47–51 (1998).
2. H. Huang, C. H. Liu, Y. Wu, and S. Fan, *Adv. Mater.* **17**, 1652–656 (2005).
3. H. Liem, and H. S. Choy, *Solid State Commun.* **163**, 41–45 (2013).
4. D. C. Hurley, "Quantitative Measurements of Elastic Properties with Ultrasonic-Based AFM and Conventional Techniques," in *Acoustic scanning probe microscopy*, edited by F. Marinello, D. Passeri, and E. Savio, Springer Berlin Heidelberg, 2012, chap. 12, pp. 351–373.
5. A. Bettucci, *Nanoscience and Nanometrology* **1**, 15–19 (2015).
6. J. Tamayo, and R. García, *Appl. Phys. Lett.* **71**, 2394–2396 (1997).
7. D. Passeri, M. Rossi, E. Tamburri, and M. L. Terranova, *Anal. Bioanal. Chem.* **405**, 1463–1478 (2013).
8. A. X. Cartagena-Rivera, W.-H. Wang, R. L. Geahlen, and A. Raman, *Sci. Rep.* **5**, 1169 (2015).
9. D. Passeri, E. Tamburri, M. L. Terranova, and M. Rossi, *Nanoscale* **7**, 14358–14367 (2015).
10. J. Domke, and M. Radmacher, *Langmuir* **14**, 3320–3325 (1998).
11. A. L. Weisenhorn, M. Khorsandi, S. Kasas, V. Gotzos, and H. J. Butt, *Nanotechnology* **4**, 106–113 (1993).
12. M. Radmacher, *Methods Cell Biol.* **83**, 347–372 (2007).
13. B. Cappella, and G. Dietler, *Surf. Sci. Rep.* **34**, 1–104 (1999).
14. E. Tomasetti, R. Legras, and B. Nysten, *Nanotechnology* **9**, 305–315 (1998).
15. C. A. Clifford, and M. P. Seah, *Appl. Surf. Sci.* **252**, 1915–1933 (2005).
16. C. Reynaud, F. Sommer, C. Quet, N. El Buonia, and D. Tran Minh, *Surf. Interface Anal.* **30**, 185–189 (2000).
17. W. Zhao, R. P. Singh, and C. S. Korach, *Compos. Part A - Appl. S.* **40**, 675–678 (2009).
18. Y. Liu, S. Chen, E. Zussman, C. S. Korach, W. Zhao, and M. Rafailovich, *Macromolecules* **44**, 4439–4444 (2011).
19. J. P. Killgore, D. G. Yablon, A. H. Tsou, A. Gannepalli, P. A. Yuya, J. A. Turner, R. Proksch, and D. C. Hurley, *Langmuir* **27**, 13983–13987 (2011).
20. D. G. Yablon, A. Gannepalli, R. Proksch, J. Killgore, D. C. Hurley, J. Grabowski, and A. H. Tsou, *Macromolecules* **45**, 4363–4370 (2012).

21. F. Marinello, A. Pezzuolo, S. Carmignato, E. Savio, L. De Chiffre, L. Sartori, and R. Cavalli, *AIP Conf. Proc.* **1667**, 020009 (2015).
22. D. Passeri, A. Bettucci, A. Biagioni, M. Rossi, A. Alippi, M. Lucci, I. Davoli, and S. Berezina, *Rev. Sci. Instrum.* **79**, 066105 (2008).
23. D. Passeri, A. Bettucci, A. Biagioni, M. Rossi, A. Alippi, E. Tamburri, M. Lucci, I. Davoli, and S. Berezina, *Ultramicroscopy* **109**, 1417–1427 (2009).
24. D. Passeri, A. Alippi, A. Bettucci, M. Rossi, A. Alippi, E. Tamburri, and M. L. Terranova, *Synth. Met.* **161**, 7–12 (2011).
25. E. Tamburri, V. Guglielmotti, R. Matassa, S. Orlanducci, S. Gay, G. Reina, M. L. Terranova, D. Passeri, and M. Rossi, *J. Mater. Chem. C* **2**, 3703–3716 (2014).
26. G. M. Pharr, W. C. Oliver, and F. R. Brotzen, *J. Mater. Res.* **7**, 613–617 (1992).
27. U. Rabe, J. Janser, and W. Arnold, *Rev. Sci. Instrum.* **67**, 3281–3293 (1996).
28. U. Rabe, M. Kopycinska-Müller, and S. Hirsekorn, "Atomic force acoustic microscopy," in *Acoustic scanning probe microscopy*, edited by F. Marinello, D. Passeri, and E. Savio, Springer-Verlag (Berlin, Heidelberg), 2012, chap. 5, pp. 123–153.
29. D. Passeri, A. Bettucci, M. Germano, M. Rossi, A. Alippi, V. Sessa, A. Fiori, E. Tamburri, and M. L. Terranova, *Appl. Phys. Lett.* **88**, 121910 (2006).
30. K. Yamanaka, Y. Maruyama, T. Tsuji, and K. Nakamoto, *Appl. Phys. Lett.* **78**, 1939–1941 (2001).
31. K. Yamanaka, and T. Tsuji, "Ultrasonic atomic force microscopy UAFM," in *Acoustic scanning probe microscopy*, edited by F. Marinello, D. Passeri, and E. Savio, Springer Berlin Heidelberg, 2012, chap. 6, pp. 155–187.
32. D. Passeri, A. Bettucci, M. Germano, M. Rossi, A. Alippi, A. Fiori, E. Tamburri, M. L. Terranova, and J. J. Vlassak, *Microelectr. Eng.* **84**, 490–494 (2007).
33. G. Stan, and W. Price, *Rev. Sci. Instrum.* **77**, 103707 (2006).
34. F. Marinello, M. Balcon, S. Carmignato, and E. Savio, *Mechatronics* **21**, 1272–1278 (2011).
35. F. Marinello, M. Balcon, P. Schiavuta, S. Carmignato, and E. Savio, *Meas. Sci. Technol.* **22**, 094016 (2011).
36. S. Banerjee, N. Gayathri, S. Dash, A. K. Tyagi, and B. Raj, *Appl. Phys. Lett.* **86**, 211913 (2005).
37. D. Passeri, P. Anastasiadis, E. Tamburri, V. Guglielmotti, and M. Rossi, *Nuovo Cimento C* **36**, 83–88 (2013).
38. A. G. Pedroso, and D. S. Rosa, *Carbohyd. Polym.* **59**, 1–9 (2005).
39. D. H. Chen, L. Hong, X. W. Nie, X. L. Wang, and X. Z. Tang, *Eur. Polym. J.* **39**, 871–876 (2003).
40. M. C. Guimarães Rocha, M. E. Leyva, and M. G. de Oliveira, *Polimeros* **24**, 23–29 (2014).
41. D. M. Knauss, T. H. Yoon, and J. E. McGrath, *Polymer* **43**, 6415–6420 (2002).
42. C. O. Phillips, and T. C. C. D. T. Gethin, *J. Mater. Process. Tech.* **200**, 221–231 (2008).
43. D. Passeri, A. Bettucci, M. Germano, M. Rossi, A. Alippi, S. Orlanducci, M. L. Terranova, and M. Ciavarella, *Rev. Sci. Instrum.* **76**, 093904 (2005).
44. D. Passeri, M. Rossi, A. Alippi, A. Bettucci, M. L. Terranova, E. Tamburri, and F. Toschi, *Physica E* **40**, 2419–2424 (2008).
45. D. Passeri, M. Rossi, A. Alippi, A. Bettucci, D. Manno, A. Serra, E. Filippo, M. Lucci, and I. Davoli, *Superlattices Microstruct.* **44**, 641–649 (2008).
46. M. Reggente, M. Rossi, L. Angeloni, E. Tamburri, M. Lucci, I. Davoli, M. L. Terranova, and D. Passeri, *JOM* **67**, 849–857 (2015).
47. D. Passeri, A. Bettucci, and M. Rossi, *Anal. Bioanal. Chem.* **396**, 2769–2783 (2010).
48. F. Marinello, P. Schiavuta, S. Carmignato, and E. Savio, *CIRP Journal of Manufacturing Science and Technology* **3**, 49–54 (2010).
49. F. Marinello, P. Schiavuta, S. Vezzù, A. Patelli, S. Carmignato, and E. Savio, *Wear* **271**, 534–538 (2011).
50. D. Passeri, M. Rossi, and J. J. Vlassak, *Ultramicroscopy* **128**, 32–41 (2013).

Contact resonance atomic force microscopy for viscoelastic characterization of polymer-based nanocomposites at variable temperature

Marco Natali*, Daniele Passeri*, Melania Reggente*, Emanuela Tamburri†, Maria Letizia Terranova† and Marco Rossi*,**

*Department of Basic and Applied Sciences for Engineering, SAPIENZA University of Rome, Via A. Scarpa 16, 00161, Rome, Italy
†Department of Chemical Sciences and Technologies, University of Rome Tor Vergata and MinimaLab, Via della Ricerca Scientifica, 00133 Rome, Italy
**Research Center for Nanotechnology applied to Engineering of SAPIENZA University of Rome (CNIS), Piazzale A. Moro 5, 00185, Rome, Italy

Abstract. Characterization of mechanical properties at the nanometer scale at variable temperature is one of the main challenges in the development of polymer-based nanocomposites for application in high temperature environments. Contact resonance atomic force microscopy (CR-AFM) is a powerful technique to characterize viscoelastic properties of materials at the nanoscale. In this work, we demonstrate the capability of CR-AFM of characterizing viscoelastic properties (i.e., storage and loss moduli, as well as loss tangent) of polymer-based nanocomposites at variable temperature. CR-AFM is first illustrated on two polymeric reference samples, i.e., low-density polyethylene (LDPE) and polycarbonate (PC). Then, temperature-dependent viscoelastic properties (in terms of loss tangent) of a nanocomposite sample constituted by a epoxy resin reinforced with single-wall carbon nanotubes (SWCNTs) are investigated.

Keywords: Contact resonance atomic force microscopy; viscoelasticity; loss tangent; temperature; polymer; nanocomposite; carbon nanotubes;
PACS: 68.37.Ps; 68.47.Mn; 62.25.-g; 68.60.Bs; 81.05.Qk

INTRODUCTION

Reinforcement of polymers using suitable nanomaterials is a smart procedure to obtain nanocomposite materials with enhanced physical properties, including electric and/or thermal conductivity, strength, elasticity, toughness and durability, also in thermal management applications [1–3]. To set up reproducible synthetic routes, the properties of the obtained materials must be characterized from the macroscopic to the microscopic and sub-microscopic scale in the range of temperature of interest. As far as mechanical properties are concerned, dynamic mechanical analysis (DMA) is a well-established techniques which allows the independent measurement of the real and imaginary parts of the complex mechanical modulus of viscoelastic materials, i.e, the storage and loss modulus, respectively [4]. DMA can be performed at variable temperature, e.g., the so-called dynamic mechanical thermal analysis (DMTA), allowing for instance the identification of glass transition and other thermal transitions in polymeric materials [5]. Also, based on atomic force microscopy (AFM), counterparts of DMA have been developed which enable the characterization of viscoelastic materials at sub-micrometer and nanometer scale [6]. Due to its high spatial resolution, nanometer dimensions of the probed volume of materials, and nondestructive nature of measurements, AFM is currently a broadly used tool for the mechanical investigation of polymers community. AFM-based quasi-static nanoindentation is a well-established technique for the characterization of elastic properties of compliant materials [7, 8], also when they are represented by layered ultrathin films on stiff substrates [9, 10]. Also, it can be used to study viscoelasticity of soft materials through relaxation indentation tests [11]. Contact resonance AFM (CR-AFM) is a well-established but continuously evolving technique, in which the elastic modulus of samples is measured from the analysis of the flexural modes of the cantilever oscillating with the tip in contact with the sample surface [12, 13]. CR-AFM enables accurate measurement and mapping of elastic modulus in a broad range of values, e.g., from stiff crystals to polymers and biological materials [14, 15]. Also, CR-AFM characterization of elastic modulus of polymer blends at different temperatures was demonstrated [16]. Moreover, a recent improvement of CR-AFM, the so-called contact resonance AFM for viscoelasticity (CRAVE) [17, 18], has been recently improved to enable measurement and mapping of storage

NanoItaly 2015
AIP Conf. Proc. 1749, 020008-1–020008-8; doi: 10.1063/1.4954491
Published by AIP Publishing. 978-0-7354-1406-8/$30.00

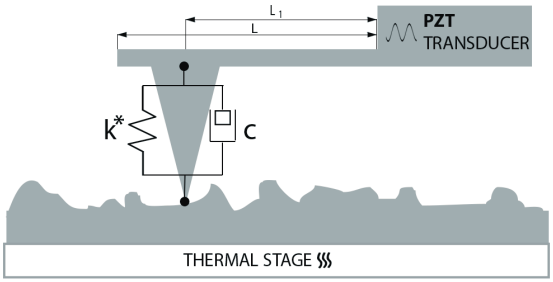

FIGURE 1. Sketch of the model used to analyze CR-AFM data.

and loss moduli as well as of loss tangent of viscoelastic materials [19–23]. Also, CR-AFM was recently demonstrated for the mapping of loss tangent of polymer blends at variable temperature from room temperature to about 80°C [24]. In this work, we describe the use of CR-AFM for the viscoleastic characterization of polymer-based nanocomposites at variable temperature. First, the method was demonstrated on two polymeric reference materials, i.e, low-density polyethylene (LDPE) and polycarbonate (PC), by studying the thermal dependence of their storage and loss moduli as well as of their loss tangent. Then, CR-AFM was demonstrated for polymeric nanocomposites by presenting a case study on epoxy resin loaded with single-wall carbon nanotubes (SWCNTs).

EXPERIMENTAL

Materials

A commercial blend of polystyrene (PS) and low-density polyethylene (LDPE) on Si substrate (PS/LDPE, Bruker Inc.) was used to assess the accuracy of the technique at room temperature [15, 25]. LDPE and polycarbonate (PC) sheets 1 mm thick (Goodfellow Cambridge Ltd.) were used as reference samples to verify the accuracy of CR-AFM for viscoelastic characterizations [26, 27]. LDPE and PC are characterized by different glass transition temperature, i.e., about -120°C and 140°C, respectively.

The case study was carried out on low viscosity epoxy resin formed by condensation between bisphenol A and epichlorhydrin, loaded with single-wall carbon nanotubes (SWCNTs) [28]. Triethylenetetramine was used as hardener, with a mixing ratio of 30:70 w/w. SWCNTs were produced by arc discharge and then purified in order to remove amorphous carbon and other residues. Nanocomposite sample was prepared by loading the epoxy resin with 3% in weight of SWCNTs, after dispersion of SWCNTs in $CHCl_3$ in ultrasonic bath with 9 runs of 1 h. The mixture was then further sonicated with ultrasonic bath and hand-stirring in order to optimize the dispersion. Finally, the corresponding weight fraction of hardener was added and the whole mixture has been dispersed again in an ultrasonic bath and hand-stirring for several minutes [28].

Experimental apparatus and equipment

Experiments have been performed using a standard AFM apparatus (Solver P47H, NT-MDT, Russia), in air and at room conditions. The samples are mounted on a heating stage (SU003, NT-MDT, Russia), consisting of a holder (15×17 mm^2), a temperature sensor (semiconducting diode), an a heating device (resistance) controlled by the AFM electronics with a voltage of 5 V and a maximum power of 4 W to reach a maximum temperature as high as 130°C. The sample and the holder were coupled using a Silver-based thermally conductive paste. Before carrying out CR-AFM measurements, we have to wait until the surface of the sample has reached the desired temperature to avoid thermal drift during the experiment. The time required for reaching the thermal equilibrium depends on the sample thermal conductivity and thickness. In case of LDPE and PC, thermal equilibrium was reached in 5 minutes, while the thicker epoxy and epoxy/SWCNTs required at least 10 minutes. CR-AFM experiments have been performed using commercial

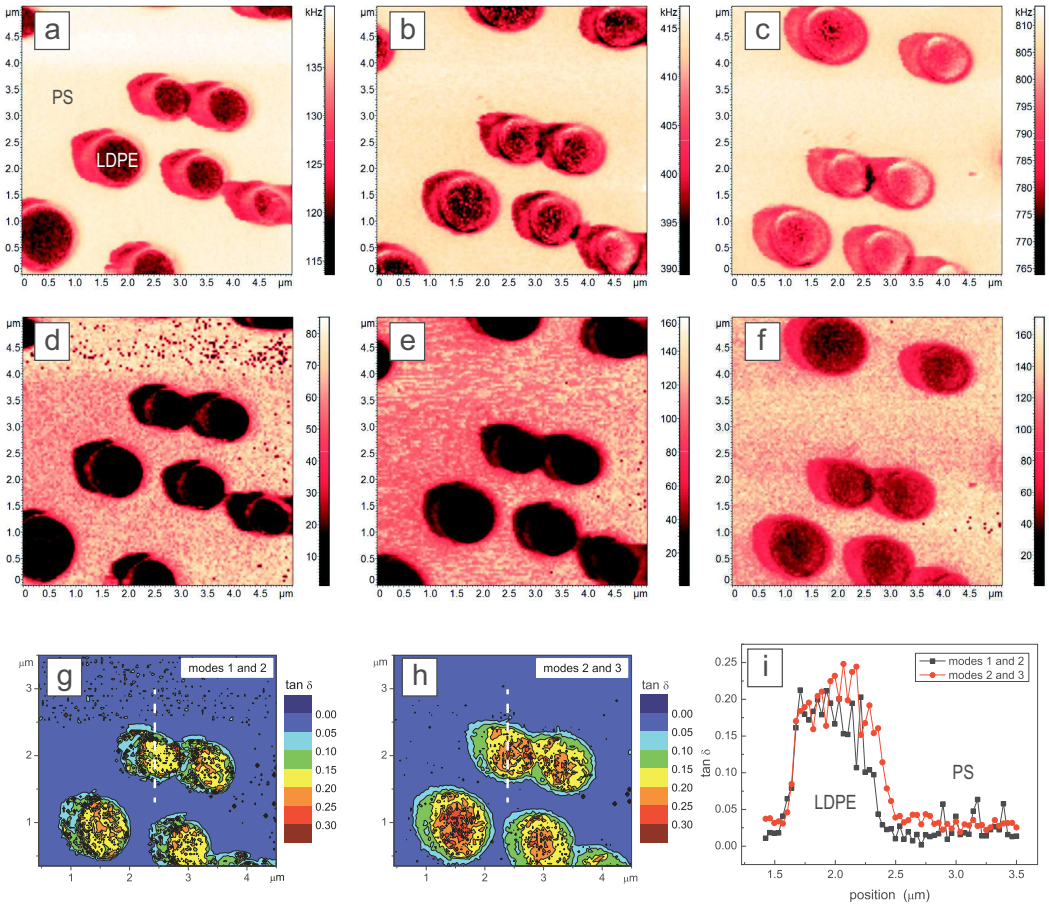

FIGURE 2. CR-AFM characterization of a reference LDPE/PS polymeric blend at room temperature. Maps of the contact resonance frequencies f_1 (a), f_2 (b), and f_3 (c), and maps of the corresponding quality factors Q_1 (d), Q_2 (e), and Q_3 (f). Maps of $\tan\delta$ obtained from the analysis of modes 1 and 2 (g) and of modes 2 and 3 (h). (i) Profiles of $\tan\delta$ values extracted in correspondence of the dotted lines in (g) and (h).

Si cantilevers (CSG-10, NT-MDT, Russia), with nominal dimensions: length L$= 230 \pm 5$ μm, width w$= 40 \pm 3$ μm and thickness t $= 2 \pm 0.5$ μm. In the experimental configuration used in this work, the ultrasonic piezoelectric transducer is coupled with the cantilever chip [16]. During CR-AFM experiments, we noticed a significant reduction in the reproducibility of our results above 70°C, in correspondence of which we observed a dramatic lowering of the cantilever deflection signal, preventing the immediate re-use of the probe. This problem is due to the presence of the Au reflective layer on the cantilever back. As temperature increases, a deformation of the cantilever is expected due to the different thermal expansion coefficients of Si and Au, which brings the cantilever out from the focusing conditions. Furthermore, even after the subsequent cooling, the previous signal heating characteristics are no longer obtained, which is probably due to a delamination of the Au reflective layer.

TECHNIQUE

In the first step of CR-AFM experimental procedure, the oscillation spectrum of the cantilever free of oscillating in air is analyzed to determine some of its flexural modes. For the n-th selected mode, the free resonance frequency f_n^0 and the quality factor Q_n^0 are measured and used to determine some characteristic parameters of the cantilever [17, 18]. The AFM tip is then brought in contact with the sample surface. The cantilever-tip-sample system is set into oscillation, e.g., through piezoelectric actuator coupled with the back of the sample [29] or with the cantilever chip [30, 31], through Schottky barrier depletion-layer actuation [32], or through photothermal excitation [33]. The contact between the sample and the tip, the latter placed at distance L_1 from the cantilever chip being L the cantilever length, can be modeled as the parallel between a spring with elastic constant k^* and a dashpot of damping σ. These new boundary conditions determine the contact modes of the cantilever. From the analysis of the cantilever oscillation spectrum, the contact resonance frequency (CRF) f_n and the corresponding quality factor Q_n are measured for the n-th mode. These parameters are used to evaluate the normalized contact stiffness $\alpha = k^*/k_c$ and the normalized damping $\beta = \sigma\sqrt{L_1^2/(9EI\rho A)}$, where k_c is the spring constant, E the Young's modulus, I the area moment of inertia, ρ the density, and A the cross-sectional area of the cantilever [17, 18]. In particular, to evaluate the tip position expressed in terms of the ration $r = L_1/L$, the contact resonance frequencies corresponding to two different modes are measured (say f_n and f_m, with $n \neq m$). r is obtained as the value in correspondence of which the two CRFs give the same contact stiffness, $k^*(f_n, r) = k^*(f_m, r)$, neglecting the damping σ [34–36]. After calibration of the tip geometry and mechanical properties [37–39], knowledge of α and β allows one to evaluate the sample storage and loss moduli, E' and E'', respectively [19, 20]. Calibration procedure, however, is a source of uncertainty and is responsible for the lengthening of each measurement session. To avoid calibration, viscoelastic properties of the sample can be obtained in terms of the loss tangent $\tan\delta$ defined as

$$\tan\delta = \frac{E''}{E'} \quad . \tag{1}$$

From CR-AFM data, $\tan\delta$ can be calculated as

$$\tan\delta = (\lambda_n r)^2 \frac{\beta}{\alpha} \frac{f_n}{f_n^0} \quad , \tag{2}$$

where λ_n is the solution of the characteristic equation for free flexural vibrations of the cantilever $1 + \cos\lambda_n \cosh\lambda_n = 0$, which can be calculated as high as $\lambda_1 = 1.8751$, $\lambda_2 = 4.6941$, $\lambda_3 = 7.8548$ for the first, second, and third flexural mode, respectively [21, 23]. Eq. (2) allows one to determine $\tan\delta$ without the explicit calculation of E' and E'' and, thus, without calibration of the tip using reference materials.

RESULTS AND DISCUSSION

Validation on reference materials

In order to assess the accuracy of CR-AFM at room temperature, we characterized the PS/LDPE reference sample which is constituted by circular regions of LDPE randomly dispersed in the PS matrix. Having elastic modulus of about 100 MPa, LDPE is softer than PS which has elastic modulus of about 2 GPa [15, 40]. The maps of the resonance frequencies of the first three modes, i.e., f_1, f_2, and f_3, respectively, are shown in Fig. 2a , b, and c, respectively. The Q-factor maps of the same modes are shown in Fig. 2d, e, and f, respectively. From the frequency images of the first two modes, the map of r was obtained neglecting the damping. The maps of r, f_1, and Q_1 were then combined to numerically solving the (complex) characteristic equation of the system in Fig. 1. The maps of α and β were thus obtained (images not shown). Using Eq. (2), these were finally used to obtain the map of $\tan\delta$ relative to modes 1 and 2 reported in Fig. 2g. An analogous analysis of the images of the second and third modes allowed us to obtain the map of $\tan\delta$ relative to modes 2 and 3 reported in Fig. 2h. The values of $\tan\delta$ obtained for the two couples of modes are in good agreement with each other as shown by the superimposition of two representative profiles reported in Fig. 2i. The measured values of $\tan\delta$ on LDPE and PS are 0.19 ± 0.01 and 0.025 ± 0.005, in good agreement with data reported in literature [41–43].

To verify the effect of the choice of the analyzed couple of modes, on the same area of the sample In order to verify

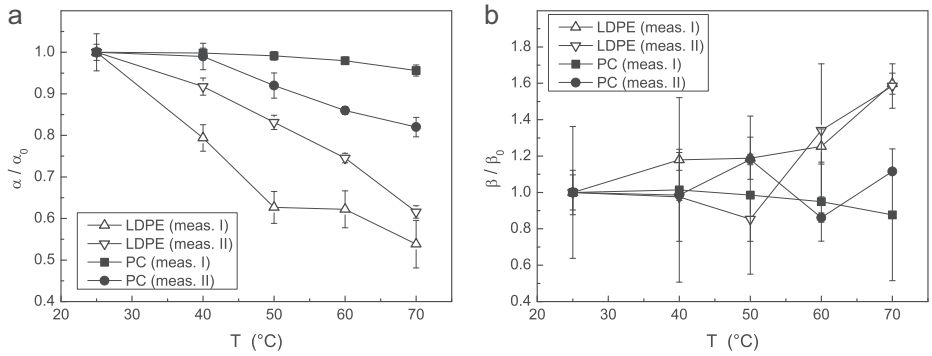

FIGURE 3. (a) Measured values of storage modulus E' normalized by its value at room temperature E'_0 as a function of the temperature T obtained in two different measurements on LDPE (open symbols) and PC (full symbols). (b) Measured values of loss modulus E'' normalized by its value at room temperature E''_0 as a function of the temperature T obtained in two different measurements on LDPE (open symbols) and PC (full symbols).

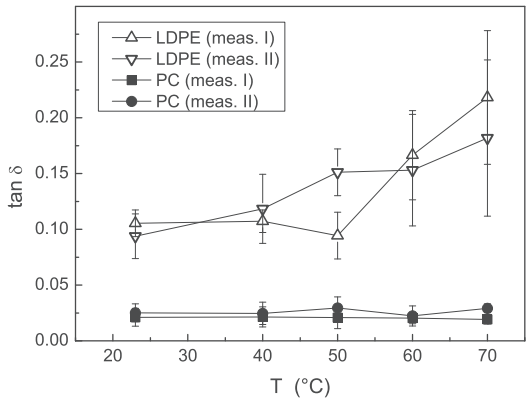

FIGURE 4. Measured values of $\tan\delta$ as a function of the temperature T obtained in two different measurements on LDPE (open symbols) and PC (full symbols).

the accuracy of CR-AFM for viscoelastic characterization at variable temperature, in the first part of this work two polymers with well-known mechanical properties (LDPE and PC) were studied. For each sample, each measurement session was performed using a different cantilever, the values of f_1^0, Q_1^0, and f_2^0 were preliminarily measured. At each temperature from 23°C to 70°C, f_1 and Q_1 were evaluated from statistics on maps, the size of which was chosen aiming at containing the time required for each measurement having nevertheless a statistically significant number of points, while f_2 was obtained by single point measurement in order to avoid excessive lengthening of the measurements session. Thus, f_1 and f_2 have been used to determine r by numerically solving the characteristic equation of the system depicted in Fig. 1 assuming $\sigma = 0$. The values of r we obtained were found to slightly vary among different measurements, doing range between 0.93 and 0.98. These values are in any case lower than the real value of $r = 0.985$ determined by scanning electron microscopy (SEM) images [25]. This can be attributed to the fact that lateral forces at the tip-sample contact increase the CRFs associated to each mode at relatively large values of k^*/k_c [44]. Neglecting these forces in CR-AFM data analysis results in 'effective' values of r smaller than the real one [39]. The determined values of r and the experimental values of f_1 and Q_1 were finally used to numerically solve the characteristic equation of the system in Fig. 1 in order to calculate α and β. Figure 3a shows the values of α normalized by the corresponding

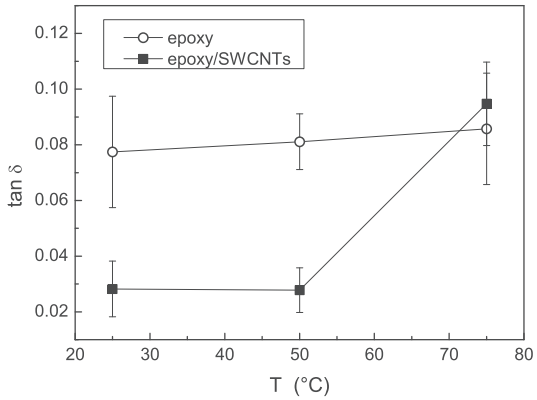

FIGURE 5. Experimental values of the loss tangent ($\tan\delta$) as a function of the temperature measured through CR-AFM on the epoxy (open symbols) and epoxy/SWCNTs (full symbols) samples.

value at room temperature α_0 obtained in two different experimental sessions on LDPE (open symbols) and in two different experimental sessions on PC (full symbols). α, which is proportional to the storage modulus E', is found to decrease on both the samples as temperature increases. In the case of PC, α is reduced to no less than 85% at 70°C, while more significant reductions to $55-60\%$ is observed in the case of LDPE. Figure 3b shows the values of β normalized by the corresponding value at room temperature β_0 obtained in two different experimental sessions on LDPE (open symbols) and in two different experimental sessions on PC (full symbols). In the case of PC, β (proportional to the loss modulus E'') is independent (within the experimental error) on temperature in the investigated range. Conversely, in the case of LDPE, β increases to 160% of its room temperature value at 70°C. The difference between PC and LDPE is more evident when the corresponding values of $\tan\delta$ (reported in Fig. 4) are considered. Indeed, in the case of PC, $\tan\delta$ is found to be independent on temperature, its mean value being 0.023 ± 0.004. The latter is in good agreement with the value of about 0.025, measured using DMA in the same range of temperature, recently reported in literature [45]. Conversely, $\tan\delta$ measured on LDPE definitely increases with temperature from 0.1 at room temperature to about 0.2 at $T=70$°C. These values are consistent with those (approximately from 0.13 to 0.23) obtained in the same range of temperature using DMA recently reported [41]. It should be explicitly noted, however, that the comparison among the results of mechanical characterizations obtained by different techniques on polymers reported in literature may be not significant and misleading. Indeed, mechanical properties of polymers may dramatically depend on the specific synthetic procedure and the aging of the material. Also, viscoelastic response is frequency dependent and thus a certain discrepancy may result from the different frequency ranges of CR-AFM and DMA [6, 46]. Finally, CR-AFM and DMA generally probe different volumes of sample under the surface. Thus, these techniques are differently affected by the presence of softer layers at the polymer surface [15]. Nevertheless, the results of the characterization of $\tan\delta$ of both PC and LDPE demonstrate the accuracy of CR-AFM technique for the viscoelastic characterization of polymer-based materials at variable temperature.

Case study: Epoxy/SWCNTs nanocomposites

In order to demonstrate the technique on polymer-based nanocomposites, we selected epoxy resin loaded with SWCNTs as a significant case study. The choice of this particular material is due to the scientific and technological interest in nanocomposites obtained by functionalization of polymeric matrices with Carbon-based nanomaterials, e.g., carbon nanotubes [47, 48] or nanodiamonds [49, 50]. The experimental procedure is the same we followed in the analysis of LDPE and PC, which is described above in details. Two different cantilevers were used to characterize the epoxy and the epoxy/SWCNTs samples, the values of f_1^0 and Q_1^0 of which are reported in Table 1. When in contact,

TABLE 1. CR-AFM experimental data obtained on epoxy and epoxy/SWCNTs samples. The parameters of the first mode of the free cantilevers (namely, the resonance frequency f_1^0 and the quality factor Q_1^0) are reported together with the corresponding ones with the tip in contact with the sample surface (namely, the contact resonance frequency f_1 and the quality factor Q_1) measured at three different temperature values.

			$T = 25°C$		$T = 50°C$		$T = 70°C$	
Sample	f_1^0 (kHz)	Q_1^0	f_1 (kHz)	Q_1	f_1 (kHz)	Q_1	f_1 (kHz)	Q_1
epoxy	27.5	55	141.8 ± 1.5	33 ± 1	139.2 ± 1.3	31 ± 1	137.2 ± 1.5	29 ± 1
epoxy/SWCNTs	24.5	88	138.5 ± 1.3	31 ± 1	137.5 ± 1.2	29 ± 1	134.5 ± 1.2	28 ± 1

values of f_1 and Q_1 were recorded for each sample on an area of $5 \times 1\ \mu m^2$, by applying a normal load of about 20 nN at three different temperatures, as reported in Table 1. As expected, for both the sample f_1 and Q_1 decrease as temperature increases f_1. The values of f_1 and Q_1 were used to calculate those of $\tan\delta$, which are shown in Fig. 5. The epoxy is characterized by a value of $\tan\delta$ of about 0.08, which seems to slightly increase but can be considered definitely constant in the investigated temperature range. From room temperature to 50°C, the epoxy/SWCNTs sample is characterized by $\tan\delta = 0.03$, lower than that of epoxy of more than 60%. At higher temperature, however, the value of $\tan\delta$ is the same of epoxy within the experimental uncertainty. This suggests that (at least in a region of the sample near the surface) at lower temperature the nanocomposite is actually reinforced by the presence of the SWCNTs fillers, while at high temperature its viscoelastic response is dominated by that of the epoxy matrix and the reinforcing effect of the nano-filler is lost.

CONCLUSIONS

CR-AFM is an AFM-base technique which allows one to characterize the elastic and viscoelastic response of materials at the nanometer scale at variable temperature. In this work, the potential of CR-AFM for the viscoelastic characterization of polymer-based nanocomposites has been demonstrated. First, the technique is illustrated on two polymeric reference materials, i.e., LDPE and PC. The analysis of the measured storage and loss moduli as well as of the loss tangent confirmed the accuracy of the technique. In particular, the loss tangent could be measured without any additional time-consuming calibration step. Then, a case study was presented in which CR-AFM was successfully employed in the characterization of a nanocomposite sample formed by epoxy resin reinforced with SWCNTs. CR-AFM measurements of $\tan\delta$ confirmed the reinforcement of surface of the material due to the presence of SWCNTs from room temperature to 50°C, while at higher temperature the viscoelastic response of the nanocomposite is mainly due to the epoxy matrix.

REFERENCES

1. C. Zweben, *JOM* **50**, 47–51 (1998).
2. H. Huang, C. H. Liu, Y. Wu, and S. Fan, *Adv. Mater.* **17**, 1652–656 (2005).
3. H. Liem, and H. S. Choy, *Solid State Commun.* **163**, 41–45 (2013).
4. C. C. White, M. R. Vanlandingham, P. L. Drzal, N. K. Chang, and S. H. Chang, *J. Polym. Sci. B Pol. Phys.* **43**, 1812–1824 (2005).
5. R. E. Wetton, R. D. L. Marsh, and J. G. Van-de-Velde, *Macromolecules* **175**, 1–11 (1991).
6. J. Le Rouzic, P. Delobelle, P. Vairac, and B. Cretin, *Eur. Phys. J. Appl. Phys.* **48**, 11201 (2009).
7. A. L. Weisenhorn, M. Khorsandi, S. Kasas, V. Gotzos, and H. J. Butt, *Nanotechnology* **4**, 106–113 (1993).
8. J. Domke, and M. Radmacher, *Langmuir* **14**, 3320–3325 (1998).
9. A. Kovalev, H. Shulha, M. Lemieux, N. Myshkin, and V. V. Tsukruk, *J. Mater. Res.* **19**, 716–728 (2004).
10. D. Passeri, A. Alippi, A. Bettucci, M. Rossi, A. Alippi, E. Tamburri, and M. L. Terranova, *Synth. Met.* **161**, 7–12 (2011).
11. S. Tripathy, and E. J. Berger, *J. Biomech. Eng. - T. ASME* **131**, 094507 (2009).
12. U. Rabe, J. Janser, and W. Arnold, *Rev. Sci. Instrum.* **67**, 3281–3293 (1996).
13. U. Rabe, M. Kopycinska-Müller, and S. Hirsekorn, "Atomic force acoustic microscopy," in *Acoustic scanning probe microscopy*, edited by F. Marinello, D. Passeri, and E. Savio, Springer-Verlag (Berlin, Heidelberg), 2012, chap. 5, pp. 123–153.
14. D. Passeri, A. Bettucci, and M. Rossi, *Anal. Bioanal. Chem.* **396**, 2769–2783 (2010).
15. D. Passeri, M. Rossi, E. Tamburri, and M. L. Terranova, *Anal. Bioanal. Chem.* **405**, 1463–1478 (2013).

16. F. Marinello, A. Pezzuolo, S. Carmignato, E. Savio, L. De Chiffre, L. Sartori, and R. Cavalli, *AIP Conf. Proc.* **1667**, 020009 (2015).
17. P. A. Yuya, D. C. Hurley, and J. A. Turner, *J. Appl. Phys.* **104**, 074916 (2008).
18. P. A. Yuya, D. C. Hurley, and J. A. Turner, *J. Appl. Phys.* **109**, 113528 (2011).
19. J. P. Killgore, D. G. Yablon, A. H. Tsou, A. Gannepalli, P. A. Yuya, J. A. Turner, R. Proksch, and D. C. Hurley, *Langmuir* **27**, 13983–13987 (2011).
20. D. G. Yablon, A. Gannepalli, R. Proksch, J. Killgore, D. C. Hurley, J. Grabowski, and A. H. Tsou, *Macromolecules* **45**, 4363–4370 (2012).
21. D. C. Hurley, S. E. Campbell, J. P. Killgore, L. M. Cox, and Yifu, *Macromolecules* **46**, 9396–9402 (2013).
22. D. G. Yablon, J. Grabowski, and I. Chakraborty, *Meas. Sci. Technol.* **25**, 055402 (2014).
23. A. B. Churnside, R. C. Tung, and J. P. Killgore, *Langmuir* **31**, 11143–11149 (2015).
24. I. Chakraborty, and D. G. Yablon, *Polymer* **55**, 1609–1612 (2014).
25. M. Reggente, M. Rossi, L. Angeloni, E. Tamburri, M. Lucci, I. Davoli, M. L. Terranova, and D. Passeri, *JOM* **67**, 849–857 (2015).
26. D. Passeri, A. Bettucci, A. Biagioni, M. Rossi, A. Alippi, M. Lucci, I. Davoli, and S. Berezina, *Rev. Sci. Instrum.* **79**, 066105 (2008).
27. D. Passeri, A. Bettucci, A. Biagioni, M. Rossi, A. Alippi, E. Tamburri, M. Lucci, I. Davoli, and S. Berezina, *Ultramicroscopy* **109**, 1417–1427 (2009).
28. D. Passeri, M. Rossi, A. Alippi, A. Bettucci, M. L. Terranova, E. Tamburri, and F. Toschi, *Physica E* **40**, 2419–2424 (2008).
29. D. Passeri, A. Bettucci, M. Germano, M. Rossi, A. Alippi, A. Fiori, E. Tamburri, M. L. Terranova, and J. J. Vlassak, *Microelectr. Eng.* **84**, 490–494 (2007).
30. K. Yamanaka, A. Noguchi, T. Tsuji, T. Koike, and T. Goto, *Surf. Interface Anal.* **27**, 600–606 (1999).
31. K. Yamanaka, and T. Tsuji, "Ultrasonic atomic force microscopy UAFM," in *Acoustic scanning probe microscopy*, edited by F. Marinello, D. Passeri, and E. Savio, Springer Berlin Heidelberg, 2012, chap. 6, pp. 155–187.
32. K. Schwarz, U. Rabe, S. Hirsekorn, and W. Arnold, *Appl. Phys. Lett.* **92**, 183105 (2008).
33. R. Wagner, and J. P. Killgore, *Appl. Phys. Lett.* **107**, 203111 (2015).
34. D. Passeri, A. Bettucci, M. Germano, M. Rossi, A. Alippi, S. Orlanducci, M. L. Terranova, and M. Ciavarella, *Rev. Sci. Instrum.* **76**, 093904 (2005).
35. D. Passeri, A. Bettucci, M. Germano, M. Rossi, A. Alippi, V. Sessa, A. Fiori, E. Tamburri, and M. L. Terranova, *Appl. Phys. Lett.* **88**, 121910 (2006).
36. D. Passeri, M. Rossi, A. Alippi, A. Bettucci, D. Manno, A. Serra, E. Filippo, M. Lucci, and I. Davoli, *Superlattices Microstruct.* **44**, 641–649 (2008).
37. G. Stan, and W. Price, *Rev. Sci. Instrum.* **77**, 103707 (2006).
38. F. Marinello, P. Schiavuta, S. Vezzù, A. Patelli, S. Carmignato, and E. Savio, *Wear* **271**, 534–538 (2011).
39. D. Passeri, M. Rossi, and J. J. Vlassak, *Ultramicroscopy* **128**, 32–41 (2013).
40. D. Passeri, A. Biagioni, M. Rossi, E. Tamburri, and M. L. Terranova, *Eur. Polym. J.* **49**, 991–998 (2013).
41. M. C. Guimarães Rocha, M. E. Leyva, and M. G. de Oliveira, *Polimeros* **24**, 23–29 (2014).
42. V. Mathur, K. S. Rathore, and K. Sharma, *World Journal of Nano Science and Engineering* **3** (2013).
43. A. Shojaei, and G. Li, *Proc. R. Soc. A* **470** (2014).
44. D. C. Hurley, and J. A. Turner, *J. Appl. Phys.* **102**, 033509 (2007).
45. A. S. Babal, R. Gupta, B. P. Singh, and S. R. Dhakate, *RSC Adv.* **5**, 43462–43472 (2015).
46. P. Vairac, J. Le Rouzic, P. Delobelle, and B. Cretin, "Scanning Microdeformation Microscopy: Advances in Quantitative Micro- and Nanometrology," in *Acoustic scanning probe microscopy*, edited by F. Marinello, D. Passeri, and E. Savio, Springer Berlin Heidelberg, 2012, chap. 8, pp. 227–259.
47. E. Tamburri, S. Orlanducci, M. L. Terranova, F. Valentini, G. Palleschi, A. Curulli, F. Brunetti, D. Passeri, A. Alippi, and M. Rossi, *Carbon* **43**, 1213–1221 (2005).
48. D. Sordi, S. Orlanducci, E. Tamburri, D. Passeri, M. Lucci, and M. L. Terranova, *Carbon* **43**, 2227–2234 (2011).
49. E. Tamburri, V. Guglielmotti, R. Matassa, S. Orlanducci, S. Gay, G. Reina, M. L. Terranova, D. Passeri, and M. Rossi, *J. Mater. Chem. C* **2**, 3703–3716 (2014).
50. D. Passeri, E. Tamburri, M. L. Terranova, and M. Rossi, *Nanoscale* **7**, 14358–14367 (2015).

Melania REGGENTE

Synthèse et caractérisation multiéchelle de matériaux et de systèmes pour applications biomédicales

Résumé

Des matériaux sandwichs fabriqués sans colle époxy on été conçu pour réduire les contraintes mécaniques, ou “stress shielding”, entre l’os environnant et l’implant. Le titane (Ti) et le polyméthacrylate de méthyle (PMMA) sont les matériaux les plus utilisés dans les applications biomédicales, et on été choisi comme composants de base. Pour cela, on a élaboré des interfaces Ti/polymère dans lesquelles le métal et le polymère sont liés par une liaison covalente; cette couche de polymère permettra ultérieurement l’adhésion entre le métal et une feuille de polymère qui constituera le cœur du sandwich.

Dans ce but, une stratégie en trois étapes permettant d’obtenir une fonctionnalisation de la surface du titane a été développé. Tout d’abord, la surface du Ti a été activée chimiquement; ensuite un initiateur de polymérisation y a été greffé de façon covalente. Enfin, la croissance des chaines polymères a été obtenue en utilisant une polymérisation par transfert d’atomes à partir de l’initiateur (SI-ATRP). Les sandwichs ont été préparés en insérant une feuille de polymère entre les deux feuilles de Ti recouvertes de polymère greffé et en pressant les trois composants à une température supérieure à celle de la transition vitreuse du polymère.

Mots-clés: Titanium, Polyméthacrylate de méthyle, Adhésives, Biomatériaux.

Résumé en anglais

A procedure aimed at designing innovative epoxy resin-free sandwich materials (i.e., layered structure composed of two metal skin and a polymer core) able to reduce stress-shielding effect at the implant/bone interface was developed. For this purpose, titanium (Ti) and poly methymethacrilate (PMMA), the most extensively materials used for biomedical applications, were employed. In particular, surface-confined PMMA layers were proposed as adhesives to stick a PMMA foil (used as core of the structure) on the metallic Ti skin sheets exploiting the miscibility between the tethered polymer chains (previously grown on the Ti) and those of an adhering PMMA foil.

To this purpose, a three steps strategy based on a suitable functionalization of Ti surface was developed. First of all, a chemical activation of Ti surface was performed. Then, a “grafting from” method was used to immobilize a polymerization initiator on the activated Ti surface. Finally, the polymer chains were grown from the initiator-modified surfaces using a surface initiation atom transfer radical polymerization (SI-ATRP). Biocompatible Ti/PMMA/Ti sandwiches were then prepared by hot-pressing, inserting between the two PMMA-coated Ti surfaces a thick PMMA foil.

Keys-words: Titanium, Poly methymethacrilate, Adhesives, Biomaterials.